U.PORTO
FACULDADE DE CIÊNCIAS
UNIVERSIDADE DO PORTO

PhD

3.º
CICLO

FCUP
2017

U.PORTO

Sea Level Studies in Indonesia from Improved Coastal Satellite Altimetry

Eko Yuli Handoko

FC

U.PORTO
FACULDADE DE CIÊNCIAS
UNIVERSIDADE DO PORTO

Sea Level Studies in Indonesia from Improved Coastal Satellite Altimetry

Eko Yuli Handoko

Tese de Doutoramento apresentada à
Faculdade de Ciências da Universidade do Porto,
Engenharia Geográfica

2017

PhD

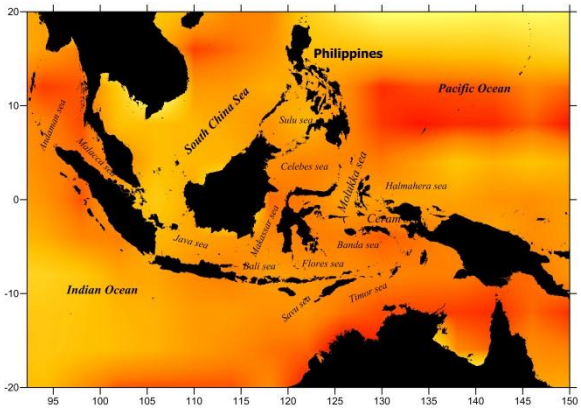

Sea Level Studies in Indonesia from Improved Coastal Satellite Altimetry

Eko Yuli Handoko
Engenharia Geográfica
Departamento de Geociências, Ambiente e Ordenamento do Território
2017

Orientador
Maria Joana Afonso Pereira Fernandes, Professor Auxiliar, Faculdade de Ciências, Universidade do Porto

Coorientador
Maria Clara Gomes Quadros Lázaro da Silva, Professor Auxiliar, Faculdade de Ciências, Universidade do Porto

This page is intentionally left blank

I would like to dedicate this work for my wife and my lovely daughter Ilona K. Handoko and to the memory of my mother (1953 – 2012) and my father (1948 – 2014).

This page is intentionally left blank

ABSTRACT

A number of sea level studies have pointed out that the rates of global mean sea level rise during the altimeter era (1992 – 2016) vary in the range of 3.0 and 3.4 mm/year. However, the sea level is not rising uniformly across the globe, e.g. the western tropical Pacific Ocean has a rate up to three times the global mean rate. The Indonesian seas, enclosed by the western Pacific Ocean, are included in the areas with the highest sea level variability. Due to its high vulnerability to the impact of sea level rise, the continuous monitoring of sea level variability in the Indonesian seas, where about 60% of the Indonesian population lives in coastal zone or low-elevation areas, becomes urgent.

Using the dense coverage, continuity, repeatability and homogeneity of satellite altimetry data, sea level can be mapped with centimetric accuracy for almost the entire global oceans.

In order to obtain sea level variability with high accuracy using altimetric data, accurate range and geophysical corrections are required. The wet tropospheric correction (WTC) is one of the main errors in the retrieval of accurate sea surface heights from altimetry, particularly in the coastal regions. The objective of this study is to determine the sea level variation in Indonesia using satellite altimetry, with focus on the effects of the WTC.

In this study, all altimeter data and corresponding corrections were used as they are made available in the Radar Altimeter Database System (RADS) for all missions (TOPEX/Poseidon, Jason-1, Jason-2, ERS-1, ERS-2, Envisat, Cryosat-2 and SARAL/AltiKa), except for the GNSS-derive Path Delay Plus (GPD+) WTC, which were provided by the University of Porto, Portugal. For improving the GPD+ WTC around the Indonesian region, zenith total delays (ZTD) from a network of 27 GNSS stations in that area were computed. These data, together with additional WTC sources, were further incorporated into the GPD+ corrections. The evaluation of the WTC from various sources (on-board microwave radiometer (MWR), ERA Interim model and GPD+) was performed using SLA variance analysis: along-track analysis (spatial pattern and function of distance from the coast) and crossover analysis, to study their coastal effects and their quality. The results of this assessment indicate that the WTC from the GPD+ algorithm is an improved correction

with respect to both ERA Interim and MWR-derived WTC, presented in RADS for all missions, not only near the coast but also in open-ocean.

The best set of range and geophysical corrections and mean sea surface models that should be selected in the Indonesian region has been identified for all missions from the results achieved in this study.

The improved altimetric data sets have been used to estimate the sea level time series around the Indonesian Seas over the 24-year period (1993 – 2016). Results show that the sea level rise in this period is 4.7 mm/year. If a correction of 0.3 mm/year due to the Glacial Isostatic Adjustment (GIA) is applied, the rate of sea level rise is 5.0 mm/year. Since the sea level variability around the Indonesian seas is highly influenced by the El Niño – Southern Oscillation (ENSO) phenomenon, the correlation between sea level variation and ENSO indices was performed. The three ENSO indices, the Multivariate ENSO Index (MEI), the regional sea surface temperature (SST) or Oceanic Niño Index (ONI) and the surface atmospheric pressure-based Southern Oscillation Index (SOI) were used. Results show that there are strong correlations between sea level anomalies in the Indonesian seas and these ENSO indices. The detrended SLA time series have a negative correlation of -0.84 and -0.85 with MEI and ONI, respectively, and a strong positive correlation of 0.7 with SOI.

RESUMO

Vários estudos sobre o nível do mar apontaram para taxas de aumento do nível médio do mar durante a era da altimetria por satélite (1992 - 2016) variam na faixa de 3,0 e 3,4 mm / ano. No entanto, o nível do mar não tem aumentado de forma uniforme em todo o globo. A zona tropical do Oceano Pacífico ocidental tem uma taxa até três vezes superior à taxa média global. Os mares indonésios, adjacentes ao Oceano Pacífico ocidental, estão incluídos nas áreas com maior variabilidade do nível do mar. Devido à sua alta vulnerabilidade ao impacto do aumento do nível do mar, o estudo contínuo da variabilidade do nível do mar nos mares indonésios, onde cerca de 60% da população indonésia vive em zonas costeiras ou áreas de baixa elevação, torna-se urgente.

Devido à cobertura densa, continuidade, repetibilidade e homogeneidade dos dados de altimetria por satélite, o nível do mar pode ser mapeado com precisão centimétrica para quase todos os oceanos globais.

Para se obter uma variabilidade do nível do mar com alta precisão utilizando dados altimétricos, é necessário ter a medida da distância do satélite à superfície o mar (*range*) com precisão, bem como as várias correções geofísicas. A correção troposférica húmida (WTC) é um dos principais erros na recuperação de alturas precisas da superfície do mar através da altimetria, particularmente nas regiões costeiras. O objetivo deste estudo é determinar a variação do nível do mar na Indonésia usando a altimetria por satélite, com foco nos efeitos da WTC.

Neste estudo foram usados todos os dados altimétricos e correções correspondentes disponíveis no Radar Altimeter Database System (RADS) para todas as missões (TOPEX / Poseidon, Jason-1, Jason-2, ERS-1, ERS-2, Envisat, Cryosat-2 e SARAL / AltiKa), exceto a WTC designada GNSS-derived Path Delay Plus (GPD+), uma correção fornecida pela Universidade do Porto, Portugal. Para melhorar a GPD+ WTC em torno da região indonésia, foram processados atrasos totais zenitais (ZTD) de uma rede de 27 estações GNSS naquela área. Estes dados, juntamente com fontes de WTC adicionais, foram incorporados nas correções GPD+. A avaliação da WTC de várias fontes (radiómetro de micro-ondas a bordo de cada satélite (MWR), modelo atmosférico ERA e GPD+) foi efetuada utilizando análises de variância da anomalia do nível do mar (SLA): análises ao longo do traço do satélite

(padrão espacial e função da distância à costa) e análises mos pontos de cruzamento dos traços dos satélites (*crossovers*), para se estudarem os efeitos costeiros e a sua qualidade. Os resultados desta avaliação indicam que o WTC a partir do algoritmo GPD+ produz uma correção melhorada em relação ao modelo ERA Interim e ao WTC obtido a partir do MWR disponível no RADS para todas as missões, não só nas zonas próximas da costa, mas também em oceano aberto.

Os conjuntos de dados com as correções geofísicas e os modelos da superfície média do mar que devem ser selecionados na região indonésia foram identificados para todas as missões, a partir dos resultados alcançados neste estudo.

Os conjuntos de dados altimétricos melhorados foram utilizados para estimar a série temporal do nível do mar para os mares indonésios., para um período de 24 anos (1993 - 2016). Os resultados mostram que o aumento do nível do mar neste período é de 4,7 mm / ano. Se for aplicada uma correção de 0,3 mm / ano devido ao Ajuste Isostático Glacial (GIA), a taxa de aumento do nível do mar é de 5,0 mm / ano. Uma vez que a variabilidade do nível do mar em torno dos mares indonésios é altamente influenciada pelo fenómeno Oscilação Sul - El Niño (ENSO), foi analisada a correlação entre a variação do nível do mar e os índices ENSO. Foram também utilizados os três índices ENSO, o índice ENSO multivariante (MEI), a temperatura regional da superfície do mar (SST) e índice El-Niño oceânico (ONI) e o índice oscilação sul baseado na pressão atmosférica de superfície (SOI). Os resultados mostram que há fortes correlações entre anomalias do nível do mar nos mares indonésios e esses índices ENSO. As séries temporais SLA obtidas após remoção da tendência têm uma correlação negativa de -0,84 e -0,85 com MEI e ONI, respetivamente, e uma forte correlação positiva de 0,7 com SOI.

ACKNOWLEDGEMENTS

I would like to express my gratitude to all who have contributed to my work, helped and supported me during my time working on this thesis.

Firstly, I would like to express my sincere gratitude to my advisor Dr. Maria Joana Fernandes and Dr. Clara Lázaro for the continuous support of my PhD study and related research, for their patience, motivation, and immense knowledge. Their guidance helped me in all the time of research and writing of this thesis.

I express my appreciation to the Ministry of Research, Technology and Higher Education of the Republic of Indonesia for financially supporting my study at Faculdade de Ciencias, Universidade do Porto. And my appreciation for my institutions: Department of Geomatics, Institut Teknologi Sepuluh Nopember (ITS) Surabaya, colleagues and staff.

My thanks go to Mr. Mulya Wirana, Ambassador of the Republic of Indonesia and the staff of the Indonesian Embassy in Lisbon, Portugal and Sr. Luciano F. Coelho da Silva, Indonesian Honorary Consulate in Porto, Portugal.

My thanks also go to Dr. Andri Irfan Rifai, Dr. Boy Berawi, Dr. Ridha Djellabi, Akuat Supriyanto, Thommy Eko Saputro and all friends of the Indonesian Student of Association (PPI) in Portugal for all kindness.

I also want to thank all my colleagues at DGAOT-FCUP, Miguel Salgado, Nelson Pires, Telmo Vieira and Eliana Vieira for the altimetry discussions.

Finally, I would like to thank for all my family for love, pray and supports.

CONTENTS

LIST OF FIGURES

LIST OF TABLES

ABBREAVIATIONS

AVISO	Archiving, Validation and Interpretation of Satellite Oceanography data
AMR	Advanced Microwave Radiometer
BM4	4-Parameters SSB Model
CS2	CyroSat-2
CLS	*Collecte Localisation Satellites*
CNES	*Centre National d'Études Spatiales*
COASTALT	ESA development of COASTal ALTimetry
DEOS	Department for Earth Observation and space System
ECMWF	European Centre for Medium-Range Weather Forecasts
ENVISAT	ENVIronmental SATellite
ERA	ECMWF Re-Analysis
ERS	European Remote-Sensing Satellite
EUMETSAT	European Organisation for the Exploitation of Meteorological Satellites
FES	Finite Element Solution
GDR	Geophysical Data Record
GIA	Glacial Isostatic Adjustment
GIM	Global Ionosphere Map
GIPSY-OASIS	GNSS-Inferred Positioning System and Orbit Analysis Simulation
GMF	Global Mapping Function
GNSS	Global Navigation Satellite System
GOOS	Global Ocean Observing System
GOT	Goddard Ocean Tide Model
GPD	GNSS-derived Path Delay
GRACE	Gravity Recovery and Climate Experiment

GSLR	Global Sea Level Rise
IPCC	Intergovernmental Panel on Climate Change
JPL	Jet Propulsion Laboratory
LRM	Low-resolution Mode
MOG2D	2-D Gravity Waves Model
MWR	Microwave Radiometer
NASA	National Aeronautics and Space Administration
NCEP	National Centers for Environmental Prediction
NIC	NOAA Ionosphere Climatology
NOAA	National Oceanic and Atmospheric Administration
NWM	Numerical Weather Model
OSTM	Ocean Surface Topography Mission
OSTST	Ocean Surface Topography Science Team
RADS	Radar Altimeter Database System
SLA	Sea Level Anomaly
SLR	Sea Level Rise
SSM/I	Special Sensor Microwave Imager
STD	Slant Total Delay
SWH	Significant Wave Height
TB	Brightness Temperature
TCWV	Total Column Water Vapor
TEC	Total Electronic Content
TECU	Total Electronic Content Unit
TMR	TOPEX Microwave Radiometer
TOPEX	TOPography EXperiment
T/P	TOPEX/Poseidon

USO	Ultra-Stable Oscillator
VLM	Vertical Land Movement
VMF1	Vienna Mapping Functions 1
WTC	Wet Tropospheric Correction
ZHD	Zenith Hydrostatic Delay
ZPD	Zenith Path Delay
ZTD	Zenith Total Delay
ZWD	Zenith Wet Delay

CHAPTER 1
INTRODUCTION

Sea level rise (SLR) can be a serious problem in the future, related to the climate change. The long-term sea level change is a crucial indicator of climate change and variability due to its close relation with the ocean, cryosphere, hydrosphere, and atmosphere systems. Several factors including ocean tides, ocean circulation, atmospheric pressure and related phenomena can cause sea level change, but the dominant contributions arise from changes in ocean heat content (thermal expansion) and the exchange of water between the ocean and the continents as a result of the melting of glaciers and ice sheets (Cazenave and Nerem, 2004).

The future projection of SLR in 2100, based on the Fifth Assessment Report (AR5) of the Intergovernmental Panel on Climate Change (IPCC), ranges from 44 to74 cm (Church et al., 2013). This prediction may be an important indicator, particularly for countries located in low-lying areas. Sea level change is likely to have a significant economic and social impact, particularly in the coastal regions where human activities are more concentrated. Sea level rise may cause inundation of low-lying areas, flooding, salt seawater intrusion into surface water and aquifers. Furthermore, these effects have a significant impact on national socio-economics, infrastructure and environment due to land-loss around coastal areas, where more than 10 % of the world's population lives (McGranahan et al., 2007).

Since the end of 19^{th} century, tide gauges have been installed to record sea level variability along coastlines and islands although in limited amount and distribution in some regions of the world. Tide gauge measurements in the 20^{th} century (1900 to 2009) indicated that the mean rate of sea level rise was 1.6 - 1.8 mm yr^{-1} (Church and White, 2011). Tide gauge measurements have some limitations due to their density of distribution, local impacts and are particularly affected by vertical land movements such as land subsidence (Wöppelmann and Marcos, 2016; Yildiz et al., 2013).

The era of satellite altimetry brought revolution in sea level measurement. TOPEX/Poseidon (T/P), Jason-1, Jason-2 and Jason-3 measure the entire global sea level up to ±66° latitudes in 10 days, providing precise and continuous datasets for sea level studies with global coverage and moderate spatiotemporal resolution. Simultaneously, ERS-1 (except

for the periods corresponding to ERS-1 ice and geodetic phases), ERS-2 and Envisat, and SARAL missions cover the ocean every 35 days within latitudes up to ±81.5°; Cryosat-2 can reach latitudes of 88° north and south, improving coverage when compared to the previous missions.

Currently, global sea level rise (GSLR) observed by satellite altimetry has been estimated to be about 3.1 – 3.4 mm/year (Ablain et al., 2009; Ablain et al., 2016; Cazenave et al., 2014; Church et al., 2013).

A satellite altimeter measures the vertical range between the satellite and the sea surface. It emits a short pulse of microwave radiation from the on-board radar antenna toward the sea surface, part of the signal being reflected back to the satellite. By measuring the two-way travel time of the signal, the range can be determined. Thus, the sea-surface height (SSH) is obtained by the difference between the satellite height above the reference ellipsoid and the range of the satellite to the sea surface.

In spite of the simple principle of the range measurement from satellite altimetry, the technical challenges to get accurate measurements are substantial. Not only precise satellite orbit determination, but also the precise knowledge of the corrections that affect the range measurement is required. Each of the corrections that must be applied to the measured range for accurate determination of SSH must be known with centimetric accuracy. These include instrument corrections, atmospheric refraction corrections (dry and wet troposphere and ionosphere), sea-state bias and geophysical corrections (tides and atmospheric pressure loading) (Chelton et al., 2001)

1.1 Motivation

As one of the largest archipelagic countries, Indonesia is characterized by its unique geographical and geophysical setting. Indonesia consists of 17,600 islands, 81,000 km of coastline and 5.8 million km^2 of sea area. The Indonesian population was approximately 255 million people in 2015 based on the Statistics Indonesia, around 60% of the population lives in coastal zones (Dahuri et al., 2008). Because of these reasons, Indonesia becomes a vulnerable country which is affected by sea level rise. Due to the unique characteristics of Indonesia, understanding sea level changes in this area is crucial. Considering the potential impacts of sea-level rise in this region, the continuous monitoring of sea level variability becomes urgent.

In order to monitor sea level variability around the Indonesian seas with high precision using satellite altimetry, the specific characteristics of this region must be taken into account, namely the fact that is a region with thousands of islands. Sea level anomaly (SLA) estimated with respect to a mean sea surface (MSS) is a common variable used in sea level studies. The determination of SLA from altimeter measurements requires the correction for all instrument, range and geophysical corrections. However, particular problems arise when satellite altimetry approaches the coastal zone. The altimeter waveform measurements are influenced by the noisier return signals, which are contaminated by land. The less reliable range and geophysical corrections in coastal regions are also important factors contributing to measurement degradation (Gommenginger et al., 2011). Several improvements are needed to overcome the specific problems in the coastal areas. Re-tracking is used to retrieve altimeter data near the coast. Specific re-tracking algorithms are expected to give better accuracy than the standard open ocean retrackers. Coastal effects which induce inaccuracies in the modeling of atmospheric and geophysical effects must be accounted for and need more attention. The wet tropospheric correction (WTC) derived from the on-board microwave radiometer (MWR) is still a significant uncertainty in coastal regions due to land contamination in the MWR footprint, a circle of 10-40 km diameter depending on the frequency. The global tide models still do not perform well in the coastal zone. Local models are also needed to improve global ocean tide models, which in general possess large errors near the coast. Although the sea state bias (SSB) correction is not the largest error source, a proper model is still needed in coastal areas to mitigate errors present in the empirical models. The ionosphere delay correction from dual frequency is influenced when the C-band or S-band altimeter footprint approaches the land. In the absence of specific corrections dealing with these effects, model-based corrections can be used, at the cost of losing some accuracy.

1.2 Objective of this thesis

Currently, satellite altimetry has turned into an important tool in sea level studies, due to its ability to measure sea level in a relatively short revisit time and with global coverage. Continuously updated data are available. However, many factors influence the estimation of sea level variability from satellite altimetry, primarily, the characteristics of the sensors and their long-term stability, and data processing methods. For the long-term estimation of sea level, it is important to ensure the consistency and stability of altimetry measurements. One factor that causes uncertainty in satellite altimetry is the path delay due to water vapor in the

atmosphere; this is called the symmetric of the WTC. Although the absolute value of the WTC is only about 50 cm, it has high variability, both in space and time, thus not being easy to model.

In the open ocean, the WTC can be retrieved within a few cm accuracy using on-board microwave radiometers. However, this does not apply to the coastal regions. The differences between ocean emissivity (around 0.5) and land emissivity (around 0.9) cause the radiometer footprint, as it approaches the coast, to contain portions of surfaces with different emissivity. Therefore, the WTC ocean retrieval algorithm originates invalid measurements in the regions close to the coast or land.

As an alternative to the WTC from on-board microwave radiometers, a number of atmospheric models, such as European Centre for Medium-Range Weather Forecasts (ECMWF) and National Centers for Environmental Prediction (NCEP), which provide data on regular grids, can be used to derive tropospheric path delays. Aiming at reducing the WTC errors, particularly in coastal regions where the on-board microwave radiometer measurements become invalid due to land contamination in the radiometer footprint, the Global Navigation Satellite System (GNSS)-derived Path Delay (GPD) algorithm was proposed by the University of Porto (UPorto), Portugal (Fernandes et al., 2010). The GPD is a method to determine the troposphere wet path delays (WPD) by space-time objective analysis from the combination of data from various sources. Global GPD solutions have been derived by UPorto for the main altimetry missions using many GNSS stations in coastal and island regions, in combination with all available valid WPD data sources (Fernandes et al., 2015).

The objective of this thesis is to study the sea level in Indonesia by (1) improving methodologies for retrieving satellite altimetry data sets in the coastal regions, with particular emphasis on the WTC, and (2) estimating the sea level variation using the improved satellite altimetry data sets.

The thesis focuses on the analysis of sea level variability in the Indonesian seas for the latitude range 20^{o}N – 20^{o}S and longitude range 90^{o}E – 150^{o}E. The area covers all the Indonesia seas surrounded by the west Pacific Ocean, the eastern Indian Ocean and the South China Sea.

In order to study the sea level variability around the Indonesian seas, several datasets have been prepared. Data from the so-called reference altimetric missions (TOPEX/Poseidon,

Jason-1 and Jason-2) have been extracted from the Radar Altimeter Database System (RADS), developed by the Delft Institute for Earth-Oriented Space Research (DEOS) and the NOAA's Laboratory for Satellite Altimetry (Scharroo, 2012). The data cover a period of more than 24 years (1993 – 2016). For complementarity, this study also used ESA altimetric missions (ERS-1, ERS-2 and Envisat), and other satellites such as Cryosat-2 and SARAL.

In order to improve the WTC in the Indonesian region based on the GPD approach, a local network of nearly 30 GNSS stations (hereinafter referred to as the Indonesian Network (INA network)) located mostly along Sumatera Island has been used to improve the GNSS coverage in the Indonesian region. Zenith Total Delays (ZTD) from GNSS stations were computed by the Precise Point Positioning (PPP) technique (Zumberge et al., 1997) using the GNSS-Inferred Positioning System and Orbit Analysis Simulation (GIPSY-OASIS) software package. To assess the accuracy of this set of ZTD computed for the INA network, this solution has been compared with the ZTD provided by the International GNSS Service (IGS). In addition, the Zenith Wet Delays (ZWD) from the local GNSS stations not used in the GPD WTC computation was used to evaluate the GPD WTC.

To assess the various wet tropospheric corrections, the analyses of the coastal effects on satellite altimetry using SLA variance were performed. Moreover, the suitability of other range and geophysical corrections and MSS models in this region was also studied. The assessment was based on SLA variance analyses, in particular along-track analysis (spatial pattern and function of distance from the coast) and crossover analysis (with a maximum time lag of 10 days). Using the improved datasets, SLA time series for the Indonesian region were derived and sea level variation in this region was estimated.

1.3 Thesis Outline

This thesis has been organized in six chapters as follows:

Chapter 1 *Introduction*; this chapter contains a general introduction and the objective of the thesis.

Chapter 2 *Satellite Altimetry: from Open Ocean to the Coastal Zone*; this chapter presents an overview of the main altimeter missions and the principles of satellite altimetry. The specific issues in coastal altimetry, corresponding to the factors that cause measurement degradation near the coast, and the techniques for correction of these effects (such as atmospheric corrections: dry and wet tropospheric corrections and ionospheric corrections,

sea state bias, tides corrections and mean sea surface are also described in this chapter. Moreover, an overview of the challenges of satellite altimetry in coastal areas is presented.

Chapter 3 *Sea Level Change*; gives a brief overview of the issues related with the sea level change. The causes of sea level variation: thermal expansion, land ice melting and non-climatic contribution are described in this chapter. The methods for determining sea level are also described, the direct methods (tide gauge measurement and satellite altimetry observations), and indirect sea level observations (using satellite gravity, temperature and salinity measurements). The last section of this chapter presents the impact of sea level change and future projections.

Chapter 4 *Wet Tropospheric Correction and its improvement*; describes the modeling of the WTC in the context of satellite altimetry. This chapter presents the most common methods to derive the WTC such as on-board microwave radiometers and numerical weather models (NWM). Moreover, the GNSS-derived Path Delay (GPD) method is also introduced as an improving method for the WTC estimation, particularly in the coastal regions such as the Indonesian seas. The processing of GNSS data, particularly for the local network around the Indonesia region (INA network), was performed to determine ZTD for further input into the GPD algorithm. In addition, this chapter also presents the analysis and implementation of improved WTC for altimeter data in the Indonesian region. In this chapter, the inter-comparison of various WTC, the assessment of the impact of different WTC on sea level change, and the assessment of the GPD WTC around Indonesian seas were performed.

Chapter 5 *Sea Level Variability around the Indonesian Seas*; presents the study area, corresponding to the Indonesian seas, and its unique characteristics. The estimation and analysis of the sea level variability using improved data sets, particularly for the wet tropospheric correction, is presented here. The sea level variability derived from SLA time series based on the reference-missions, the ESA missions, CryoSat-2 and SARAL, and multi-altimeter-missions are analyzed. The analysis of the sea level variability related to the El Niño – Southern Oscillation (ENSO) event in the Indonesian seas were performed using three ENSO indices: Multivariate ENSO Index (MEI), Oceanic Niño Index (ONI) and Southern Oscillation Index (SOI).

Chapter 6 *Conclusion*; presents the concluding remarks and recommendations for future research associated with this study.

CHAPTER 2

SATELLITE ALTIMETRY: FROM OPEN OCEAN TO THE COASTAL ZONE

The Earth observation from space using satellites brings objective coverage in both space and time. The sensors onboard remote sensing satellites gather data over the globe, including the places that are inaccessible for ground-based data acquisition. By continuously observing the Earth in the long-term, the satellites can highlight environmental changes and enable a reliable assessment of the global impact of human activity and the likely future extent of climate change.

Satellite radar altimetry is a remote sensing technique that allows the Earth's monitoring with all-weather, day and night capability. Satellite altimetry was developed in the 1960s starting with the launch of Skylab in 1973. The precise era of altimetry began in the 1990s after the European Space Agency (ESA) satellite the European Remote Sensing (ERS)-1 and TOPEX/Poseidon (T/P), a joint satellite program between National Aeronautics and Space Administration (NASA, US) and Centre National d'Études Spatiales (CNES, France), launched in 1991 and 1992, respectively. Since then, satellite altimetry became the main tool for precisely and continuously measuring sea level, due to its near global coverage and relatively short revisit time. An overview of satellite altimetry missions is described in Section 2.1.

The satellite measures the height of the spacecraft above the ocean surface, called range measurement. The absolute sea level and the variations in sea level can be inferred by subtracting the range measurement from the altitude of the satellite above a reference ellipsoid. Details of the principle of satellite altimetry and sea level anomaly (SLA) determination, the variable often used in studies of sea level variability are described in Section 2.2. The knowledge of corrections is needed to derive precise SLA. Section 2.3 describes the corrections, including the atmospheric corrections (dry and wet tropospheric corrections and ionospheric correction), sea state bias, and tides. In the coastal region, satellite altimetry faces various difficulties related with the land contamination in the

altimeter and radiometer footprints, resulting in systematic flagging and rejection of altimeter data in these regions. The present challenges in coastal altimetry are presented in section 2.4.

2.1. Overview of the Altimetry Missions

Historically, as seen in Figure 2.1, satellite altimetry began in the pioneering era when a series of early missions was launched: Skylab, GEOS-3 and Seasat. The primary objective of the Skylab altimeter experiment was to determine the engineering feasibility of the altimeter instrument and demonstrate its capability for making measurements of the sea surface topography (Mourad et al., 1975). Two years later, in April 1975, the Geodynamics Experimental Ocean Satellite (Geos-3) was launched, which was designed to improve the knowledge of the Earth's gravitational field, the size and shape of the terrestrial geoid, deep ocean tides, sea state, current structure, crustal structure, solid earth dynamics and remote-sensing technology (Stanley, 1979). The Seasat satellite, which was launched in June 1978, brought an instrument operating at 13.5 GHz, a single frequency radar system that made range measurements using only a 1-m parabolic antenna pointed at the satellite nadir (Townsend, 1980). The US Navy geodetic satellite (GEOSAT) which was launched on 12 March 1985, into an 800 km altitude and 108^{o} inclination non-repeat orbit, was maneuvered into a 17.05-day repeat orbit on 8 November 1986. It was the first mission to provide long-term altimetry data with the primary task of measuring the marine geoid for the US Navy (Wakker et al., 1993).

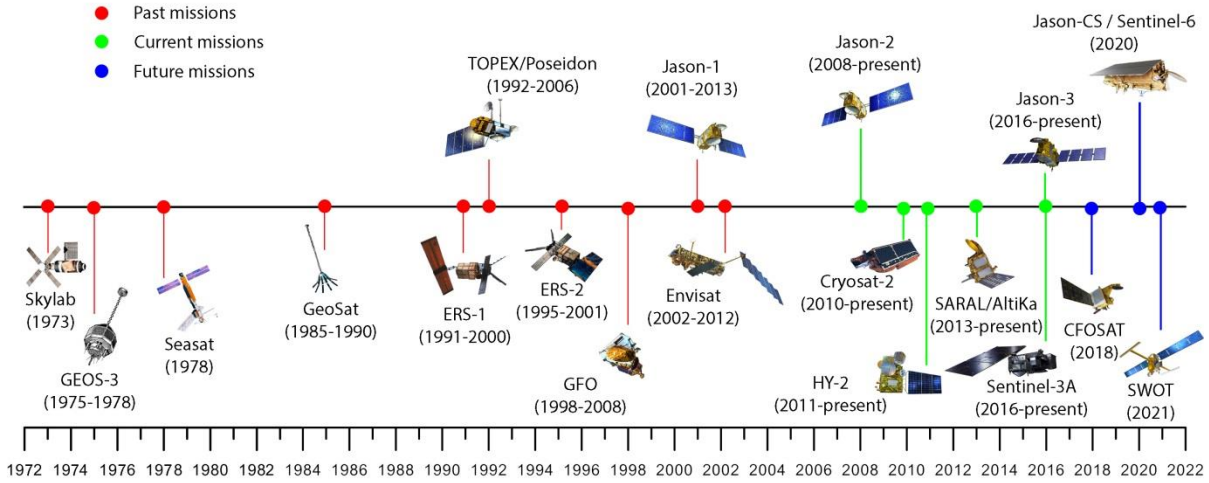

Figure 2.1 Satellite altimetry missions: past, present and future (source: www.aviso.altimetry.fr)

The satellite altimeters used in this study are shown in Table 2.1. The ESA has been building a set of altimeter missions to observe the Earth, starting with the launch of the satellites: ERS-1 and ERS-2. The objective of these satellites was to observe the Earth, in particular its ocean and atmosphere systems. The ERS-1 was the first European Earth observation satellite which used microwave sensors (Scharroo, 2002). It was launched in July 1991 and placed into an orbit with an altitude of about 790 km and an inclination of 98.5^{o}. The ERS-2, the follow-on from ERS-1, was launched in April 1995 into an identical orbit (35-day repeat cycle). Envisat was the follow-on altimetry mission to ERS-1 and ERS-2. This new mission supports ten different onboard instruments dedicated to the global observation of the environment, for observing from the marine geoid to high-resolution gaseous emissions (Soussi et al., 2011). The orbital repeat period of Envisat was 35 days during 2002 to October 2010. Since November 2010, Envisat changed the repeat cycle to 30 days with 431 orbits per cycle. Envisat mission ended on May 9^{th}, 2012 after Envisat has stopped sending data in April 2012.

Meanwhile, the Joint Mission between NASA and CNES was developing the Topography Experiment (TOPEX) and Poseidon (T/P). The T/P satellite was launched in August 1992. This mission had an altitude of 1336 km with an inclination of 66^{o}, an equatorial cross-track separation of 316 km, and made sea surface height measurements along the same surface track, within ±1 km, every 9.916 days (~10 days). The main science objective was to improve the knowledge of the global ocean circulation for understanding of the ocean's rule in global climate change. After ten years in the original ground track orbit, T/P shifted to the interleaved orbit since September 2002 (cycle 368, pass 171), with Jason-1 (J1) occupying the original ground track thereafter.

In 2001, J1 was successfully launched, following the previous mission, TOPEX/Poseidon. The main objective of the mission was to maintain the high accuracy altimeter measurements, ensure continuity in observing and monitor the ocean for intra-seasonal to inter-annual changes, mean sea level and tides (Ménard et al., 2003). J1 was a mini-satellite, with four times less mass and power than T/P and its orbit was the same as T/P. J1 payload includes the same package as for T/P, but some upgraded instruments, example Jason-1 Microwave Radiometer (JMR). After the launch of OSTM/Jason-2 (J2) and several months of tandem mission with J2, J1 was moved to a new interleaved orbit. After 11.5 years of operation, Jason-1 terminated on July 1^{st} 2013.

Table 2.1 Satellite Altimetry missions used in this study

Altimeter	Start and End Missions	Inclination	Altitude	Band	Repeat Period	Microwave Radiometer
ERS-1	July 1991 – March 2000	98.5^{o}	790 km	Ku-band (13.8 GHz)	Phase A, B and D : 3 days Phase C & G: 35 days Phase E & F: 168 days	23.8 GHz and 36.5 GHz
TOPEX/ Poseidon	August 1992 – September 2002	66^{o}	1336 km	Ku-band (13.6 GHz) C-band (5.3 GHz)	9.9 days	TMR 18 GHz, 21 GHz and 37 GHz
ERS-2	April 1995 – September 2011	98.5^{o}	790 km	Ku-band (13.8 GHz)	35 days	23.8 GHz and 36.5 GHz
Jason-1	December 2001 – July 2013	66^{o}	1336 km	Ku-band (13.6 GHz) C-band (5.3 GHz)	9.9 days	JMR 18.7 GHz, 23.8 GHz and 34 GHz
Envisat	March 2002 – May 2012	98.5^{o}	790 km	Ku-band (13.6 GHz) S-band (3.2 GHz)	35 days	23.8 GHz and 36.5 GHz
Jason-2	June 2008 – present	66^{o}	1336 km	Ku-band (13.6 GHz) C-band (5.3 GHz)	9.9 days	AMR 18.7 GHz, 23.8 GHz and 34 GHz
CyroSat-2	April 2010 – present	92^{o}	717 km	Ku-band (13.6 GHz)	360 days with 30 day sub-cycle	Not Available
SARAL	February 2013 – present	98.5^{o}	790 km	Ka-band (35.7 GHz)	35 days	23.8 GHz & 37 GHz

J2 was launched on June 8th 2008 and took over and continued T/P and J1 missions. This mission is under cooperation of NASA (US), CNES (France), European Organisation for the Exploitation of Meteorological Satellites (EUMETSAT) and National Oceanic and Atmosphere Administration (NOAA). The main objectives of this mission are to establish a multidecadal climate record to allow scientists to study global sea level rise and to better understand how ocean circulation and climate change are related. After more than 8 years of service on this nominal ground track, Jason-2 shifted to the interleaved orbit since October 2016 that was used by T/P from 2002-2005 and J1 from 2009-2012. The new successor of T/P, J1 and J2 is Jason-3 (J3), which was launched on 17th of January 2016. The objective of this mission is to extend the high-precision ocean altimetric data record to support climate monitoring, operational oceanography and seasonal forecasting. J3 uses the same repeat track as T/P and Jason series. These sets of altimetric missions are often called reference missions.

SARAL (SAtellite for ARgos and AltiKa) is a follow-on mission to ENVISAT ESA's mission and uses the same ground track. SARAL/AltiKa is a new collaboration between CNES and ISRO (Indian Space Research Organization). The AltiKa is based on a Ka-band altimeter (35.75 GHz), the first oceanographic altimeter using such a high frequency. The use of the Ka-band frequency supplies more accurate measurements (improvement of the spatial and vertical resolution) enabling a better observation of ocean mesoscale, ice, coastal areas, continental water bodies as well as waves height. The drawback of this Ka-band frequency is its sensitivity to rain that can lead to signal attenuation (Bronner et al., 2013). Using a single high frequency, the effect of ionosphere is small due to the fact that the ionospheric correction is function of the inverse of the squared frequency). The main advantage of this higher frequency (Ka versus Ku/C altimeters) is the reduced altimeter footprint that leads to a better spatial resolution. A dual-frequency Microwave Radiometer (23.8 GHz / 37 GHz) is used to correct altimetry measurements from wet troposphere effects. The 23.8 GHz channel is the primary water vapor sensing channel, meaning higher water vapor concentrations will lead to larger 23.8 GHz brightness temperature values. The addition of the 37 GHz channel, which has less sensitivity to water vapor, facilitates the removal of the contributions from cloud liquid water, which also acts to increase the 23.8 GHz brightness temperature. The SARAL sun-synchronous satellite flies on the same ground-track as ENVISAT with a 501-orbit, 1002-pass, 35-day repeat cycle, at 98.55^{o} of inclination and about 800 km of altitude.

Most altimeter sensors such as TOPEX/Poseidon, Jason-1, Jason-2, ERS-1/2 and Envisat use the pulse-limited or low-resolution mode (LRM). The signal is transmitted from the antenna towards the sea surface point at nadir and its echo is reflected back to the antenna. The footprint, the area of the reflecting surface illuminated by the altimeter, is approximately a circle with a diameter of about 7-10 km depending on the altitude of the satellite, surface slope and roughness. Unlike conventional radar altimeters, the Synthetic Aperture Radar (SAR) altimeter mode performs with a higher spatial resolution than LRM, for example, by Cryosat-2. In this mode, the radar footprint is divided into strips of cells (Doppler cells) and the pulse-repetition frequency is increased to allow coherent processing of the echoes along-tracks. This improves the resolution up to 300 m in the along-track direction (Wingham et al., 2006; Ricker et al., 2015), being an added value to coastal altimetry.

Cryosat-2, an altimeter mission with special emphasis on land and marine ice monitoring, carries a Synthetic Interferometry Radar ALtimeter (SIRAL) and is the first SAR

altimeter, with an along-track resolution of approximately 250 m (ESA, 2012; Ray et al., 2015). The primary objective of Cryosat-2 radar altimeter mission is to measure the extent of thinning Artic ice due to climate change. The mission, launched on the 8th of April 2010, flies in an orbit at 717 km, with 92^{o} of inclination, and reaches latitudes of 88^{o}. SIRAL is the primary instrument onboard Cryosat-2 and has extended capabilities to meet the measurement requirements for ice-sheet elevation and sea-ice freeboard. Over the oceans and ice-sheet interiors, Cryosat-2 operates like a traditional radar altimeter in LRM. Over sea ice, coherently transmitted echoes are combined via SAR processing, to reduce the surface footprint so that Cryosat-2 can map smaller ice floes. This mode is used to carry out high-resolution measurements of floating sea ice and land ice-sheets, enabling the indirect measurement of sheet's thickness.

2.2. Principle of Satellite Altimetry

The principle of satellite altimetry can be explained as shown in Figure 2.2. The short pulse of microwave radiation is emitted from the on-board radar altimeter toward the sea surface point at nadir and is partly returned back to the satellite, its round-trip travel time being measured by the ultra-stable oscillator (USO).

The observation range (R_{obs}) is the range between the instantaneous sea surface and the spacecraft antenna, which is determined from the travel time of the radar pulse (t) and the speed of the radar pulse (c), as expressed by the following equation:

$$R_{obs} = {}^{c.t}/_{2} \tag{2.1}$$

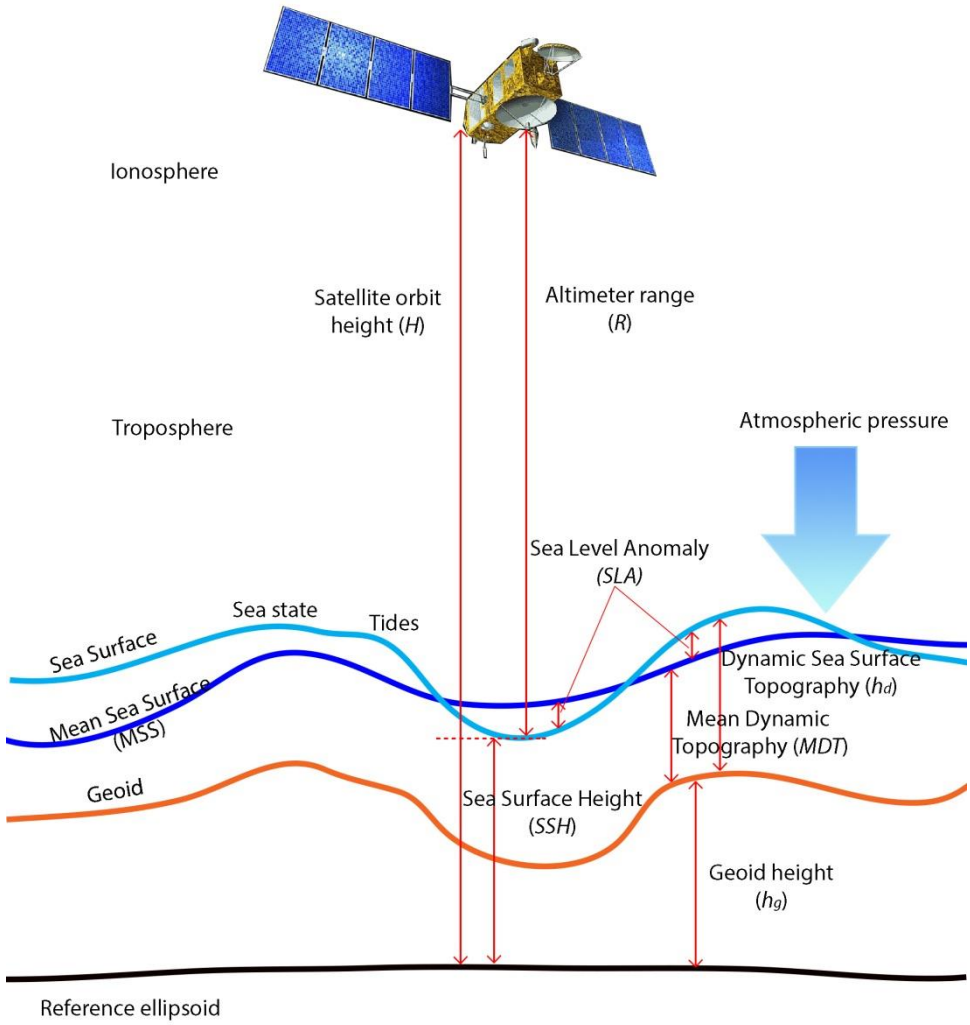

Figure 2.2 Basic principle of satellite altimetry (Andersen and Scharroo, 2011)

However, several corrections must be applied to the observed altimeter range before it can be used to determine the sea surface height (SSH). SSH is the height (h) of the sea surface relative to the reference ellipsoid. Equation 2.2 shows the relationship among SSH (h), satellite height above a reference ellipsoid (H) determined by precise satellite orbit determination, observation range (R_{obs}) and corrections (ΔRG_{Corrs}).

$$h = H - R_{obs} - \Delta RG_{Corrs} \tag{2.2}$$

To obtain accurate satellite heights, precise orbit determination (POD) combines accurate and complex mathematical models for the dynamics of a satellite's motion with high precision

physical observations of e.g. satellite's positions and velocity. Mostly satellite altimeters use various tracking techniques such as Satellite Laser Ranging (SLR), Doppler Orbitography and Radiopositioning Integrated by Satellite (DORIS), Precise Range and Range-rate Equipment (PRARE, only used in ERS-2) and Global Positioning System (GPS). Fortunately, the accuracy of POD has improved from tens of meters by the time of the first altimeters to about 1 cm currently (Bertiger et al., 2010).

ΔRG_{Corrs} refers to the set of range and geophysical corrections: dry and wet tropospheric corrections, ionospheric correction, sea state bias, dynamic atmospheric correction, and tides (solid earth, ocean, load and pole), as shown in Equation 2.3 (Andersen and Scharroo, 2011)

$$\Delta RGeo_{Corrs} = \Delta h_{dry} + \Delta h_{wet} + \Delta h_{iono} + \Delta h_{SSB} + h_{DAC} + h_{tides} \quad (2.3)$$

Δh_{dry}, Δh_{wet}, Δh_{iono} and Δh_{SSB} are range corrections due to the interaction between the radar signal with the atmosphere and with the sea surface, respectively. h_{DAC} and h_{tides} are corrections related with geophysical phenomena that must be accounted for in order to separate them from the signal of interest. All values must be given in a fixed coordinate system based on a mathematical determinable ellipsoid model of the Earth.

Since the focus of satellite altimetry is the study of the dynamic sea surface height above the geoid (h_d) related to oceanographic processes, it is necessary to isolate or remove the dominant geophysical contributors to sea surface height variations, such as tides and dynamic atmosphere correction. The geoid undulations relative to a geocentric ellipsoid such as GRS80 or WGS84 range from -105 m in the south of India to +85 m in the northeast coast of New Guinea.

As shown in Figure 2.3, sea surface height (h), already accounting for range corrections, is affected by undulation of geoid (h_g) above the ellipsoid, tidal height variation (h_{tides}) and the ocean surface response (h_{DAC}) to atmospheric pressure loading or the dynamic atmospheric correction (DAC).

$$h = h_d + h_{geoid} + h_{tides} + h_{DAC} \quad (2.4)$$

or

$$h_d = h - h_{geoid} - h_{tides} - h_{DAC} \quad (2.5)$$

where h_d is the dynamic sea surface height, h_{geoid} is the geoid undulation, h_{tides} is the tides correction and h_{DAC} is the dynamic atmospheric correction. In order to combine the range

and geophysical corrections into a combined set of corrections, the dynamic sea surface height (h_d) is derived from the height (H) of the spacecraft, and the range (R_{obs}) according to the following equation,

$$h_d = H - R_{obs} - \Delta h_{dry} - \Delta h_{wet} - \Delta h_{iono} - \Delta h_{SSB} - h_{tides} - h_{DAC} - h_{geoid} \qquad (2.6)$$

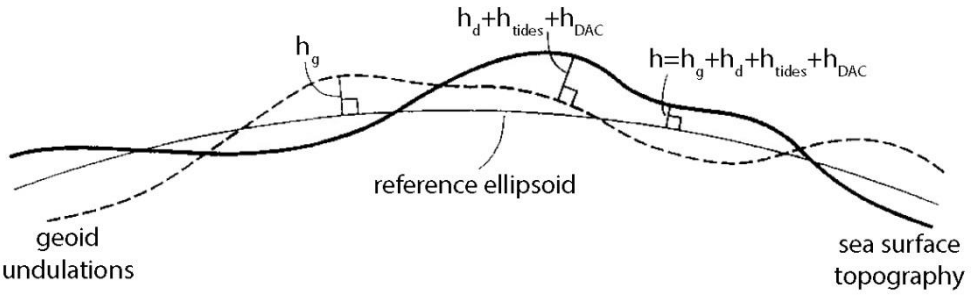

Figure 2.3 The various contributions to the sea surface height (h) relative to a reference ellipsoid (Chelton et al., 2001).

The dynamic sea surface height (h_d) has two components, a permanent and a time-variable component. The permanent stationary component or the temporal average of ocean dynamic topography is called the mean dynamic topography (MDT), the quantity bridging the geoid and the mean sea surface (MSS). For studies of sea surface height variations, it is often more convenient to refer the sea surface height to the mean sea surface height rather than to the geoid, thus creating the sea level anomalies (SLA) (Anderson and Scharroo, 2011). By subtracting the mean sea surface from SSH, the temporal mean of the dynamic sea surface height is removed.

The determination of SLA from altimeter measurements requires the correction for all instrument, range and geophysical corrections. SLA is determined as follows:

$$h_{SLA} = H - R_{Obs} - \Delta h_{dry} - \Delta h_{wet} - \Delta h_{iono} - \Delta h_{SSB} - h_{DAC} - h_{tides} - h_{mss} \qquad (2.7)$$

2.3. The Corrections in Satellite Altimetry

As mentioned above, the corrections that have to be applied to the altimeter measurements to get precise SSH or SLA are atmospheric corrections (dry and wet

tropospheric and ionospheric corrections), dynamic atmospheric correction, sea state bias and tides. The description of the main corrections in satellite altimetry is given in the next sub-sections.

2.3.1. Ionospheric Correction

The ionosphere layer contains free electrons and ions that can influence the propagation of electromagnetic waves both in the speed and in the propagation direction of the signal. The velocity of the signal is slowed by the free electrons in the atmosphere. The ionization process is driven by the sun activity (larger near the geomagnetic equator), the season of the year and varies with time of the day (generally peaks at around 14:00 local solar time). The ionosphere delay can be determined in terms of total electron content (TEC), which is the integral of the electron density along the signal path. TEC is measured in Total Electron Content Unit (TECU), with 1 TECU equivalent to 10^{16} electrons/m^2. As a dispersive medium, the ionosphere refraction is frequency-dependent. The ionosphere correction can be determined as function of the frequency:

$$\Delta h_{iono} = -k \frac{TEC}{f^2} \tag{2.8}$$

where k is a constant of 0.40250 m.GHz^2/TECU, TEC is the total electron content, f is the frequency in GHz and Δh_{iono} is given in meters (Anderson and Scharroo, 2011).

Satellite altimetry missions such as TOPEX, Jason-1, Jason-2 and Envisat carry dual frequency altimeters to provide the ionosphere information. For TOPEX and Jason series, flying at approximately 1350 km altitude, the primary frequency, Ku-band, operates at 13.6 GHz and the secondary frequency, C-band, at 5.3 GHz. The lower flying Envisat mission (800 km altitude) operates in the Ku band and S band (3.2 GHz). Using the difference between the ranges at the two frequencies, it is possible to directly estimate TEC along the satellite track,

$$TEC = \frac{f_{Ku}^2 f_{C,S}^2}{f_{Ku}^2 - f_{C,S}^2} \frac{R_{C,S} - R_{Ku}}{k} \tag{2.9}$$

R_{Ku} and $R_{C,S}$ are the ranges measured on the primary Ku-band and the second C-band or S-band, respectively, neglecting the effects of atmospheric refraction. In other words, the altimeter-derived TEC (in TECU) is 82.3 (TOPEX, Jason-1 and Jason-2) or 26.9 (Envisat)

times the range difference (in m) on the two frequencies. Due to the fact that the second frequency is less precise than the Ku-band, differencing the range measurements at two frequencies creates an additional noise in the derived ionospheric correction which needs to be smoothed around 200 km along the track in order to reduce this error (Andersen and Scharroo, 2011).

The single altimeter missions (such as Cryosat-2, ERS-1, ERS-2, Geosat, GFO and Poseidon) depend on observational or climatological models to estimate the ionospheric range correction. The Bent model and the International Reference Ionosphere (IRI) are examples of climatology models. The Bent model is a purely phenomenological electron density model which is deduced from satellite measurements, F_2 peak layer models and profiles from ground stations. The densities in the topside are represented by exponential and parabolic profiles and those in the bottom-side by biparabolic profiles, whose parameters are computed from observed electron density profiles (Köhnlein, 1978). The IRI model is a climatology mainly based on ionosonde data measurements since the 1930s. The IRI model has a good accuracy for the northern-mid latitudes, but is less accurate for low and high latitudes, due to poor spatial distribution of ionosonde stations (Bilitza, 1990; Bilitza and Reinisch, 2008).

The global ionosphere maps (GIM) of vertical TEC is an observational model based on more than hundred GPS stations from the International Global Navigation Satellite System (GNSS) Service (IGS) network. This model, developed by the Jet Propulsion Laboratory (JPL) and the University of Berne, is available in 2-hourly TEC maps and 2.5^o in latitude and 5^o in longitude spatial resolution (Komjathy et al., 2005). In addition, NIC09 (NOAA Ionosphere Climatology 2009) is a climatology model based on GIM for the period from 1998 to 2008, which can be applied to estimate the ionospheric correction prior to 1998 (Scharroo and Smith, 2010). While GIM uses actual measurements of the vertical TEC, the NIC09 uses a proxy of the solar activity to model the vertical TEC.

In order to use GNSS-derived TEC to estimate the ionospheric correction of altimetric measurements, the altitude scaling has to be applied (example: Envisat at 800 km and T/P and Jason at 1350 km), since the altimeters fly at a much lower altitude than the GPS satellites (altitude of about 20,200 km), they capture only part of the ionosphere. According to Iijima et al. (1999), the formula is the following:

$$TEC_{<800\ km} = TEC_{GIM} \frac{TEC_{IRI95<800\ km}}{TEC_{IRI95<1400\ km}} \tag{2.10}$$

where $TEC_{<800}$ km is the TEC below 800 km at a given time and place, TEC_{GIM} is the GIM TEC interpolated at the same time and location, and $TEC_{IRI95<800\ km}$ and $TEC_{IRI95<1400\ km}$ are the TECs below 800 and 1400 km determined by the IRI95 model. However, there are essentially no free electrons left above 1400 km, so that no scaling is needed for the higher flying altimeters (TOPEX, Jason-1, and Jason-2).

As mentioned above, the vertical TEC has spatial and temporal variations. It can be seen in Figure 2.4 that the ionospheric delay presents latitude dependence. The highest TEC occurs in the low-latitudes, the mean become smaller towards the poles. Diurnal TEC variations generally peaks around 14:00 local time and is lowest around 02:00 during the night. Dependency on solar activity is mostly related to the 11-year cycle in the solar radio flux (see Figure 2.5).

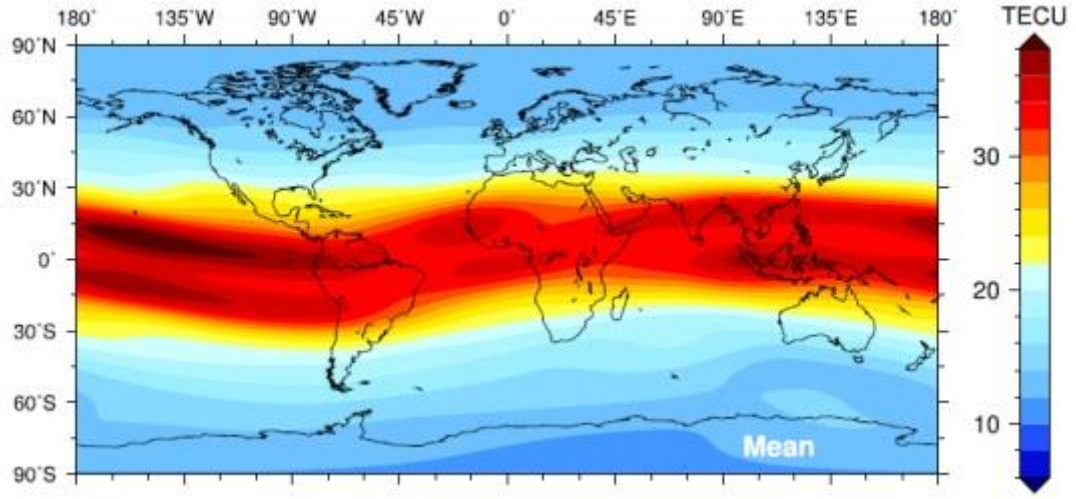

Figure 2.4 Mean of the Ku-band ionosphere path delay on 16 years of JPL global ionosphere map (GIM) TEC maps (Fernandes et al., 2014).

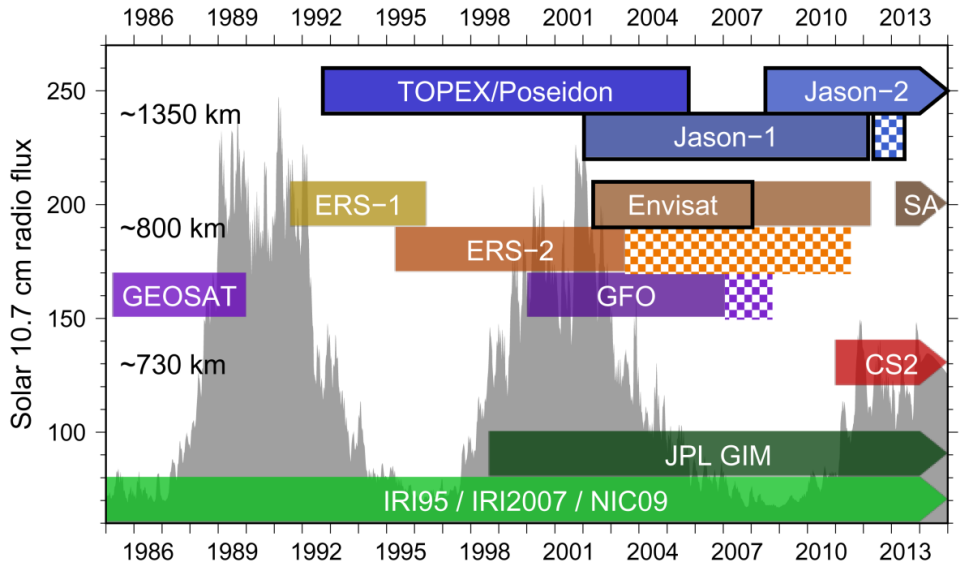

Figure 2.5 Variation of the solar 10.7 cm radio flux during the last two solar cycles (Fernandes et al., 2014).

2.3.2. Dry Tropospheric Correction

The path of the radar altimetry signal through the atmosphere is delayed by the presence of neutral gases in the troposphere. This delay is corrected by the dry tropospheric correction (DTC). The absolute value of the dry path delay at sea level is around 2.3 m. Although the DTC is the largest range correction in satellite altimetry, it can be modeled from surface pressure measurements at sea level (sea level pressure, SLP) using the modified Saastamoinen model (Davis et al., 1985),

$$\Delta h_{dry} = -\frac{0.0022768\, p_s}{1 - 0.00266 \cos 2\varphi - 0.28\,.\,10^{-6}\, h_s} \tag{2.11}$$

where p_s is the surface pressure in hPa, φ is geodetic latitude, h_s is the surface height above the geoid (in meters) and Δh_{dry} results in meters.

Due to the limited number and distribution of in situ measurements, SLP can be obtained from a Numerical Weather Model (NWM), such as the European Centre for Medium-Range Weather Forecasts (ECMWF) (Miller et al., 2010) and the National Centers for Environmental Prediction (NCEP) (Caplan et al., 1997). Global grids of sea level pressure (SLP) and surface pressure (SurfP) data are distributed on regular grids at 6-hour intervals. ECMWF provides two models: the operational model at $0.125^{o}\times0.125^{o}$ or about 16 km

(Gaussian grid) and ERA-Interim (Dee et al., 2011) at $0.75^o \times 0.75^o$ or about 80 km (Gaussian grid) resolution, while for NCEP data are provided in RADS at $2.5^o \times 2.5^o$.

Recent studies indicate that the dry tropospheric correction is not significantly affected by land (Andersen and Scharroo, 2011), for example, the accuracy of the DTC in coastal areas is about 0.7 cm for T/P (Fu et al., 1994), Jason-1 (Ménard et al., 2003) and Jason-2 (Lambin et al., 2010), but it is influenced by the height dependence (Fernandes et al., 2014). The height reduction of the DTC can be performed according to the following equation:

$$p_s = p_0(1 - 0.0000226(h_s - h_0))^{5.225} \tag{2.12}$$

where p_0 and p_s are the atmospheric surface pressures (in hPa) at heights h_s and h_0 (in meters), respectively. In Equation 2.12, the variation of sea level temperature is neglected. The more precise equation can be expressed as follows (Hopfield, 1969),

$$p_s = p_0 \, exp\left[-\frac{g_m(h_s - h_0)}{RT_m}\right] \tag{2.13}$$

where R is the specific constant for dry air (287.053 $J.K^{-1}.kg^{-1}$), T_m is the mean temperature (in K) of the layer between heights h_0 and h_s and g_m is the mean gravity, as given by:

$$g_m = 9.784\,(1 - 0.00266\,cos\,2\varphi - 0.28.10^{-6}h_s) \tag{2.14}$$

T_m can be estimated as the mean value of temperature T_0 and T_s at height h_0 and h_s, respectively, obtained. T_0 can be estimated using the Global Pressure and Temperature (GPT) model (Boehm et al., 2007) and considering a value of -0.0065 $K.m^{-1}$ for normal lapse rate of temperature with height (for estimation of T_s) (Fernandes et al., 2014).

2.3.3. Wet Tropospheric Correction

The wet tropospheric correction (WTC) is one of major uncertainty sources in satellite altimetry. The WTC includes the water vapor and cloud liquid water droplet contribution to atmospheric refraction. Although the absolute value of the WTC is about 50 cm, it has high variability, both in space and time, thus not being easy to model.

The wet tropospheric correction is computed from on-board microwave radiometers by measuring the brightness temperature (TBs) at two or three frequencies in the range of 18 and 37 GHz, in spectral bands sensitive to water vapor and cloud liquid water.

TOPEX/Poseidon carried the three-channel TOPEX Microwave Radiometer (TMR), which operated at 18, 21 and 37 GHz, while for Jason-1 and Jason-2 the Jason-1 Microwave Radiometer (JMR) and the Advanced Microwave Radiometer (AMR) operate at 18.7, 23.8 and 34 GHz, respectively. ERS-1, ERS-2 and Envisat carried two-channel which operated at 23.8 and 36.5 GHz (37 GHz for SARAL/AltiKa) (Scharroo et al., 2004; Picard et al., 2015).

In the open ocean, the WTC can be retrieved within a few cm accuracy using on-board microwave radiometers. However, this does not apply to the coastal regions. The differences between ocean emissivity (around 0.5) and land emissivity (around 0.9) cause the radiometer footprint, as it approaches the coast, to contain portions of surfaces with different emissivity. Therefore, the WTC ocean retrieval algorithm originates invalid measurements in the regions close to the coast or land. The invalid data for TMR and JMR start from about 50 km from the coast; while for AMR on Jason-2 begin around 25 km from land (Brown, 2010; Desportes et al., 2007). However, the JMR and AMR data present on RADS are already enhanced near the coast, thus these effects are expected to be much smaller for these satellites when compared to TOPEX/Poseidon.

As an alternative to the WTC from onboard microwave radiometers, a number of atmospheric models, such as ECMWF and NCEP, which provide data on regular grids, can be used to derive tropospheric path delays. Using ECMWF parameters such as sea level pressure (SLP), surface temperature (2-metre temperature, 2T) and total column water vapor (TCWV), the WTC can be calculated. The model grids of WTC are then used to estimate the WTC at each satellite ground track point by bilinear interpolation in space, followed by a linear interpolation in time. The comparison between the WTC derived from the ECMWF operational and ERA-Interim, performed by Fernandes et al. (2010) and Fernandes et al. (2013) showed that the use of the ECMWF operational model prior to 2004 is not advisable for altimetry studies. For this reason, ERA-Interim is considered the best available model for the whole altimeter era.

To reduce the WTC errors, particularly in coastal regions where the on-board microwave radiometer measurements become invalid due to land contamination in the radiometer footprint, a method to determine the troposphere wet path delays, by space-time objective analysis from the combination of data from various sources, was proposed by the University of Porto (UPorto), Portugal (Fernandes et al., 2010). Global GNSS-derived Path Delay (GPD) solutions have been derived by UPorto for the main altimetry missions (ERS-1,

ERS-2, Envisat, T/P, J1, J2, CryoSat-2, SARAL and Geosat Follow-on) using more than 800 GNSS stations in coastal and island regions (Fernandes et al., 2015)

Other methodologies to improve the WTC retrieval in the coastal regions have been derived by other authors as reported in Cipollini et al. (2017), such as Basic extrapolation of the last valid measurement over the ocean, Dynamically-Linked Model (DLM) or Composite approach where the invalid MWR data in coastal region (< 50 km) are replaced by the closest points with valid MWR or WTC (Obligis et al., 2011), Land Contamination Algorithm (LCA), which is based on the removal of the land contamination from the MWR measured TBs values prior to their use in the WTC retrieval algorithm (Desportes et al., 2007) and Mixed-Pixel Algorithm (MPA) which is designed to tackle the WTC retrieval for mixed land-ocean scenes, the mixed-pixel retrieval algorithm coefficients are determined as function of land fraction using a large database of simulated coastal land TBs (Brown, 2010).

2.3.4. Sea State Bias

Sea state bias (SSB) is an altimeter ranging error caused by the influence of sea-state effects in the radar altimeter measurements, since the surface scattering elements do not contribute equally to the radar return (Figure 2.6). The SSB correction consists of the electromagnetic bias (EMB), tracker bias and skewness. In the absence of waves, the reflecting surface coincides with the actual instantaneous mean sea surface averaged over the footprint. In the presence of ocean waves, the radar pulse is reflected more strongly by wave troughs than by the wave crests. The discrepancy between the mean sea surface and the mean reflecting surface is called the electromagnetic bias. The tracker bias is caused by onboard tracker instrument errors and errors associated with the re-tracking algorithm. In addition, the altimeter range is in fact based on the median rather than the mean reflecting surface. The skewness is linked to the effect of a non-Gaussian surface height distribution, inducing an error due to the difference between the determined median sea surface and the true mean sea surface (Scharroo and Lillibridge, 2004; Gommenginger and Srokoz, 2006).

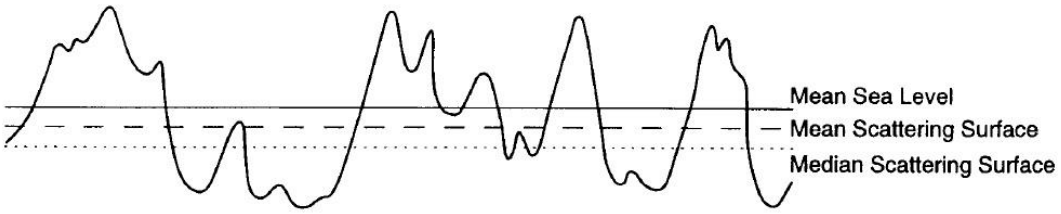

Figure 2.6 The difference between mean sea level, the mean scattering surface, and the median scattering level (Chelton et al., 2001).

The magnitude of SSB depends strongly on the significant wave height (SWH), thus, as a first approximation, it can be modeled as a simple percentage of SWH. The SSB also depends on the wind speed (U_{10}) and the different waves, therefore advanced parametric models consisting of three or four parameters have been used to estimate the SSB. The coefficients are derived by e.g. least squares fit of crossover height differences. The BM4 parametric model (Gaspar et al., 1994) is given by the following equation (see also Table 2.2):

$$SSB = SWH(a_1 + a_2 SWH + a_3 U + a_4 U^2) \tag{2.15}$$

where *SWH* is the significant wave height (in meters), *U* is the altimeter-derived wind speed (in meters per second), and a_1, .., a_4 are coefficients of BM4.

Table 2.2 Coefficients of BM4 models for various satellite altimeters (Scharroo and Lillibridge, 2004)

Missions	a_0	a_1	a_2	a_3	a_4
ERS-1	0.054265	-0.075043	0.001413	-0.001790	0.000098
ERS-2	0.107618	-0.068219	0.001465	-0.001701	0.000082
ENVISAT	0.026530	-0.052849	0.001746	-0.001713	0.000068
TOPEX A	0.012450	-0.030578	0.002776	-0.002962	0.000127
TOPEX B	0.028889	-0.032113	0.002992	-0.002780	0.000101
Poseidon	0.015731	-0.062778	0.001894	-0.001194	0.000057
Jason-1	0.110106	-0.034376	0.001145	-0.001969	0.000083
GFO	0.092034	-0.055742	0.002743	-0.003756	0.000153

Non-parametric sea state bias models can be derived by a statistical methodology based e.g. on kernel smoothing. Millions of crossover points can be used to estimate sea state

bias on a regular grid of wave height and wind speed. This method can resolve the problem of parameter-derived SSB due to the complexity of the relation between sea state bias, wave height and wind speed. However, there are two disadvantages of the non-parametric models: there is no availability of sea state bias estimate for outside the range of wave heights and wind speeds covered by the data that went into the modeling, and sea state bias estimates will be poor in the poorly covered areas of the wind speed/wave height space (Scharroo and Lillibridge, 2004). Another non-parametric model approach is the direct model (Vandemark et al., 2002), used to estimate sea state bias on a regular grid of wave height and wind speed by using directly sea surface height residuals.

The hybrid model developed by Scharroo and Lillibridge (2004) combines the simplicity and high resolution of the direct method with the smoothness of parametric models. Using this model, the technique becomes easy to implement and requires only a small amount of data.

The Tran model, proposed by (Tran et al., 2006; Tran et al., 2012), uses three-input estimators, SWH, U_{10} and the mean gravity wave period (T_m) from a numerical ocean wave model, NOAA's WAVEWATCH III (NWW3). The Tran model gives a good result by reducing SSH variance at global and regional scales. The University of Porto (UPT) SSB models also use three estimators (SWH, U_{10} and the mean wave period (T_z)), solely derived from altimetry data. They use the direct method, together with smoothing splines. The result shows a good performance for a wide range of ocean conditions, providing the best compromise between simplicity and reasonable results (Pires et al., 2016).

The sea state bias is associated to the ionosphere, due to the frequency-dependent nature of these corrections. An error in the SSB model will cause an error in the ionosphere correction of about 0.175 in scale for TOPEX and Jason-1, function of Ku-band and C-band frequencies (Chambers et al., 2003).

2.3.5. Tide Corrections

The ocean tide dominates the tide signal observed over the oceans, representing more than 80% of the total signal. There are several tidal signals which have smaller amplitudes than the ocean tide: load tide, solid earth tide and pole tide. Unlike the tide gauge measurement, which only measures the ocean tide, the altimeter measurement includes the sum of ocean tide and the small loading displacement of the ocean's bottom due to the

loading by the water column. Using appropriate mathematical formulation, solid earth and pole tide can be derived with centimetric accuracy. The sum of tidal corrections can be written as (Andersen and Scharroo, 2011)

$$\Delta h_{tides} = \Delta h_{ocean\ tide} + \Delta h_{load\ tide} + \Delta h_{solid\ earth\ tide} + \Delta h_{pole\ tide} \quad (2.16)$$

The global ocean tide models can be grouped as follows: hydrodynamic models, assimilation models and empirical models. The hydrodynamic models are derived by solving the Laplace Tidal Equation (LTE) using a finite difference or finite element method based on bathymetry data, with tidal heights from tidal constituents (of nearly all tide gauge records as boundary conditions). Assimilation models are determined by combining altimetry data and tide gauge data into a hydrodynamic model. The 2D Finite Element Solution (FES) model pioneered by Le Provost et al. (1994) is a widely ocean tide model based on assimilation of satellite altimetry into a hydrodynamic model. The FES model FES2012 uses more than 1.5 million nodes and high-resolution global bathymetry, this model proved to be more accurate than the previously FES model (FES2004) and GOT4.8, particularly in shallow water and coastal regions (Carrère et al., 2012). The model is distributed on 1/16^o grids and consists of 32 tidal constituents. Unfortunately, tide-loading effects have not yet been computed for FES2012; therefore, Global Ocean Tide (GOT) ocean tidal loading model should be used to complete the FES2012 ocean tide and ocean tidal loading model. Empirical models are determined from altimetry data only. These models can be divided to semi-empirical and pure empirical. The semi empirical models, such as the GOT model, were determined using satellite altimetry data with 0.5^{o}x0.5^o rectangular grids (Ray, 1999). The coarse resolution of the grids becomes a problem in coastal regions when the grids do not cover the coastal area. The latest version of GOT is GOT4.10.

The solid earth tides are the motion induced in the solid Earth and the changes in its gravitational potential induced by the tidal forces from external bodies due to the response of gravitational forces of the sun and the Moon (Wahr, 1995).

The pole tide is caused by the variation of the Earth's axis of rotation with respect to its mean geographic pole. The variation, also called the Chandler Wobble, has a period around 365-433 days (Desai, 2002). Polar motion causes the centrifugal force to change at every point within the Earth and that induces deformation (Wahr et al., 2015). Desai (2002) explained that the pole tide in the solid Earth is derived by applying classical Love number theory to the pole tide potential just as the lunisolar body tides are derived from the lunisolar

tidal potential. Similarly, the pole tide in the oceans can be derived by extending lunisolar ocean tide theory to the pole tide potential. Fundamentally, the displacement of the oceans that is caused by the lunisolar or pole tide potential is dependent on the inherent dynamics of the oceans.

2.3.6. Dynamic Atmospheric Correction

The response of the sea surface to changes in atmospheric pressure has a large effect on the measured surface height. The dynamic atmosphere correction can be divided into low-frequency (periods longer than 20 days) and high-frequency (periods shorter than 20 days).

The low-frequency of atmospheric pressure loading has been comprehensively reviewed by Wunsch and Stammer (1997). The simplest model for inverse barometer correction is as follows:

$$\Delta h_{ib} \approx -0.99484\ (P_0 - P_{ref}) \tag{2.17}$$

where P_0 is the sea level pressure, P_{ref} is the global mean pressure (reference pressure), usually a constant global value of 1,013.3 hPa. One hecto-Pascal increase in atmospheric pressure corresponds to a linear response in sea level producing a decrease of about 1 cm. The accuracy of the inverted-barometer correction is also limited by uncertainty in the actual sea surface atmospheric pressure. The global sea level pressure can be derived from the numerical weather prediction model (Chelton et al., 2001).

The dynamic response of the ocean due to pressure forcing at high frequencies occurs on periods less than 5 days. The accurate estimation of high-frequency barotropic motions has important implications in the analysis of altimeter measurements. The global adjustment for high-frequency sea level variability has been implemented using the MOG2D model. MOG2D, proposed by Carrère and Lyard (2003), is a barotropic, nonlinear and time stepping model with the model's governing equations being classical shallow water continuity and momentum equations. The model can include tides and its main originality is a finite element space discretization (FE), which allows increasing the resolution in strong topographic gradient areas or in shallow seas. The grid size ranges from 400 km in deep ocean to 20 km in coastal, shallow areas.

MOG2D_IB is a combined dynamic atmosphere correction that combines an inverse barometer correction for time scales longer than 20 days with MOG2D model for high-frequency variability with timescales shorter than 20 days.

2.3.7. Mean Sea Surface

The MSS is a geometrical description of the averaged sea surface height and can be an essential parameter in geodesy and physical oceanography. For geodesy, the MSS is fundamental for deriving marine gravity anomalies as well as for bathymetry prediction (Andersen and Knudsen, 1998). For physical oceanographers, the MSS defines depth averaged geostrophic currents relative to the geoid (Chelton et al., 2001).

MSS is also the most important reference surface in studies of sea level variation and it is used to estimate SLA aiming at removing the temporal mean of the dynamic sea surface topography. The MSS and the geoid do not coincide because the dynamic sea surface height (h_d in Equation 2.4 and 2.5) has both permanent and time-variable components. The permanent component reflects the steric expansion of sea water and the temporal average of dynamic topography is called mean dynamic topography (MDT) (Andersen and Scharroo, 2011). The MSS is associated to the sum of the geoid and the MDT, as follows

$$h_{MSS} = h_g + h_{MDT} \tag{2.18}$$

The geoid has an irregular shape, being an equipotential surface of the Earth's gravity field. The most recent improvement in the estimation of geoid models consists in using data from dedicated gravimetric satellites, such as the Gravity Recovery and Climate Experiment (GRACE) and the Gravity Field and Steady-State Ocean Circulation (GOCE). The Earth Gravitational Model 2008 (EGM2008) (shown on Figure 2.8) is a spherical harmonic model of the Earth's gravitational potential, a 5 arc-minute equiangular grid, degree 2190 and order 2159, developed by a least squares combination of the ITG-GRACE03S gravitational model (Pavlis et al., 2012). The most recent high resolution models include data from GRACE and GOCE, such as EIGEN_6C4. The EIGEN_6C4 is a global gravity field model up to degree and order 2190 from the combination of the different satellites (LAGEOS, GOCE and GRACE) and surface data sets (DTU and EGM2008) (Shako et al., 2014; Förste et al., 2014).

The MSS and the geoid vary up to ±100 m relative to the reference ellipsoid (Figure 2.8 and Figure 2.9). The MDT only varies up to a few meters reflecting the steady state ocean circulation as well as the oceans response to thermohaline expansion (Andersen and Knudsen, 2009).

The MSS is determined by averaging sea surface height observations from satellite altimetry. There are several MSS models such as DTU MSS model (Andersen et al., 2015) and CNESCLS MSS model (Schaeffer et al., 2012). The CNESCLS2011 MSS is a mean sea surface model from Centre National d'Études Spatiales (CNES)/Collecte Localisation Satellites (CLS), derived from observations covering 16 years of multiple satellite altimeters (TOPEX/Poseidon, ERS-1 Geodetic Mission, ERS-2, Jason-1, TOPEX/Poseidon interleaved mission, GFO and Envisat). The CNESCLS11 MSS has been computed using a least-square collocation technique based on statistical a priori knowledge on the data and its error. The method uses the Optimal Interpolation (OI) to allow building a covariance matrix and the remove/restore technique to focus the correlation/covariance model on wavelengths lower than 100 km. To avoid possible jumps near the coast, the estimate is connected to the geoid 100 km inland. This means that the estimator is switched to an extrapolation mode from 20 km after the last altimetric data up to 100 km on the mainland (Schaeffer et al., 2012). Denmark's National Space Institute or DTU releases the MSS model, namely DTU series. The latest DTU MSS model is DTU15MSS (Piccioni et al., 2015; Andersen et al., 2016) which is an update of DTU13MSS (Andersen et al., 2015). The DTU15MSS was determined using extended time series period of more than 20 years, using Cryosat-2 LRM and SAR data particularly in the Arctic Ocean. The availability of Cryosat-2 enables to determine an accurate MSS up to 88^{o} N (Andersen et al., 2015).

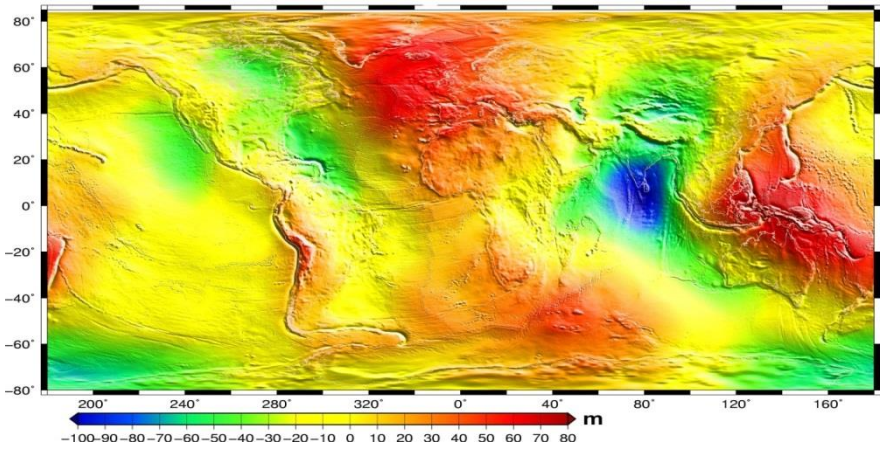

Figure 2.7 Mean sea surface CNESCLS2011 model (Source: http://www.aviso.altimetry.fr).

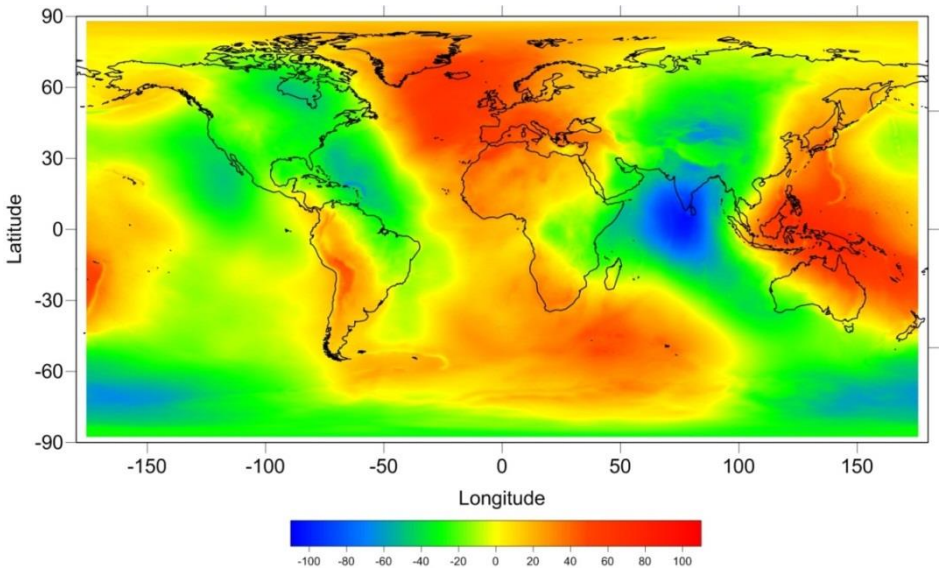

Figure 2.8 Geoid undulation EGM2008 in units of meter (Source: NGA Office of Geomatics; http://earth-info.nga.mil/GandG/wgs84/gravitymod/egm2008/egm08_gis.html).

2.4. The Challenges in Coastal Altimetry

Radar altimetry is a remote sensing technique for directly measuring sea level from space, providing along-track sea surface height measurements, wave height and wind speed (Chelton et al., 2001). Satellite altimeters are routinely used to map the variability of ocean surfaces, in all weather and day/night conditions. Since TOPEX/Poseidon was launched in 1992, the researches of sea level variability stepped into the new satellite altimetry era, with high accuracy both in the spatial and temporal domains. Nowadays, the satellite altimetry

studies have been continued to the coastal zones and its potential can be extended to many coastal applications. In addition, the coastal zones are very important because the population and the socio-economic activities and infrastructures are concentrated around the coastlines. The main challenge in coastal altimetry is how to overcome the problems and extending the capabilities of current and future altimeters as close as possible to the coast (Cipollini et al., 2010).

In the open ocean, satellite altimetry is a powerful tool to measure sea level and monitor the ocean circulation. It is clear that conventional altimeters were designed with research priorities for the open ocean. In contrast, working over the coastal zone has some extra difficulties due to the proximity of land. The altimeter data near the coast (at distances approximately less than 50 km from coast) are not accurate and difficult to interpret. The return radar signal measured by the altimeter sensor near the coast might be degraded by land contamination within the footprint, with some possible effects on path delay and geophysical corrections.

The problems concerning the coastal zones can be separated into two parts. Firstly, the problem associated with the altimeter waveform which is contaminated by land signal. Over the open ocean, the waveforms are well fitted by the Brown model (Brown, 1977). However in the coastal zone, waveforms become contaminated by non-ocean like reflections, being corrupted. Therefore, waveform retracking is needed to recover the sea surface height (SSH) signal close to the coast due to the fact that coastal waveforms do not conform to the Brown model. Specific coastal retrackers should give better accuracy and precision than generic deep ocean retrackers. Secondly, there are problems due to inaccuracies related to some corrections, both due to geophysical effects and those related with the path delay. The most critical corrections in coastal zones are the ocean tides, wet path delay and the sea state bias. The inaccurate correction of the wet path delay is still a major problem in coastal regions. Its effect is due to the signal contamination within the large footprint of the on-board MWR used to retrieve the WTC from land. The impact of land contamination for the satellites that carry a two-band radiometer is quite large due to the algorithms used to retrieve the WTC (parametric method for ERS and neural network algorithm for Envisat) (Lázaro and Fernandes, 2015) and the altimeter backscatter coefficient as a third input parameter, need to be well calibrated across the altimeter mission and need to be monitored for long term stability (Scharroo et al., 2004). Coastal tides have a more complex spectrum than those in the open ocean, together with additional complexity of nonlinear interactions in the coastal

zone. The global tide models still do not perform well in coastal and shelf regions, suggesting that local tide models are required to account for local ocean corrections. The sea state bias model in coastal zone needs further investigation to migrate from empirical model to the physically-based (Cipollini et al., 2013).

A number of authors have developed methods to overcome the altimeter problems in the coastal zones. The improvement of altimeter waveforms is needed to retrieve waveforms if these are not fitted by the Brown model as well as over the open ocean (Gommenginger et al., 2011). In the Low Resolution Mode (LRM), the altimeter footprint size is several kilometers, depending on the satellite altitude, surface slope and roughness, pulse duration and width of the analysis window (Chelton et al., 2001). In SAR mode, the altimeter performs with a higher spatial resolution than LRM, up to 300 m in the along-track direction (Wingham et al., 2006; Ricker et al., 2015). Cryosat-2, for example, carries the Synthetic Interferometric Radar ALtimeter (SIRAL), which has an along-track resolution of approximately 250 m (Ray et al., 2015; Rey et al., 2001). Due to the degradation of the microwave radiometer signal in coastal zones as the effect of the land contamination, several methods have been developed to improve the WTC retrieval in the coastal zones (Cipollini et al., 2017). One such a method is the GPD developed by the Universidade do Porto (Fernandes et al., 2010, 2015, 2016). Improved tide models have also been developed such as FES2014 and GOT-4.10c. Moreover, the extended SSB model using 3 parameters (Tran et al., 2006; Tran et al., 2012) and the mean sea surface model such as DTU series (Andersen et al., 2016) and CNESCLSS are further advances to improve altimeter data in the coastal region.

In addition, several projects, such as the Altimeter-based Investigations in Corsica, Capraia and Contiguous Areas (ALBICOCCA), the ESA Development of Coastal Altimetry for Envisat (COASTALT), the Prototype Innovant de Système de Traitement pour les Applications Côtières et l'Hydrologie (PISTACH) and the SAR Altimetry Mode Studies and Applications (SAMOSA) have addressed most of the above mentioned issues. The ALBICOCCA project (Vignudelli et al., 2008) generated a coastal product in the Northwest Mediterranean by adopting data filtering and screening techniques in combination with state of the art tidal and atmospheric modeling. COASTALT was a project on the development of radar altimetry data processing in the coastal zone funded by the European Space Agency. PISTACH, part of the Jason-2 Project and funded by CNES, aimed at improving satellite radar altimetry products over coastal areas and continental waters (Mercier et al., 2010).

Meanwhile, SAMOSA, initiated in 2007, is an ESA-funded project to study and investigate the improvements brought by Synthetic Aperture Radar (SAR) mode (or Delay Doppler mode) altimetry over ocean, coastal and inland water surfaces (Cotton et al., 2010). The main goal of all these projects is to bring radar altimeter closer to the coast through the development improved methods.

The advantage of current radar altimetry for coastal studies is that it can fill gaps in the vast areas around tide gauges, which are running continuously, but in only a limited number of places. Future missions will be designed with higher resolution capabilities than their predecessors and advances in technology (e.g. delay-Doppler and Interferometry) (Vignudelli et al., 2011). While Delay Doppler or SAR altimetry has been implemented in Cryosat-2 and Sentinel-3, still being subject of intensive research to fully exploit its capabilities, interferometric techniques are being designed for the future SWOT mission. SWOT (Surface Water and Ocean Topography), a collaborate project developed by NASA, CNES, the Canadian Space Agency (CSA) and the United Kingdom Space Agency (UKSA), is both a continental hydrology and oceanography mission, planned for launch in 2020 (Biancamaria et al., 2015). This mission brings the Ka-Band Radar Interferometer (KaRIN), which contains two Ka-band SAR antennae at opposite ends of a 10-meter boom, and will fly in a 77.6^{o} inclination and 21-day repeat orbit. SWOT will have two modes depending on the over-flight surface: LRM for over ocean and High Resolution Mode for land areas (rivers, lakes, wetlands and reservoirs) and coastal regions (Andral et al., 2015).

CHAPTER 3

SEA LEVEL CHANGE

The human activities, industries, and agriculture have been producing gases, such as carbon dioxide, methane, nitrogen oxide, which created a greenhouse effect. These gases cause the atmosphere to trap increasing amounts of heat energy in the Earth's surface, making the planet warmer than usual. The increasing rate of the global temperature reaches 0.85 degrees Celsius per year for 1880 to 2012 (Church et al., 2013). This increasing can undergo changes in the climate, which is affecting the life on land and water.

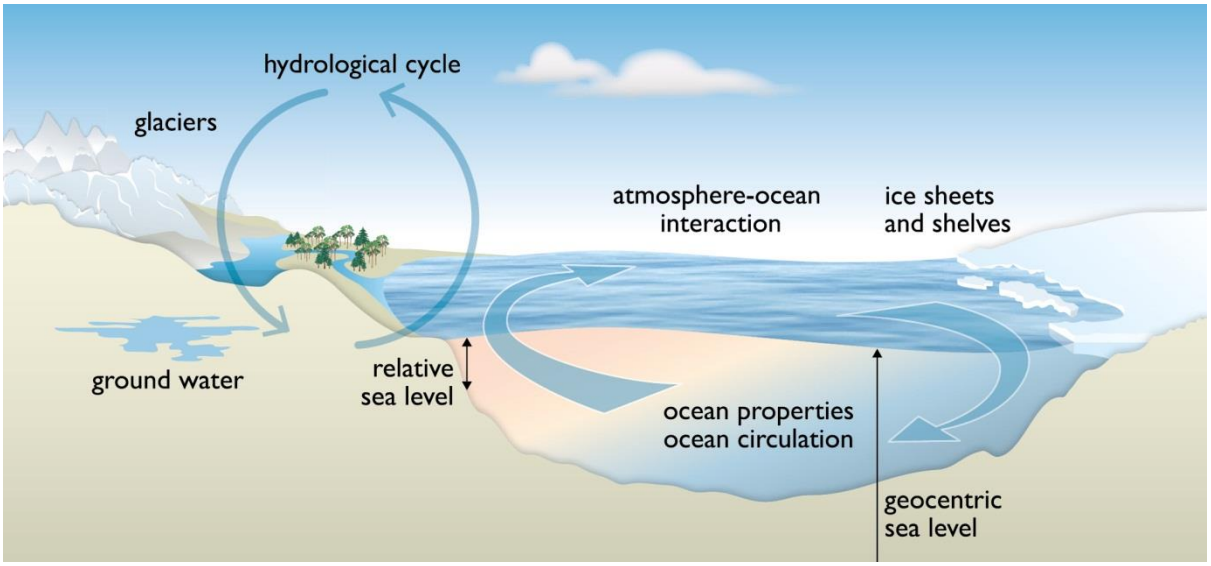

Figure 3.1 Climate-sensitive processes and components that can influence global and regional sea level (Church et al., 2013).

As shown in Figure 3.1, changes in any of the components or processes that influence sea level will result in a sea level variation in space and time scales from short events to several decades or century. The term “ocean properties” refers to ocean temperature, salinity and density, which influence and are dependent on ocean circulation. The oceans are a central component of the climate system, storing and transporting large quantities of heat. As the oceans warm, they expand and sea level rises. The amount of expansion depends on the

quantity of heat absorbed and on the water temperature (greater expansion in warm water), pressure (greater expansion at depth) and, to a smaller extent, salinity (greater expansion in saltier water). Both the temperature (thermosteric) and salinity (halosteric) contributions (or their combined impact on density (and volume), the steric contribution) are important for regional changes in sea level, but the thermosteric contribution is the dominant factor in globally averaged changes (Church et al., 2010; Church et al., 2013).

The Global Mean Sea Level (GMSL) is represented as the average height of the sea surface relative to the center of the Earth, within a certain period and over the global oceans. The increase of the global mean sea level, called Global Sea Level Rise (GSLR), can be recognized physically as the change of ocean volume and ocean-basin shape. The change related to sea-water volume is caused by thermal expansion and fresh water exchange between the continents and the ocean. The geophysical processes, such as the Glacial Isostatic Adjustment (GIA), which is the rebound of the Earth's mantle as response from ice sheet loss in the North America and Europe in the end of ice age, influence the change of ocean-basin shape.

Since the last glacial about 20,000 years ago, sea level has risen by over 120 m due to the melting of ice sheets over North America, northern Europe, and Antarctica. Using paleo-ecological or morphological information in the geological record, the evidences of sea level change during the past few hundreds to thousands of years were revealed. Historically, geomorphic features have provided the clearest evidence of a former change in sea level. Geological data from salt marshes show a clear acceleration from relatively low rates of sea level change during the past two millennia to modern rate (Kemp et al., 2011)

The instrumental record of sea level change is mainly comprised of tide gauge measurements over the past two or three centuries and satellite altimeter measurements since early 1990s. Established in the 18^{th} century around Northern Europe and North American coast and in the 19^{th} century around the southern hemisphere, tide gauge measurements have a long historical data record. Unfortunately, tide gauge records are affected by the effect of vertical land movement (VLM), due to e.g. glacial Isostatic adjustment (GIA), tectonic activity and subsidence. For detecting climate related variability of the ocean volume, the VLM signal must be removed. The sea level rise estimated during the 20^{th} century based on tide gauge data is 1.6 – 1.8 mm yr^{-1} (Church and White, 2011). The high-precision satellite altimetry record started in 1992 and provides nearly global sea level measurements at 10-day intervals. After correcting the measurements for several known corrections and possible

drifts, satellite altimeter data have proved to be a very useful technique to estimate global sea level rise. Numerous authors agree that sea level has been rising at around 3.1 – 3.4 mm/year during the last two decades (Ablain et al., 2015; Cazenave et al., 2014; Church et al., 2013; Nerem et al., 2010). Satellite altimetry indicates that the rate of rise is not uniform around the globe. The spatial patterns reflect climate variability with a greater rate in the western Pacific compared with the eastern Pacific, as a result of the transition from El Niño and La Niña conditions. There are significant seasonal and inter-annual fluctuations around the linear trend.

Sea level rise is likely to be a serious problem for coastal populations in the future. Low-lying coastal plains are vulnerable to inundation, threaten coastal ecosystems and suffer serious consequences of salt intrusion into aquifers. According to the projections of future global mean sea level rise estimated by the IPCC Fifth Assessment Report (AR5), from 28 to 98 cm in 2100 (Church et al., 2013), there is a need to urgently reduce the emission of greenhouse gases and a plan to adapt to the inevitable consequences of sea level rise.

The following sections present details associated with contributions to sea level change (section 3.1), sea level observation methods (section 3.2) and impact of sea level change and future projection (section 3.3).

3.1. The Contributions to Sea Level Change

The long-term variation of global mean sea level can be caused by a variety of different phenomena. The major contributions to 20th and 21st century global mean sea level change are the thermal expansion of sea waters in response to ocean warming and the addition of freshwater to ocean basin as result of land ice loss and water exchange with terrestrial reservoirs. The IPCC Fifth Assessment Report (Church et al., 2013) presents some contributors to global sea level rise as shown in Table 3.1.

3.1.1. The Steric Change

Observations of ocean temperature and salinity play a critical role in understanding global sea level. These temperature and salinity variations affect seawater density and cause changes in sea level. The variation of sea level caused by expansion of ocean volume due to temperature (thermosteric) and salinity (halosteric) changes is called the steric sea level, but

the thermosteric is the dominant factor in globally averaged changes.

Table 3.1 Observed contributions to global mean sea level (GMSL) rise in mm/year (Church et al., 2013).

Source	**1901 – 1990**	**1971 – 2010**	**1993 – 2010**
Thermal expansion	-	0.8	1.10
Glacier except in Greenland and Antarctic	0.54	0.62	0.76
Glacier in Greenland	0.15	0.06	0.10
Greenland ice sheet	-	-	0.33
Antarctic ice sheet	-	-	0.27
Land water storage	-0.11	0.12	0.38
Total of contribution	-	-	2.8
Observed GMSL rise	1.5	2.0	3.2

Global investigations of ocean heat storage and thermosteric sea level staring from 1950 were performed by Levitus (Levitus et al., 2000; Levitus et al., 2005) and by Ishii (Ishii et al., 2006). Over the previous decades, the hydrographic measurements, in particular temperature and salinity have been measured with expandable bathythermographs (XBT) along ship tracks, complemented by mechanical bathythermographs (MBT) and Conductivity-Temperature-Depth (CTD) systems to obtain upper-ocean temperature profiles. The problems of XBT measurement are systematic bias due to uncertainty in assigning a correct depth value to each temperature measurement (temperatures unrealistically high or low) which can be as large as the decadal variability of thermal expansion itself and poor in data coverage both geographically and in the deep ocean (Lombard et al., 2005). Since 2000, the profiling floats data (ARGO project) measure the ocean physical properties (temperature, salinity and density) periodically to a depth of about 2000 m and transmit the data every 10 days via the global telecommunications system (both temperature and salinity), with nearly global coverage. More than 3000 floats data profiling equipped with CTD were distributed

around the global oceans in late 2007 (Roemmich et al., 2009).

Figure 3.2 shows the time series of thermosteric sea level (mm) relative to 700 m based on temperature anomalies from Levitus (2005), Ishii et al. (2006), Ishii and Kimoto (2009), and Domigues et al. (2008). The dash lines illustrate the time series affected by documented-bias in XBTs and the solid curves present the time series with bias-corrected. The time series determined by Domigues et al. (2008), the error range was shown by shaded curve. The overall shape of the time series is similar (low frequency signal) but there are differences in both the estimated inter-annual variability and long-term trends. The differences vary in their input data, quality control procedures, gridding and infilling methodology (the assumptions made in areas of missing data), bias corrections and choice of reference climatology (Palmer et al., 2010).

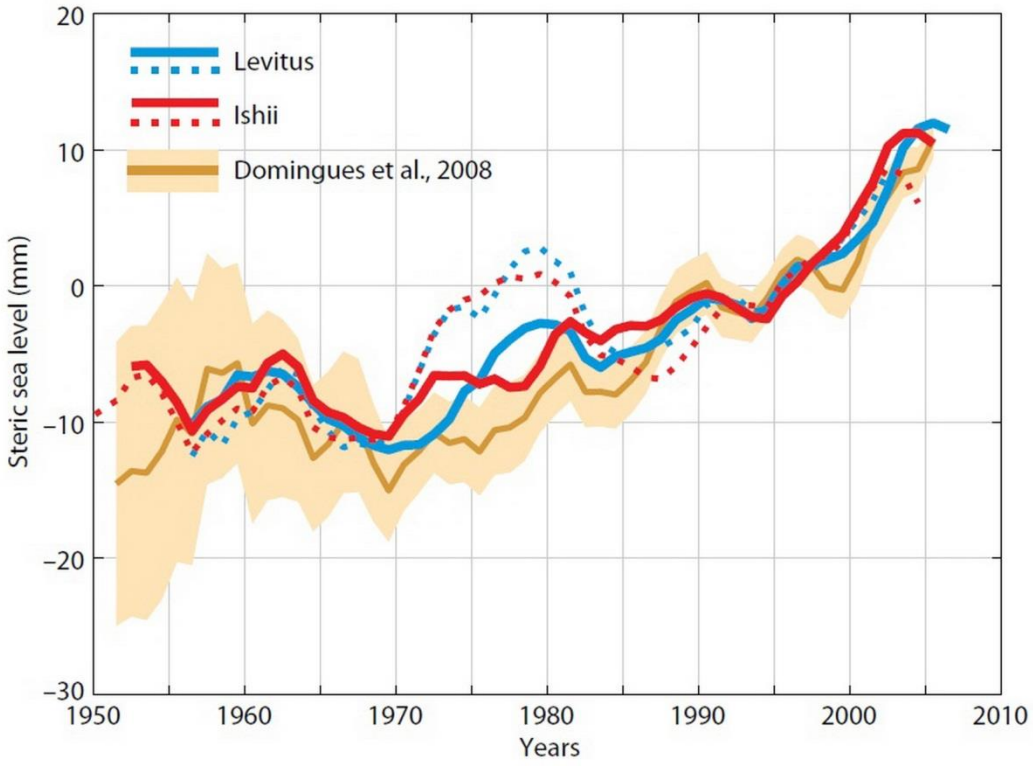

Figure 3.2 Time series of thermosteric sea level (mm) relative to 700 m based on temperature anomalies from Levitus (2005), Ishii et al. (2006), Ishii and Kimoto (2009), and Domigues et al. (2008) (from Johnson and Wijffels (2011)).

The oceans do not warm up uniformly. Satellite altimetry has clearly shown the spatial patterns in sea level due to the non-uniform ocean warming. The variations of

thermosteric sea level are dominated by the decadal oscillations of the main couple ocean-atmosphere climatic perturbations, such as the El Niño Southern Oscillation (ENSO) and Pacific Decadal Oscillation (PDO) (Lombard et al., 2005). In the decadal oscillation of global mean sea level, volcano eruptions lead to change in ocean heat. The aerosols injected into the stratosphere during volcanic eruptions cause a rapid cooling of the atmosphere and a reduction in rainfall. The large volcano eruptions, such as Mt. Agung, Indonesia (1963), El Chichon, Mexico (1982) and Mt. Pinatubo, Philippines (1991), inject particles and gases into the atmosphere, thus increasing the fraction of incident radiation reflected by the planet and hence reducing the amount of solar energy reaching Earth's surface. Because of the reduction of the net solar flux at the ocean surface, volcanic eruptions induce an immediate cooling of the surface layers, and so a decrease in heat content and sea level (Cazenave, 2005). According to Church et al. (2005) and Grinsted et al. (2007), the impact of volcano eruptions to sea level produced a drop up to 9 mm in the first year and 7 mm in the period 2-3 years after the eruption, relative to pre-eruption sea level.

Global mean sea level change estimates have mostly neglected halosteric effects due to the fact that salinity does not drive any significant halosteric changes when averaged globally. However, the regional salinity changes can significantly impact on some regional sea level change patterns, such as in the tropical Pacific (Durack et al., 2014; Durack, 2015).

3.1.2. The Mass Change

The ice melting gives a significant contribution to sea level rise. Both the Glacier and ice caps (but excluding the Greenland and Antarctic ice sheet) contain enough water to increase the sea level up to 37 cm (Lemke et al., 2007). The ice sheets of Greenland and Antarctic have a potential high contribution to sea level rise. If the ice sheets covering Greenland and Antarctic were melt completely, they would raise sea level about 65-70 m (Cazenave and Nerem, 2004). Even a small loss of ice mass from the ice sheets would have a great impact on sea level. The observations using remote sensing data, such as satellite radar altimeter, inSAR, airborne laser and satellite gravity, indicate the acceleration of ice mass loss in those areas. From the observations on Greenland and Antarctic ice sheets show that the Greenland ice sheet (GIS) gives an increase contribution to sea level rise: 0.09 mm/year for 1992-2001 to 0.59 mm/year for 2002-2011. The West Antarctic ice sheet (WAIS) also increased from 0.08 mm/year for 1992-2001 to 0.40 mm/year for 2002-2011. Therefore, both

GIS and WAIS have a significant contribution to future sea level rise as shown in Table 3.1, about 0.33 mm/year and 0.27 mm/year over 1993 – 2010 for GIS and WAIS, respectively (Church et al., 2013).

Glaciers are defined as all land-ice masses, including those peripheral to (but not including) the Greenland and Antarctic ice sheets. Glaciers are very sensitive to temperature change due to global warming. There are about 300 glaciers worldwide tracked over the last decades by the World Glacier Monitoring Service (WGMS). Since 1970, the observations indicate that most of the glaciers are retreating and thinning, with noticeable acceleration since the early 1990s (Cazenave and Llovel, 2010). The IPCC AR5 estimated the glaciers contribution to sea level rise at 0.76 mm/year over 1993-2010 (see Table 3.1) (Church et al., 2013).

Changes in water storage on land in response to climate change and variability (i.e., water storage in rivers, lakes, wetlands, aquifers and snow pack at high latitudes and altitudes) and from direct human-induced effects (i.e., storage of water in reservoirs and ground water pumping) have the potential to contribute to sea level change about 0.38 mm/year over 1993-2010 (Church et al., 2013). However, if terrestrial water storage increases, the rate of sea level rise will be reduced. Gornitz (2001) estimated that the reservoirs and dams were potentially reducing sea level rise by an average of 0.27 to 0.33 mm/year.

3.1.3. Non-Climatic Contribution

The causes of changes in sea level are not only limited to those related to climate change, but can also be caused by non-climate processes such as the changes in the size and shape of the ocean basin. These changes include Isostatic adjustment of land mass (GIA), tectonic movement associated with earthquakes, ground subsidence/uplift. The tide gauges measure sea level relatively to the ground. However, this measurement is influenced by vertical land movement such as GIA, tectonic or volcanic activities and human activities.

The Earth's crust has been continuing a rebound (visco-elastic response) to the melt of large glaciers during the present interglacial period. This movement is apparent in northern Europe, the northern part of North America, Siberia, and around Antarctica. The distribution of GIA is estimated by calculating the response of the crust to the disappearance of heavy ice sheets, assuming a visco-elastic body (Peltier, 2001). The mean rate of sea level change due

to GIA is estimated from models approximately at -0.3 mm/year (Peltier, 2001; Peltier, 2009). By applying a correction for GIA, the sea level time series reflects purely oceanographic phenomena.

Tectonic and volcanic activities such as earthquake (Melini et al., 2004) and human activities, such as extracting ground water pumping and oil/gas extraction (Zerbini et al., 2002) can cause vertical land movement (subsidence or uplift). Subsidence in a number of cities is of greater magnitude than sea level rise. For example, in Bangkok, the Gulf of Thailand is rising about 0.25 cm per year but the city is sinking up to 4 cm per year (Fuchs et al., 2011); in Jakarta, the typical rates of subsidence in spatial and temporal variations are of about 3-10 cm per year (Abidin et al., 2015) and sea level rise is about 3.8 mm per year (Fenoglio-Marc et al., 2012).

3.2. The Sea Level Observation methods

Global sea level rise is caused by mass and volume changes, which have been recognized as consequences of the global climate change. The precise estimation of sea level change and its rate is a complex problem. There are two types of observations for measuring the sea level: direct and indirect methods. Firstly, direct methods to observe sea level variability are tide gauge measurements and satellite altimetry. Indirect methods are those that can support the estimation of the sea level changes, such as ocean temperature, salinity and measurements of gravity changes. These methods are presented in the next subsections.

3.2.1. Tide Gauge Measurement

Prior to the satellite altimetry era, tide gauge measurements are the major dataset used to estimate sea level change because they have long-historical records. Since the mid of the 18^{th} century, tide gauges have been installed to record sea level variability along coastlines and islands. The first tide gauges were installed in several locations of Europe, such as Amsterdam (the Netherlands), Stockholm (Sweden), Liverpool (UK), Brest (France), and Swinoujscie (Poland), and there were only 71 gauges in the beginning of 1900, mostly in the northern hemisphere (Church and White, 2011; Meyssignac and Cazenave, 2012; Mitchum et al., 2010). At present, the largest tide gauge database is provided by the Permanent Service for Mean Sea Level (PSMSL), based at the Proudman Oceanographic Laboratory in the United Kingdom. The PSMSL manages sea level data from about 200 national authorities

and serves monthly and annual mean sea level records from approximately 2000 stations, as shown in Figure 3.3 (Holgate et al., 2013).

The basic principle of a tide gauge is to measure the sea level relative to a nearby geodetic benchmark. Despite the simple method of measurement (as shown in Figure 3.4), tide gauge measurements have many problems. The main problems are their poor spatial distribution and the effect of land vertical movement. Tide gauge stations are located only along continental coastlines and islands and have limited spatial coverage. Because a tide gauges measures the height of sea surface relative to the fixed point on adjacent land, the corresponding ground motions directly affect tide gauges measurements. The tectonic, volcanic, and subsidence caused by natural or human activities such as groundwater extraction are sources of vertical movement.

The incompleteness of tide gauge data, the presence of large data gaps, the length of records, tide gauge benchmark jumps due to human error and data quality are the issues that must be considered in the determination of long-term sea level from these data.

Douglas (1991) pointed out that, when using tide gauges for the study of sea level variation, an adequate selection of the tide gauges may be required. By ignoring the tide gauges located around active tectonic and volcanic areas, the computation of sea level becomes more consistent, minimizing the impact of vertical land motion at each station.

Tide gauge measurements in the 20th century indicate that the mean rate of sea level rise vary about 1.6 – 2.8 mm·year^{-1}, as shown in Table 3.2.

Table 3.2 Various rates of sea level rise derived by tide gauge measurements (from http://sealevel.colorado.edu/).

Sea level rise (mm/year)	**Data used (years)**	**Number of tide gauges**	**References**
1.7 ± 0.2	1900-2009	>38 since 1900	Church and White (2011)
2.8 ± 0.8	1993-2009	~200	Church and White (2011)
1.9 ± 0.4	1961-2009	>190 since 1960	Church and White (2011)
1.8 ± 0.1	1880-1980	21	Douglas (1991)
2.4 ± 0.9	1920-1970	40	Peltier and Tushingham (1989)
1.62 ± 0.38	1807-1988	213	Unal and Ghill (1995)

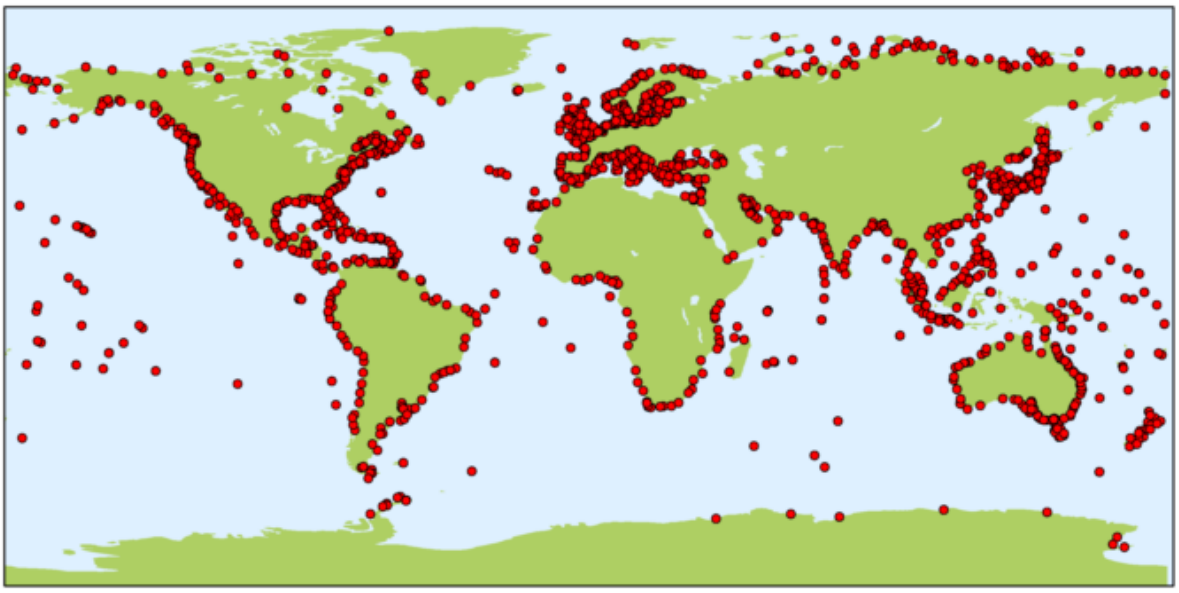

Figure 3.3 Distribution of PSMSL stations (Source: http://www.psmsl.org/).

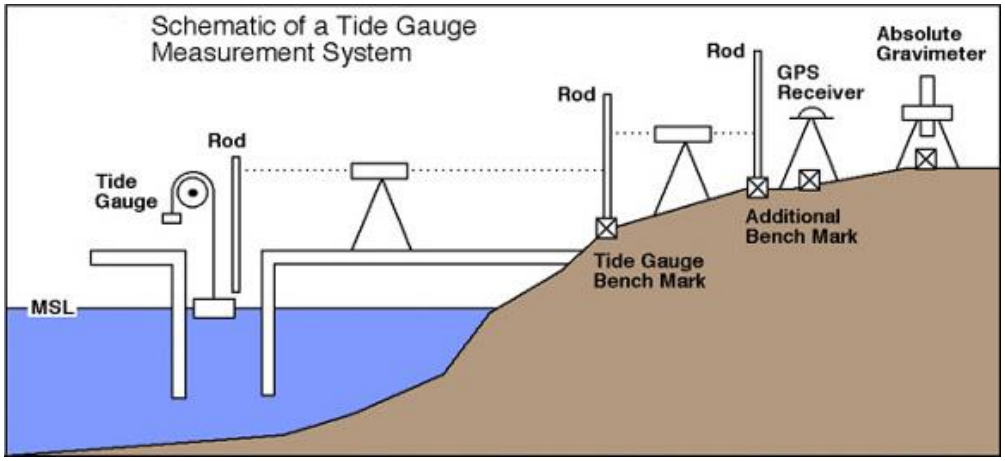

Figure 3.4 Principle of tide gauge measurement (source: http://sealevel.colorado.edu/).

Tide gauges and satellite altimetry provide independent and complementary data sets. Tide gauge measurements can be used e.g. to diagnose various problems in altimeter instruments. The comparison of satellite altimetry with gauge measurements provides relative calibration of the former and gauges are used to estimate altimeter sea surface height drift (Andersen and Cheng, 2013). A number of locations used as calibration sites are usually placed near the coast, such as Harvest platform (California), Bass Strait, Corsica (Senetosa) and Gradvos (Crete, Greece).

3.2.2. Satellite Altimetry

Since the 1990s, satellite altimetry became the most important tool to monitor sea level and ocean circulation. Satellite altimeters provide high quality data of absolute sea level with respect to a known reference system. The advantages of satellite altimetry over tide gauges are the independent measurement of land movement effects and near globally coverage.

Currently, the global sea level rise observed by satellite altimetry has been estimated to be about 3.1 – 3.4 mm/year (Figure 3.5 (a)) (Ablain et al., 2015; Cazenave et al., 2014; Church et al., 2013, Nerem et al., 2010). However, satellite altimetry shows that the spatial trend pattern in sea level is not rising uniformly across the globe (Figure 3.5 (b)). In some regions sea level is rising rapidly due to non-uniform ocean warming and variation of salinity. In some regions such as the Western and Northern Pacific, the Southern Indian Ocean and south of Greenland, the rates of sea level rise have been faster than the global rate over the past two decades. The Western Pacific Ocean exhibits rates of sea level rise up to more than 3 times the global mean during the altimetry period. Opposite to the Western Pacific, the Eastern Pacific Ocean dropped during the same period (Johnson and Wijffels, 2011; Nicholls and Cazenave, 2010).

The high variability of sea level around the Pacific Ocean is dominated by the El Niño and La Niña events. As evidence of ENSO effects, the comparison between the detrended global mean sea level variations and Multivariate ENSO Index (MEI), shows a strong correlation (0.7) (Cazenave et al., 2012; Nerem et al., 2010)

As mentioned previously, the rates of global sea level trend are between 3.1 and 3.4 mm per year. The trend of global mean sea level determined from altimetry has an uncertainty of 0.5 mm/year, estimated over the whole altimetry era (1993 – 2015) within a confidence interval of 95% (Ablain et al., 2016). According to Ablain et al. (2009) and Legeais et al. (2014), the wet tropospheric correction (WTC) is one of the error sources with a drift uncertainty in the range of 0.20 – 0.30 mm/year. Programs such as the European Space Agency (ESA) Climate Change Initiative (ESA-CCI) aim at improving the altimetry sea level data mainly for climate studies (Ablain et al., 2015; SL_cci, 2016).

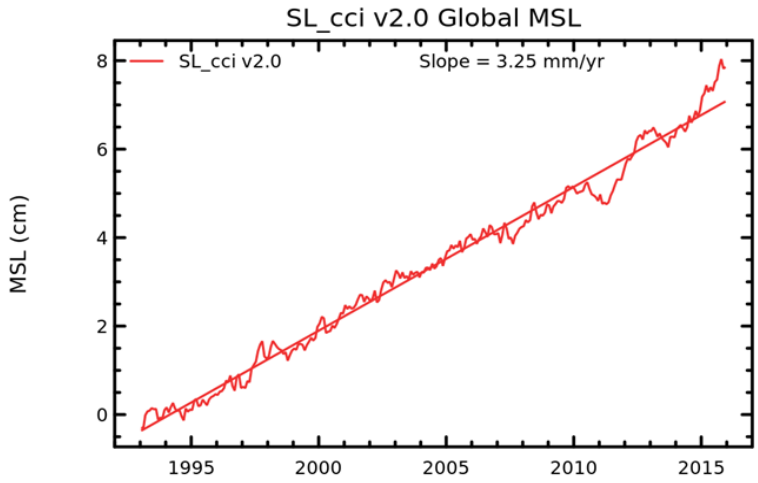

(a)

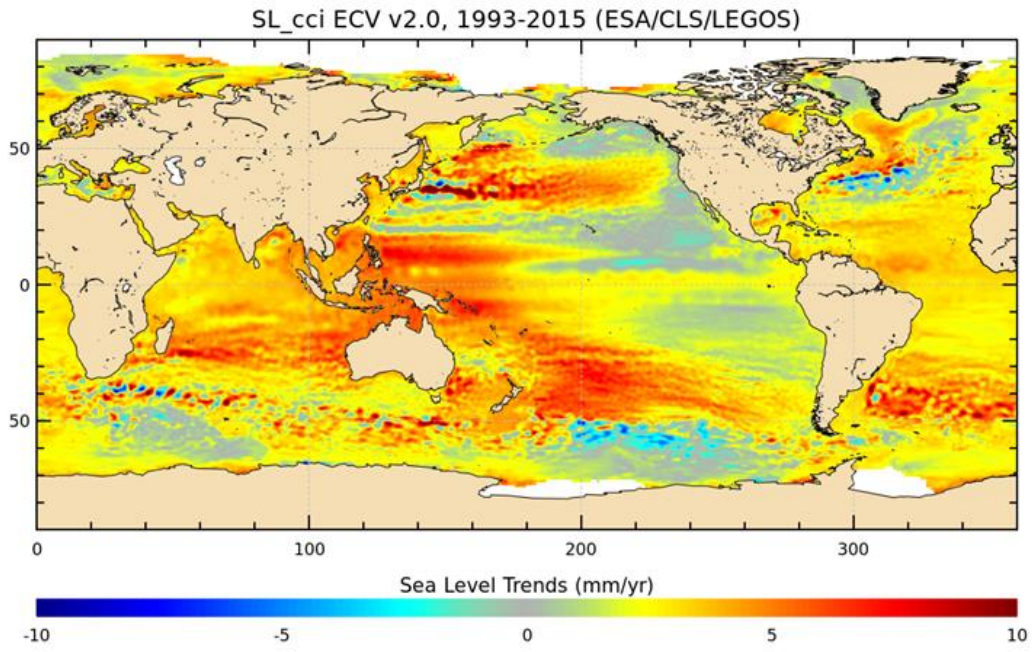

(b)

Figure 3.5 (a) The rates of global sea level rise and (b) spatial pattern of sea level trend derived from satellite altimetry over 1993-2015 (SL_cci, 2016).

3.2.3. Indirect measurements of Sea Level

For the purpose of studying sea level change, two observing systems can complement the information gathered from satellite altimetry: the Gravity Recovery and Climate Experiment (GRACE) and the ARGO network. GRACE, launched in 2002 jointly by NASA and the German Aerospace Centre, is a pair of satellites to measure the variation of Earth's gravity. GRACE time-variable gravity field. GRACE observations can be used to study mass redistribution within the Earth system, including the estimation of mass loss from ice sheets in Greenland, Antarctica, and glaciers in Alaska, all contributing to sea level change (Cazenave et al., 2009; Milne et al., 2009; Cazenave and Llovel, 2010). In addition, GRACE data provide estimates of the total increase in ocean mass from freshwater exchange with continents, changes in ocean bottom pressure associated with ocean circulation, and GIA in certain continental regions with large signals caused by postglacial rebound (Willis et al., 2008).

Other important data for understanding the mechanisms of sea level change are direct measurements of temperature and salinity in the water column. Although such measurements (particularly salinity) were relatively sparse even in the upper ocean before 2000, over the last decade there has been a rapid increase in the abundance of such measurements due to build-up of the ARGO array of profiling floats. The ARGO Project is a global array of profiling floats that measure the temperature and salinity of the upper layer of the ocean (Roemmich and Owens, 2000). The deployment of the ARGO array began in 2000, and they are now more than 3,000 floats (Roemmich et al., 2009). Together, GRACE and the ARGO measurement system can separate out the contributions to sea level change from changes in ocean mass and ocean water density. It is also possible, with the GRACE system, to determine the transfer of land-based water to the ocean (Milne et al., 2009).

3.3. Impacts of Sea level and the Future Projection

Global-mean sea level change is one of the most certain impacts of human-induced climate change, although the magnitude of future change remains uncertain. The sea level rise is becoming an important issue because it has big potential impacts in the future, as a potential catastrophe for the living people in the world. Given the large and growing concentration of population and economic activity in the coastal zone, the impacts of sea

level change have evoked widespread concern for more than two decades (Nicholls et al., 2014).

Since the industrial era began, changes in global sea level have been driven in part by the accumulation of greenhouse gases in the atmosphere, which trap heat and raise global temperatures. The primary processes responsible for modern sea-level rise are thermal expansion of ocean water and melting from glaciers, ice caps and the Greenland and Antarctic ice sheets.

A global sea level rise of 1.6 – 1.8 mm/year was observed through the twentieth century, faster than that of the nineteenth century (Church and White, 2011). Since the 1990s, the global sea level rise is estimated to be about 3 mm/year based on satellite altimetry (Cazenave et al., 2014; Church et al., 2013, Nerem et al., 2010). The IPCC AR5 has projected a total rise in the range of 0.52 m to 0.98 m in 2100 (scenario of RCP8.5) (Church et al., 2013) and this projection is larger than that in the AR4, of up to 0.76 m (Meehl et al., 2007).

As the magnitude of sea level rise increases, the impacts will become more relevant, especially in low-elevation zone. The immediate effect of a rise in sea level concerns submergence and increased flooding of coastal land, and saltwater intrusion of surface waters. Longer-term effects include morphological change and saltwater intrusion into groundwater as the coast adjusts to the new environmental conditions (Nicholls, 2002).

More than approximately 600 million people, or 10% of the global population, live in the low-areas and 77 million people of lying coastal them reside in megacities and these numbers will continue to grow (McGranahan et al., 2007). Most countries in South, Southeast and East Asia appear to be highly threatened because of the widespread occurrence of densely populated deltas, often associated with large growing cities (Nicholls and Cazenave, 2010). The fact that many people reside in megacities near coastlines, and that these cities continue to grow, the impact of sea level rise can cause major socioeconomic losses.

Understanding the cause of sea level variability is important, in particular for improving sea level predictions and mitigating potential impacts of sea level rise, particularly in vulnerable coastal areas. Global sea level rise projections are made using models of the ocean-atmosphere-climate system, extrapolations, or semi-empirical methods. Ocean-atmosphere models are based on the knowledge of the physical processes that contribute to sea-level rise, and they predict the response of those processes to different scenarios of future greenhouse gas emissions. These models provide a plausible estimate of steric sea level rise,

but they underestimate the land ice contribution because they do not fully account for rapid changes in the behavior of ice sheets and glaciers as melting occurs (ice dynamics). Estimates of the total land ice contribution can be made by extrapolating observations of recent ice loss rates from glaciers, ice caps, and ice sheets into the future. Extrapolations of future ice melt are most reliable for time frames in which the dynamics controlling behavior are stable, in this case, up to several decades. Semi-empirical methods, presented by Vermeer and Rahmstorf (2009), avoid the difficulty of estimating the individual contributions to sea-level rise by simply postulating that sea level rises faster as the Earth gets warmer. This approach reproduces the sea-level rise observed in the past, but reaching the highest projections would require acceleration of glaciological processes to levels not previously observed or understood as realistic.

IPCC made the projections of sea level rise which is reported in its assessment report. The newest prediction was presented in the Fifth Assessment Report (AR5) (Church et al., 2013). In this report, the projections of sea level rise are larger than the prediction in the AR4, primarily because of improved modeling of land-ice contributions. Thermal expansion is still the largest contribution, accounting for about 30 to 55 % of the projection.

To improve the understanding of the complex interactions of the climate system, ecosystems, and human activities and conditions, the research community develops and considers possible scenarios. These scenarios provide plausible descriptions of how the future might unfold in several key areas: socioeconomic, technological and environmental conditions, emissions of greenhouse gases and aerosols, and climate. These scenarios are called the Representative Concentration Pathways (RCPs), which form a set of greenhouse gas concentration and emissions pathways, designed to support research on impacts and potential policy responses to climate change (Moss et al., 2010).

In all the IPCC reports, sea level projections have been assembled using the conventional method of estimating sea level rise by simulating contributions for individual sea level components, such as thermal expansion, and melting ice from glaciers and ice sheets (Jevrejeva et al., 2014). The upper limits of the estimation confidence interval for RCP8.5 scenario projection of sea level in 2100 in IPCC AR5 is 0.98 m which corresponding to a high greenhouse gas emissions pathway.

Continued observation of global sea level and its causes will remain an important observational priority. Warming over the next century will continue to cause thermal

expansion related to sea level rise but the dominant contribution may become that of the melting ice from continents of Greenland and Antarctica. Considering this contribution, the largest uncertainties in sea level projections are due to the limited number of ice sheet models able to drive changes in ice sheet dynamics with climate forcing (Jevrejeva et al., 2014).

CHAPTER 4

WET TROPOSPHERIC CORRECTION AND ITS IMPROVEMENT IN THE INDONESIAN REGION

Since the 1990s, the global mean sea level (GMSL) rise can be estimated precisely using satellite altimeter measurements. However, several corrections need to be applied to the sea surface height measurement, such as the delay in the atmosphere (ionospheric, dry and wet tropospheric corrections), effects of sea state bias on ocean surface, tides corrections (ocean, solid earth and polar tides, as well as loading effects), and the ocean response to atmospheric dynamics (inverse barometric correction for low frequencies and atmospheric dynamic correction for high frequencies).

Regarding the GMSL trend, an uncertainty of 0.5 mm/year was estimated over the satellite era (1993 – 2015) within a confidence interval of 95% (Ablain et al., 2016). One of the main error sources affecting the mean sea level is the radiometer wet tropospheric correction with a drift uncertainty in range of 0.2 - 0.3 mm/year (Ablain et al., 2009; Legeais et al., 2014). This correction is potentially contaminated by long-term instrumental drift, such as the changes of internal temperature due to yaw maneuvers (Ablain et al., 2009; Desai and Hains, 2004; Scharroo et al., 2004). Calibrations with external measurements are periodically performed to detect drifts on the on-board microwave radiometers. The algorithms used to retrieve the WTC from the measured brightness temperatures of the various microwave radiometer (MWR) channels assume a constant surface ocean emissivity and are valid for ocean conditions, light rain and wind speed lower than 20 ms^{-1}. Therefore, in the presence of surfaces with different emissivity (such as land or ice) the measurements become invalid, particularly in coastal and polar regions (Fernandes et al., 2015).

A number of approaches have been proposed for correcting the altimeter measurements in the coastal regions, where the MWR measurements become invalid due to land contamination in the radiometer footprint. In this study, particular attention has been given to one of these approaches, the GNSS-derived path delay (GPD), developed at the University of Porto. This study is a contribution to improve the WTC in the Indonesian region through the implementation of an improved GPD correction for this region.

In this chapter, the various methods used in the retrieval of the WTC are first presented in section 4.1 (on-board MWR, Numerical Weather Models, the GPD, and WTC from GNSS observations). Section 4.2 describes the WTC improvement for the Indonesian region.

Regarding the objective of this thesis, the study of sea level around the Indonesia region with emphasis on the wet path delay, the various WTC available for this region are assessed, in order to select the most suitable WTC in this region (Section 4.3).

4.1. Methods for retrieving the Wet Tropospheric Correction

4.1.1. WTC definition

The atmosphere affects the velocity of microwave signals through an effect referred to as refraction. Since the velocity and the ray bending of light varies between different media, the refractive index (n) for any medium is introduced:

$$n = \frac{c_0}{c} \tag{4.1}$$

Where c_0 is the speed of light in vacuum and c is the speed of light in a given medium. The refractive index is expressed in terms of the refractivity N which is related to n as $N = (n - 1)\ 10^6$.

The troposphere contains about 80% of the total molecular mass of the atmosphere, nearly all the water vapor and aerosols. The electrically neutral atmosphere is composed by dry gases (e.g. N_2, O_2, Ar, CO_2, Ne and He) and water vapor (H_2O). The propagation delay due to neutral atmosphere has been recognized as a major modeling error for many space-based electromagnetic ranging techniques, such as very long baseline interferometry, one-way and two-way satellite-based positioning systems, satellite altimetry, satellite laser ranging, radio science experiments and planetary spacecraft tracking (Mendes, 1999).

In particular, the atmospheric total path delay due to troposphere in the zenith direction, or zenith total delay (ZTD), may be written as (Saastamoinen, 1972)

$$ZTD = \int_0^h (n-1)dh = \ 10^{-6} \int_0^h N\ dh \tag{4.2}$$

where *n* is the refractive index of the troposphere, *h* is the height of the atmosphere, and *N* is the refractivity. The refractive index (*N*) as given by Thayer (1974):

$$N = \left(k_1 \frac{P_d}{T} \right) + \left(\frac{k_2 \frac{P_w}{T} + k_3 \frac{P_w}{T^2}}{Z_w} \right) \tag{4.3}$$

$$\frac{1}{Z_d} = 1 + P_d \left[57.97 \; x \; 10^{-8} \left(1 + \frac{0.52}{T} \right) - \frac{9.4611 \; x \; 10^{-4} t}{T^2} \right] \tag{4.4}$$

$$\frac{1}{Z_w} = 1 + 1650 \left(\frac{P_w}{T^3} \right) (1 - 0.01317t + 1.75 \; x \; 10^{-4} t^2 + 1.44 \; x \; 10^{-6} t^3) \tag{4.5}$$

where k_1 and k_2 are microwave refractivity constants due to the induced polarization of both polar and non-polar molecules, while k_3 is due to the orientation polarization of a polar molecule (water vapor). P_d and P_w are the dry air and water vapor partial pressures in millibars, respectively, and T is the temperature in Kelvin. Z_d and Z_w are compressibility factors with the subscripts having the same meaning as for the pressures. t is the temperature in degrees Celsius. The first term of Equation 4.3 can be called the dry tropospheric delay and the last two terms may be called the wet delay. The values for k_1, k_2 and k_3 have been determined from laboratory experiments and from theoretical calculations. As shown in Table 4.1, some empirical values of refractivity constants are presented from various authors.

Table 4.1 Empirical values of the microwave refractivity constants (Bevis et al., 1994).

Reference	k_1 **(K/hPa)**	k_2 **(K/hPa)**	$k_3 \times 10^3$ **(K²/hPa)**
Essen and Froome (1951)	77.636 ± 0.03	64.69 ± 0.2	371.8 ± 0.4
Essen (1953)	77.636 ± 0.03	74.99 ± 0.2	368.2 ± 0.4
Thayer (1974)	77.60 ± 0.014	64.79 ± 0.08	377.6 ± 0.4

Instead of dividing the refractivity into its dry and water vapor parts, it is useful to express it as its hydrostatic and non-hydrostatic, or wet component, parts. The ZTD can be separated into the sum of the hydrostatic (dry) component, i.e. the zenith hydrostatic delay (ZHD), and the wet component, the zenith wet delay (ZWD). The hydrostatic component, accounts for nearly 90% of the ZTD. Although the mean value at sea level of the hydrostatic component is about 2.3 m, it is usually modeled with high accuracy from in situ

measurements of surface pressure, from a Numerical Weather Model (NWM) or from alternative sources. The wet component, accounting only for nearly 10% of the total path delay, is much more variable in space and time and therefore difficult to model (Fernandes et al., 2013a).

The wet troposphere path delay strongly affects the altimeter range. Because of its high variability in space and time, being difficult to model, attention is needed in order to determine the wet troposphere path delay with enough accuracy for satellite altimetry. Particular problems in the modeling of the wet path delay in altimeter studies occur at coastal areas. The effect of land on the radiometer-derived wet tropospheric correction decreases the accuracy of this correction in these regions. The discrepancy of the emissivity between ocean and land on the altimeter footprint near the coast causes the algorithms used to retrieve the WTC to output invalid measurements. A number of authors have been proposed techniques to improve the WTC, particularly in coastal zones, examples in Bennartz (1999), Brown (2010), Fernandes et al. (2010) and Obligis et al. (2011).

The following subsections present a description of wet tropospheric corrections which are used in altimeter studies, included from on-board microwave radiometer, from numerical weather model, from the GPD and from GNSS observations.

4.1.2. WTC from on-board Microwave Radiometers

The wet tropospheric correction depends on the atmospheric vertical profile of humidity, temperature and pressure which can be retrieved from microwave radiometer measurements. The wet tropospheric correction is computed from the onboard MWR by measuring the brightness temperature (TBs) at two or three frequencies in the range of 18 and 37 GHz, in spectral bands sensitive to water vapor and cloud liquid water.

TOPEX/Poseidon carried the three-channel TOPEX Microwave Radiometer (TMR), which operated at 18, 21 and 37 GHz, while for Jason-1 and Jason-2 the Jason-1 Microwave Radiometer (JMR) and the Advanced Microwave Radiometer (AMR) operate at 18.7, 23.8 and 34 GHz, respectively. The algorithm for the TMR/JMR/AMR performs the retrieval in three steps. First, a term analogous to a surface “radiometer wind” and a term due to cloud liquid water are estimated using a linear combination of the TBs from the 3 channels. Then, a first approximation of the wet path delay is estimated. Finally, the wet path delay is obtained by adding to the cloud liquid water term, a term obtained from a log-linear combination of

the TBs from the 3 channels, with coefficients depending on the "radiometer wind" and wet path delay class interval obtained in the first two steps (Keihm and Ruf, 1995).

The ERS-1/MWR and ERS-2/MWR algorithm was developed using a direct log-linear combination of the two channels TBs (23.8 and 36.5 GHz) and the altimeter wind speed (Eymard and Obligis, 2006). For the Envisat/MWR algorithm, a mixed method, already used for ERS-1/MWR and ERS-2/MWR processing, which is a compromise between statistical and physical methods, was used. To better account for the non-linear relationship between the TBs and the tropospheric correction, as well as to prevent from errors in the altimeter wind calculation, the two channels TBs and the altimeter backscattering coefficient σ_0 in Ku-band have been used as inputs in a neural network algorithm (Obligis et al., 2006)

Similar to ERS-1/2-MWR and Envisat/MWR, the two channels of the microwave radiometer on SARAL mission (23.8 GHz and 37 GHz) are combined with the altimeter backscattering coefficient (σ_0) to determine the WTC. The third channel, which is sensitive to wind-driven variations in the sea surface, is replaced by the roughness information contained in Ka-band σ_0 altimeter measurements. The wet tropospheric correction is thus derived from the combination of the two brightness temperatures and the altimeter σ_0 (Picard et al., 2015; Steunou et al., 2015). Cryosat-2 does not carry an on-board microwave radiometer. The wet tropospheric correction provided by the ECMWF operational model is the default correction applied to the CryoSat-2 radar altimeter data.

In the open ocean, with homogeneous water surface, the on-board microwave radiometer retrieves the wet path delay with adequate accuracy, about 1 cm root mean square (RMS) error (Brown, 2010). Near the coast, this is not true due to the algorithms used to determine the wet path delay from the brightness temperatures (TBs) measurements, being only valid on homogeneous water surface, because they are based on sea-surface emissivity models. The emissivity of the ocean is near 0.5 between frequencies 18 GHz and 34 GHz, while land has an emissivity above 0.9 at these frequencies. The radiometer footprint may contain both portions of water and land, causing the WTC retrieval algorithm to produce invalid measurements. The radiometer measurements are flagged as invalid data for TMR on T/P and JMR on Jason-1 starting from about 50 km from land, while AMR on Jason-2 is flagged around 25 km from land (Brown, 2010). For ERS-1/2 and Envisat, the invalid data measurements start from 50 km to coast (Desportes et al., 2007).

Several methods were proposed to solve this problem by improving the MWR retrieval algorithm. Bennartz (1999) proposed an algorithm to correct the brightness temperatures on the mixed footprint (contaminated by land) using Special Sensor Microwave Imager (SSM/I) data. Desportes et al. (2007) analyzed and tested several algorithms for retrieving the wet path delay in coastal regions. They found the method of SSM/I mixed land-water footprints proposed by Bennartz (1999) to have good performance, reducing by about 50% the error relative to the analytical and theoretical correction of TBs, when applied to TMR. A new near-land radiometer wet path-delay retrieval algorithm was proposed by Brown (2010). The algorithm uses a function of the 18.7 GHz land fraction based on the database of modeled coastal TBs. The results show that this algorithm gives an error of less than 0.8 cm up to 15 km from land, and less than 1.5 cm up to the coastline when it is applied to the AMR on Jason-2.

Global mean sea level rise derived by satellite altimetry is estimated to be about 3.4 ± 0.4 mm/year over 1993 to 2014 (Ablain et al., 2015; Cazenave et al., 2014; Nerem et al., 2010). The wet tropospheric correction is still highly impacting the uncertainty in the estimation of the mean sea level trend. According to Ablain et al. (2009), the radiometer wet tropospheric correction, due to possible drifts on TMR and JMR, contributes about 0.3 mm/year to the trend of MSL computation. Thus, this correction is potentially contaminated by long-term instrumental drifts. Concerning the reduction of this potential error, a number of authors have investigated the microwave radiometer instrument drifts. Scharroo et al. (2004) assessed on-board radiometers from several altimeter satellites, such as ERS-1, ERS-2, Envisat, TOPEX/Poseidon, GFO and Jason-1. They found that there were significant drifts due to unmodeled errors in path delay of up to 1 mm/year. A number of authors used data from the Global Positioning System (GPS) to monitor the microwave radiometer for most satellite altimeter missions: TOPEX/Poseidon (Haines and Bar-Sever, 1998), Jason-1 (Desai and Haines, 2004; Edwards et al., 2004), Jason-2 (Sibthorpe et al., 2011), data from GPS and VLBI for TOPEX/Poseidon and Jason-1 (Macmillan et al., 2004) and the Special Sensor Microwave Imager (SSM/I) and the Tropical Rainfall Mapping Mission's Microwave Imager (TMI) data for Jason-1 (Zlotnicki and Desai, 2004).

4.1.3. WTC from Numerical Weather Models

At present, various global atmospheric models are available to determine the wet tropospheric correction, such as the European Center for Medium-range Weather Forecasts (ECMWF) and the National Centre for Environment Prediction (NCEP).

ECMWF provides global $0.125^{o}\times0.125^{o}$ grids for the Operational model and $0.75^{o}\times0.75^{o}$ grids for ERA Interim of several atmospheric parameters every 6 hours (Dee et al., 2011). Both models provide global grids of sea level pressure, total column water vapor (TCWV) and surface temperature (2-m temperature, 2T). These parameters can be used to compute the wet tropospheric correction.

The TCWV, integrated water vapor (IWV) or precipitable water (PW) is the total water vapor contained in an air column from the Earth's surface to the top of the atmosphere and is usually expressed in kg/m^2 or millimeters (mm), as the length of an equivalent column of liquid water.

According to Stum et al. (2011), the TCWV (or IWV or PW) in centimeters is given by

$$TCWV = IWV = PW = \int_0^H \rho_v dz \tag{4.6}$$

where ρ_v is the water vapor density in grams per cubic centimeter, z is the altitude (in meter), and H is the altitude above which the water vapor density is considered to be negligible.

The water vapor path delay correction or WTC can be approximated by Keihm et al. (1995):

$$WTC = 1.763 \int_0^H \frac{\rho_w}{T} dz \tag{4.7}$$

where WTC is in centimeters and T is the temperature in Kelvin.

The ratio between *WTC* and *TCWV* can be described by a decreasing function of water vapor content, which expresses its temperature dependence. The temperature and humidity profiles from the ECMWF model outputs were used to derive the following function to calculate WTC from TCWV (Stum et al., 2011):

$$\frac{WTC}{TCWV} = -(a_0 + a_1 TCWV + a_2 TCWV^2 + a_3 TCWV^3) \quad (4.8)$$

with a_0 = 6.8544, a_1 = -0.4377, a_2 = 0.0714, a_3 = -0.0038. *WTC* and *TCWV* are in centimeters. Keeping TCWV in cm, the corresponding WTC values in meters are obtained as follows (Fernandes et al., 2013b)

$$WTC = -(a_0 + a_1 TCWV + a_2 TCWV^2 + a_3 TCWV^3)\, TCWV.10^{-2} \quad (4.9)$$

The relation between WTC and TCWV is a function of various physical constants and of the weight mean temperature T_m of the atmosphere. The WTC can be estimated from TCWV and T_m using the equation (Bevis et al., 1994):

$$WTC = -\left(0.101995 + \frac{1725.55}{T_m}\right)\frac{TCWV}{1000} \quad (4.10)$$

where T_m is the mean temperature of the troposphere, which may be in turn modeled from the surface temperature (T_0) (Mendes et al., 2000).

$$T_m = 50.40 + 0.789\, T_0 \quad (4.11)$$

with T_0 in kelvin, TCWV in millimeters and WTC in meters.

For less accurate studies, the WTC can be estimated as being proportional to TCWV by (Fernandes et al., 2013b; Keihm et al., 2000):

$$WTC(in\ m) = -\frac{(6.759\, TCWV - 0.0291\, TCWV^2 + 0.00031\, TCWV^3)}{1000} \quad (4.12)$$

By neglecting higher order terms in Equation (4.12) it can be rewritten by

$$WTC(in\ m) = -0.0067\, TCWV(in\ mm) \quad (4.13)$$

where TCWV is measured in mm.

In order to evaluate the consistency of NWM data from ECMWF, Fernandes et al. (2013b) compared the WTC derived from ERA Interim and ECMWF operational models. They report that ECMWF operational model is not suitable for use in altimetric studies over the years prior to 2004, since prior to that date the errors increase considerably. The accuracy of ERA Interim model is similar to present ECMWF operational model since about 2004.

Although the spatial resolution of ERA Interim is lower than ECMWF operational, the fact that it is a reanalysis has the advantage of being homogeneous, unlike the operational model.

4.1.4. WTC from the GPD algorithm

Wet troposphere from the on-board near-nadir-looking microwave radiometer is the best source of information to compute the wet tropospheric correction for altimeter data. The main problem of the MWR-derived WTC in coastal areas is associated with the invalid MWR data measurements. In addition, the accuracy of present NWM-derived WTC is still not good enough for most altimetry applications (Fernandes and Lázaro, 2016). Therefore, a method using Global Navigation Satellite System (GNSS) measurements at inland and coastal stations to determine precise tropospheric path delays (PDs) was proposed by the University of Porto (UPorto), Portugal (Fernandes et al., 2010).

The GNSS-derived Path Delays (GPD) methodology is based on the combination, by objective analysis (OA), of wet path delay observations from various sources (valid MWR measurements at the nearby points and ZWD derived from GNSS datasets), to update a first WTC guess value given by an atmospheric model (Fernandes et al., 2015). The estimate of the WTC field at each point P, F(P), is thus given by the sum of the first guess, FG(P), and a weighted average of the set of *N* WTC anomalies X_i^{ano} with respect to the first guess, at the *N* points X_i within given space and time search radiuses around point P:

$$F(P) = FG(P) + \sum_{i=1}^{N} W_i X_i^{ano} \tag{4.14}$$

$$X_i^{ano} = X_i - FG(P) \tag{4.15}$$

The weights W_i are estimated from the statistical properties of the WTC field:

$$W_i = \sum_{k=1}^{N} C_k \, A_{ik}^{-1} \tag{4.15}$$

where C_k is the covariance between the computation point P and the nearby measurement point *k* and *k* = 1, …, N, and A_{ik}^{-1} is the inverse of the variance-covariance matrix of the WTC measurement. Each covariance is normalized by dividing by the variance of the WTC field at the estimation point P, so in fact correlations instead of covariance are used.

Fernandes et al. (2010) described that the spatial and temporal variability of ZWD field is taken into account by correlation function *F(r, Δt)*

$$F(r, \Delta t) = F(r) \text{ x } F_{\Delta t}(\Delta t) \tag{4.17}$$

In the absence of the knowledge of empirical covariance model of the background field, the correlation function *F(r)* that decreases exponentially with the square of the distance between acquisitions was adopted:

$$F(r) = e^{-\frac{r^2}{D^2}} \tag{4.18}$$

where *r* is the distance between each pair of point and *D* is the spatial correlation scale. Based on Fernandes and Lázaro (2016), the spatial correlation scales were determined from a set of ECMWF operational model grids at $0.125^o \times 0.125^o$ and computed for a grid of points centered on $2^o \times 2^o$ "boxes". For each box, the correlation between all pairs of points separated by a distance *r*, for classes of *r* spaced by 10 km, were determined. The corresponding correlation scale *D* is obtained by either fitting a Gaussian function to the correlation table (*r*, corr(*r*)) or by computing the value of *r* corresponding to a correlation equal to 1/*e*. Both approaches give similar results and the resulting spatial correlation scales are within 40 to 93 km. The temporal variability of the field is also taken into account and the covariance function is therefore represented by a space-time analytical function *F(r, Δt)* that is obtained by multiplying the space correlation function *F(r)* by a stationary Gaussian decay of the form:

$$F_{\Delta t}(\Delta t) = e^{-\frac{\Delta t^2}{T^2}} \tag{4.19}$$

where *Δt* is the time interval between the acquisitions of the measurements associated to each pair of locations and *T* is the temporal correlation scale, set to 100 minutes (Bosser et al., 2007).

In summary, the implementation of the method requires the knowledge of the following quantities:

- First guess of WTC;
- Variance of WTC field;
- White noise associated with the measurement of each WTC data set (required to compute the diagonal elements of the variance-covariance matrix, A_{ik});
- Parameters defining the correlation function: space and time correlation scales;

- Space and time search radiuses.

As first guess, the WTC derived from a numerical weather model are adopted, such as from the ECMWF ERA Interim model for all missions with data prior 2004 and the ECMWF Operational for the most recent missions (Fernandes and Lázaro, 2016). The data used for each WTC estimation are the WTC values from all data sets within the spatial and temporal influence regions, centered at the location and instant of the altimeter measurement at which the estimation is required, that should equal the spatial and temporal correlation scales.

At present, ZWD data from more than 800 GNSS stations have been used. Only stations up to 100 km from the coast and with an orthometric height less than 1000 m were considered. GPD corrections are available for most altimeter missions, both for the missions that do not carry any on-board microwave radiometer (as CryoSat-2) and the missions which carry this sensor.

The most recent version of the GPD algorithm, GPD Plus (GPD+), incorporates WTC observations derived from water vapor products from a dataset of 19 scanning imaging microwave radiometers (SI-MWR) on board various remote sensing satellites, provided by NOAA Comprehensive Large Array-Data Stewardship System (CLASS) and Remote Sensing System (RSS), have also been used in the WTC estimation. Besides the additional SI-MWR datasets, the GPD+ has improved spatial correlation scales and criteria for detecting valid/invalid MWR values. The algorithm allows the recovery of a significant number of measurements, ensuring the continuity and consistency of the correction in the open ocean/coastal transition zone and at high latitudes (Fernandes and Lázaro, 2016).

4.1.5. WTC from GNSS observations

At present, the number of permanent GNSS stations has been increasing worldwide, particularly in the coastal regions. Apart from determining the position and time, the GNSS allows the determination of zenith total delays at station height with an accuracy of a few millimeters (Fernandes et al., 2010; Pacione et al., 2011; Snajdrova et al., 2005).

Several studies using GNSS to determine tropospheric delays associated with the monitoring of radiometers on-board altimeter satellites have been proposed, such as

monitoring the microwave radiometer of T/P (Haines and Bar-Sever, 1998), Jason-1 (Desai and Haines, 2004; Edwards et al., 2004) and Jason-2 (Sibthorpe et al., 2011).

The tropospheric propagation delay is modeled in GNSS processing as (Davis et al., 1985):

$$STD(E) = ZHD\ mf_h(E) + ZWD\ mf_w(E) \tag{4.20}$$

where STD is the measured slant total delay, E is the elevation angle of the GNSS satellite and mf_h and mf_w are the mapping functions for hydrostatic and wet components, respectively, relating the zenith delays with those in the slant direction.

A priori ZHD can be estimated from surface pressure data using the modified Saastamoinen model (Davis et al., 1985). An error in the a priori ZHD will be absorbed by the estimated ZWD; therefore the knowledge of the ZHD with high accuracy is of major importance (Kouba, 2009).

There are various GNSS software packages which can be used for ZTD computation, such as GAMIT (Herring et al., 2006), GIPSY-OASIS (GNSS-Inferred Positioning System and Orbit Analysis Simulation Software) (Zumberge et al., 1997) and Bernese (Dach et al., 2007). GAMIT processes simultaneous observations from a set of GNSS at least one of these receivers must be in a known location within a specific reference frame. Unlike the differential method, the Precise Point Positioning (PPP) refers to the mm-cm positioning of a GNSS station using a single receiver. The PPP is a typical absolute positioning method using un-differenced dual-frequency pseudo-range and carrier-phase observations along with precise satellite orbit and clock information to determine the position of a stand-alone GPS station (Zumberge et al., 1997). The PPP method has been integrated into several scientific GPS software packages, such as the GIPSY/OASIS software developed by the Jet Propulsion Laboratory (JPL) and the Bernese GPS software developed by the Astronomical Institute of the University of Berne. PPP has become a choice for positioning in many remote areas, in which nearby base stations are unavailable, or the establishment of base stations is difficult or not cost-effective.

4.1.6. Computation of GNSS-derived ZWD for coastal altimetry

It has been shown that the ZTD can be computed from GNSS with an accuracy of a few mm using Equation 4.20 (Davis et al., 1985). In equation 4.20, STD is the slant GNSS

observation and ZWD is the unknown wet tropospheric delay in the zenith direction. To determine ZWD, *a priori* ZHD is required as well as the mapping functions mf_h and mf_w. Thus equation 4.20 provides an accurate combined ZTD value, the sum of ZHD and ZWD.

To get accurate ZWD, the ZTD has to be corrected for an accurate ZHD (more accurate than the *a priori* value used in Equation 4.20). ZHD can be computed with an accuracy of a few millimeters (Fernandes et al., 2013a; Niell et al., 2001), either from in situ reliable pressure data or from global grids of a model such as ECMWF. The study performed by Fernandes et al. (2013a) pointed that ZHD at GNSS coastal sites with heights up to 1000 m can be computed, at surface point, with accuracy of a few mm from sea level pressure (SLP) field from an atmospheric model. ZHD has significant height dependence as shown at Equation 2.13. In this study and in the processing of all GNSS-derived ZTD, ZHD from the SLP fields of the ERA Interim model (Equation 2.11), further reduced to station height, using Equation 2.13, have been used.

The quantities derived so far (ZTD, ZHD and ZWD) are all given at station height. To be used in coastal altimetry they are required at sea level where the altimetric measurements are referred to. ZHD is directly given at sea level from SLP values using Equation 2.11. The ZWD values must be reduced from the GNSS station elevation to sea level using e.g. the expression by (Kouba, 2008)

$$ZWD(h_0) = ZWD(h_s)\, e^{\frac{h_s - h_0}{2000}} \tag{4.21}$$

where h_0 and h_s are the orthometric heights of sea surface and the GNSS station, respectively.

This procedure has been adopted in this study to compute the ZWD at sea level for the Indonesia region (Indonesian network or INA network). These ZWD were then used as observations in the GPD+ estimations, together with all other datasets (valid MWR points and SI-MWR observations), to get an improved GPD for the Indonesian region.

4.2. Wet Tropospheric Correction in the Indonesian Region

4.2.1. Invalid MWR observations in the Indonesian region

As mentioned in previous sections, the on-board MWR provides invalid measurements in the coastal regions. These invalid data can be within different bands of distance from the coast depending on the altimetry missions. For example, for T/P and Jason-1 the invalid data start at distances from the coast of about 50 km, for Jason-2 the corresponding distance is about 25 km (Brown, 2010) and for Envisat it is 50 km (Desportes et al., 2007).

The GPD+ algorithm identifies the invalid MWR measurements due to all considered error sources: land, ice, rain, instrument malfunction, outliers, etc. The invalid MWR points are detected and flagged (flag_MWR_rej) using a set of criteria as given below, according to Fernandes and Lázaro (2016):

- flag_MWR_rej = 1 — if the rad_surf_type flag is 1, usually related with land contamination, but also with instrument problems;
- flag_MWR_rej = 2 — if the measurement was acquired at a distance from the coast less than a given threshold, e.g., 30 km for GFO and TOPEX/Poseidon; 20 km for Jason-1 and 15 km for Jason-2;
- flag_MWR_rej = 3 — if the ice_flag is 1, indicating ice contamination. More generally, an invalid point located at latitudes $|\varphi| > 45^{o}$ may be flagged as ice even if this is not the actual cause of invalidity;
- flag_MWR_rej = 4 — based on statistical parameters, including median filters, function the differences between MWR and model WTC, not only at the same measurements but also at neighbouring points (related with ice, land, rain or outlier detection);
- flag_MWR_rej = 5 — if the MWR WTC is $\geq$ 0.0 m or < -0.5 m, usually associated with rain or ice contamination, or instrument failure.

Figure 4.1 shows the invalid on-board microwave radiometer measurements for the various missions, for the Indonesian region, using the set of criteria described above. The results show the different impact of the land contamination on the measurements of the various altimetric missions used in this study. The plot for TMR on TOPEX shows a lot of

invalid measurements near the coast, while the plots for JMR on Jason-1 and AMR on Jason-2 show a reduction of invalid measurement due to the fact that their algorithms have already been enhanced near the coast (Brown, 2010). The dual frequency MWR on ERS-1, ERS-2, Envisat and SARAL also generate a lot of invalid measurements in coastal areas.

As expected, results show that in the Indonesian region, land contamination is the most important source of data invalidity, although a few invalid data can also be seen in open ocean due to other invalidity sources, such as rain or outliers.

For the Indonesian region, the percentage of invalid MWR points with respect to the assumed valid data in the GPD+ WTC is 14.6 % for TOPEX/Poseidon, 5.4% for Jason-1, 5.3% for Jason-2, 10.7% for ERS-1 (only cycles 144 to 156), 11.2% for ERS-2, 15.3% for Envisat and 13.1% for SARAL, respectively. This means that when the GPD+ WTC is used instead of the on-board MWR WTC, all these points will be recovered. These results were obtained using the whole period of analysis for each altimetric mission.

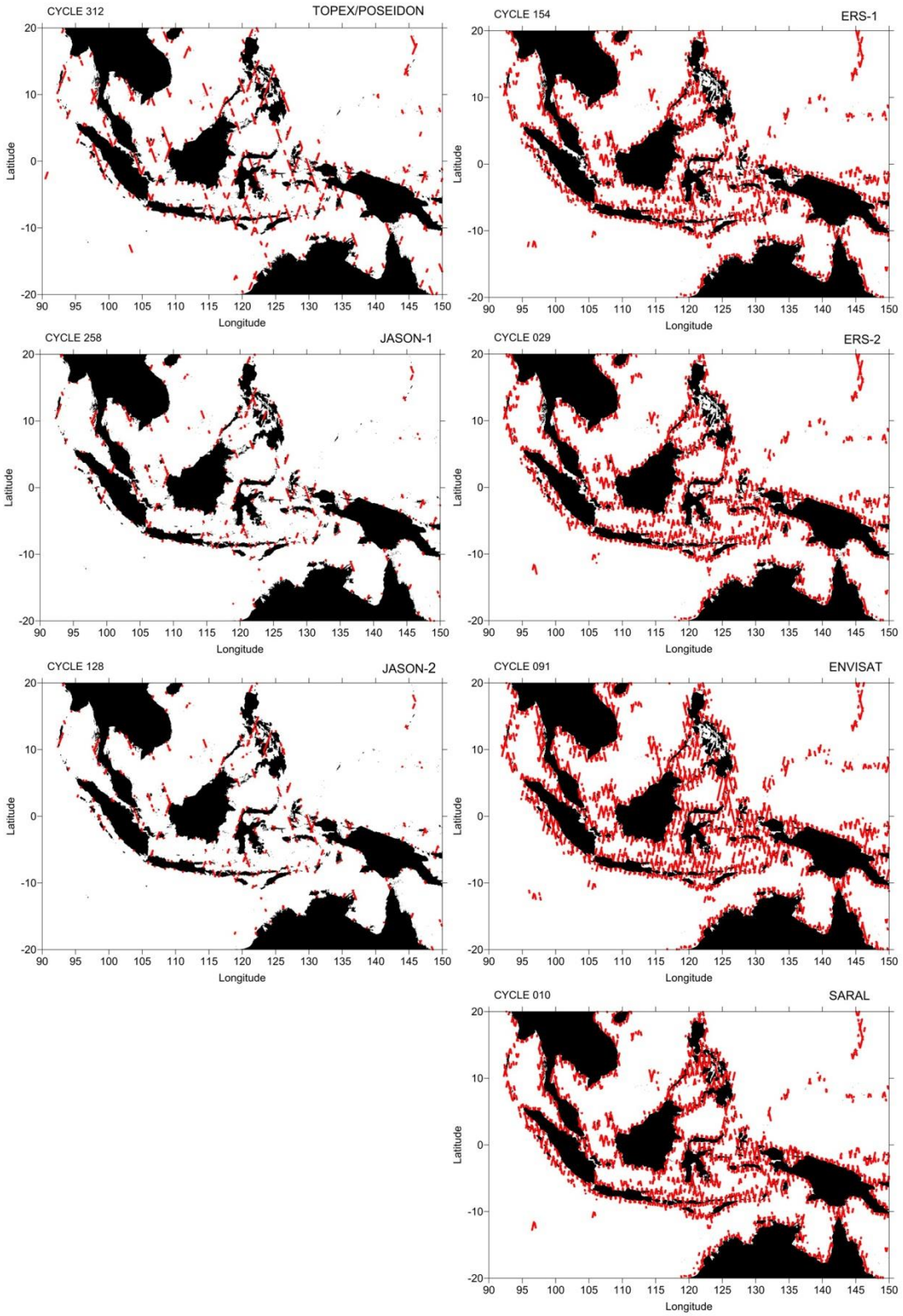

Figure 4.1 The invalid points in the radiometer-derived wet tropospheric correction for several altimeter missions around the Indonesian region, according to the rejection criteria used in the GPD+ algorithm (red dots). These results refer to the whole period of analysis for each altimetric mission.

4.2.2. Computation of GNSS-derived ZTD in the Indonesian region.

To increase the coverage over Indonesia, a set of additional ZTD were computed in the scope of this study. For this purpose, GNSS data from a set of nearly 30 stations, located mostly along the Sumatera Island have been obtained from the Sumatera GPS array (SUGAR), the Indonesian Geospatial Information Agency (BIG) and Système d'Observation du Niveau des Eaux Littorales (SONEL) (Figure 4.2 (bottom)). These data are GNSS observations, provided in Receiver Independent Exchange (RINEX) format, from which the corresponding ZTD are computed. In the following paragraphs the method used in these computations is explained.

Regarding the computation of ZTD in the Indonesian region, GNSS data were processed using GIPSY-OASIS package which applies the PPP technique. GIPSY-OASIS is a GNSS data processing package developed by JPL, and maintained by the Near Earth Tracking Application and Systems groups, California Institute of Technology. In this study, the GIPSY-OASIS version 6.3 was used. GNSS data were obtained in RINEX format. The data were sampled with 7 degree elevation cut off angle and 30 second recording intervals. The IGS combined final precise orbits and clock parameters were used in the analysis. The ZHD was modeled using VMF1 mapping function (Boehm and Schuh, 2004; Boehm et al., 2006). The zenith delay was estimated with a temporal resolution of 5 minutes. The ionospheric delay was eliminated from L1 and L2 data combination using both pseudo-range and carrier phase observations. Satellite and receiver antenna phase center variation (APV) maps were automatically applied following the IGS standards (Byun and Bar-Sever, 2009). This set of ZTD computed for the INA network will be further referred as INA ZTD.

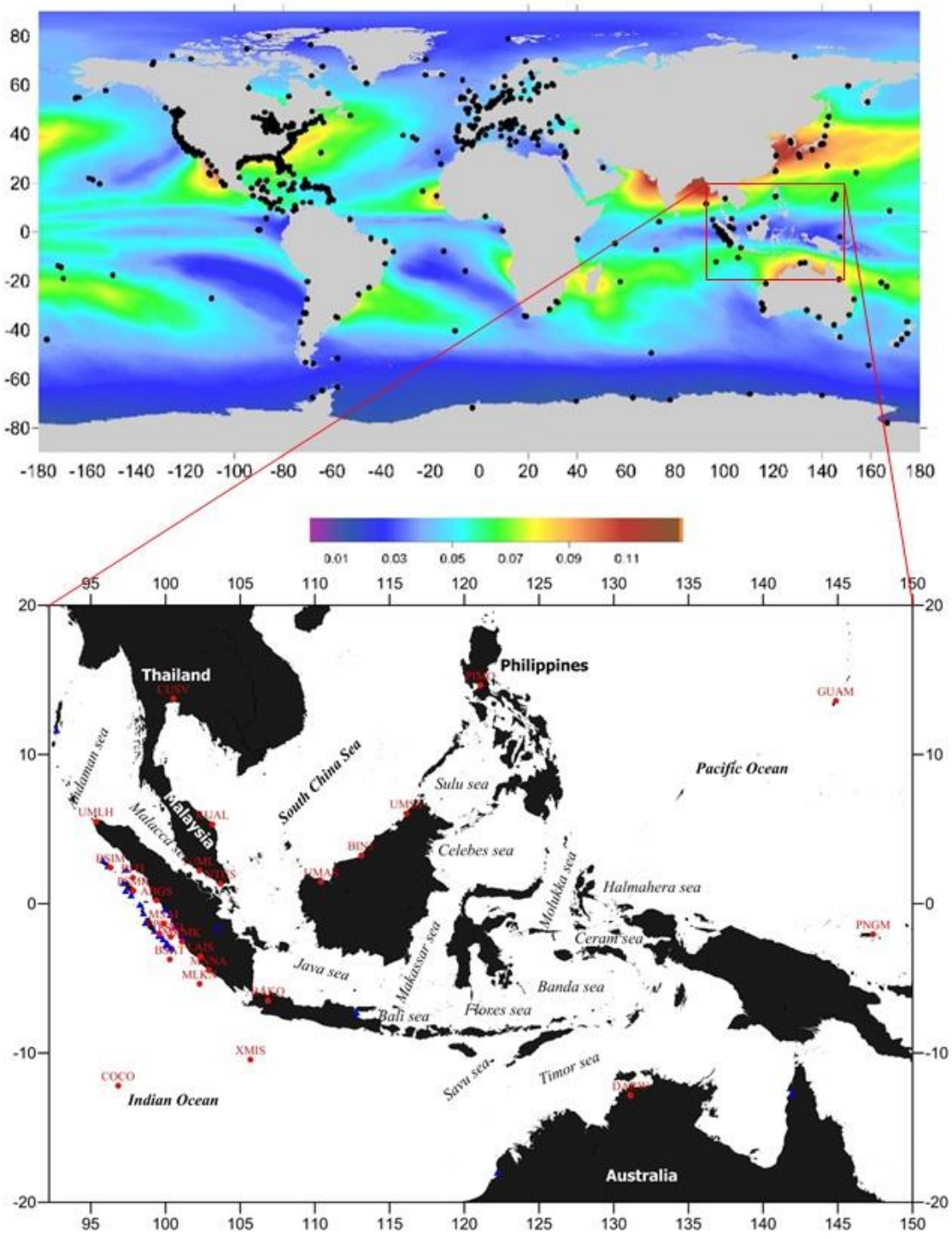

Figure 4.2 Distribution of GNSS stations. Top plot: global set of coastal and island stations (black dots) used in the GPD+, with the map of the standard deviation of the wet tropospheric correction in the background (Fernandes et al., 2015). Bottom plot: GNSS stations around the Indonesian region (INA network); red dots are stations used in the GPD+ and blue triangles are GNSS stations not used in GPD+.

Table 4.2 shows the 27 GNSS stations within and nearby the Indonesian region. As mentioned above, those GNSS data come from different sources and cover various periods. Most GNSS stations that belong to the IGS network cover a long period, since 1996, such as COCO, DARW, GUAM, KARR, PIMO, NTUS, BAKO (since 1998), and CUSV and XMIS (since 2008). However, data from the GNSS stations from Sumatera GPS array (SUGAR), the Indonesian Geospatial Information Agency (BIG) and Système d'Observation du Niveau des Eaux Littorales (SONEL) span various periods, starting from 2002.

Table 4.2 GNSS stations around the Indonesian region used to derive the GPD WTC (INA network).

Station	Latitude	Longitude	Height Ortho	Start
ABGS	99.387523	0.220842	251.115	2004
BAKO	106.848910	-6.491055	139.789	1998
BIN1	113.094340	3.240317	20.676	2007
BITI	97.811364	1.078616	15.524	2005
BSAT	100.284550	-3.076700	20.214	2002
BSIM	96.326165	2.409260	9.563	2005
COCO	96.833964	-12.188352	4.791	1996
CUSV	100.533910	13.735913	107.74	2008
DAWR	131.132720	-12.843694	75.124	1998
GUAM	144.868360	13.589329	147.308	1996
JUML	102.256100	2.211753	20.174	2007
KARR	117.097190	-20.981436	116.992	1996
KUAL	103.139150	5.318888	60.387	2007
LAIS	102.033930	-3.529213	21.501	2006
MKMK	101.091410	-2.542654	9.305	2004
MLKN	102.276500	-5.35254	26.263	2006
MNNA	102.890270	-4.450324	28.537	2006
MSAI	99.089481	-1.32641	48.238	2002
NTUS	103.679960	1.345802	68.504	1997
PIMO	121.077730	14.63572	52.163	1999
PNGM	147.366010	-2.043229	39.439	2002
PPNJ	99.603685	-1.993967	55.230	2004
PSKI	100.353400	-1.124665	58.410	2005
PSMK	97.860906	-0.089308	31.964	2002
UMAS	110.424700	1.468309	18.657	2007
UMLH	95.338984	5.053123	23.348	2005
UMSS	116.112030	6.039233	30.064	2007
XMIS	105.688500	-10.449972	265.523	2008

4.2.3. Assessment of GNSS-derived ZTD and ZWD for the Indonesian network

In order to assess the accuracy of the GNSS-derived ZTD of the INA network, integrated in the GPD+ algorithm, the following comparisons were performed: INA ZTD were compared with the corresponding values from IGS and ERA for the stations common to INA and IGS networks; the derived INA ZWD were compared with the corresponding ZWD values from ERA and GNSS data not used in the GPD+ computations.

a. Comparison between INA ZTD and ZTD from IGS and ERA

The IGS ZTD data are available online from IGS website. These ZTD values are estimated using a PPP approach (Zumberge et al., 1997) using the GIPSY software and the IGS combined final orbit and clock parameters. An elevation cutoff angle of 7 degrees and mapping functions of Niell (1996) and GMF were applied. The IGS ZTD was estimated with a temporal resolution of 5 minutes (see detail in Byun and Bar-Sever (2009)).

Since 2000, IGS has been using the ITRF2000 as the reference frame for the IGS product. The IGS switched the reference frame from ITRF2000 to ITRF2005 in November 2006 and implemented the new standard of antenna phase center variation (PCV) maps for all the GPS satellite transmit antennas, and for most of the ground antennas (Schmid et al., 2007). The standardized PCV were applied only for the GPS satellite antennas prior to that period. The IGS ZTD data used in this study are those computed after the 2008 update of the whole IGS network.

As mentioned previously, ERA-Interim provides sea level pressure, total column water vapor and surface temperature in global grids, which can be used to retrieve the zenith tropospheric delays (ZHD and ZWD) at the GNSS station height. ZHD can be obtained using equations 2.11 and 2.13 in Chapter 2 and ZWD can be estimated by equation 4.9 or 4.10. Because the ZWD from ERA refers to the model orography height, equation 4.21 is applied to retrieve ZWD at GNSS station height.

For the purpose of ZTD evaluation of the INA network, the nine common stations (BAKO, COCO, CUSV, DARW, GUAM, KARR, NTUS, PIMO and XMIS) to the INA and IGS solutions in the Indonesian region have been compared by analyzing the ZTD differences.

Figure 4.3 shows (a) scatter plots of ZTD from INA and IGS, and (b) scatter plots of ZTD from INA and ERA Interim. The coefficient of correlation between INA ZTD and IGS ZTD is high (between 0.98 and 0.99). It means that the two data sets are similar. This may be due to the identical parameters used in both solutions, the only difference being the adopted mapping function (IGS uses Niell and GMF (Kouba, 2009), while in the INA computations the VMF1 have been used). The coefficient of correlation between INA ZTD and ZTD from ERA Interim varies in a range 0.88 – 0.98.

For all stations in the INA network, using all observation, the statistical parameters for the differences between INA and IGS ZTD are, in mm, -0.6, 8.0, -68.5, and 386.3 for the mean, standard deviation, minimum and maximum, respectively. By applying a rejection with a threshold of 50 mm for the maximum values of differences, the percentage of rejected point is only 0.04% of the total estimates (11490972). After considering the above rejection criterion the corresponding statistics are in mm, -0.7 and 5.5 for the mean and standard deviation, respectively (Table 4.3).

Using a similar statistical computation, the results of the ZTD differences between INA and ERA Interim are, in mm, 0.7, 19.6, -299.3 and 105.1 for the mean, standard deviation, minimum and maximum, respectively. A threshold of 100 mm for the absolute maximum values of differences between INA ZTD and ERA gives 0.004 % of rejected points from a total number of 4282019 estimates. The results after applying the rejection criterion are shown in Table 4.3. The corresponding statistics are in mm, 0.7 and 19.6 for the mean and standard deviation, respectively. There is no reduction for the mean and standard deviation, only for the minimum and maximum values.

According to the results for each individual station, the mean varies between -7.2 mm and 1.1 mm and the standard deviation between 3.1 mm and 8.7 mm for the ZTD differences between INA and IGS. For the ZTD differences between INA and ERA interim, the corresponding values are from -27.6 to 9.8 mm and from 15.1 to 20.6 mm for the mean and standard deviation, respectively.

Table 4.3 Statistical results of ZTD differences at the station height (in millimeters).

	dif. INA – IGS ZTD			dif. INA – ERA ZTD		
Station	**N**	**Mean**	**Sigma**	**N**	**Mean**	**Sigma**
BAKO	1521778	-7.2	8.7	526041	9.8	20.6
COCO	1678271	0.7	3.6	599093	5.5	15.4
CUSV	608453	-4.6	3.9	205147	-4.6	17.1
DARW	1383181	0.3	3.6	521449	8.2	16.0
GUAM	1621810	0.9	4.4	627114	-10.0	16.6
KARR	1607333	1.1	3.1	569128	2.2	15.1
NTUS	1309383	0.4	3.2	478971	0.5	15.9
PIMO	1189146	0.1	5.0	477821	7.9	19.3
XMIS	567126	-0.1	3.3	277113	-27.6	15.5

The average standard deviation of 5.5 mm is a clear indicator of the level of precision of the INA ZTD solutions. Generally, no significant biases have been found between INA and IGS ZTD. The standard deviation of the differences between INA and ERA is within the expected values, considering that this is a region of high variability of the WTC. A few stations show biases with respect to ERA with absolute values larger than 1 cm. These can be attributed to wrong station coordinates, local biases in the ERA model or errors due to the height reduction performed when reducing ERA fields from the model orography to station height, particularly in the ZWD field, due to the inherent low accuracy of equation 4.21.

Figure 4.4 illustrates the differences between the INA and IGS ZTD (orange curves), and between INA and ERA Interim ZTD (blue curves) for the set of nine common stations. At BAKO station, the INA-IGS differences prior to 2007 are higher than after 2007, these may be the result of changing to a new PCV standard which has induced a systematic bias in the estimated ZTD value (Byun and Bar-Sever, 2009). Figure 4.4 also allows concluding that the jumps found in the INA-IGS differences, which are not present in the INA-ERA differences, are attributed to IGS and not to the INA solutions.

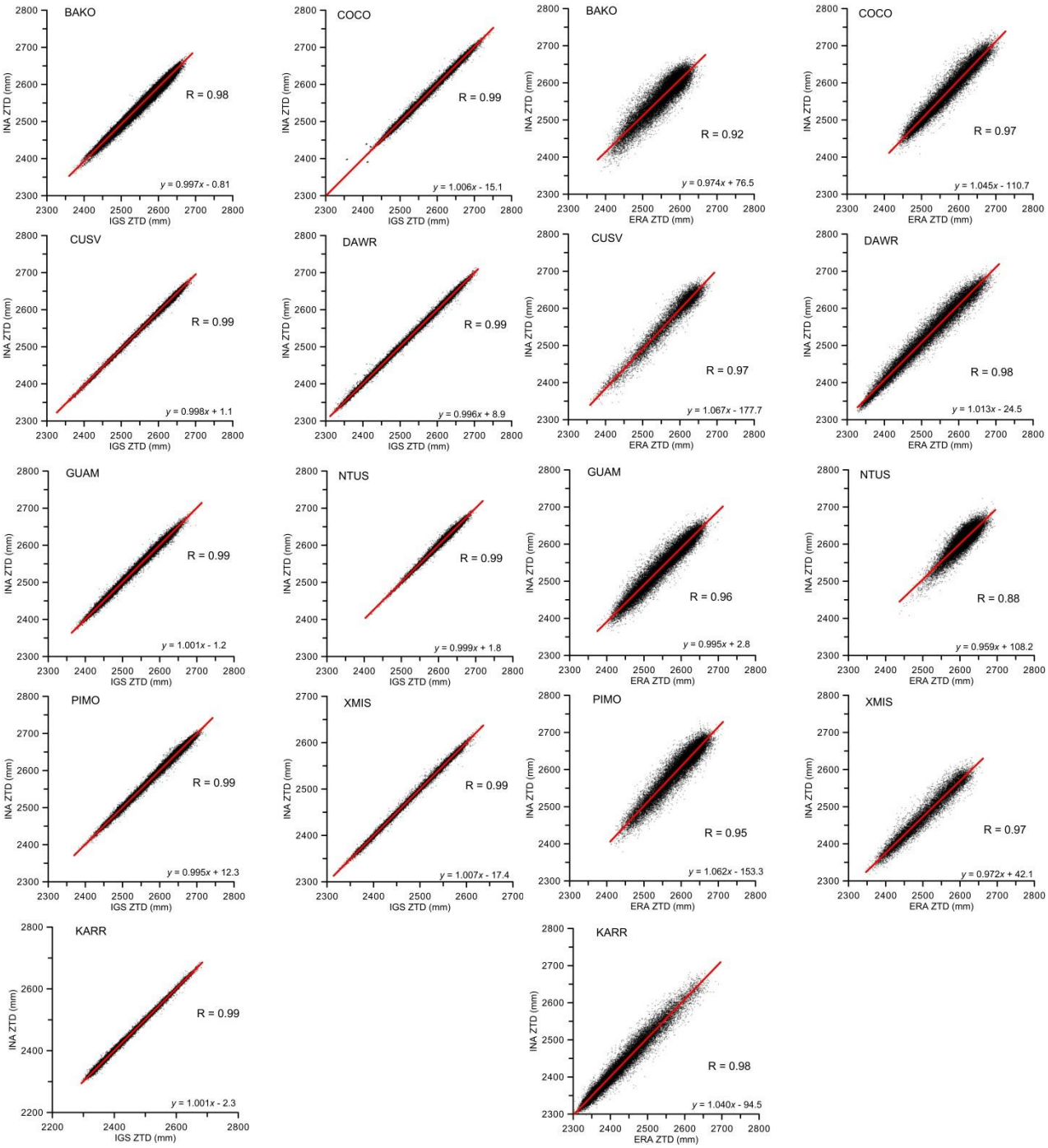

(a) INA vs IGS (b) INA vs ERA

Fig. 4.3 Scatter plots of (a) INA vs IGS and (b) INA vs ERA interim Zenith Total Delay, at station height, for the GNSS stations BAKO, COCO, CUSV, DARW, GUAM, KARR, NTUS, PIMO and XMIS.

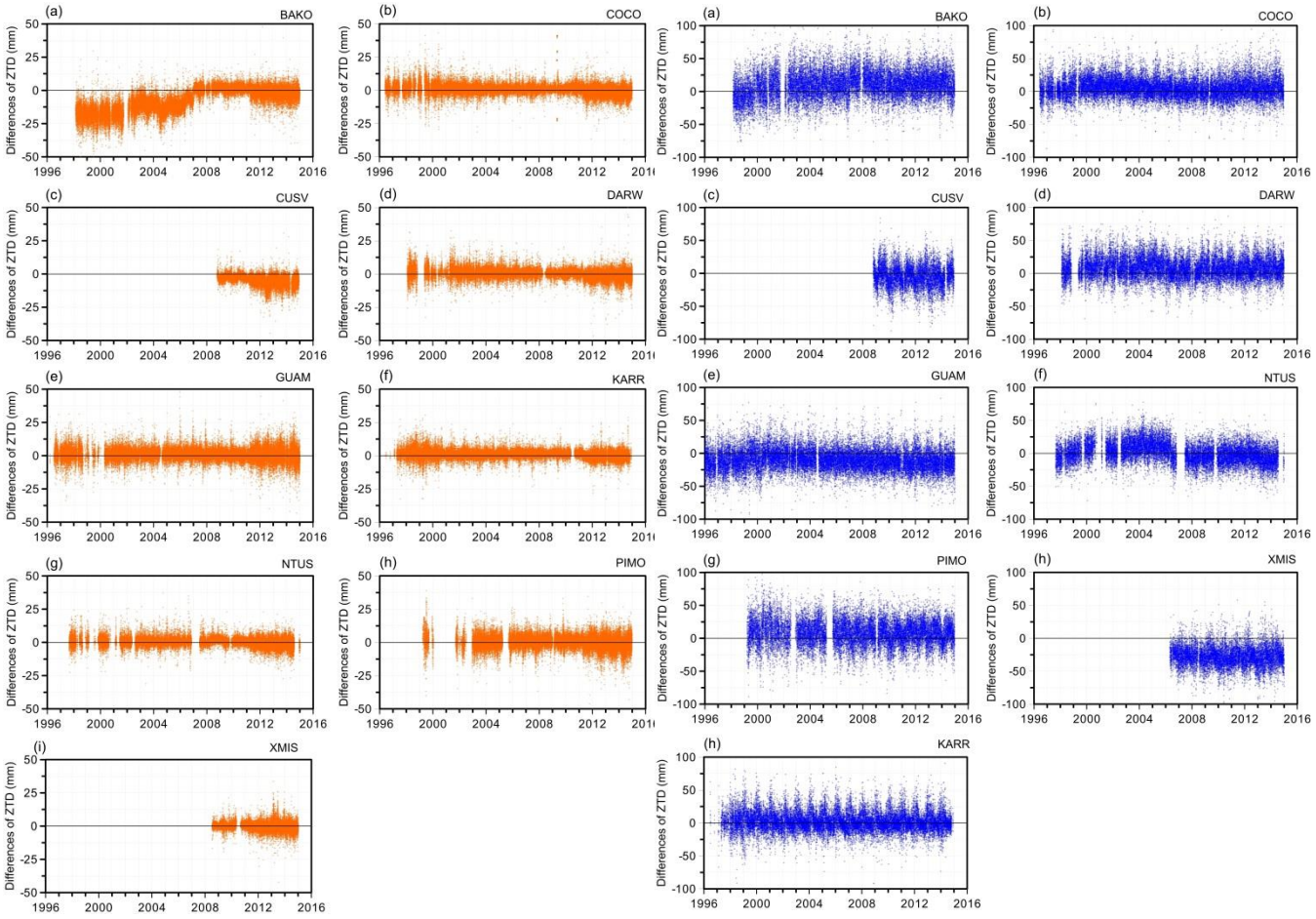

(a) INA and IGS

(b) INA and ERA

Figure 4.4 ZTD differences between (a) INA and IGS (orange curves) (b) INA and ERA Interim (blue) at GNSS stations: BAKO, COCO, CUSV, DARW, GUAM, KARR, NTUS, PIMO and XMIS.

b. Comparison between INA ZWD and ZWD from ERA

To assess the zenith wet delay (ZWD) from the INA solution, a comparison between INA-derived and ERA Interim-derived ZWD at station height was performed. Data from all 27 stations covering various periods in Indonesia region were now used in the computation, since ERA Interim is a global model and can be interpolated at any point. Using the two single level parameters Total Column Water Vapor (TCWV) and surface temperature (2-meter temperature, T_0), the ZWD at ECMWF orography level (ZWD_{h_s}) can be determined by

Equations 4.10 and 4.11. According to Equation 4.21 (Kouba, 2008), the ZWD at station height is calculated from ZWD at ECMWF orography level.

Figures 4.5 and 4.6 illustrate the scatterplot of ZWD data and ZWD differences between INA and ERA Interim at station height, respectively. The coefficient of correlation for the set of stations varies from 0.83 to 0.93. From Figure 4.6, the patterns of the differences are almost uniform for the whole period.

The result of the comparison for all points is shown in Table 4.4. The ZWD mean value of the differences between INA and ERA is, in absolute value, about 4.9 mm and the standard deviation is 17.9 mm. Considering the whole set of 27 stations, the mean value of the differences varies from -27.5 mm to 26.2 mm and the standard deviation between 15.1 mm and 20.7 mm.

Table 4.4 Statistical results of ZWD differences between INA and ERA Interim (in mm) at station height.

Station	n	Mean	Sigma	Station	n	Mean	Sigma
ABGS	273043	-4.6	19.6	MLKN	210842	4.1	17.9
BAKO	528678	9.8	20.7	MNNA	240099	25.1	20.7
BIN1	163735	5.9	16.5	MSAI	261019	-1.1	19.9
BSAT	287485	2.8	19.2	NTUS	481562	0.5	15.8
BSIM	244985	5.8	18.8	PIMO	480416	7.9	19.3
COCO	601685	5.5	15.4	PNGM	352585	-3.2	16
CUSV	206874	-4.7	17.0	PPNJ	252864	-0.6	18.6
DARW	524041	8.2	16.1	PSKI	257888	24.8	20.2
GUAM	629701	-10	16.7	PSMK	276529	-0.4	17.8
JUML	216974	-5.9	15.7	UMAS	204961	4.4	15.3
KARR	569129	2.2	15.1	UMLH	248756	15.1	20.7
KUAL	191730	-4.7	15.6	UMSS	174897	24	17.3
LAIS	240027	22.5	20.4	XMIS	279417	-27.5	15.6
MKMK	223506	26.2	20.3				

From Table 4.4, it is possible to conclude that there is no significant bias between INA and ERA ZTD. The bias values of all stations with respect to ERA ZTD are between -27.5 and 24.8 mm. As mention previously, the biases may be associated to local bias in the ERA model, height reduction error (Equation 4.21) or station coordinates error.

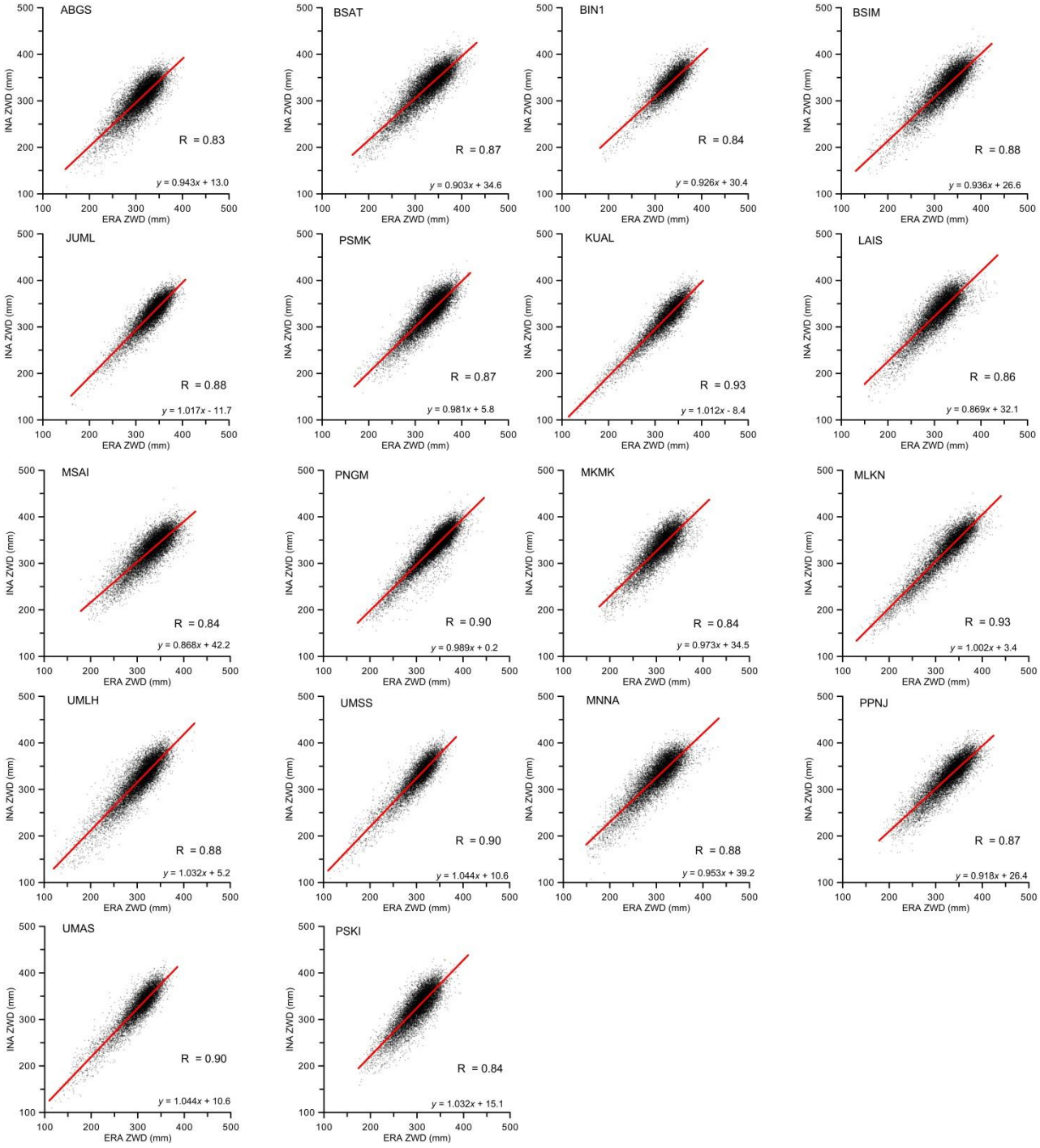

Figure 4.5 Scatterplots of ZWD from INA and ERA interim, for a representative set of local GNSS stations.

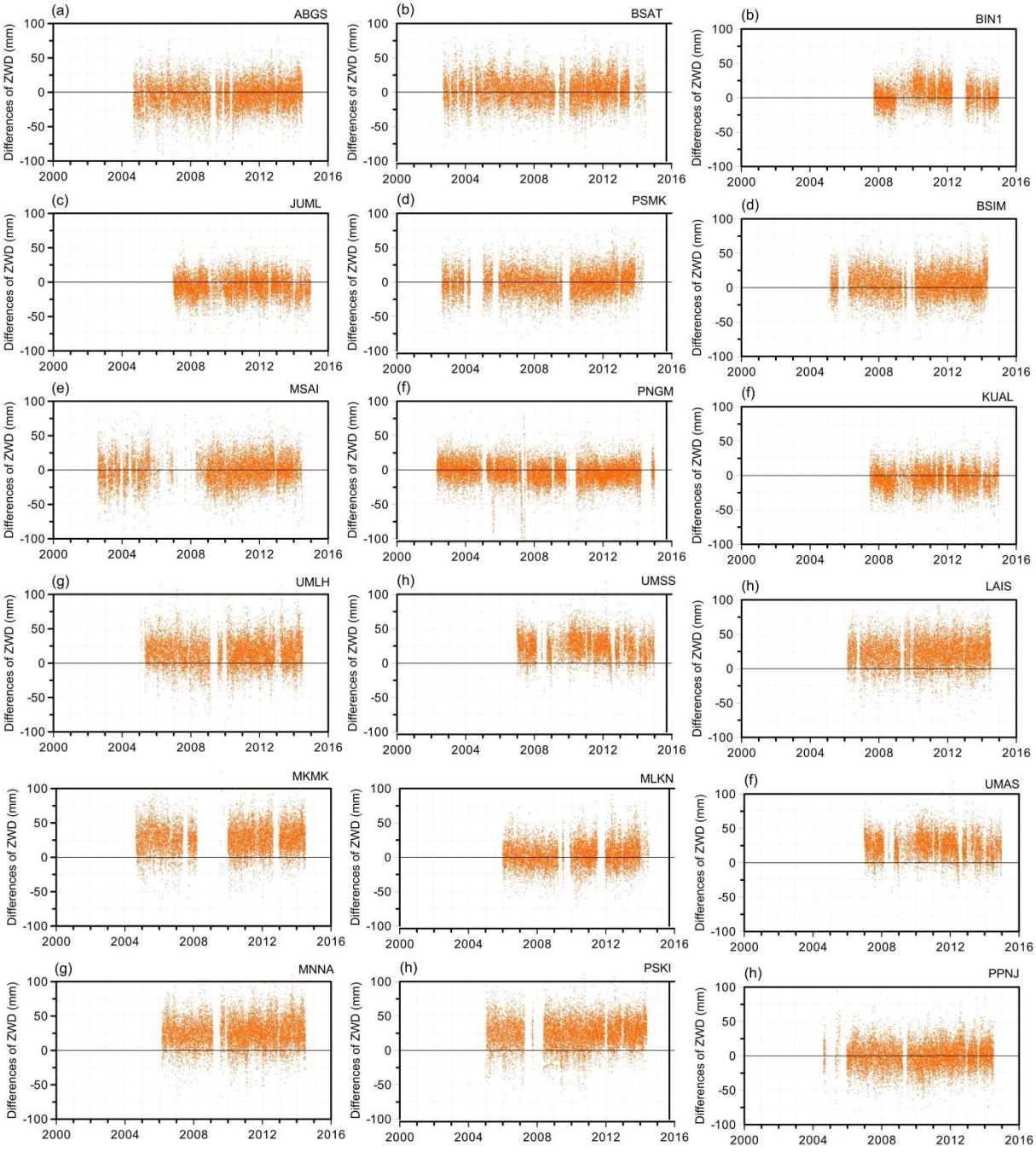

Figure 4.6 Comparison between from INA and ERA interim ZWD, for a representative set of local GNSS stations.

4.3. Assessment of Wet Tropospheric Corrections in the Indonesian Region

As mentioned before, using all available data sources, including the ZWD from the INA network of GNSS stations, the WTC from the GPD+ algorithm has been computed for all missions used in this study. This section presents the assessment of the GPD+ WTC in the Indonesian region. For comparison, the WTC from the on-board radiometers and that from the ERA Interim model (the best model for the whole altimeter era) are assessed. The following altimetric datasets were used in this assessment:

- TOPEX/Poseidon, cycles 1 to 364
- Jason-1, cycles 1 to 259
- Jason-2, cycles 1 to 280
- ERS-1, cycles 083 to 156
- ERS-2, cycles 1 to 85
- Envisat, cycles 6 to 112
- Cryosat-2, cycles 4 to 40
- SARAL, cycles 1 to 38

4.3.1. Illustration of the WTC for the Altimeter Mission

For illustrative purposes only, the WTC derived from ERA Interim, on-board MWR and GPD+ for the along-track altimeter measurements of Envisat (cycle 068 pass 709 and cycle 077 pass 666) are shown in Figure 4.7. It is clear, from this figure, that the WTC from the on-board microwave radiometer shows the largest variability when MWR approaches the coast.

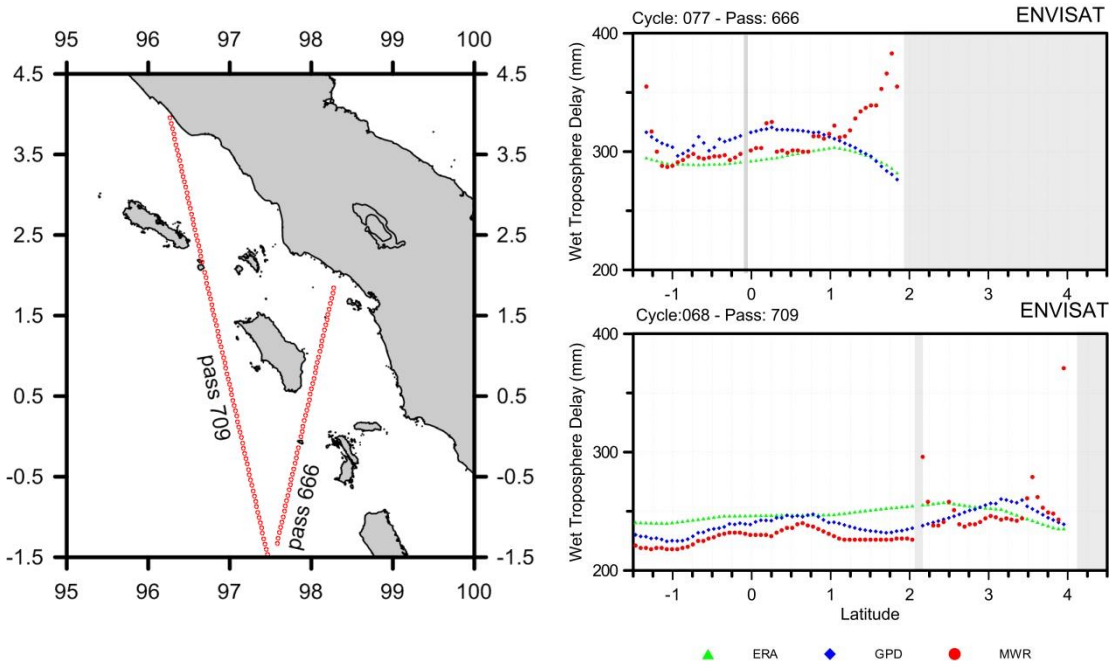

Figure 4.7 Along-tracks data measurement of various WTC for Envisat cycle 077 pass 666 and cycle 068 pass 709.

4.3.2. Comparison of the various WTC with GNSS-derived ZWD at stations not used in the GPD computations

Another method to evaluate various ZWD is by means of the comparison between ZWD from GNSS data not used in GPD+ WTC computation and various ZWD. For this purpose, the ZWD at GNSS stations not used in the GPD+ estimations was compared with the ZWD from ERA Interim, MWR and GPD+ at along-track altimeter points in the vicinity of each station, within distances less than 200 km from the GNSS station and less than 100 km from the coast.

There are another 22 GNSS stations in the Indonesian region not used in GPD computation (Table 4.5). The periods covered by the various GNSS stations are not homogenous; twelve stations have observations starting before 2010 and ten stations after 2010.

For this purpose the RMS of the various ZWD differences was computed and analyzed for most missions, function of distance from coast. The period for which GNSS data

not used in GPD computations are available corresponds to the periods of the following 5 missions: Cryosat-2, Envisat, Jason-1, Jason-2 and SARAL). Thus, this comparison is only performed for these missions.

Table 4.5 GNSS stations around the Indonesian region not used to derive the GPD+ WTC covering the period up to 2014.

Sta.	Lat. (º)	Lon. (º)	H_ort (m)	Start
BNON	2.520821	96.150829	41.231	2010
BRO1	-18.003968	122.20909	21.047	2011
BTET	-1.281536	98.643944	38.834	2005
BTHL	0.569199	97.710643	91.572	2005
CARI	11.614185	92.719553	61.430	2005
HNKO	0.867911	97.340822	30.577	2010
ITSS	-7.279983	112.79463	17.373	2010
KTET	-2.362540	99.840710	52.318	2010
LEWK	2.923604	95.804059	41.796	2005
LHW2	1.387745	97.170312	39.815	2010
LNNG	-2.285322	101.15649	42.515	2004

Sta.	Lat. (º)	Lon. (º)	H_ort (m)	Start
NGNG	-1.799645	99.268324	63.815	2004
PARY	-0.752548	100.31864	120.254	2010
PBJO	-0.636492	98.515709	54.656	2005
PBLI	2.308536	97.405277	21.401	2005
PKRT	-2.151371	99.542774	51.441	2008
PRKB	-2.966590	100.39960	37.618	2004
PTLO	-0.054583	98.280038	36.092	2002
SLBU	-2.766398	100.00972	20.239	2004
SMGY	-2.614480	100.10264	23.782	2008
TIKU	-0.399105	99.944187	31.882	2006
WEIP	-12.678317	141.92046	24.252	2010

According to Figure 4.8, the results can be summarized as follows:

- The RMS of ZWD differences between GNSS-derived not used in GPD+ (GNSS) and ERA Interim-derived (ERA) for all satellites seems similar.
- The RMS of ZWD differences between GNSS and INA looks similar, particularly near coast (less than 60 km). The small increase at larger distances is due to the decreasing accuracy of the corrections farther from the coast and from the stations.
- The RMS of ZWD differences between GNSS and microwave radiometer (MWR) shows different results for the various missions. For Jason-1 and SARAL, the noisiness data occur for distances less than 10 km and gradually decrease as distance from the coast increase, while for Jason-2 the noisiness is relative stable. It may be due to the coastal improvement of ZWD from the AMR on Jason-2. The Envisat MWR data are very noisy in the coastal regions, particularly for distances less than 25 km.

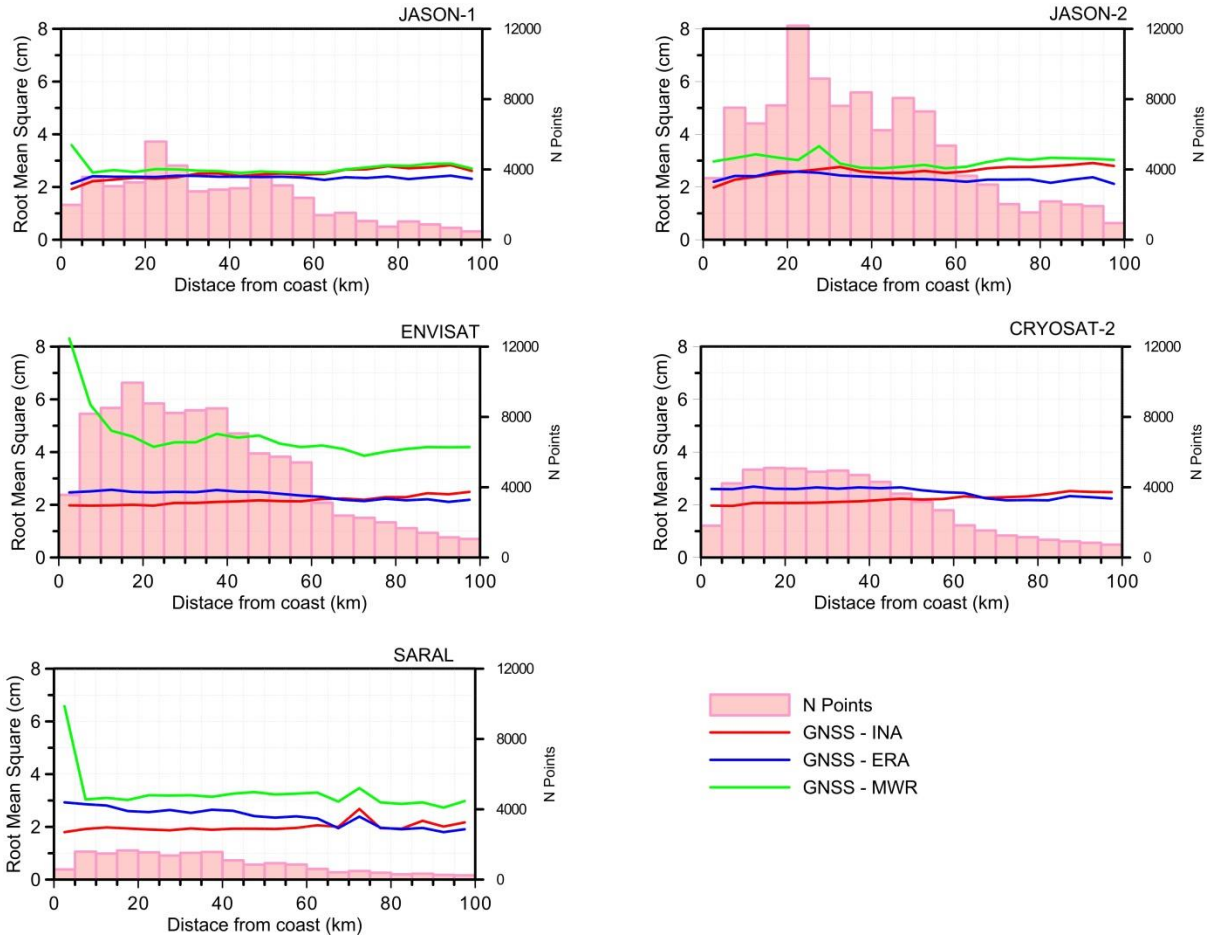

Figure 4.8 RMS of ZWD differences, function of distance from coast: GNSS – ERA Interim (*blue*), GNSS – MWR (*green*) and GNSS – INA (*red*). N represents the number of points used in the analysis of each 5-km interval of distance from coast.

4.3.3. SLA variance analysis

The analysis of SLA variance, derived from different WTC datasets, was used to study the coastal effects of the various WTC applied to altimeter data and to assess their quality. The rationale behind this is the assumption that the more accurate the wet tropospheric correction is, the smaller the corresponding SLA variance estimated using that correction. The analysis of SLA variance is a common technique used to assess the quality of a correction such as the WTC, which affects the final accuracy of the derived SLA. This technique uses "variance" to measure the data dispersion. Since variance is a quadratic measure, its values are larger than those for example of the standard deviation, making it easier to detect small differences between the analyzed data sets. However, variance is very sensitive to noisy or extreme data values and this can only be overcome by using appropriate

criteria for removing those values. This approach has been adopted in this study by applying to the SLA values the standard rejection criteria, for example for the acceptable maximum and minimum values for the SLA and for the WTC used in the SLA computation.

The assessment of the WTC has been performed by means of a set of statistical analyses of SLA variance: SLA along-track variance differences; weighted mean values per cycle (weights function of the co-sine of latitude) and at collocated points (spatial pattern and function of distance from the coast); SLA analysis at crossover (spatial pattern). SLA WTC datasets are first derived, for each cycle, using the standard geophysical corrections under comparison. Then, in the first case, the difference between the variance of each SLA WTC dataset, computed using all along-track points, is estimated for each cycle. The variance of collocated along-track SLA measurements for a given period and using each WTC, is computed in regular latitude×longitude grids (4°×4°) intervals (or bins) or in bins of distance from coast and then the differences considered. In the second case, crossovers are first estimated using each SLA WTC dataset, the SLA variance at crossovers is then computed in regular latitude×longitude grids (4°×4°) and subtracted for selected pairs of SLA WTC datasets. It is commonly accepted in the altimeter community that using SSH crossover differences with a maximum time lag of 10 days reduces the impact of ocean variability, mainly capturing differences due to measurement errors; therefore, only crossover points with time difference less than 10 days have been considered. The along-track and crossover variance analyses are two complementary diagnostics, helpful in the assessment of the various analyzed variables.

Figure 4.9 and Figure 4.10 illustrate the geographical pattern of the along-track SLA WTC variance differences (cm^2) between GPD+ and ERA interim (GPD – ERA), and between GPD+ and the microwave radiometer (GPD – MWR), respectively. These figures indicate that GPD+ is an improved correction with respect with the ERA-Interim and the on-board MWR WTC corrections presented in RADS for all missions, not only near the coast but also in open-ocean. This is expected since GPD+ is based on actual observations, not only from the on-board MWR but also from GNSS and SI-MWR. Results also show that the improvement with respect to ERA is more pronounced for the most recent missions. However, the most significant result is the improvement of the GPD+ correction with respect to the on-board MWR in the coastal regions, particularly for TOPEX/Poseidon, ERS-1, ERS-2 and Envisat. This is due to the presence of land contaminated and erroneous measurements

due to instrument malfunction present in those missions, which rarely occur for Jason-1 and Jason-2 (Fernandes et al., 2015).

Figure 4.11 illustrates the SLA variance differences of WTC (cm^2), function of distance from coast, GPD+ – ERA Interim (orange) and GPD+ – MWR (blue). This figure shows that for TOPEX/Poseidon, the wet tropospheric correction from GPD+ reveals a significant improvement with respect to the MWR correction present in RADS, particularly near the coast for distances less than 25 km and still has a small improvement with respect to ERA-Interim (less than 2 cm^2). For Jason-1 and Jason-2, the GPD+ WTC significantly reduces the SLA variance with respect to the ERA model (about 6 cm^2). Regarding the comparison with the MWR-derived WTC, for Jason-1, the GPD+ correction shows a significant improvement (average differences of 4 cm^2). For Jason-2, the GPD+ correction shows a smaller, still significant improvement (less than 3 cm^2), in spite of the fact that this correction is already improved in coastal regions (Brown 2010). For ERS-1, ERS-2 and Envisat, the comparison with MWR-derived WTC shows a significant variance reduction in the coastal region of 8 cm^2 to 12 cm^2. However, the GPD+ correction shows a small improvement with respect to ERA Interim model (about 2 cm^2 to 4 cm^2). The GPD+ WTC gives a significant reduction in SLA variance when compared to the MWR-derived WTC for distances less than 10 km from the coast, and still has a small improvement after 10 km. The result of comparison between GPD+ and ERA Interim WTC shows an improvement about 4 cm^2 in SLA variance.

Figure 4.12 illustrates the SLA variance differences at crossovers (cm^2) between GPD+ and ERA interim (GPD – ERA), while Figure 4.13 illustrates the SLA variance differences at crossovers (cm^2) between GPD+ and the MWR-derived correction (GPD – MWR). These figures show an SLA variance reduction of GPD+ WTC with respect to both the ERA Interim and MWR-derived WTC at the crossovers for most altimeter missions. The GPD+ correction gives the largest reduction with respect to MWR, particularly for ESA satellites (ERS-1, ERS-2 and ENVISAT).

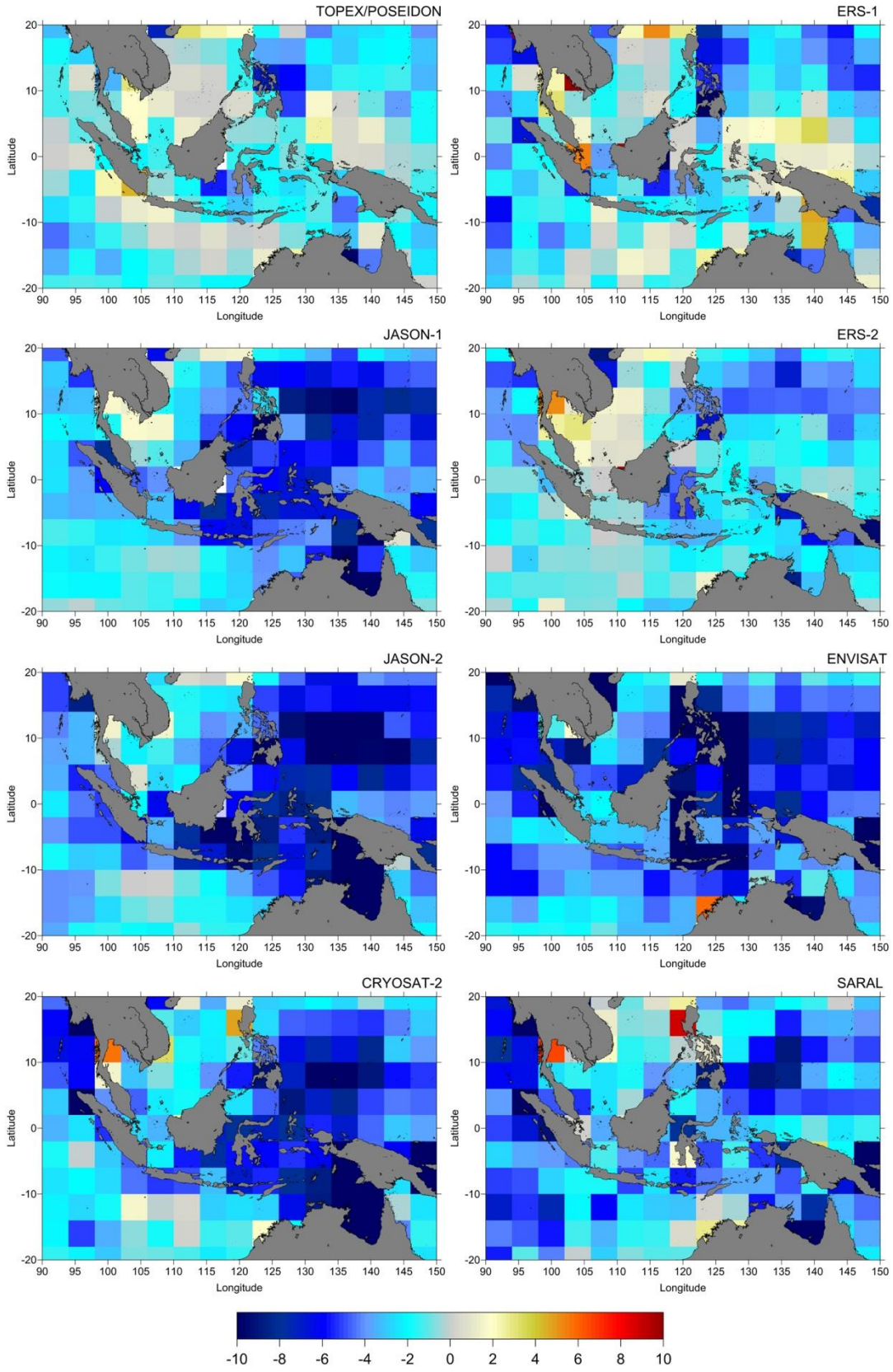

Figure 4.9 Along-track SLA WTC variance differences (cm^2) between GPD+ and ERA interim (GPD – ERA).

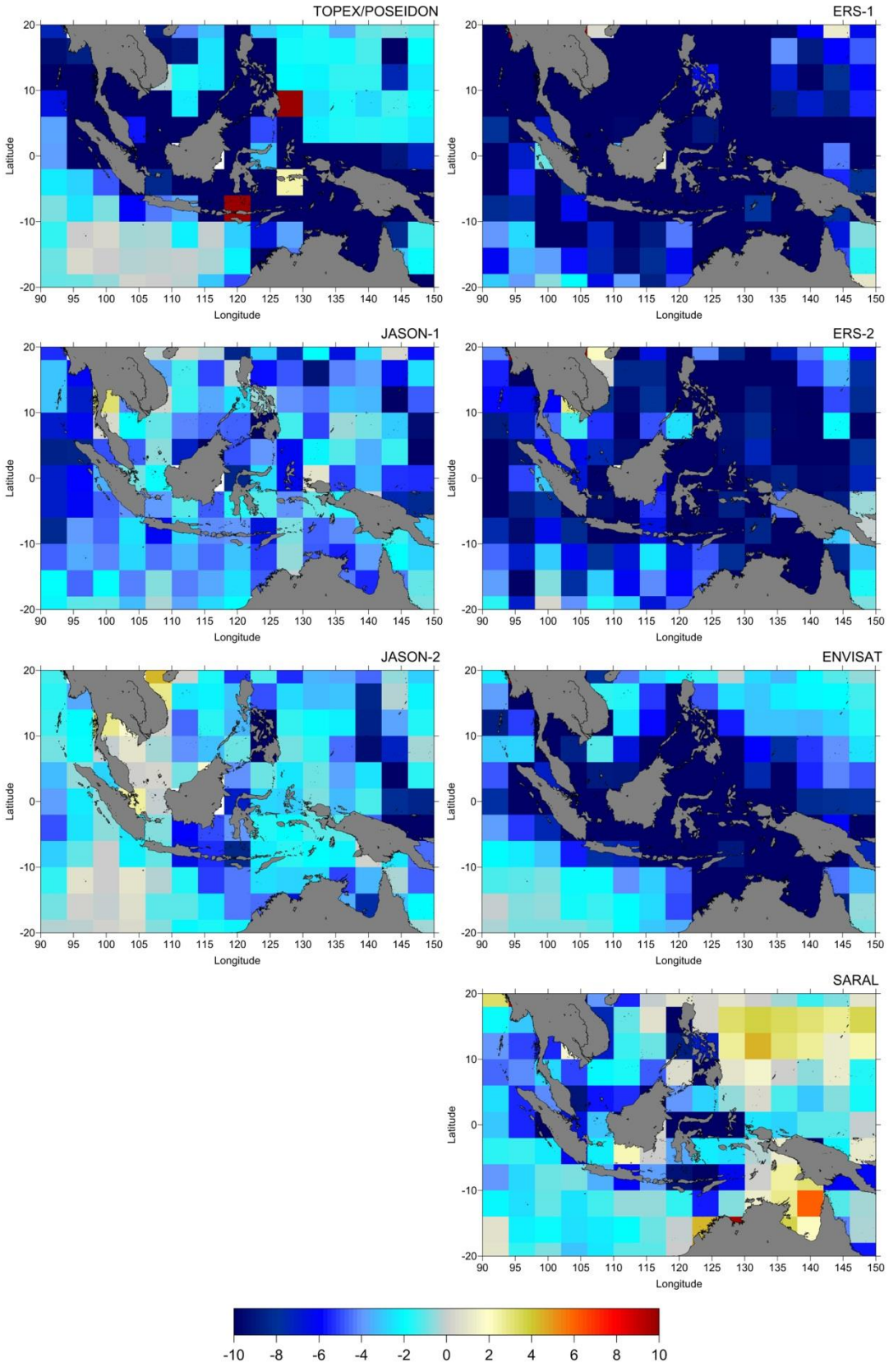

Figure 4.10 Along-track SLA WTC variance differences (cm^2) between GPD+ and the MWR-derived correction (GPD – MWR).

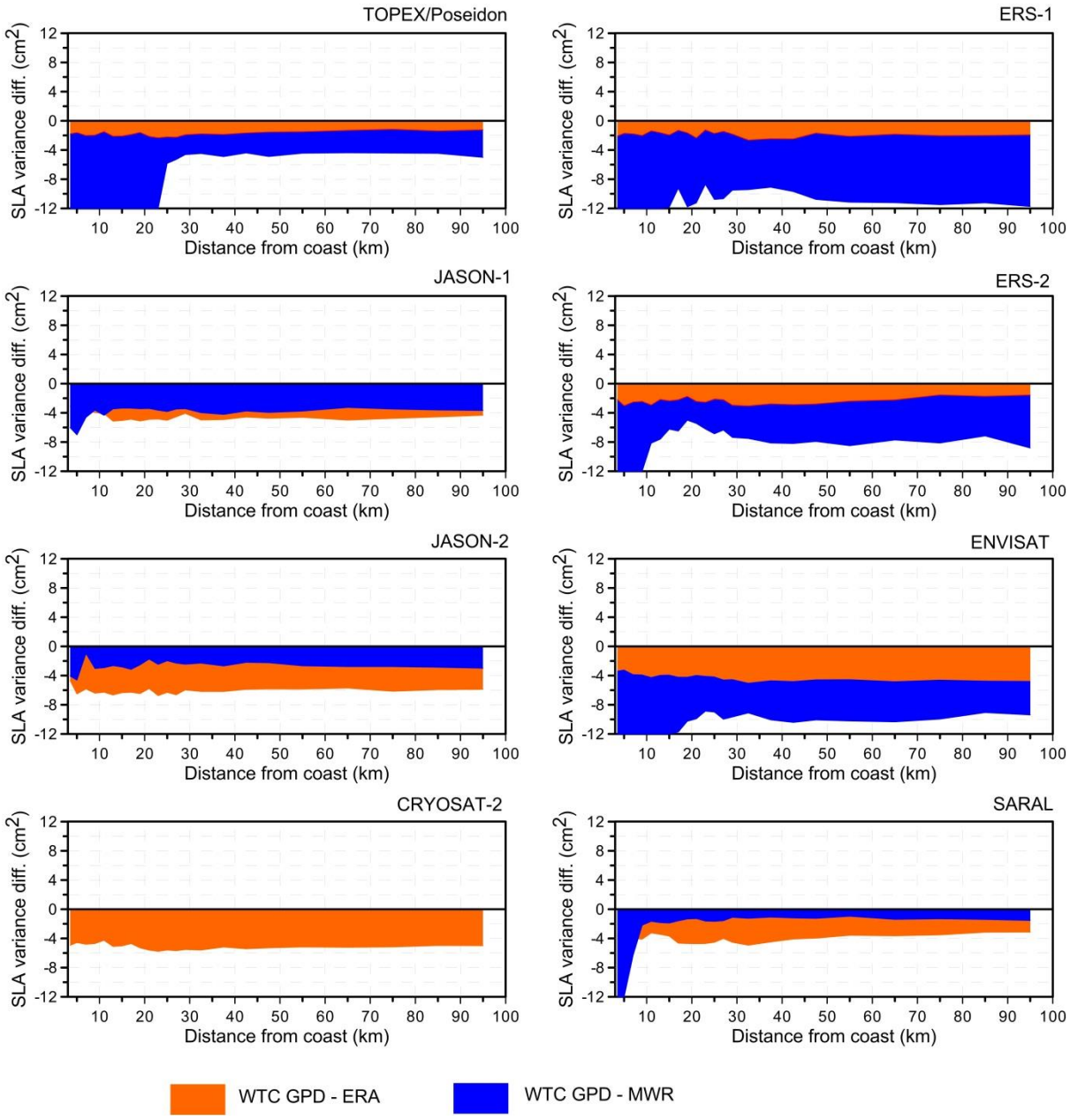

Figure 4.11 SLA variance differences of WTC (cm^2), function of distance from coast, GPD+ – ERA Interim (orange) and GPD+ – MWR (blue).

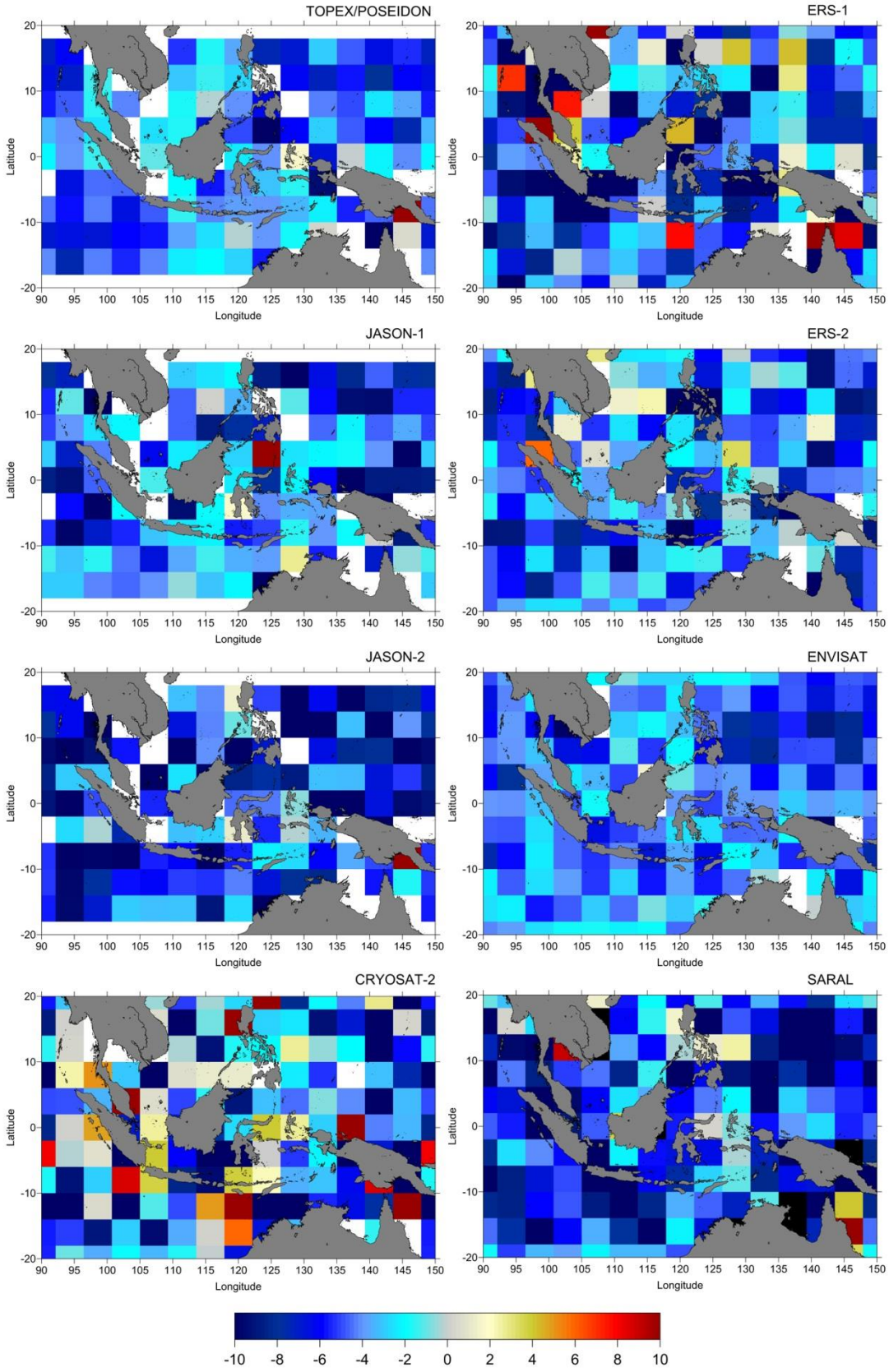

Figure 4.12 SLA variance differences at crossovers (cm^2) between GPD+ and ERA interim WTC (GPD – ERA).

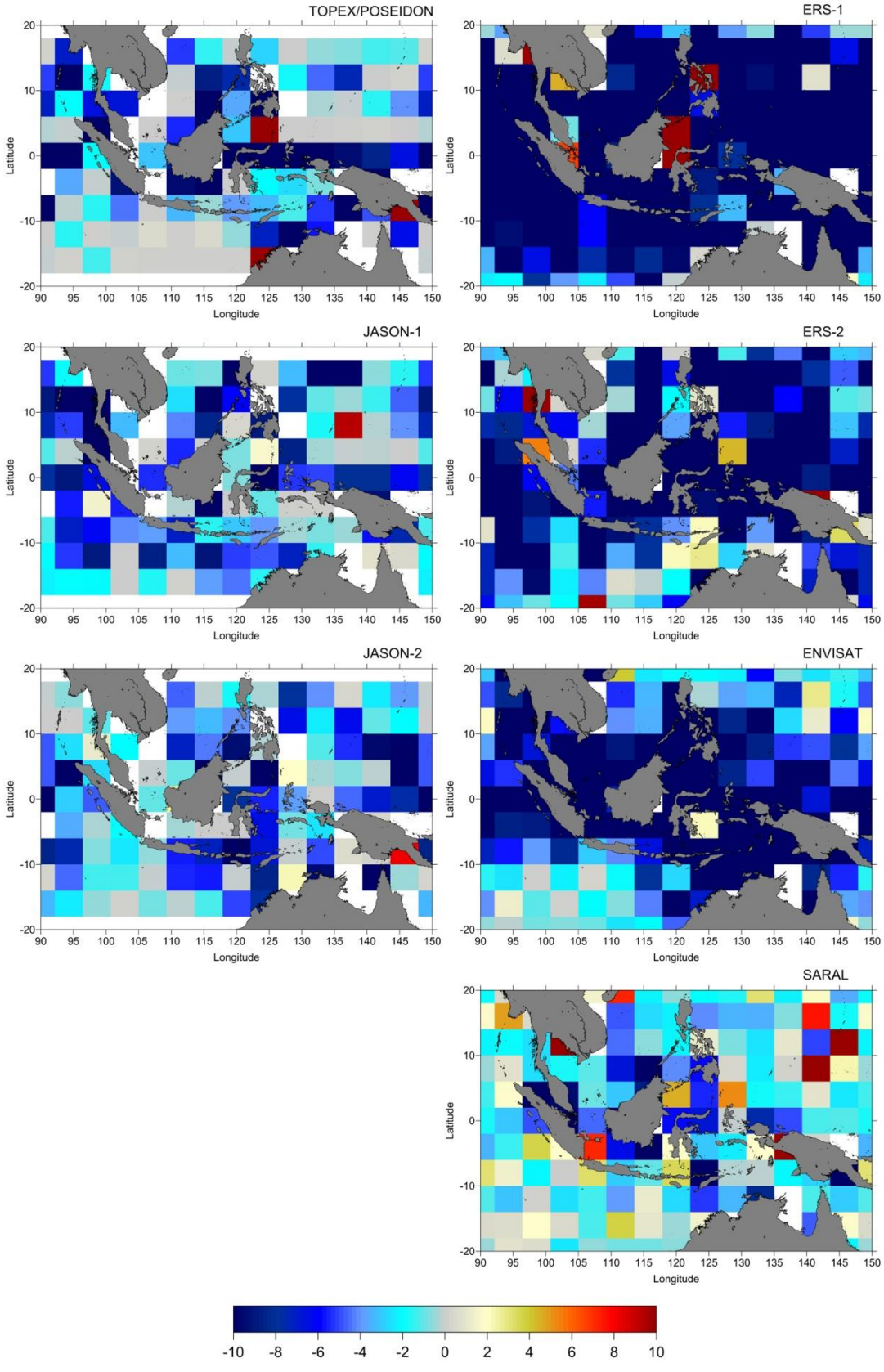

Figure 4.13 SLA variance differences at crossovers (cm^2) between GPD+ and MWR-derived WTC (GPD – MWR).

CHAPTER 5

SEA LEVEL VARIABILITY AROUND THE INDONESIAN SEAS

Globally, sea level has been rising up to 3.4 mm/year according to the results derived from satellite altimetry (Ablain et al., 2015; Cazenave et al., 2014; Church et al., 2013; Nerem et al., 2010). However, some places have higher rates of sea level variation, such as the Southern Indian Ocean and the Western Pacific Ocean. The El Niño – Southern Oscillation (ENSO) occurrences are correlated with the inter-annual global mean sea level (GMSL) (Cazenave et al., 2012), notably in the tropical Pacific Ocean (Church et al., 2006). The Indonesian seas, located between the Pacific and Indian oceans are strongly impacted by ENSO (Fenoglio et al., 2012). The sea level variability in Indonesian seas and its relation with the ENSO is presented throughout the following sections.

A brief description of the characteristics of the Indonesian seas is given in Section 5.1, including the description of the Indonesian Throughflow (ITF), of major importance in the region. A summary of the results achieved by the most recent studies of sea level in the Indonesian sea also presented in this section.

Section 5.2 describes the sea level variability in the Indonesian seas. The estimation of sea level variability using selected parameters was performed for the following altimetry missions: T/P, Jason-1, Jason-2, ERS-1/2, Envisat, CryoSat-2, and SARAL. In this section, the Sea Level Anomaly (SLA) time series and the spatial pattern of sea level variability from these missions over the 24-year period is also presented.

Due to the ENSO influence in the Indonesian seas, three indices of ENSO were used to assess the correlation with sea level variability in the region. The three indices are the Multivariate ENSO Index (MEI), the Oceanic Niño Index (ONI) and the Southern Oscillation Index (SOI), and the results of this analysis are shown in Section 5.3.

5.1. The Indonesian Seas

The tropical Pacific and Indian Ocean regions have high sea level variability associated with atmosphere-ocean phenomena such as the ENSO, the Indian Ocean Dipole (IOD) and the Asian-Australian monsoon (Church and White, 2006; England and Huang, 2005; Lan et al., 2008). The Indonesian seas, located between the Pacific Ocean and the Indian Ocean (Figure 5.1), is the oceanic pathway for the Pacific and Indian inter-ocean exchange, known as the Indonesian Throughflow (ITF) (Gordon, 2005). The ITF brings relatively warm and fresh water from the west Pacific Ocean into the southeast Indian Ocean via the series of passages between the islands of the Indonesian archipelago, a primary inflow through the Makassar Strait, and outflow through the Lombok Strait directly to Indian Ocean and another way through the Flores Sea, the Banda Sea, and then via the Ombay Strait and the Timor Passage before exit to the Indian Ocean (Sprintall et al., 2014). The fresh water and low-salinity from the South China Sea (SCS) flows through the Karimata Strait and the Java Sea, thus mixing into the primary ITF inflow in the southern Makassar Strait (Wei et al., 2016; Gordon et al., 2003) and through Sibutu Passage to the northern Makassar Strait (Gordon et al., 2012).

Since the heat and salinity variations become important in terms of sea level variability, the ITF strongly influences the heat and freshwater budgets of the Pacific and Indian Oceans and it may be considered to play the global and regional ocean circulation (Gordon, 2005; Sprintall et al., 2014). Several studies have indicated that the sea level variability in the Indonesian seas is influenced by the surrounding oceans and seas (Sprintall et al., 2014), such as the Pacific Ocean (Chang et al., 2013; van Sebille et al., 2014), Indian Ocean (Saji and Yamagata, 2003; Lan et al., 2008) and the South China Sea (Gordon et al., 2012; Liu et al., 2006, Tozuka et al., 2009).

A number of studies using various satellite altimetry data and processing methodologies pointed out that sea level rise in this region was about 1.7 to 8 mm/year during the period 1993-2011. Fenoglio-Marc et al. (2012) reported that the trend in sea level measured using satellite altimetry during the period 1993–2011 was about 4 mm/year at near selected tide gauge stations. In Strassburg et al. (2015), the sea level rise in the Indonesian seas was separated into several sea areas according to the Limit of Ocean and Seas published by the International Hydrographic Organization (IHO) in 1953. For these areas they report sea level trends from 4 to 8 mm/year, based on altimetric measurements during 1993 to 2009. However, in Passaro et al. (2016), the trends of several seas in the Indonesian region, derived

using CryoSat-2 data and retracked Envisat data using ALES, are 2.9 mm/year, 2.9 mm/year, 1.7 mm/year and 3.3 mm/year for Java, Flores, Banda and Ceram seas, respectively, during the period 2002 to 2015.

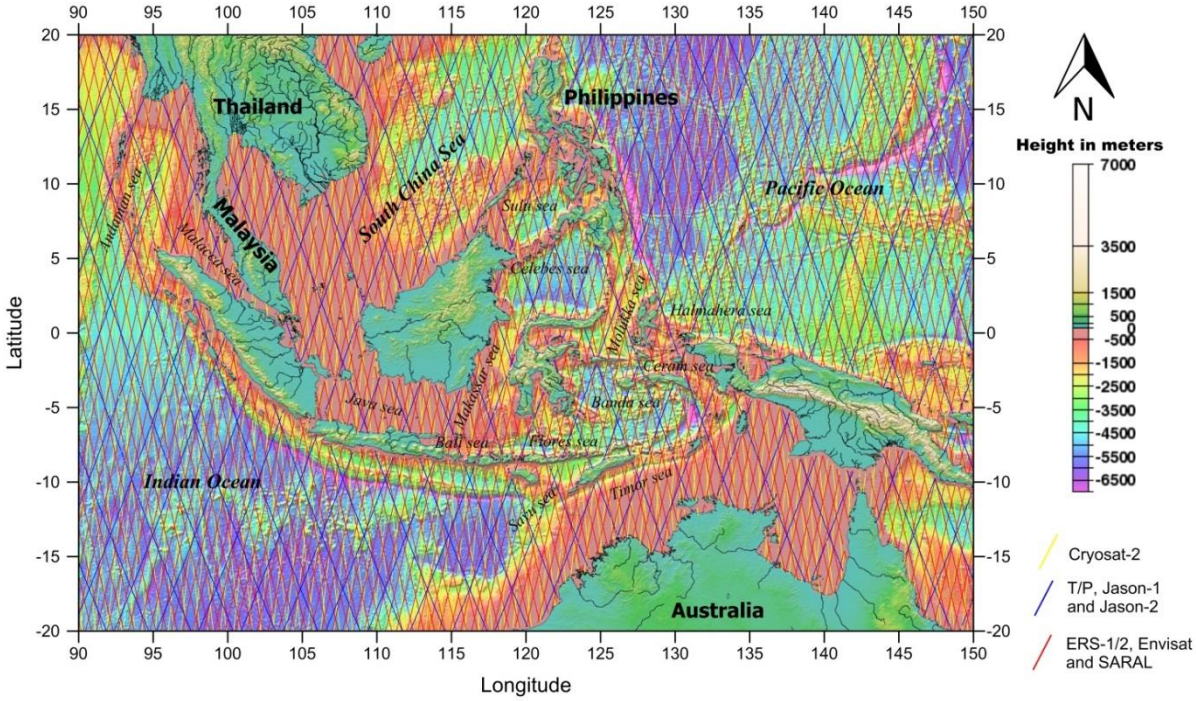

Figure 5.1 The Indonesian Seas: geographic and bathymetric setting. Along-tracks of altimeter missions: Cryosat-2 (yellow lines), TOPEX/Poseidon, Jason-1 and Jason-2 (blue lines) and ERS-1, ERS-2, Envisat and SARAL (red lines).

5.2. Sea Level Variability in the Indonesian region

Indonesia is known as the largest archipelago country since it comprises more than 17,000 islands, 81,000 km coastline and 5.8 million km^2 of sea areas. According to the Special Publication (SP) no. 23 of the IHO, the Indonesian seas were divided into twelve seas, one strait and two gulfs, as shown in Figure 5.1 (IHO, 1953). Several big cities and a large amount of population are located on coastlines that are particularly vulnerable to sea level rise. The Indonesian seas are a key domain connecting the Pacific and Indian Oceans and show a higher trend of sea level rise than the global one. Therefore, it is important to understand the sea level variability around this area.

Satellite altimetry has also been used to analyze regional sea level change. To determine sea level variability with high precision using satellite altimetry, accurate range and geophysical corrections have to be involved in the sea level computation. These corrections include the ionospheric and both the wet and dry tropospheric delays, the response of the sea surface to dynamic atmosphere pressure, both ocean and solid earth tides, and sea state bias. Using Equation 2.7 in Chapter 2, the SLA with respect to a mean sea surface (MSS) can be estimated.

In Handoko et al. (2017) a detailed assessment of the best range and geophysical corrections and MSS models for use in the processing of altimetry data from the reference missions has been performed. The best choice and adopted models for the range corrections are, for T/P, Jason-1 and Jason-2 missions: the ERA-Interim model for the dry tropospheric correction, the wet tropospheric correction from the GPD+ algorithm and the smoothed dual-frequency ionospheric correction; the parametric sea state bias (SSB) BM4 model for TOPEX-A and Poseidon, the non-parametric-CLS model for TOPEX-B; the Tran2012 model for Jason-1 and Jason-2. Regarding the geophysical effects, the ocean tide FES2012 shows the best performance in the coastal area up to 60 km, while GOT4.10 evidences the best overall performance in the open ocean. The CNESCLS_2011 mean sea surface model was adopted for all missions due to the SLA variance reduction this model causes, particularly in the coastal band up to about 40 km from the coast, when compared with DTU13 MSS. Based on this study, the best set of corrections has also been selected for the remaining altimetric missions used in this thesis. The estimation of SLA around the Indonesian seas adopted the various corrections from Handoko et al. (2017), Ablain et al. (2016) and SL_cci (2016) is shown in Table 5.1.

For estimating sea level change from various altimetric missions, attention must be taken to determine the biases of measurements between these different missions. It is also important to understand the differences in the corrections and other parameters that affect the measurements between the different altimeter systems. The tandem missions take place when two satellites fly together simultaneously along the same repeating period and ground track, with a short time difference, e.g. one minute; therefore, both satellites should be observing the same real ocean variability. The tandem missions are important for detecting a number of problems in both satellites, e.g. the tandem mission between T/P and Jason-1 detected some problems in the sea state bias model, the radiometer instabilities related to the yaw regime

and geographically correlated errors related to differences in the reference frames used to compute satellite orbits (Nerem et al., 2010).

In sea level studies using multi-mission satellite altimetry, the inter-satellite SLA altimetric series should be inter-calibrated using data for the periods of the tandem phases between consecutive missions. This procedure has been adopted in this study for the reference missions and the set of satellites ERS-1, ERS-2, and Envisat. In the computations, weighted SLA (weights are function of the co-sine of latitude) were applied. Furthermore, all time series have been decomposed into seasonal, inter-annual and residual signal using Seasonal Trend decomposition based on LOESS (STL) (Cleveland et al., 1990). For the reference missions, the SLA time series have been smoothed prior to the signal decomposition to account for the 59-day signal apparent in the GMSL record. This signal is the aliasing of a higher frequency error inherited from the tide model correction: the semi-diurnal wave S2 (Zawadzki et al., 2016). Finally, the linear sea level trend was computed by original least squares (OLS) fitting of the inter-annual signal.

Table 5.1 Selected range and geophysical corrections and mean sea surface for estimating sea level anomalies around the Indonesian seas (Handoko et al., 2017; Ablain et al., 2016; SL_cci, 2016)

	TOPEX/ Poseidon	**Jason-1**	**Jason-2**	**ERS-1**	**ERS-2**	**Envisat**	**Cryosat-2**	**SARAL**
Year	1993 - 2002	2002 - 2008	2008 - 2016	1995 - 1996	1996 - 2003	2003 - 2010	2010 - 2013	2013 - 2016
Cycles	011 - 353	011 - 248	010 - 312	144 - 156	012 - 85	018 - 093	008 - 038	001 - 040
Dry Troposphere	ERA-Interim	ERA-Interim	ERA-Interim	ERA-Interim	ERA-Interim	ERA-Interim	ERA-Interim	ERA-Interim
Wet Troposphere	GPD+	GPD+	GPD+	GPD+	GPD+	GPD+	GPD+	GPD+
Ionosphere	Smoothed Dual Frequency	Smoothed Dual Frequency	Smoothed Dual Frequency	NIC09	NIC09	Smoothed Dual Frequency (cycle 1 to 65) and JPL GIM afterwards	JPL GIM	JPL GIM
Sea State Bias	TOPEX_A: BM4 TOPEX_B: NP-CLS Poseidon: BM4	Tran2012 Model	Tran2012 Model	BM4	BM4	SSB Hybrid	SSB Hybrid	SSB Hybrid
Ocean and Load Tide	FES2012 for <60 km GOT 4.10 for >60 km	FES2012 for <60 km GOT 4.10 for >60 km	FES2012 for <60 km GOT 4.10 for >60 km	GOT4.10	GOT4.10	GOT4.10	GOT4.10	GOT4.10
Mean Sea Surface	CNES CLS 2011	CNES CLS 2011	CNES CLS 2011	CNES CLS 2011	CNES CLS 2011	CNES CLS 2011	CNES CLS 2011	CNES CLS 2011

5.2.1. The reference-missions: TOPEX/Poseidon, Jason-1 and Jason-2

The precise altimeter satellites, TOPEX/Poseidon (T/P) and its successors Jason-1 (J1) and Jason-2 (J2), measure sea surface height along the same surface track with a repeat orbit period of 9.9 days (~10 days) at an altitude about 1336 km with an inclination of 66 degrees. Due to the long term data record and their precisions, TOPEX/Poseidon, Jason-1 and Jason-2 can be called the reference-missions.

The sea level variability around the Indonesian Seas was analyzed by combining the time series from T/P, J1 and J2. To make a stable and continuous time series across these satellites during the nominal reference orbit phase, the inter-satellite sea level anomalies are calibrated during the tandem phases when the pair of satellites sampled the same ground track within one minute of each other. The tandem cycles for T/P and J1 are cycles 343–364 and 001–020 respectively, while for J1 and J2 the corresponding tandem cycles are 240–259 and 001–020 respectively. The relative difference between TP and J1 (J1, TP) was determined by averaging the differences between all corresponding tandem mission cycles. Similarly, the relative difference (J2, J1) was determined by the average of the differences from all tandem cycles between Jason-2 and Jason-1.

$$SLA_{Corrected}(\mathrm{J1}) = SLA(\mathrm{J1}) - bias(\mathrm{J1},\mathrm{TP}) \tag{5.1}$$

$$SLA_{Corrected}(\mathrm{J2}) = SLA(\mathrm{J2}) - bias(\mathrm{J2},\mathrm{J1}) - bias(\mathrm{J1},\mathrm{TP}) \tag{5.2}$$

By computing the average difference for the 20 cycles of J1 and T/P (J1,T/P), as show in Figure 5.2, a relative difference of 4.6 ± 9.3 mm was found. Similarly, the average of 20 cycle-per-cycle differences of sea level anomaly for J2 and J1 (J2, J1) was computed and a relative difference of 32.8 ± 5.4 mm was obtained. Despite the fact that the relative difference between J2 and J1 (J2, J1) is slightly bigger than the corresponding relative difference between TP and J1, the standard deviation of (J2, J1) differences is smaller than the bias of (J1,T/P) and the pattern of the differences between J1 and J2 seems more homogenous. This may be due to the identical instrument of the J1 and J2 altimeters (Nerem et al., 2010), but also mainly due to the fact that different corrections were applied to each mission. Using T/P as a reference, relative differences of 4.6 mm and 37.4 mm were applied to J1 and J2 data, respectively (as shown in Figure 5.3).

Figure 5.4 presents the inter-calibrated, relative difference-corrected sea level anomalies SLA time series around the Indonesian seas from T/P, J1 and J2 missions between 1993 and 2016. No seasonal signal has been removed from the SLA time series; the original series has been filtered (to eliminate the 59-day signal) and then were decomposed into seasonal (annual) and inter-annual. There is a significant trend in the time series 4.7 mm/year. If a correction of 0.3 mm/year due to glacial isostatic adjustment (GIA) is applied, the rate of sea level rise is 5.0 mm/year.

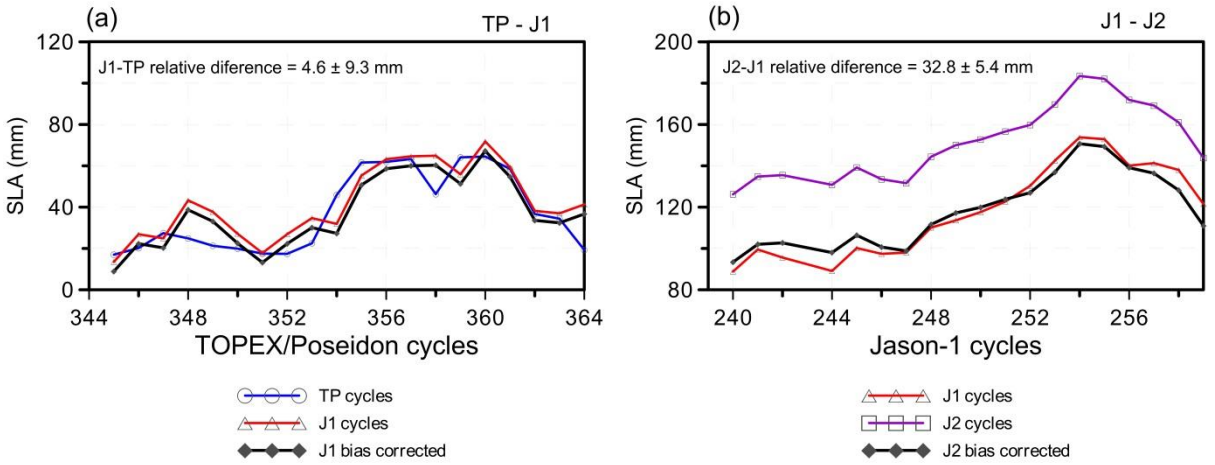

Figure 5.2 Mean SLA values (mm) for (a) the TOPEX/Poseidon – Jason-1 and (b) the Jason-1 – Jason-2 tandem mission periods. Jason-1 values corrected by the (J1, TP) and J2 values corrected by the (J2, J1) biases are also shown.

Figure 5.5 shows the geographical pattern of the SLA trend for the 24-year period (1993 – 2016). The map has been computed on a $4^{o}\times4^{o}$ grid from mean cycle values of SLA time series. It is clear that sea level is not rising uniformly due to the spatial variation of ocean warming, with the light yellow to dark red colors indicating rising sea levels. The variability of sea level rates in this region has strong correlation with the ENSO event (Cazenave et al., 2012).

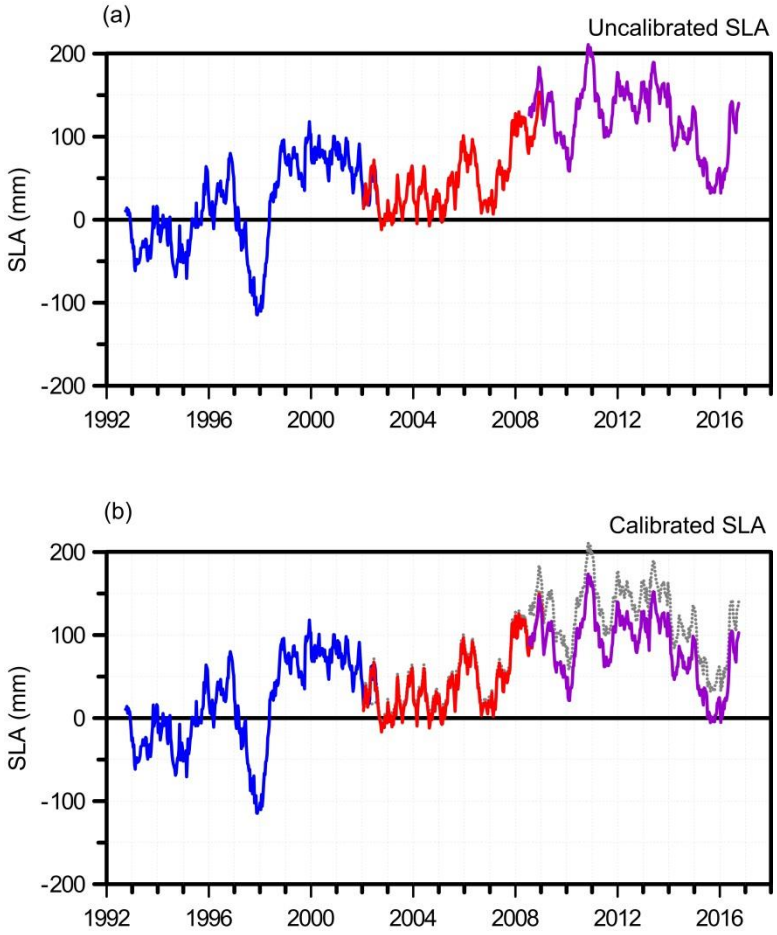

Figure 5.3 (a) Uncalibrated and (b) calibrated SLA time series: T/P (blue), J1 (red), J2 (purple) and uncalibrated SLA (dashed grey as a background).

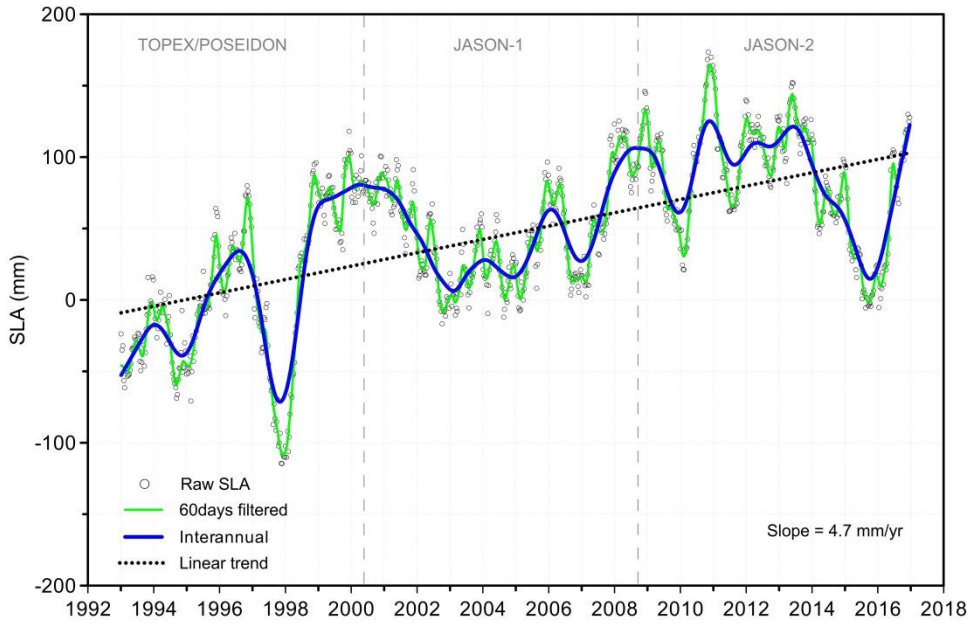

Figure 5.4 Sea level anomaly (mm) time series around the Indonesia seas from three different satellite altimeters 8T/P, J1 and J2): original series represented by the grey dots; 60-day smoothed series in green; inter-annual signal in blue and linear trend represented by the dashed line.

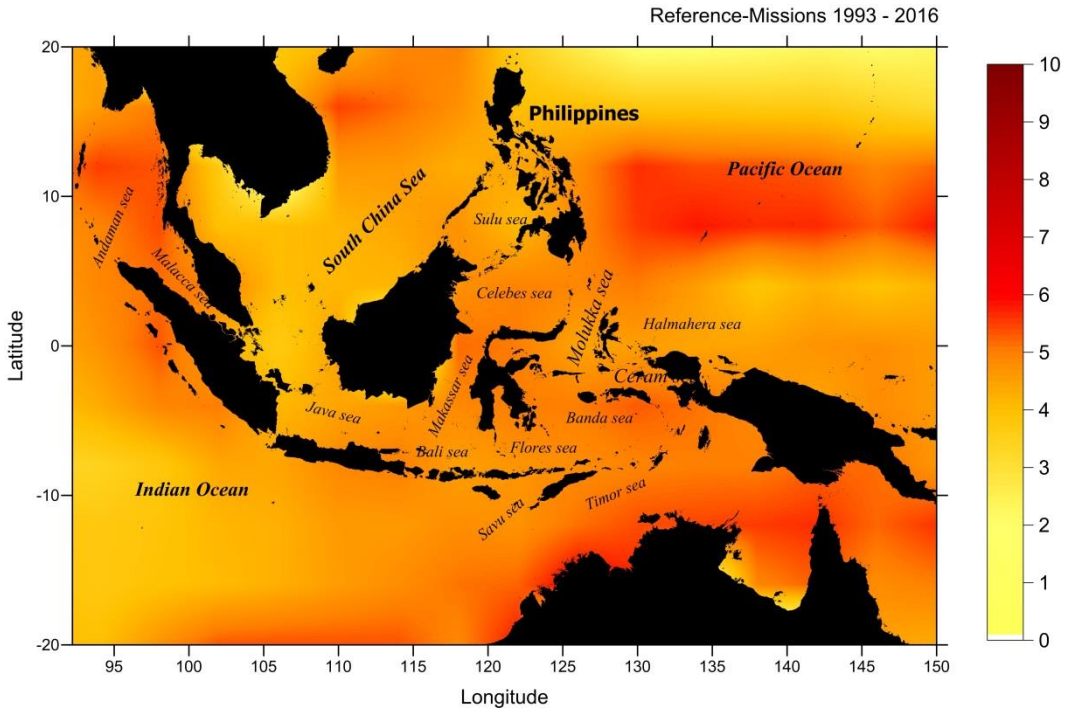

Figure 5.5 Map of sea level trend (mm/year) in the Indonesian seas, estimated from the reference-missions: T/P, J1 and J2 over 24 years (1993 – 2016).

5.2.2. The ESA missions (ERS-1, ERS-2 and Envisat), Cryosat-2 and SARAL

Unlike the reference-missions, the ESA altimeter satellites, Cryosat-2 and SARAL have different repeat orbit periods. ERS-1, ERS-2 and Envisat are flying in the same orbital plane with an inclination of about 98.5 degrees to the Earth's equatorial plane, covering the whole surface of the Earth up to ±81.5° latitude. Each satellite pattern of orbital tracks over the Earth's surface repeats itself exactly after a certain number of days. This 'repeat cycle' depends upon the altitude of the orbit; ERS-1, ERS-2 and Envisat are both flying at the same mean altitude of 785 km, providing a repeat cycle of 35 days. However, after May 2012, when ESA declared the end for the Envisat mission, there was no satellite using the same ground tracks. Since 2013, SARAL, the altimeter satellite of the joint mission between the French Space Agency *Centre National d'Etudes Spatiales* (CNES) and ISRO (Indian Space Research Organization) was placed in the same orbital plane of Envisat with a repeat period of 35 days. Therefore, for the purpose of making an SLA time series with these satellites, there is a gap between 2012 and 2013. Cryosat-2 launched in 2010, which has a long 369-day repeat cycle with sub-cycles of about 30 days, may be used to fill the gap between 2012 and 2013 in the 35-day repeat cycle time series.

To create the sea level anomaly time series for these satellites, two methods were used, the adjustment using data from the tandem-mission periods, which has been used only for the ERS-1, ERS-2 and Envisat, since these satellites have tandem phases with the same ground track and repeat orbit period of 35 days, and the adjustment using SLA differences at crossover with the reference-missions. The latter method has been used for all but the reference missions. The period of analysis is 1995 – 2012 for the tandem-mission method and 1995 – 2016 for the adjustment using crossover analysis.

a. ESA 35-day tandem missions

Using a similar method as for the reference-missions, data from the tandem phases were used to calibrate the SLA time series for the ESA missions (ERS-1, ERS-2 and Envisat). The ERS-1/ERS-2 tandem mission took place during ERS-1 cycles 146 to 156 and ERS-2 cycles 1 to 11. For ERS-2 and Envisat, the tandem cycles are 74 to 85 and 6 to 17, respectively. Using Equations 5.3 and 5.4, the SLA relative differences between ERS-1 and ERS-2 (E2, E1) and ERS-2 and Envisat (EN, E2) were determined.

$$SLA_{Corrected}(\mathrm{E2}) = SLA(\mathrm{E2}) - bias(\mathrm{E2}, \mathrm{E1}) \tag{5.3}$$

$$SLA_{Corrected}(\mathrm{EN}) = SLA(\mathrm{EN}) - bias(\mathrm{EN}, \mathrm{E2}) - bias(\mathrm{E2}, \mathrm{E1}) \tag{5.4}$$

By computing the average differences, a relative difference of 21.2 ± 5.7 mm between ERS-1 and ERS-2 was found. Similarly, a relative difference between ERS-2 and Envisat of -21.2 ± 6.6 mm was obtained. Figure 5.6 illustrates these results. By choosing ERS-1 as a reference, the relative differences of 21.2 mm and 0.0 mm were applied to ERS-2 and to Envisat data, respectively.

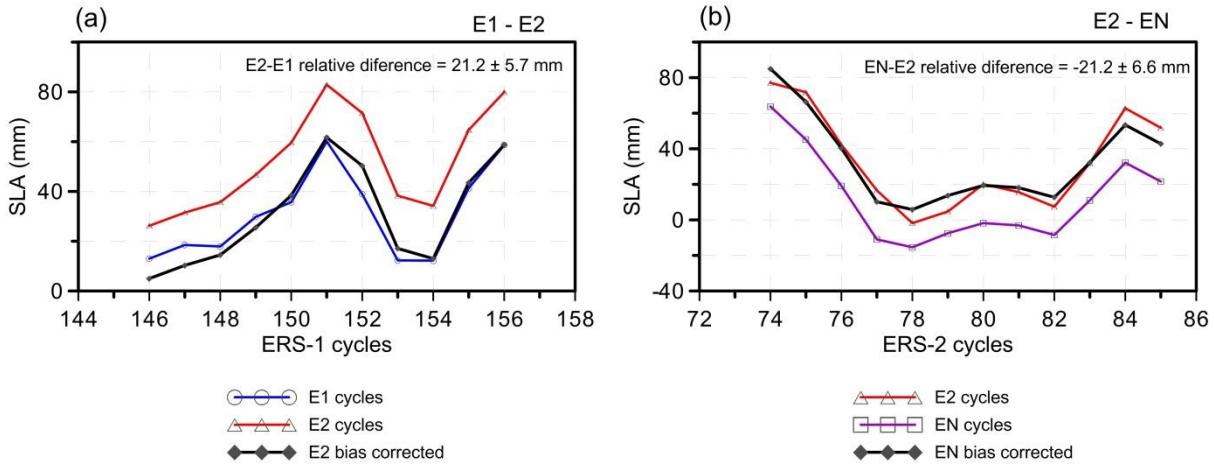

Figure 5.6 Mean SLA values (mm) for the cycles of (a) the ERS-1 – ERS-2 tandem mission and (b) the ERS-2 – Envisat tandem mission. ERS-2 values corrected by the (E2, E1) and Envisat values corrected by the (EN, E2) biases are also shown.

The inter-calibrated sea level anomaly time series from the three missions, ERS-1, ERS-2 and Envisat, between 1995 and 2012 is presented in Figures 5.7 and 5.8. Figure 5.7 illustrates (a) the un-calibrated and (b) calibrated missions; ERS-1 is represented by the blue curve, ERS-2 by the red curve, and Envisat by the purple curve.

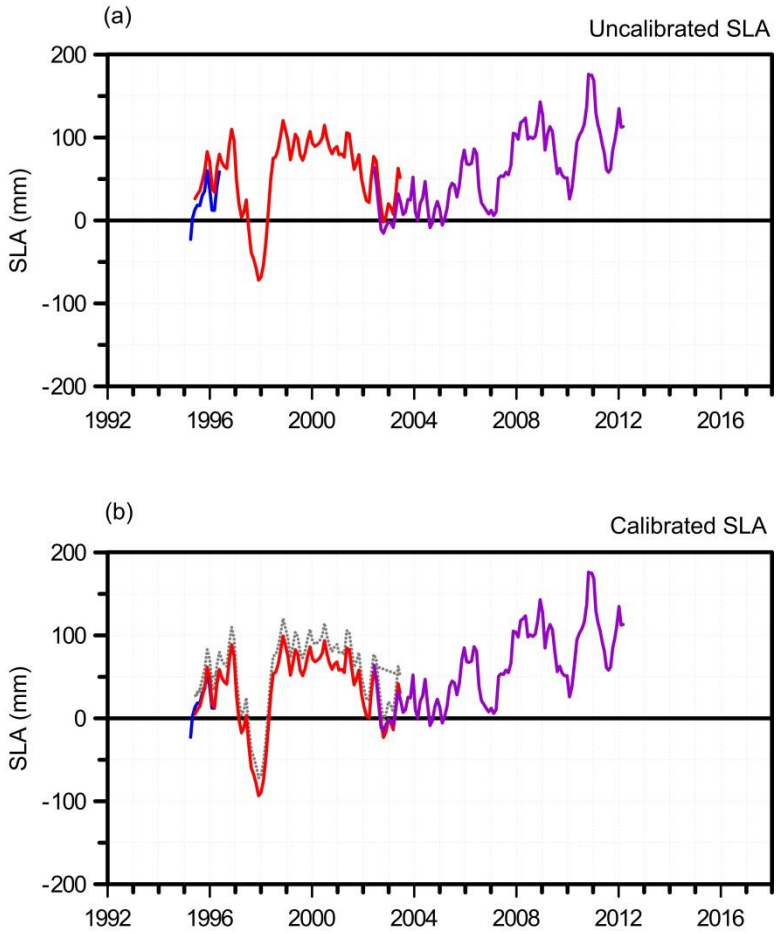

Figure 5.7 (a) Uncalibrated and (b) calibrated SLA time series: ERS-1 (blue), ERS-2 (red), Envisat (purple) and uncalibrated SLA (dashed grey).

Figure 5.8 presents the SLA time series from three ESA satellite altimeters for the 18-year period. The inter-annual signal was shown by blue curves and the linear trend presented by dashed line. The rate of SLA trend is 5.3 mm/year in the 18-year period from 1995 to 2012. By adding 0.3 mm/year to account for the GIA effect, the rate is 5.6 mm/year. In this period, it is also clear that the inter-annual signal of sea level variability is influenced by the ENSO event. Figure 5.9 illustrates the map of sea level trends computed from the SLA time series of mean cycle values in $1^{o}\times1^{o}$ grid, and sea level trend has been determined using least squares over the 18 years (1995 – 2012). In this period, the highest rate of sea level occurs around the western Pacific Ocean (~10 mm/year). In contrast, the lowest sea level rate was found in the eastern Indian Ocean (less than ~2 mm/year).

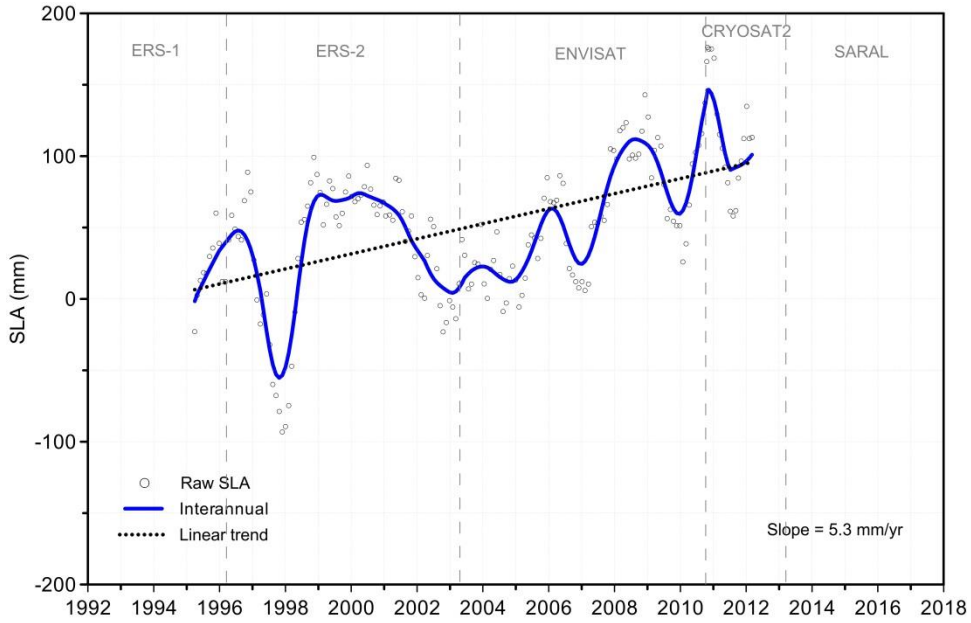

Figure 5.8 Sea level anomalies (mm) time series around the Indonesia seas estimated using data from three ESA satellite altimeters for the 18-year period (1995 – 2012): original series represented by the grey dots; inter-annual signal represented in blue and SLA linear trend in black (dashed line).

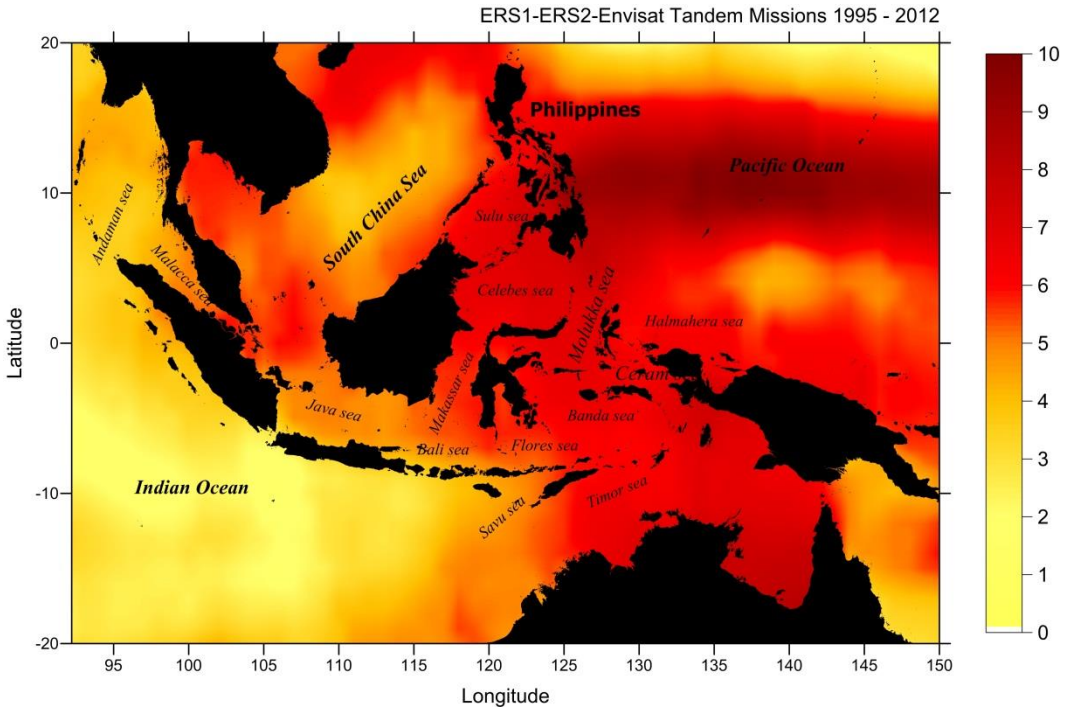

Figure 5.9 Map of sea level trends (mm/year) in the Indonesian seas, estimated using ERS-1, ERS-2 and Envisat missions for the 1995 – 2012 period.

b. Crossover adjustment with respect to reference-missions

It has already been shown that there is a one year gap between the ESA 35-day missions and SARAL. Cryosat-2, launched in 2010, may be an alternative mission for filling this gap. However, Cryosat-2 has an orbital plane and a repeat orbit cycle (369-day repeat period with a 30-day sub-cycle) different from the ESA missions and SARAL.

The intercalibrated SLA is required in order to make the merged-multi-satellite data sets. To obtain intercalibrated data sets, the precise altimetric missions (T/P, J1 and J2) are used as a reference for the other altimetric missions. The crossover adjustment is usually used to improve the orbit errors (Bosch et al., 2014; Le Traon and Ogor, 1998; Tai and Fu, 1986). This approach can also be used to calibrate the long-term sea level anomaly signals. Using dual-satellite crossover adjustment, between ERS-1, ERS-2, Envisat, CryoSat-2 and SARAL with respect to the reference-missions (already intercalibrated as described previously), the intercalibrated SLA time series for the former missions were obtained. The mean values of these crossover adjustments were used to calibrate the non-reference altimetric missions.

The overlapping period between the reference-missions and other missions is about 22 years (1995 – 2016), starting with ERS-1 phase G or cycle 144 and T/P cycle 93. The unadjusted and adjusted sea level time series from the other but the reference missions with respect to these are illustrated in Figure 5.10. Figure 5.11 shows the mean crossover differences between the reference missions and other altimetric missions. The larger differences are obtained for ERS-1 and ERS-2 (maximum mean difference is less than 5 cm). Small mean crossover differences of about 1 cm have been found for Envisat, Cryosat-2 and SARAL.

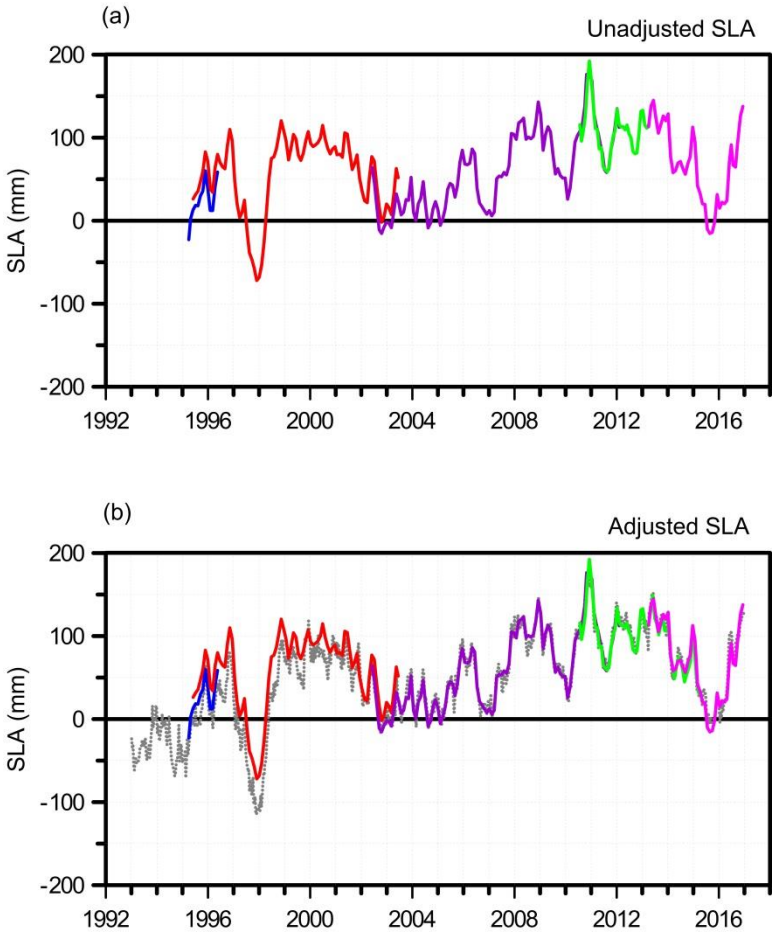

Figure 5.10 (a) Unadjusted and (b) adjusted to reference missions SLA time series for ERS-1 (blue), ERS-2 (red), Envisat (purple), Cryosat-2 (green), SARAL (magenta) and SLA of reference-missions (dashed grey).

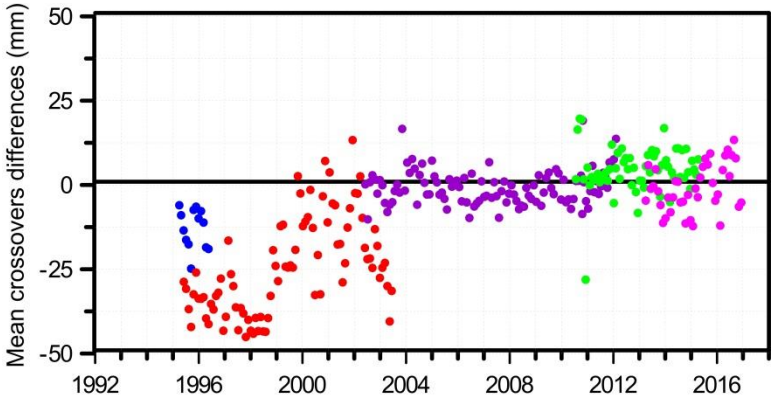

Figure 5.11 The mean cross-over differences for satellites ERS-1 (blue), ERS-2 (red), Envisat (purple), Cryosat-2 (green) and SARAL (magenta) relative to reference missions (T/P, Jason-1 and Jason-2).

In order to evaluate the intercalibration of the various SLA time series, the comparison of the SLA trend, computed using the tandem-mission and crossover adjustment to reference-missions methods, is performed for the three ESA missions. The results of the comparison are presented in Table 5.2 and Figure 5.12.

For the same period (1995 – 2012), the comparison between the sea level time series for the ESA missions, which were derived using the described methodology (tandem mission and adjustment of crossover differences), and the sea level time series for the reference-missions were analyzed. The trend values are 5.3 mm/year, 5.7 mm/year and 5.6 mm/year for the SLA derived by tandem mission calibration, the SLA derived by adjustment of crossover differences and the SLA from reference-missions, respectively. These results show that the SLA from adjusted crossover differences is similar to the SLA derived from crossover adjustment to the reference-missions. However, the calibrated SLA that is derived using the tandem mission is the independent SLA time series.

A similar analysis is used to compare the SLA time series using a crossover adjustment (Adjusted ESA+) and the SLA for the reference-missions for the longer period (1995 – 2016). The results show that there is a small difference of 0.1 mm/year in the SLA trend difference (see in Table 5.2).

Figures 5.13 and 5.14 illustrate the sea level anomaly time series over the 22-year (1995 – 2016) period. The SLA trend in this period is 3.9 mm/year and 4.2 mm/year if GIA effect is added. The geographical pattern of sea level rate is shown in Figure 5.14.

Table 5.2 Comparison of the various SLA time series, computed using tandem- mission and crossovers to reference-missions methods, as shown in Figure 5.12.

SLA time series Periods	**Tandem ESA**	**Adjusted ESA**	**Reference Mission**	**Adjusted ESA+**	**Reference Mission**
(a) 1995 - 2012	5.3 mm/yr	5.7 mm/yr	5.6 mm/yr	-	-
(b) 1995 - 2016	-	-	-	3.9 mm/yr	3.8 mm/yr

Notes :

ESA	ERS-1, ERS-2, Envisat
ESA+	ERS-1, ERS-2, Envisat, Cryosat-2, and SARAL
Reference-missions	T/P, J1, and Jason-2

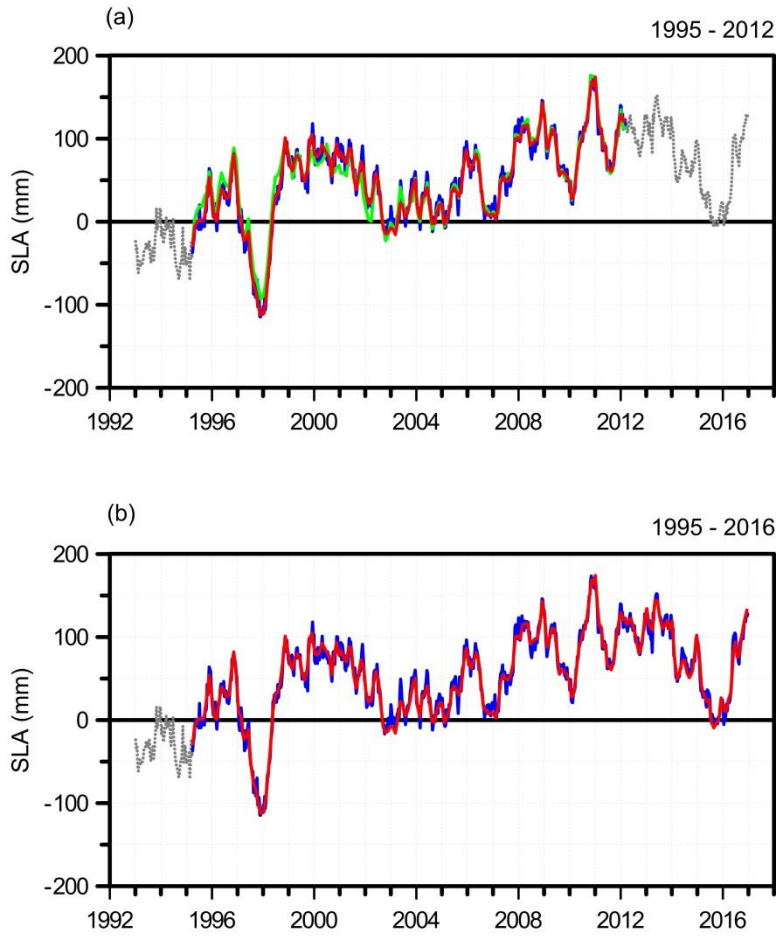

Figure 5.12 Comparison of various SLA between sea level time series derived using (a) tandem missions and (b) adjusted relative to reference-missions.

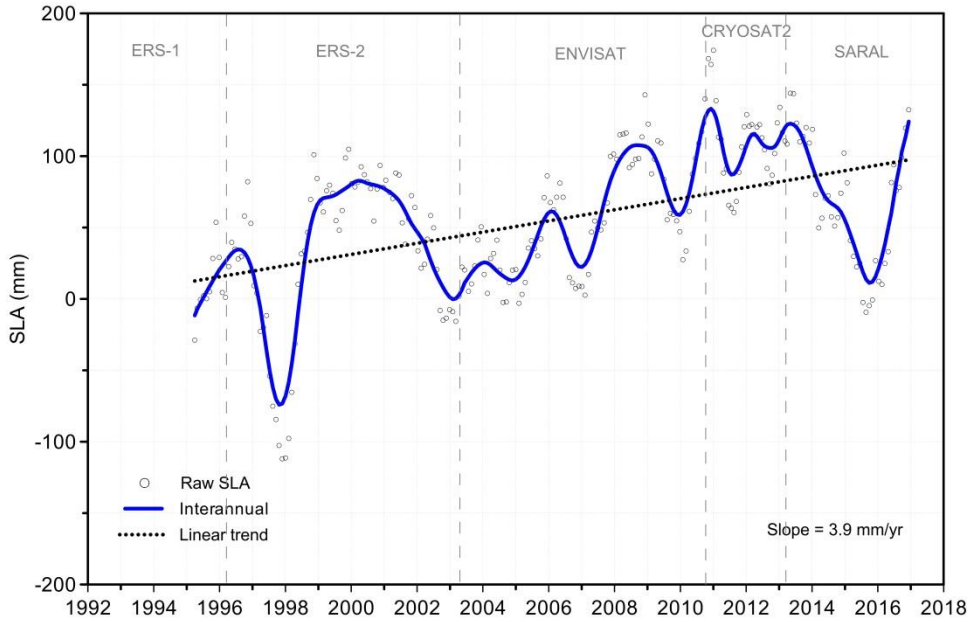

Figure 5.13 Sea level anomaly (mm) time series in the Indonesia seas estimated using ERS-1, ERS-2, Envisat, Cryosat-2 and SARAL adjusted to reference-missions, over 22 years (1995 – 2016).

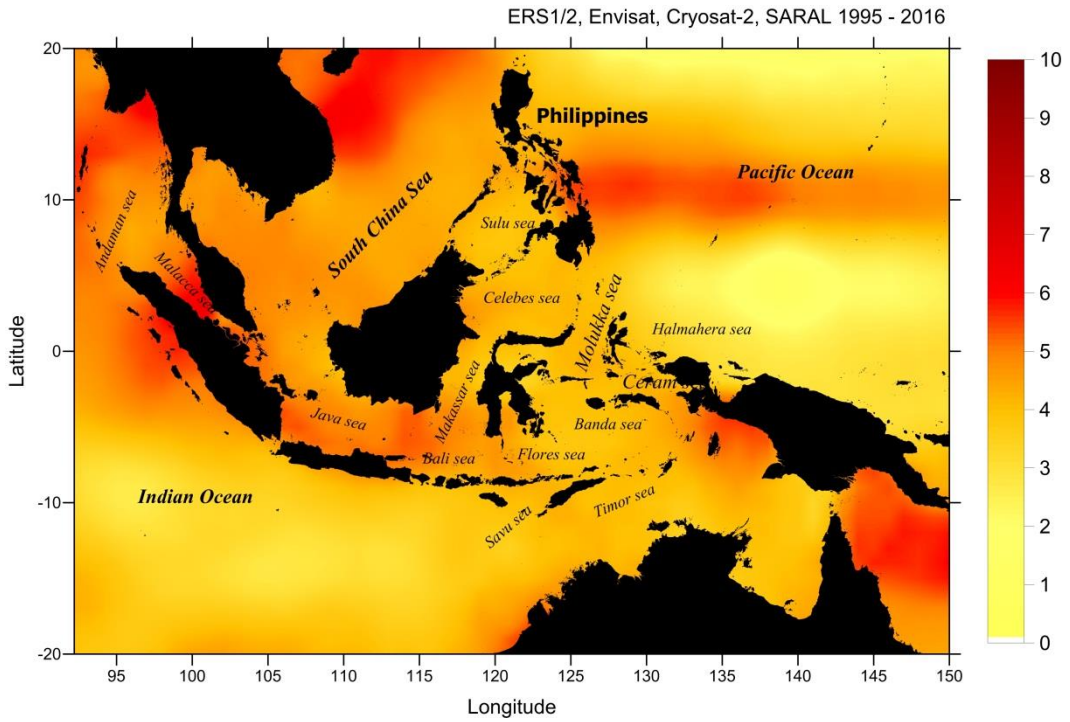

Figure 5.14 Map of sea level trends (mm/year) in the Indonesian seas, estimated using ERS-1, ERS-2, Envisat, Cryosat-2 and SARAL adjusted to reference-missions for the period (1995 – 2016).

5.2.3. Multi-Altimeter-missions

The intercalibrated missions with respect to the reference missions were obtained in the previous section. However, the repeat cycle of the various non-reference mission are still different, ERS-1, ERS-2, Envisat, and SARAL have 35 day repeat cycle, while Cryosat-2 has a 30-day sub-cycle (369-day repeat cycle). In order to be combined with the reference-missions, the non-reference mission cycles should be close to the repeat cycle of the reference missions i.e. around 10 days. Using pseudo-cycles, the other missions have been "re-arranged" into the new 10-day cycles based on the T/P cycles. In this way, a multi-mission time series was built, considering, for each 10-day period, the weighted mean of all observations for that period, from all satellites.

Figure 5.15 illustrates the multi-mission and the reference-missions sea level anomaly time series over 1993 – 2016. There are no significant differences between both time series. The linear trend is 4.7 mm/year or 5.0 mm/year when GIA effect is added. This rate is similar to the linear trend obtained for the SLA time series from reference-missions. The difference

between them is that when computing the regional trends, the multi-mission data sets have more data, since the distances between adjacent tracks at the equator are 80 km and 300 km for ERS-1/ERS-2/Envisat/SARAL and reference-missions, respectively. Thus, a mean grid of SLA can be set to finer $1^o \times 1^o$ regular grids when compared to the $4^o \times 4^o$ regular grids used for the reference missions.

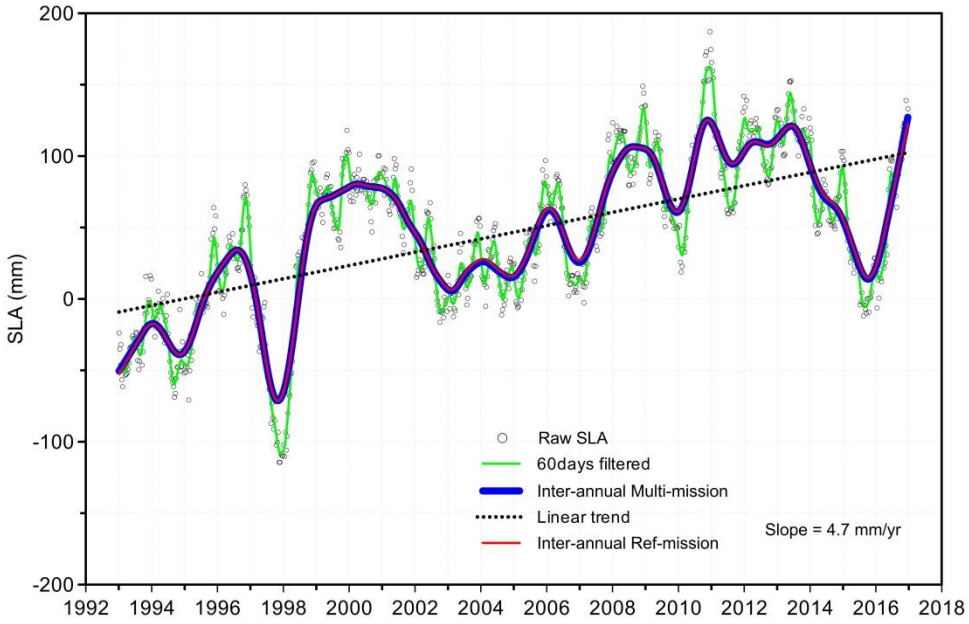

Figure 5.15 Sea level anomaly (mm) time series in the Indonesia seas from multi-mission satellite altimeters (grey dots) for the 1993 – 2016 period, 60-day smoothed (green curve), inter-annual signal of multi-missions (bold blue curve), inter-annual signal of reference-missions (thin red curve) and SLA linear trend (dashed line).

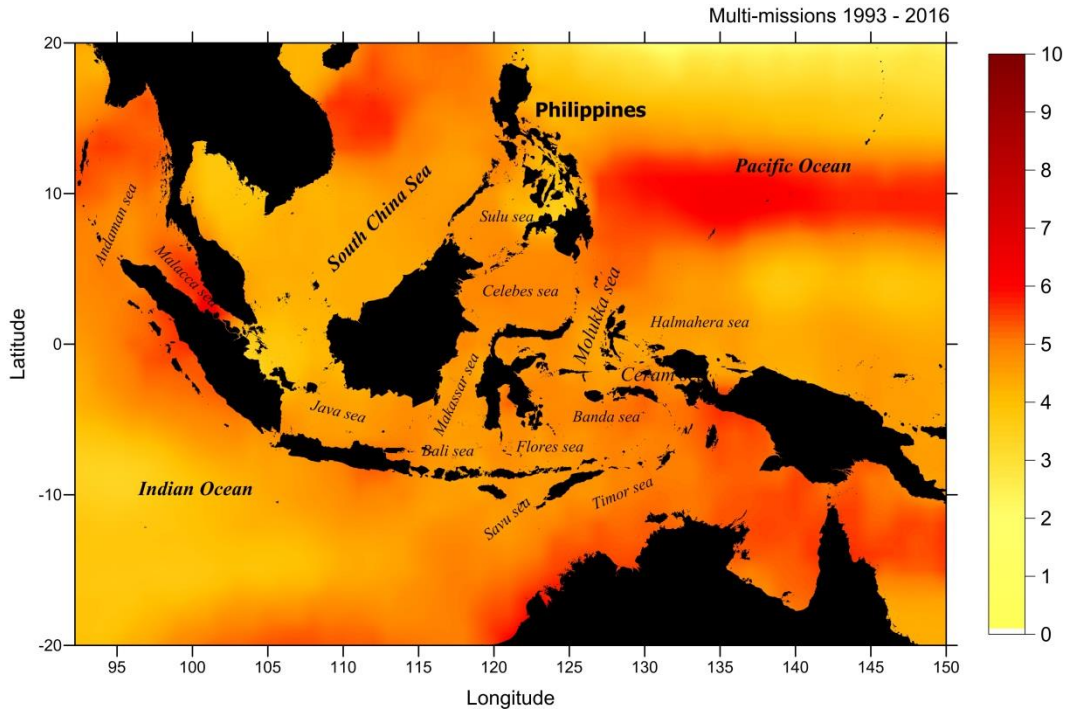

Figure 5.16 Map of sea level trend (mm/year) in the Indonesian seas from multi-mission SLA data for the 1993 – 2016 periods.

5.3. Analysis of Sea Level Variability related to El Niño-Southern Oscillation event

El Niño-Southern Oscillation (ENSO) is a natural couple cycle in the ocean-atmospheric system over the tropical Pacific. ENSO phenomenon is an important component of global climate change, characterized by the appearance of warmer surface water along the equatorial Eastern Pacific Ocean at 2- to 7- year intervals that can change the precipitation rate, temperature and water vapor during that period. ENSO has three phases: warm tropical Pacific sea surface temperatures (El Niño), cold tropical Pacific sea surface temperatures (La Niña) and near-neutral conditions (Hanley et al., 2003).

The global impact of the El Niño-Southern Oscillation (ENSO) event affects the inter-annual variation of the global mean sea level (GMSL), particularly over the tropical and sub-tropical Pacific Ocean (Church and White, 2006). Its effect on the Indonesian seas is significant. The Indonesian seas are considered an oceanic pathway for the Pacific and Indian Oceans where the waters from the Pacific Ocean flow to the Indian Ocean through the Indonesian seas, the so-called Indonesian Throughflow (ITF) (Gordon, 2005; Sprintall et al., 2014). The sea surface height and temperature in the Indonesian seas decrease during El Niño

periods. In contrast, the trade winds, the sea surface height and the sea surface temperature increase along La Niña events (England and Huang, 2005; Merrifield et al., 2012; Potemra and Schneider, 2007).

ENSO events can be classified by year of occurrence, strength, duration, or timing. La Niña and El Niño ENSO years are categorized into three different types: weak, moderate, and strong. ENSO event appeared in the Indonesian region in several periods, but the strongest El Niño was during 1997 – 1998 and the strongest La Niña was in 2011. Another noticeable feature of the inter-annual variability seen in Figures 5.4, 5.13 and 5.15 is the strong decrease in sea level since 2013, associated with the most recent 2015-16 El Niño.

In order to investigate the correlation between SLA and the ENSO event in the Indonesian seas region, three indices of ENSO were selected: the Multivariate ENSO Index (MEI), the regional sea surface temperature (SST) indices or Oceanic Niño Index (ONI) and the surface atmospheric pressure-based Southern Oscillation Index (SOI).

5.3.1. Multivariate ENSO Index (MEI)

MEI is an index that is defined as the first seasonally varying principal component of six atmosphere–ocean variable fields of the Comprehensive Ocean-Atmosphere Data Set (COADS) measured over the tropical Pacific and can reflect multiple characteristics of the ENSO phenomena (Wolter and Timlin, 2011). These variables are sea level pressure (P), zonal (U) and meridional (V) components of the surface wind, sea surface temperature (S), surface air temperature (A), and total cloudiness fraction of the sky (C). The MEI is computed separately for each of twelve sliding bimonthly seasons (Dec-Jan, Jan-Feb, …, Nov-Dec) to filter out 30 – 60 day oscillations. After spatially filtering the individual fields into clusters, the MEI is calculated as the first unrotated Principal Component (PC) of all six observed combined fields. This is accomplished by normalizing the total variance of each field first, and then performing the extraction of the first PC on the co-variance matrix of the combined fields (Wolter and Timlin, 1993). Negative values of the MEI represent the cold ENSO phase, La Niña, while positive MEI values represent the warm ENSO phase (El Niño).

Figure 5.17 shows the detrended SLA for the Indonesian seas overlaid with the Multivariate ENSO Index (MEI). The El Niño periods are indicated in red while La Niña periods are shown in blue. The striking feature of this figure is a perfect match of the periods when SLA is positive with those when MEI is negative and of the periods when SLA is

negative with those when MEI is positive. The strong negative correlation is shown by the correlation index (-0.84) between the detrended SLA time series and MEI index, for both the SLA time series from the reference-missions and from the multi-mission time series. The highly value of correlation indicates that the inter-annual sea level variability in the Indonesian region is strongly influenced by ENSO event.

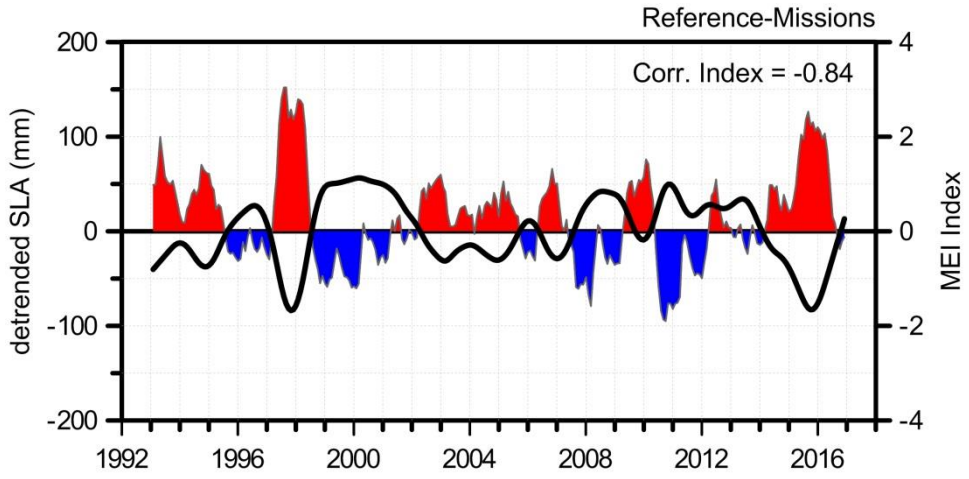

Figure 5.17 The detrended SLA time series around the Indonesian seas (black curve) and Multivariate ENSO Index (MEI): El Niño (red) and La Niña (blue) for the reference missions.

5.3.2. Oceanic Niño Index (ONI)

The temperature-based indices are defined using mean sea surface temperatures within different regions of the equatorial Pacific (Table 5.3). As shown in Figure 5.18, the Niño-1 region is located off the coast of Peru and Ecuador, while the Niño-2 region is located near the Galapagos Islands. The Niño-1+2 region is a combination of the Niño-1 and Niño-2 regions and covers the extreme eastern equatorial Pacific. This region is also highly responsive to seasonal and El Niño-induced changes. The Niño-3 region is located in the central equatorial Pacific and is much less responsive to continental influences than the Niño-1 and the Niño-2 regions. The Niño-4 region includes the part of the western equatorial Pacific where the warmest SST values are found. Changes in SST over the Niño-4 region are related to the longitudinal shift of the strong east-west temperature gradients along the equator. The Niño-3.4 region overlaps portions of the Niño-3 and the Niño-4 regions and is interpreted as the average equatorial SST across the Pacific (Hanley et al., 2003). The Niño

3.4 index typically uses a 5-month running mean, and El Niño or La Niña events are defined when the Niño 3.4 SST values exceed +/- 0.4°C for a period of six months or more.

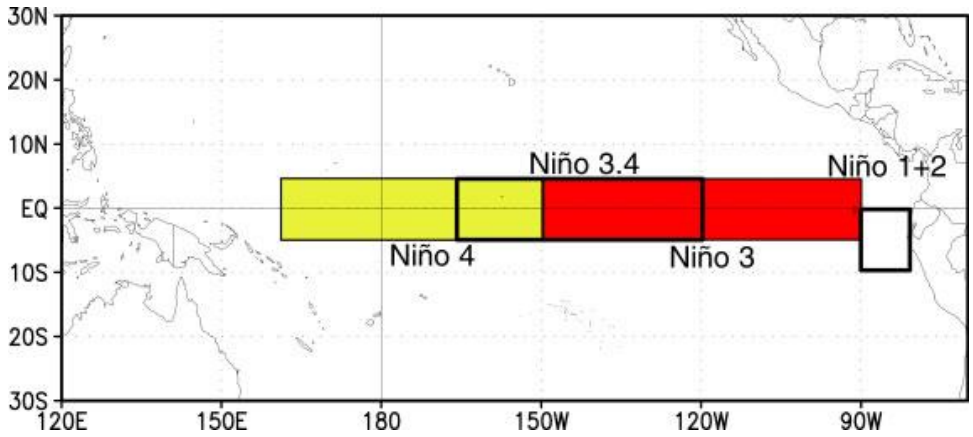

Figure 5.18 Location of the geographic regions for computing Niño regional sea surface temperature Indices: Niño-1+2, Niño-3, Niño-3.4, and Niño-4.

Table 5.3 Latitude and longitude range for the areas used in the computation of SST indices (Hanley et al., 2003).

Index	Latitude	Longitude
Niño-1+2	0^o – 10^o S	90^o – 80^o W
Niño-3	5^o N – 5^o S	150^o – 90^o W
Niño-3.4	5^o N – 5^o S	170^o – 120^o W
Niño-4	5^o N – 5^o S	160^o E – 90^o W

The Ocean Niño Index (ONI) uses the same region as the Niño 3.4 index. The ONI uses a 3-month running mean, and to be classified as a full-fledged El Niño or La Niña, the anomalies must exceed +0.5°C or -0.5°C for at least five consecutive months. This is the operational definition used by NOAA.

Figure 5.19 shows the SST anomalies from the Niño-1+2, Niño-3, Niño-3.4 and Niño-4. The Niño-4 SST anomalies have smaller positive values. The weakness in the positive Niño-4 SST anomalies is caused by the fact that the Niño-4 region has the deeper mixed layer of seawater, which reduces the amount of warming in the SST. The Niño-4 index has a strong response to La Niña, but a poor response to El Niño. The Niño-1+2 index has the opposite characteristics. According to Barnston et al. (1997), Niño-3.4 is slightly more

correlated with the core ENSO phenomenon than Niño-3, its standardized SST anomalies during ENSO periods usually have higher amplitude than those of Niño-3.

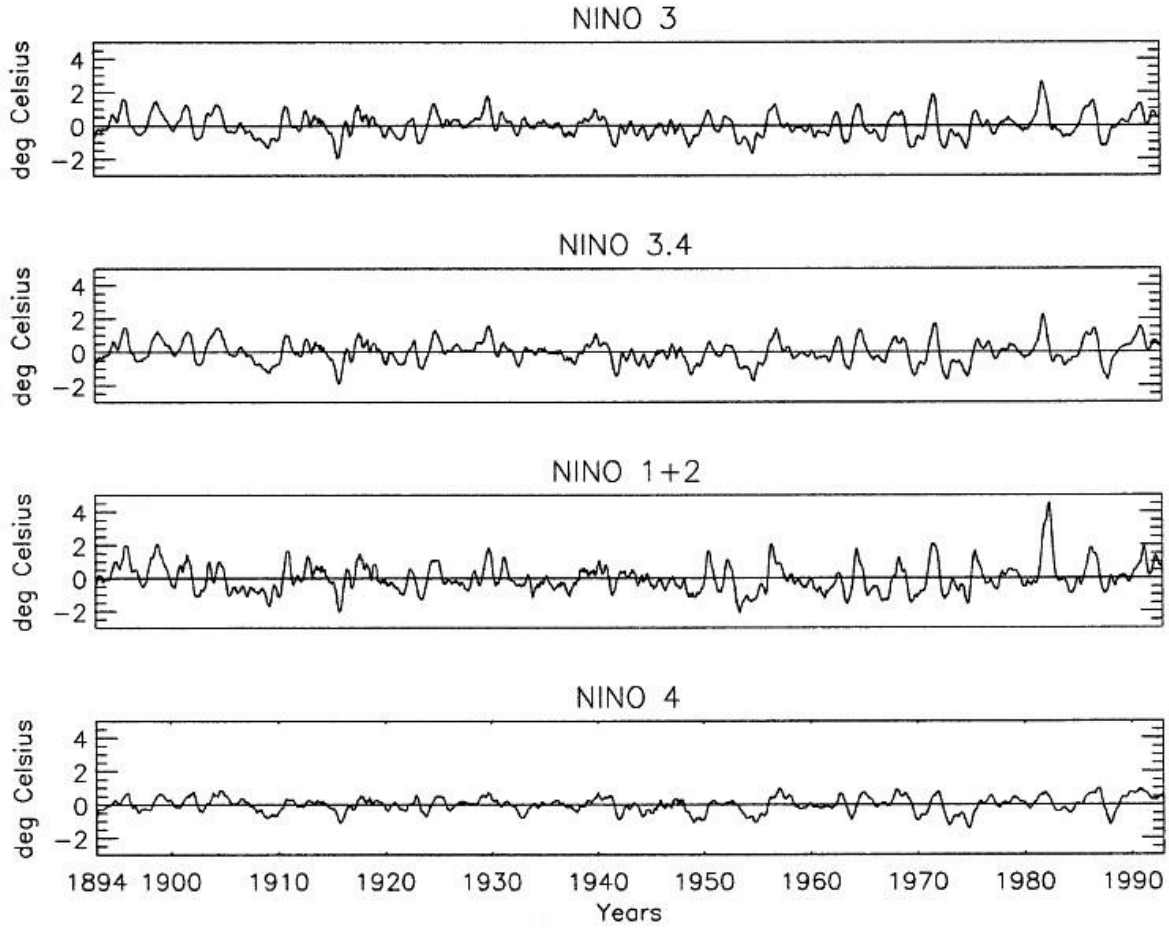

Figure 5.19 Niño Regional SST Indices (^{o}C) time series over 1894-1990. The abscissa of each panel is the time in years and the ordinate is temperature indices in ^{o}C (Hanley et al., 2003).

In order to estimate the influence of ENSO in the Indonesian region, the correlation between detrended SLA in the Indonesian seas and the Oceanic Niño Index (ONI) based on Niño-3.4 was computed. Both the reference-missions and multi-mission SLA time series indicate a high negative correlation between both time series (the correlation index is -0.85) as shown in Figure 5.20.

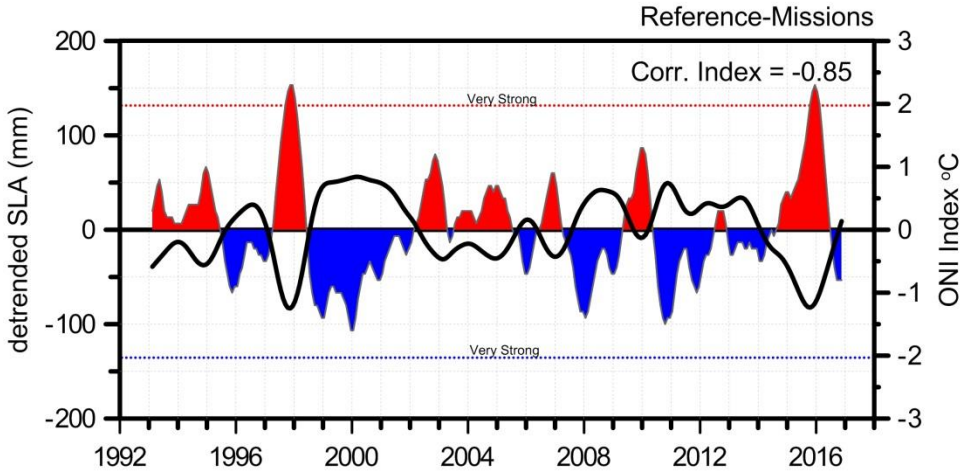

Figure 5.20 Detrended SLA around the Indonesian seas (black curve) and Oceanic Niño Index (ONI)-Niño-3.4: El Niño (red) and La Niña (blue) for SLA time series from reference missions.

5.3.3. Southern Oscillation Index (SOI)

El Niño is linked to major changes in the atmosphere known as the Southern Oscillation (SO). Southern Oscillation (SO) is described as the periodic change in sea level pressure (SLP) differences across the tropical Pacific that have been found to highly correlate with El Niño and La Niña events. During El Niño, higher-than-normal surface air pressures develop over Australia, Indonesia, Southeast Asia and the Philippines, producing drier conditions or even droughts. Dry conditions also prevail in Hawaii, parts of Africa, and northeastern Brazil and Colombia. Lower pressures develop over the central and eastern Pacific, along the west coast of South America, parts of South America near Uruguay and southern parts of the United States in winter, often producing heavy rains and flooding. Regions that are typically dry during El Niño events tend to become excessively wet during La Nina events, and vice versa.

The monthly Southern Oscillation Index (SOI) is calculated based on standardized sea level pressure difference between Tahiti (French Polynesia) and Darwin (Australia). A negative value of the SOI associates to a warming of central and eastern tropical Pacific Ocean, the strength of the Pacific trade winds decreasing, and rainfall reduction over eastern and northern Australia. Otherwise, a positive value of the SOI usually follows with stronger Pacific trade winds and a warmer sea surface temperature to the north of Australia.

The correlation between the SOI index and the two SLA time series was determined. The result shows a strong positive correlation of 0.7 between the detrended SLA and SOI time series, as illustrated in Figure 5.21.

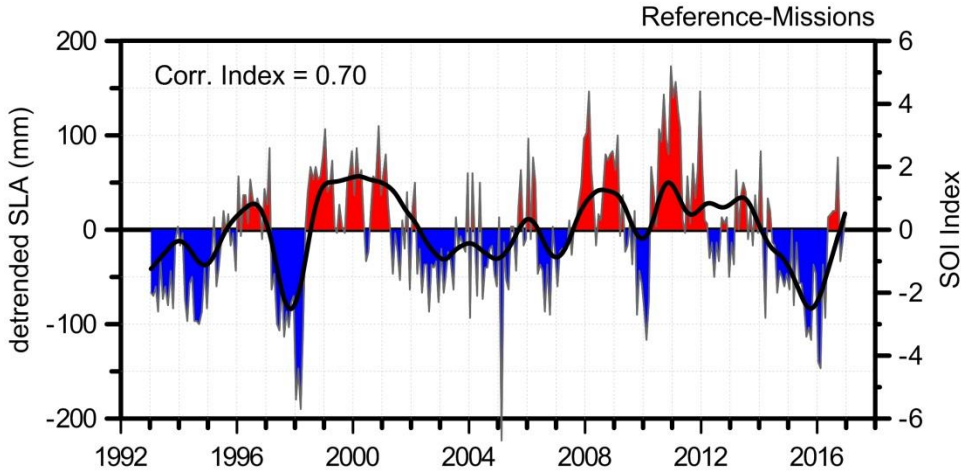

Figure 5.21 Detrended SLA time series for the Indonesian seas (black curve) and Southern Oscillation Index (SOI): El Niño (red) and La Niña (blue) for reference-missions.

CHAPTER 6

CONCLUSIONS AND FUTURE WORK

6.1. Conclusions

The study of the sea level in the Indonesian region by improving satellite altimeter datasets in the coastal region, with particular emphasis on the wet tropospheric correction, and the estimation of the sea level variation using the improved datasets were performed in this thesis. The datasets from the several altimeter missions (TOPEX/Poseidon, Jason-1, Jason-2, ERS-1, ERS-2, Envisat, Cryosat-2 and SARAL) were extracted from the Radar Altimeter Database system (RADS), except the GNSS-derived Path Delay Plus (GPD+) wet tropospheric correction that has been provided by the University of Porto, and span a period of 24 years (1993 – 2016).

The main conclusions of this work are presented in this subsection.

Considering the unique characteristics of the Indonesian region, the main problems and challenges associated with the use of satellite altimetry for sea level studies in such a region have been analyzed. The main errors correlated with coastal altimetry studies are those in the retrieved altimeter range when approaching the coast, requiring dedicated retracking and those in the range and geophysical corrections, namely on the wet tropospheric correction, ocean tides and sea state bias.

The focus of this thesis was on the improvement of the wet tropospheric correction. For that purpose, a set of zenith wet delays has been derived at a local network of GNSS stations using the GIPSY-OASIS software and state-of art methodologies. These ZWD have subsequently been use to derive an improved GPD+ wet tropospheric correction for the Indonesian region.

Three sets of wet tropospheric corrections, from the on-board microwave radiometer, ERA Interim and GPD+, were evaluated for this region. The assessment of the various wet tropospheric correction was performed using SLA variance analysis: along-track analysis (spatial pattern and function of distance from the coast) and crossover analysis. The result indicates that GPD-derived wet tropospheric correction is an improved correction with

respect to the wet tropospheric correction derived from the on-board microwave radiometer and the ERA Interim atmospheric model for all missions, not only near the coast but also in open-ocean.

In addition to the WTC, using SLA variance analysis, the best set of corrections and mean sea surface models to use in the calculation of the sea level anomaly for the study region was identified and SLA datasets using the selected corrections were generated for all missions. The study concerning the selection of the best set of range and geophysical corrections for the three reference missions is described in detail by Handoko et al. (2017).

Moreover, by using the altimeter 1 Hz ranges extracted from RADS, the use of the best altimeter datasets has been ensured, as far as standard (i.e. no retracked) products are concerned.

Using the selected range and geophysical corrections and mean sea surface models, the sea level trend (linear trend and spatial pattern) has been estimated as 4.7 ± 0.2 mm/year, both for the reference-missions and for multi-altimeter missions. If Glacial Isostatic Adjustment (GIA) (0.3 mm/year) is applied, sea level trend is 5.0 mm/year. The rate of sea level rise in this region, derived from altimeter missions over 24 years is higher than the global mean sea level rate about 3.1–3.4 mm/year. The sea level in this region is very sensitive to the time span used in the analysis due to the strong inter-annual signal.

The variability of sea level around the Indonesia seas is high mainly due to the effect of ENSO event. The ENSO effect on the sea level around the Indonesian seas was shown by the correlation between detrended SLA and ENSO indices, strong negative correlation (-0.84) with the Multivariate ENSO Index (MEI) and (-0.85) with the Ocean Niño Index (ONI). However, a strong positive correlation (0.7) with the Southern Oscillation Index (SOI) has been obtained.

6.2. Future Work

In this study, the sea level rate in the Indonesian region has been obtained only from satellite altimetry data. Regarding the improvement of coastal altimetry data, this study shows that much improvement could be obtained if a local ocean tide model was available for this region (Handoko et al., 2017). Moreover, better results could also be obtained if improved retracked data in the coastal regions from algorithms such as ALES (Passaro et al., 2014) become available for all missions.

Complementary and relevant information on sea level variation can be derived from tide gauge data. However, due to the instability of the region, tide gauge measurements are often not reliable. Moreover, when analyzing tide gauge data, the vertical movement caused by tectonic and volcanic activities, as well as anthropogenic subsidence, directly affects the tide gauge measurements. GNSS-derived vertical velocities are thus needed to correct the tide gauge-derived relative sea level trend.

For the future work, due to the high seismic activity around Indonesia, the analysis of altimetry, tide gauge measurements and information of vertical motion can be expected to better characterize the actual sea level change in the Indonesian region, particularly at coastal areas. However, due to the instability of the region, poor quality of most tide gauge data and the lack of permanent GNSS stations, a series of problems can be anticipated making this a difficult and challenging task.

REFERENCES

Abidin, H. Z., Andreas, H., Gumilar, I. and Wibowo, I. R. R. (2015) 'On correlation between urban development, land subsidence and flooding phenomena in Jakarta', *Proceedings of the International Association of Hydrological Sciences*, 370, pp. 15-20.

Ablain, M., Cazenave, A., Valladeau, G. and Guinehut, S. (2009) 'A new assessment of the error budget of global mean sea level rate estimated by satellite altimetry over 1993–2008', *Ocean Science*, 5, pp. 193-201.

Ablain, M., Cazenave, A., Larnicol, G., Balmaseda, M., Cipollini, P., Faugère, Y., Fernandes, M. J., Henry, O., Johannessen, J. A., Knudsen, P., Andersen, O., Legeais, J., Meyssignac, B., Picot, N., Roca, M., Rudenko, S., Scharffenberg, M. G., Stammer, D., Timms, G. and Benveniste, J. (2015) 'Improved sea level record over the satellite altimetry era (1993–2010) from the Climate Change Initiative project', *Ocean Science*, 11(1), pp. 67-82.

Ablain, M., Legeais, J. F., Prandi, P., Marcos, M., Fenoglio-Marc, L., Dieng, H. B., Benveniste, J. and Cazenave, A. (2016) 'Satellite Altimetry-Based Sea Level at Global and Regional Scales', *Surveys in Geophysics*, 38(1), pp. 7-31.

Andersen, O. B. and Knudsen, P. (1998) 'Global marine gravity field from the ERS-1 and Geosat geodetic mission altimetry', *Journal of Geophysical Research: Oceans*, 103(C4), pp. 8129-8137.

Andersen, O. B. and Knudsen, P. (2009) 'DNSC08 mean sea surface and mean dynamic topography models', *Journal of Geophysical Research*, 114(C11).

Andersen, O. B. and Scharroo, R. (2011) 'Range and Geophysical Corrections in Coastal Regions: And Implications for Mean Sea Surface Determination', in Vignudelli, S., Kostianoy, A.G., Cipollini, P. and Benveniste, J. (eds.) *Coastal Altimetry*. Berlin Heidelberg: Springer-Verlag, pp. 103-145.

Andersen, O. B. and Cheng, Y. (2013) 'Long term changes of altimeter range and geophysical corrections at altimetry calibration sites', *Advances in Space Research*, 51(8), pp. 1468-1477.

Andersen, O., Knudsen, P. and Stenseng, L. (2015) 'The DTU13 MSS (Mean Sea Surface) and MDT (Mean Dynamic Topography) from 20 Years of Satellite Altimetry', *International Association of Geodesy Symposia International Association of Geodesy Symposia*. Switzerland: Springer International Publishing.

Andersen, O. B., Stenseng, L., Piccioni, G. and Knudsen, P. (2016) 'The DTU15 MSS (Mean Sea Surface) and DTU15LAT (Lowest Astronomical Tide) reference surface - DTU Orbit'. *ESA Living Planet Symposium 2016*, Prague, Czech Republic.

Andral, A., Bronner, E., Dejus, M., Srinivasan, M. and Peterson, C. (2015) 'Report of 1st SWOT Applications User Workshop'. La Jolla Beach and Tennis Club, La Jolla California: CNES - France and JPL - NASA.

Barnston, A. G., Chelliah, M. and Goldenberg, S. B. (1997) 'Documentation of a Highly ENSO-Related SST Region in the Equator Pacific', *Atmosphere-Ocean* 35 (3), pp. 367-383.

Bennartz, R. (1999) 'On the Use of SSM/I Measurements in Coastal Regions', *Jounal of Atmospheric and Oceanic Technology,* 16, pp. 417-431.

Bertiger, W., Desai, S. D., Dorsey, A., Haines, B. J., Harvey, N., Kuang, D., Sibthorpe, A. and Weiss, J. P. (2010) 'Sub-Centimeter Precision Orbit Determination with GPS for Ocean Altimetry', *Marine Geodesy,* 33(sup1), pp. 363-378.

Bevis, M., Businger, S., Chiswell, S., Herring, T. A., Anthes, R. A., Rocken, C. and Ware, R. H. (1994) 'GPS Meteorology: Mapping Zenith Wet Delays onto Precipitable Water', *Jounal of Applied Meteorology,* 33, pp. 379-386.

Biancamaria, S., Lettenmaier, D. P. and Pavelsky, T. M. (2015) 'The SWOT Mission and Its Capabilities for Land Hydrology', *Surveys in Geophysics,* 37(2), pp. 307-337.

Bilitza, D. (1990) *International Reference Ionosphere 1990.* Natl. Space Sci. Data Center, Lanham, Md.

Bilitza, D. and Reinisch, B. W. (2008) 'International Reference Ionosphere 2007: Improvements and new parameters', *Advances in Space Research,* 42(4), pp. 599-609.

Boehm, J. and Schuh (2004) 'Vienna mapping functions in VLBI analyses', *Geophysical Research Letters*, 31(1).

Boehm, J., Werl, B. and Schuh, H. (2006) 'Troposphere mapping functions for GPS and very long baseline interferometry from European Centre for Medium-Range Weather Forecasts operational analysis data', *Journal of Geophysical Research: Solid Earth,* 111(B2).

Bosch, W., Dettmering, D. and Schwatke, C. (2014) 'Multi-Mission Cross-Calibration of Satellite Altimeters: Constructing a Long-Term Data Record for Global and Regional Sea Level Change Studies', *Remote Sensing,* 6(3), pp. 2255-2281.

Bosser, P., Bock, O., Pelon, J. and Thom, C. (2007) 'An Improved Mean-Gravity Model for GPS Hydrostatic Delay Calibration', *IEEE Geoscience and Remote Sensing Letters,* 4(1), pp. 3-7.

Bronner, E., Guillot, A. and Picot, N. (2013) *SARAL / AltiKa Products Handbook.* Issue 2 Rev 4 edn.: CNES and ISRO.

Brown, G. S. (1977) 'The average impulse response of a rough surface and its applications', *IEEE Transactions on Antennas and Propagation,* AP-25(1), pp. 67-74.

Brown, S. (2010) 'A Novel Near-Land Radiometer Wet Path-Delay Retrieval Algorithm: Application to the Jason-2/OSTM Advanced Microwave Radiometer', *IEEE Transactions on Geoscience and Remote Sensing,* 48(4), pp. 1986-1992.

Byun, S. H. and Bar-Sever, Y. E. (2009) 'A new type of troposphere zenith path delay product of the international GNSS service', *Journal of Geodesy,* 83(3-4), pp. 1-7.

Caplan, P., Derber, J., Gemmill, W., Hong, S. Y., Pan, H. L. and Parrish, D. (1997) 'Changes to the 1995 NCEP Operational Medium-Range Forecast Model Analysis–Forecast System', *Weather and Forecasting,* 12, pp. 581–594.

Carrère, L. and Lyard, F. (2003) 'Modeling the barotropic response of the global ocean to atmospheric wind and pressure forcing - comparisons with observations', *Geophysical Research Letters,* 30(6).

Carrère, L., Lyard, F., Cancet, M., Guillot, A. and Roblou, L. (2012) 'FES 2012: A New Global Tidal Model Taking Advantage of Nearly 20 Years of Altimetry'. *the 20 years of progress in Radar Altimetry,* Venice, Italy, 24-29 September 2012.

Cazenave, A. and Nerem, R. S. (2004) 'Present-day sea level change: Observations and causes', *Reviews of Geophysics,* 42(3).

Cazenave, A. (2005) 'Global Change: Sea Level and Volcanos', *Nature*, 438, pp. 35-36.

Cazenave, A., Dominh, K., Guinehut, S., Berthier, E., Llovel, W., Ramillien, G., Ablain, M. and Larnicol, G. (2009) 'Sea level budget over 2003–2008: A reevaluation from GRACE space gravimetry, satellite altimetry and Argo', *Global and Planetary Change*, 65(1-2), pp. 83-88.

Cazenave, A. and Llovel, W. (2010) 'Contemporary sea level rise', *Ann Rev Mar Sci*, 2, pp. 145-73.

Cazenave, A., Henry, O., Munier, S., Delcroix, T., Gordon, A. L., Meyssignac, B., Llovel, W., Palanisamy, H. and Becker, M. (2012) 'Estimating ENSO Influence on the Global Mean Sea Level, 1993–2010', *Marine Geodesy*, 35(sup1), pp. 82-97.

Cazenave, A., Dieng, H.-B., Meyssignac, B., von Schuckmann, K., Decharme, B. and Berthier, E. (2014) 'The rate of sea-level rise', *Nature Climate Change*, 4(5), pp. 358-361.

Chambers, D. P., Hayes, S. A., Ries, J. C. and Urban, T. J. (2003) 'New TOPEX sea state bias models and their effect on global mean sea level', *Journal of Geophysical Research*, 108(C10).

Chang, Y.-T., Du, L., Zhang, S.-W. and Huang, P.-F. (2013) 'Sea level variations in the tropical Pacific Ocean during two types of recent El Niño events', *Global and Planetary Change*, 108, pp. 119-127.

Chelton, D. B., Ries, J. C., Haines, B. J., Fu, L. L. and Callahan, P. S. (2001) 'Satellite Altimetry', in Fu, L.L. and Cazenave, A. (eds.) *Satellite Altimetry and Earth Sciences: A Handbook of Techniques and Applications*. San Diego: Academic Press, pp. 1-132.

Church, J. A., White, N. J. and Arblaster, J. M. (2005) 'Significant decadal-scale impact of volcanic eruptions on sea level and ocean heat content', *Nature*, 438(7064), pp. 74-7.

Church, J. A. and White, N. J. (2006) 'A 20th century acceleration in global sea-level rise', *Geophysical Research Letters*, 33(1).

Church, J. A., Roemmich, D., Domingues, C. M., Willis, J. K., White, N. J., Gilson, J. E., Stammer, D., Köhl, A., Chambers, D. P., Landerer, F. W., Marotzke, J., Gregory, J. M., Suzuki, T., Cazenave, A. and Le Traon, P.-Y. (2010) 'Ocean Temperature and Salinity Contributions to Global and Regional Sea - Level Change', in Church, J.A.,

Woodworth, P.L., Aarup, T. and Wilson, W.S. (eds.) *Understanding Sea-Level Rise and Variability*. West Sussex, UK: John Wiley and Sons, pp. 143-176.

Church, J. A. and White, N. J. (2011) 'Sea-Level Rise from the Late 19th to the Early 21st Century', *Surveys in Geophysics*, 32(4-5), pp. 585-602.

Church, J. A., Clark, P. U., Cazenave, A., Gregory, J. M., Jevrejeva, S., Levermann, A., Merrifield, M. A., Milne, G. A., Nerem, R. S., Nunn, P. D., Payne, A. J., Pfeffer, W. T., Stammer, D. and Unnikrishnan, A. S. (2013) 'Sea Level Change', in Stocker, T.F., D. Qin, G.-K. Plattner, M. Tignor, S.K. Allen, J. Boschung, A. Nauels, Y. Xia, V. Bex and P.M. Midgley (ed.) *Climate Change 2013: The Physical Science Basis. Contribution of Working Group I to the Fifth Assessment Report of the Intergovernmental Panel on Climate Change*. Cambridge, United Kingdom and New York, NY, USA: Cambridge University Press, pp. 1137-1216.

Cipollini, P., Benveniste, J., Bouffard, J., Emery, W., Fenoglio-Marc, L., Gommenginger, C. P., Griffin, D., Hoyer, J., Kurapov, A., Madsen, K., Mercier, F., Miller, L., Pascual, A., Ravichandran, M., Shillington, F., Snaith, H. M., Strub, P. T., Vandemark, D., Vignudelli, S., Wilkin, J., Woodworth, P. L. and Zavala-Garay, J. (2010) 'the Role of the altimetry in Coastal Observing systems '. *Proceedings of OceanObs'09: Sustained Ocean Observations and Information for Society*, Venice, Italy: ESA Publication WPP-306.

Cipollini, P., Scarrott, R. and Snaith, H. M. (2013) *Product Data Handbook: Coastal Altimetry*.

Cipollini, P., Benveniste, J., Birol, F., Fernandes, M. J., Obligis, E., Passaro, M., Strub, P. T., Valladeau, G., Vignudelli, S. and Wilkin, J. (2017) 'Satellite altimetry in coastal regions', in Stammer, D. and Cazenave, A. (eds.) *Satellite Altimetry Over Oceans and Land Surfaces*: CRC Press.

Cleveland, R. B., Cleeland, W. S., McRae, J. E. and Terpenning, I. (1990) 'STL: a Seasonal-Trend Decomposition Procedur Base on Loess', *Journal of Official Statistics*, 6(1), pp. 3-73.

Cotton, D., Martin-Puig, C., Gommenginger, C., Cipollini, P., Berry, P., Dinardo, S., Stenseng, L. and Benveniste, J. (2010) 'The SAMOSA Project: Development of SAR Altimetry studies over oceans, coastal zones and inland water'. *ESA Living Planet Symposium 2010*, Bergen, Norway.

Dach, R., Hugentobler, U., Fridez, P. and Meindl, M. (2007) *Bernese GPS software - version 5.0.* Astronomical Institute, University of Bern.

Dahuri, R., Rais, J., Ginting, S. P. and Sitepu, M. J. (2008) *Pengelolaan Sumber Daya Pesisir dan Lautan secara Terpadu.* 1 edn. Jakarta: Balai Pustaka.

Davis, J. L., Herring, T. A., Shapiro, I. I., Rogers, A. E. E. and Elgered, G. (1985) 'Geodesy by radio interferometry: Effects of atmospheric modeling errors on estimates of baseline length', *Radio Science*, 20(6), pp. 1593-1607.

Dee, D. P., Uppala, S. M., Simmons, A. J., Berrisford, P., Poli, P., Kobayashi, S., Andrae, U., Balmaseda, M. A., Balsamo, G., Bauer, P., Bechtold, P., Beljaars, A. C. M., van de Berg, L., Bidlot, J., Bormann, N., Delsol, C., Dragani, R., Fuentes, M., Geer, A. J., Haimberger, L., Healy, S. B., Hersbach, H., Hólm, E. V., Isaksen, L., Kållberg, P., Köhler, M., Matricardi, M., McNally, A. P., Monge-Sanz, B. M., Morcrette, J. J., Park, B. K., Peubey, C., de Rosnay, P., Tavolato, C., Thépaut, J. N. and Vitart, F. (2011) 'The ERA-Interim reanalysis: configuration and performance of the data assimilation system', *Quarterly Journal of the Royal Meteorological Society*, 137(656), pp. 553-597.

Desai, S. D. (2002) 'Observing the pole tide with satellite altimetry', *Journal of Geophysical Research*, 107(C11).

Desai, S. D. and Haines, B. J. (2004) 'Monitoring Measurements from the Jason-1 Microwave Radiometer and Independent Validation with GPS', *Marine Geodesy*, 27(1-2), pp. 221-240.

Desportes, C., Obligis, E. and Eymard, L. (2007) 'On the Wet Tropospheric Correction for Altimetry in Coastal Regions', *IEEE Transactions on Geoscience and Remote Sensing*, 45(7), pp. 2139-2149.

Domingues, C. M., Church, J. A., White, N. J., Gleckler, P. J., Wijffels, S. E., Barker, P. M. and Dunn, J. R. (2008) 'Improved estimates of upper-ocean warming and multi-decadal sea-level rise', *Nature*, 453(7198), pp. 1090-3.

Douglas, B. C. (1991) 'Global sea level rise', *Journal of Geophysical Research*, 96(C4), pp. 6981.

Durack, P. (2015) 'Ocean Salinity and the Global Water Cycle', *Oceanography*, 28(1), pp. 20-31.

Durack, P. J., Wijffels, S. E. and Gleckler, P. J. (2014) 'Long-term sea-level change revisited: the role of salinity', *Environmental Research Letters,* 9(11), pp. 114017.

Edwards, S., Moore, P. and King, M. (2004) 'Assessment of the Jason-1 and TOPEX/Poseidon Microwave Radiometer Performance Using GPS from Offshore Sites in the North Sea', *Marine Geodesy,* 27(3-4), pp. 717-727.

England, M. H. and Huang, F. (2005) 'On the Interannual Variability of the Indonesian Throughflow and Its Linkage with ENSO', *Journal of Climate,* 18, pp. 1435-1444.

ESA (2012) *CryoSat Product Handbook.* ESRIN-ESA and Mullard Space Science Laboratory – University College London.

Essen, L. and Froome, K. D. (1951) 'The Refractive Indices and Dielectric Constants of Air and its Principal Constituents at 24,000 Mc/s', *Proceedings of the Physical Society,* Sec. B Vo. 64(10), pp. 862-875.

Essen, L. (1953) 'The Refractive Indices of Water Vapour, Air, Oxygen, Nitrogen, Hydrogen, Deuterium and Helium', *Proceedings of the Physical Society,* Sec. B Vo.66(3), pp. 189-193.

Eymard, L. and Obligis, E. (2006) 'The Altimetric Wet Tropospheric Correction: Progress since the ERS-1 Mission'. *Proceedings of the Symposium on 15 Years of Progress in Radar Altimetry,* Venice, Italy.

Fenoglio-Marc, L., Schöne, T., Illigner, J., Becker, M., Manurung, P. and Khafid (2012) 'Sea Level Change and Vertical Motion from Satellite Altimetry, Tide Gauges and GPS in the Indonesian Region', *Marine Geodesy*, 35(sup1), pp. 137-150.

Fernandes, M. J., Lazaro, C., Nunes, A. L., Pires, N., Bastos, L. and Mendes, V. B. (2010) 'GNSS-Derived Path Delay: An Approach to Compute the Wet Tropospheric Correction for Coastal Altimetry', *IEEE Geoscience and Remote Sensing Letters,* 7(3), pp. 596-600.

Fernandes, M. J., Pires, N., Lázaro, C. and Nunes, A. L. (2013a) 'Tropospheric delays from GNSS for application in coastal altimetry', *Advances in Space Research,* 51(8), pp. 1352-1368.

Fernandes, M., Nunes, A. and Lázaro, C. (2013b) 'Analysis and Inter-Calibration of Wet Path Delay Datasets to Compute the Wet Tropospheric Correction for CryoSat-2 over Ocean', *Remote Sensing,* 5(10), pp. 4977-5005.

Fernandes, M., Lázaro, C., Nunes, A. and Scharroo, R. (2014) 'Atmospheric Corrections for Altimetry Studies over Inland Water', *Remote Sensing*, 6(6), pp. 4952-4997.

Fernandes, M. J., Lázaro, C., Ablain, M. and Pires, N. (2015) 'Improved wet path delays for all ESA and reference altimetric missions', *Remote Sensing of Environment*, 169, pp. 50-74.

Fernandes, M. and Lázaro, C. (2016) 'GPD+ Wet Tropospheric Corrections for CryoSat-2 and GFO Altimetry Missions', *Remote Sensing*, 8(10), pp. 851.

Förste, C., Bruinsma, S. L., Abrikosov, O., Lemoine, J.-M., Schaller, T., Götze, H.-J., Ebbing, J., Marty, J.-C., Flechtner, F., Balmino, G. and Biancale, R. (2014) *EIGEN-6C4: The latest combined global gravity field model including GOCE data up to degree and order 2190 of GFZ Potsdam and GRGS Toulouse. 5th GOCE User Workshop*, Paris, France.

Fu, L.-L., Christensen, E. J., Yamarone, C. A., Lefebvre, M., Ménard, Y., Dorrer, M. and Escudier, P. (1994) 'TOPEX/POSEIDON mission overview', *Journal of Geophysical Research*, 99(C12), pp. 24369.

Fuchs, R., Conran, M. and Louis, E. (2011) 'Climate Change and Asia's Coastal Urban Cities: Can they Meet the Challenge?', *Environment and Urbanization Asia*, 2(1), pp. 13-28.

Gaspar, P., Ogor, F., Le Traon, P.-Y. and Zanife, O.-Z. (1994) 'Estimating the sea state bias of the TOPEX and Poseidon altimeters from crossover differences', *Journal of Geophysical Research*, 99(C12), pp. 24981-24994.

Gommenginger, C. P. and Srokosz, M. A. (2006) 'SEA STATE BIAS – 20 YEARS ON'. *the 15 years of progress in Radar Altimetry*, Venice, Italy, 13-18 March 2006.

Gommenginger, C., Thibaut, P., Fenoglio-Marc, L., Quartly, G., Deng, X., Gómez-Enri, J., Challenor, P. and Gao, Y. (2011) 'Retracking Altimeter Waveforms Near the Coasts', in Vignudelli, S., Kostianoy, A.G., Cipollini, P. and Benveniste, J. (eds.) *Coastal Altimetry*. Berlin Heidelberg: Springer-Verlag, pp. 61-101.

Gordon, A. L., Susanto, D. and Vranesa, K. (2003) 'Cool Indonesian throughflow as a consequence of restricted surface layer flow', *Nature*, 425(6960), pp. 824-8.

Gordon, A. L. (2005) 'Oceanography of the Indonesian Seas and Their Throughflow', *Oceanography*, pp. 14–27.

Gordon, A. L., Huber, B. A., Metzger, E. J., Susanto, R. D., Hurlburt, H. E. and Adi, T. R. (2012) 'South China Sea throughflow impact on the Indonesian throughflow', *Geophysical Research Letters*, 39(11).

Gornitz, V. (2001) 'Impoundment, Groundwater Mining, and Other Hydrologic Transformations: Impacts on Global Sea Level Rise', in Douglas, B.C., Keaney, M.S. and Leatherman, S.R. (eds.) *Sea level Rise:History and Consequences International Geophysics*: Academic Press, pp. 97-119.

Grinsted, A., Moore, J. C. and Jevrejeva, S. (2007) 'Observational evidence for volcanic impact on sea level and the global water cycle', *Proc Natl Acad Sci U S A*, 104(50), pp. 19730-4.

Haines, B. J. and Bar-Sever, Y. E. (1998) 'Monitoring the TOPEX Microwave Radiometer with GPS: Stability of columnar water vapor measurements', *Geophysical Research Letters*, 25(19), pp. 3563-3566.

Handoko, E., Fernandes, M. and Lázaro, C. (2017) 'Assessment of Altimetric Range and Geophysical Corrections and Mean Sea Surface Models—Impacts on Sea Level Variability around the Indonesian Seas', *Remote Sensing*, 9(2), pp. 102.

Hanley, D. E., Bourassa, M. A., O'brien, J. J., Smith, S. R. and Spade, E. R. (2003) 'A Quantitative Evaluation of ENSO Indices', *Jounal of Climate*, 16, pp. 1249-1258.

Herring, T. A., King, R. and McClusky, S. (2006) *GAMIT reference manual - GPS analysis at MIT - Release 10.3.* Dep. of Earth, Atm, and Planetary Sciences, MIT.

Holgate, S. J., Matthews, A., Woodworth, P. L., Rickards, L. J., Tamisiea, M. E., Bradshaw, E., Foden, P. R., Gordon, K. M., Jevrejeva, S. and Pugh, J. (2013) 'New Data Systems and Products at the Permanent Service for Mean Sea Level', *Journal of Coastal Research*, 288, pp. 493-504.

Hopfield, H. S. (1969) 'Two-quartic tropospheric refractivity profile for correcting satellite data', *Journal of Geophysical Research*, 74(18), pp. 4487-4499.

IHO (1953)*: Limits of Oceans and Seas*. Monte Carlo: International Hidrographyc Organization.

Iijima, B. A., Harris, I. L., Ho, C. M., Lindqwister, U. J., Mannucci, A. J., Pi, X., Reyes, M. J., Sparks, L. C. and Wilson, B. D. (1999) 'Automated daily process for global ionospheric total electron content maps and satellite ocean altimeter ionospheric

calibration based on Global Positioning System data', *J. Atmos. Sol. Terr. Phys.*, 61, pp. 1205–1218.

Ishii, M., Kimoto, M., Sakamoto, K. and Iwasaki, S.-I. (2006) 'Steric Sea Level Changes Estimated from Historical Ocean Subsurface Temperature and Salinity Analyses', *Journal of Oceanography,* 62, pp. 155-170.

Ishii, M. and Kimoto, M. (2009) 'Reevaluation of Historical Ocean Heat Content Variations with Time-Varying XBT and MBT Depth Bias Corrections', *Journal of Oceanography,* 65, pp. 287-299.

Jevrejeva, S., Grinsted, A. and Moore, J. C. (2014) 'Upper limit for sea level projections by 2100', *Environmental Research Letters,* 9(10), pp. 104008.

Johnson, G. and Wijffels, S. (2011) 'Ocean Density Change Contributions to Sea Level Rise', *Oceanography,* 24(2), pp. 112-121.

Keihm, S. and Ruf, C. S. (1995) 'Role of Water Vapor Radiometers for In-Flight Calibration of the TOPEX Microwave Radiometer', *Marine Geodesy,* 18, pp. 139-156.

Keihm, S., Janssen, M. A. and Ruf, C. (1995) 'TOPEX/Poseidon Microwave Radiometer (TMR): III. Wet Troposphere Range Correction algorithm and Pre-Launch Error Budget', *IEEE Transactions on Geoscience and Remote Sensing,* 33 No.1.

Keihm, S., Zlotnicki, V. and Ruf, C. (2000) 'TOPEX Microwave Radiometer Performance Evaluation, 1992-1998', *IEEE Transactions on Geoscience and Remote Sensing,* 38 No.3.

Kemp, A. C., Horton, B. P., Donnelly, J. P., Mann, M. E., Vermeer, M. and Rahmstorf, S. (2011) 'Climate related sea-level variations over the past two millennia', *Proc Natl Acad Sci U S A,* 108(27), pp. 11017-22.

Köhnlein, W. (1978) 'Electron density models of the ionosphere', *Reviews of Geophysics,* 16(3), pp. 341–354.

Komjathy, A., Sparks, L., Wilson, B. D. and Mannucci, A. J. (2005) 'Automated daily processing of more than 1000 ground-based GPS receivers for studying intense ionospheric storms', *Radio Science,* 40(6).

Kouba, J. (2008) 'Testing of global pressure/temperature (GPT) model and global mapping function (GMF) in GPS analyses', *Journal of Geodesy,* 83(3-4), pp. 199-208.

Kouba, J. (2009) *A guide to using International GNSS Service (IGS) Products.* Geodetic Survey Division. Natural Resources Canada.

Lambin, J., Morrow, R., Fu, L.-L., Willis, J. K., Bonekamp, H., Lillibridge, J., Perbos, J., Zaouche, G., Vaze, P., Bannoura, W., Parisot, F., Thouvenot, E., Coutin-Faye, S., Lindstrom, E. and Mignogno, M. (2010) 'The OSTM/Jason-2 Mission', *Marine Geodesy,* 33(sup1), pp. 4-25.

Lan, J., Hong, J. and Wang, Y. (2008) 'Relationship of the interannual variability of the Indonesian Throughflow with the IOD over the tropical Indian Ocean', *Theoretical and Applied Climatology,* 97(1-2), pp. 75-79.

Lázaro, C. and Fernandes, M. (2015) 'An Enhanced MWR-Based Wet Tropospheric Correction for Sentinel-3: Inheritance from Past ESA Altimetry Mission'. *Sentinel-3 for Science Workshop,* Venice, Italy.

Le Provost, C., Genco, M. L., Lyard, F., Vincent, P. and Canceil, P. (1994) 'Spectroscopy of the world ocean tides from a finite element hydrodynamic model', *Journal of Geophysical Research,* 99(C12),

Le Traon, P. Y. and Ogor, F. (1998) 'ERS-1/2 orbit improvement using TOPEX/POSEIDON: The 2 cm challenge', *Journal of Geophysical Research: Oceans,* 103(C4), pp. 8045-8057.

Legeais, J. F., Ablain, M. and Thao, S. (2014) 'Evaluation of wet troposphere path delays from atmospheric reanalyses and radiometers and their impact on the altimeter sea level', *Ocean Science,* 10(6), pp. 893-905.

Lemke, P., Ren, J., Alley, R. B., Allison, I., Carrasco, J., Flato, G., Fujii, Y., Kaser, G., Mote, P., Thomas, R. H. and Zhang, T. (2007) 'Observations: Changes in Snow, Ice and Frozen Ground', in Solomon, S., Qin, D., Manning, M., Chen, Z., Marquis, M., Averyt, K.B., Tignor, M. and Miller, H.L. (eds.) *Climate Change 2007: The Physical Science Basis. Contributing of Working Group I to the Fourth Assessment Report of the Intergovernmental Panel on Climate Change*. Cambridge, UK and New York, NY, USA: Cambridge University Press.

Levitus, S., Antonov, J. I., Boyer, T. P. and Stephens, C. (2000) 'Warming of the World Ocean', *Science,* 287, pp. 2225-2229.

Levitus, S. (2005) 'Warming of the world ocean, 1955–2003', *Geophysical Research Letters,* 32(2).

Liu, Q., Huang, R., Wang, D., Xie, Q. and Huang, Q. (2006) 'Interplay between the Indonesian Throughflow and the South China Sea Throughflow', *Chinese Science Bulletin,* 51(S2), pp. 50-58.

Lombard, A., Cazenave, A., Letraon, P. and Ishii, M. (2005) 'Contribution of thermal expansion to present-day sea-level change revisited', *Global and Planetary Change,* 47(1), pp. 1-16.

Macmillan, D. S., Beckley, B. D. and Fang, P. (2004) 'Monitoring the TOPEX and Jason-1 Microwave Radiometers with GPS and VLBI Wet Zenith Path Delays', *Marine Geodesy,* 27(3-4), pp. 703-716.

McGranahan, G., Balk, D. and Anderson, B. (2007) 'The rising tide: assessing the risks of climate change and human settlements in low elevation coastal zones', *Environment and Urbanization,* 19(1), pp. 17-37.

Meehl, G. A., Stocker, T. F., Collins, W. D., Friedlingstein, P., Gaye, A. T., Gregory, J. M., Kitoh, A., Knutti, R., Murphy, J. M., Noda, A., Raper, S. C. B., Watterson, I. G., Weaver, A. J. and Zhao, Z.-C. (2007) 'Global Climate Projections', in Solomon, S., Qin, D., Manning, M., Chen, Z., Marquis, M., Averyt, K.B., Tignor, M. and Miller, H.L. (eds.) *Climate Change 2007: The Physical Science Basis. Contribution of working Group I to the Fourth Assessment Report on the Intergovernmental Panel on Climate Change*. Cambridge, United Kingdom and New York, NY, USA: Cambridge University Press.

Melini, D., Piersanti, A., Spada, G., Soldati, G., Casarotti, E. and Boschi, E. (2004) 'Earthquakes and relative sealevel changes', *Geophysical Research Letters,* 31(9).

Ménard, Y., Fu, L. L., Escudier, P., Parisot, F., Perbos, J., Vincent, P., Desai, S., Haines, B. J. and Kunstmann, G. (2003) 'The Jason-1 Mission', *Marine Geodesy,* 26, pp. 131-146.

Mendes, V. B. (1999) *Modeling the Neutral-Atmospheric Propagation Delay in Radiometric Space Techniques.* Ph.D. dissertation, University of New Brunswick, Fredericton, New Brunswick, Canada.

Mendes, V. B., Prates, G., Santos, L. and Langley, R. B. (2000) 'An Evaluation of the accuracy of models of the determination of the weighted mean temperature of

atmosphere'. *Proceedings of the 2000 National Technical Meeting of The Institute of Navigation*, Anaheim, CA, January 2000, pp.433-438.

Mercier, F., Rosmorduc, V., Carrere, L. and Thibaut, P. (2010) *Coastal and Hydrology Altimetry product (PISTACH) handbook.* AVISO.

Merrifield, M. A., Thompson, P. R. and Lander, M. (2012) 'Multidecadal sea level anomalies and trends in the western tropical Pacific', *Geophysical Research Letters*, 39(13).

Meyssignac, B. and Cazenave, A. (2012) 'Sea level: A review of present-day and recent-past changes and variability', *Journal of Geodynamics*, 58, pp. 96-109.

Miller, M., Buizza, R., Haseler, J. and Hortal, M. (2010) 'Increased resolution in the ECMWF deterministic and ensemble prediction systems', *ECMWF Newsletter No.124 - Summer 2010*, pp. 10-16.

Milne, G. A., Gehrels, W. R., Hughes, C. W. and Tamisiea, M. E. (2009) 'Identifying the causes of sea-level change', *Nature Geoscience*, 2(7), pp. 471-478.

Mitchum, G. T., Nerem, R. S., Merrifield, M. A. and Gehrels, W. R. (2010) 'Modern Sea-Level Change Estimates', in Church, J.A., Woodworth, P.L., Aarup, T. and Wilson, W.S. (eds.) *Understanding Sea-Level Rise and Variability*. West Sussex, UK: John Wiley & Sons, pp. 122-142.

Moss, R. H., Edmonds, J. A., Hibbard, K. A., Manning, M. R., Rose, S. K., van Vuuren, D. P., Carter, T. R., Emori, S., Kainuma, M., Kram, T., Meehl, G. A., Mitchell, J. F., Nakicenovic, N., Riahi, K., Smith, S. J., Stouffer, R. J., Thomson, A. M., Weyant, J. P. and Wilbanks, T. J. (2010) 'The next generation of scenarios for climate change research and assessment', *Nature*, 463(7282), pp. 747-56.

Mourad, A. G., Gopalpillai, S. and Kuhner, M. (1975) *The Significance of the Skylab Altimeter Experiment Results and Potential Applications*, Batelle Columbus Labs. OhioE75-10344).

Nerem, R. S., Chambers, D. P., Choe, C. and Mitchum, G. T. (2010) 'Estimating Mean Sea Level Change from the TOPEX and Jason Altimeter Missions', *Marine Geodesy*, 33(sup1), pp. 435-446.

Nicholls, R. J. (2002) 'Rising Sea Levels: Potential Impacts and Responses', in Hester, R.E. and Harisson, R.M. (eds.) *Global Environmental Change Environmental Science and Technology*. Cambridge, UK: Royal Society of Chemistry, pp. 83-108.

Nicholls, R. J. and Cazenave, A. (2010) 'Sea-level rise and its impact on coastal zones', *Science*, 328(5985), pp. 1517-20.

Nicholls, R. J., Hanson, S. E., Lowe, J. A., Warrick, R. A., Lu, X. and Long, A. J. (2014) 'Sea-level scenarios for evaluating coastal impacts', *Wiley Interdisciplinary Reviews: Climate Change*, 5(1), pp. 129-150.

Niell, A. E. (1996) 'Global mapping functions for the atmosphere delay at radio wavelengths', *Journal of Geophysical Research: Solid Earth*, 101(B2), pp. 3227-3246.

Niell, A., Coster, A. J., Solheim, F. S., Mendes, V. B., Toor, P. C., Langley, R. B. and Upham, C. A. (2001) 'Comparison of Measurements of Atmospheric Wet Delay by Radiosonde, Water Vapor Radiometer, GPS, and VLBI', *Journal of Atmospheric and Ocean Technology*, 18, pp. 830-850.

Obligis, E., Eymard, L., Tran, N., Labroue, S. and Femenias, P. (2006) 'First Three Years of the Microwave Radiometer aboard Envisat: In-Flight Calibration, Processing, and Validation of the Geophysical Products', *Journal of Atmospheric and Oceanic Technology*, 23(6), pp. 802-814.

Obligis, E., Desportes, C., Eymard, L., Fernandes, M. J., Lázaro, C. and Nunes, A. L. (2011) 'Tropospheric Corrections for Coastal Altimetry', in Vignudelli, S., Kostianoy, A.G., Cipollini, P. and Benveniste, J. (eds.) *Coastal Altimetry*. Berlin Heidelberg: Springer-Verlag, pp. 147-176.

Pacione, R., Pace, B., Vedel, H., de Haan, S., Lanotte, R. and Vespe, F. (2011) 'Combination methods of tropospheric time series', *Advances in Space Research*, 47(2), pp. 323-335.

Palmer, M. D., Antonov, J., Barker, P., Bindoff, N., Boyer, T., Carson, M., Domingues, C. M., Gille, S., Gleckler, P., Good, S., Gouretski, V., Guinehut, S., Haines, K., Harrison, D. E., Ishii, M., Johnson, G. C., Levitus, S., Lozier, M. S., Lyman, J. M., Meijers, A., Schuckmann, K. v., Smith, D., Wijffels, S. and Willis, J. (2010) 'Future Observations for Monitoring Global Ocean Heat Content'. *Proceedings of OceanObs'09: Sustained Ocean Observations and Information for Society*, Venice, Italy, 21-25 September 2009: ESA Publication WPP-306.

Passaro, M., Cipollini, P., Vignudelli, S., Quartly, G. D. and Snaith, H. M. (2014) 'ALES: A multi-mission adaptive subwaveform retracker for coastal and open ocean altimetry', *Remote Sensing of Environment*, 145, pp. 173-189.

Passaro, M., Dinardo, S., Quartly, G. D., Snaith, H. M., Benveniste, J., Cipollini, P. and Lucas, B. (2016) 'Cross-calibrating ALES Envisat and CryoSat-2 Delay–Doppler: A coastal altimetry study in the Indonesian Seas', *Advances in Space Research*, 58(3), pp. 289-303.

Pavlis, N. K., Holmes, S. A., Kenyon, S. C. and Factor, J. K. (2012) 'The development and evaluation of the Earth Gravitational Model 2008 (EGM2008)', *Journal of Geophysical Research: Solid Earth*, 117(B4)

Peltier, W. R. and Tushingham, A. M. (1989) 'Global Sea Level Rise and the Greenhouse Effect: Might They Be Connected?', *Science*, pp. 806-810.

Peltier, W. R. (2001) 'Global Glacial Isostatic Adjustment and Modern Instrumental Records of Relative Sea Level History', in Douglas, B.C., Keaney, M.S. and Leatherman, S.R. (eds.) *Sea level Rise:History and Consequences International Geophysics*: Academic Press, pp. 65-95.

Peltier, W. R. (2009) 'Closure of the budget of global sea level rise over the GRACE era: the importance and magnitudes of the required corrections for global glacial isostatic adjustment', *Quaternary Science Reviews*, 28(17-18), pp. 1658-1674.

Picard, B., Frery, M. L., Obligis, E., Eymard, L., Steunou, N. and Picot, N. (2015) 'SARAL/AltiKa Wet Tropospheric Correction: In-Flight Calibration, Retrieval Strategies and Performances', *Marine Geodesy*, 38(sup1), pp. 277-296.

Piccioni, G., Andersen, O. B. and Stenseng, L. (2015) 'SAR Altimetry for Mean Sea Surface Determination in the Arctic DTU15MSS'. *Sentinel-3 for Science Workshop*, Venice, Italy.

Pires, N., Fernandes, M., Gommenginger, C. and Scharroo, R. (2016) 'A Conceptually Simple Modeling Approach for Jason-1 Sea State Bias Correction Based on 3 Parameters Exclusively Derived from Altimetric Information', *Remote Sensing*, 8(7), pp. 576.

Potemra, J. T. and Schneider, N. (2007) 'Interannual variations of the Indonesian throughflow', *Journal of Geophysical Research*, 112(C5).

Ray, C., Martin-Puig, C., Clarizia, M. P., Ruffini, G., Dinardo, S., Gommenginger, C. and Benveniste, J. (2015) 'SAR Altimeter Backscattered Waveform Model', *IEEE Transactions on Geoscience and Remote Sensing*, 53(2), pp. 911-919.

Ray, R. D. (1999) *A Global Ocean Tide Model from TOPEX/Poseidon Altimetry: GOT99.2*. NASA Tech Memo 209478.

Rey, L., Chateau-Thierry, P. d., Phalippou, L., Mavrocordatos, C. and Francis, R. (2001) 'SIRAL, a high spatial resolution radar altimeter for the Cryosat mission'. *Geoscience and Remote Sensing Symposium, 2001. IGARSS '01. IEEE 2001 International*, 2001, 3080-3082 vol.7.

Ricker, R., Hendricks, S., Helm, V. and Gerdes, R. (2015) 'Classification of CryoSat-2 Radar Echoes', in Lohmann, G., Meggers, H., Unnithan, V., Wolf-Gladrow, D., Notholt, J. and Bracher, A. (eds.) *Towards an Interdisciplinary Approach in Earth System Science Springer Earth System Sciences*: Springer International Publishing, pp. 149-158.

Roemmich, D. and Owens, W. B. (2000) 'the Argo Project: Global ocean observations for understanding and prediction of climate variability', *Oceanography*.

Roemmich, D., Johnson, G. C., Riser, S., Davis, R., Gilson, J. E., Owens, W. B., Garzoli, S. L., Schmid, C. and Ignaszewski, M. (2009) 'The Argo program: observing the global ocean with profiling floats', *Oceanography*, pp. 34-43.

Saastamoinen, J. (1972) 'Contributions to the Theory of Atmospheric Refraction', *Bulletin Géodésique*, 105(1), pp. 279-298.

Saji, N. H. and Yamagata, T. (2003) 'Possible impacts of Indian Ocean Dipole mode events on global climate', *Climate Research* 25, pp. 151–169.

Schaeffer, P., Faugére, Y., Legeais, J. F., Ollivier, A., Guinle, T. and Picot, N. (2012) 'The CNES_CLS11 Global Mean Sea Surface Computed from 16 Years of Satellite Altimeter Data', *Marine Geodesy*, 35(sup1), pp. 3-19.

Scharroo, R. (2002) *A Decade of ERS Satellite Orbits and Altimetry*. PhD thesis, Delft University, Delft, Netherlands.

Scharroo, R. and Lillibridge, J. (2004) 'Non-Parametric Sea-state Bias Models and Their Relevance to Sea Level Change Studies'. *Proceedings of the 2004 Envisat & ERS Symposium (ESA SP-572). 6-10 September*, Salzburg, Austria.

Scharroo, R., Lillibridge, J. L., Smith, W. H. F. and Schrama, E. J. O. (2004) 'Cross-Calibration and Long-Term Monitoring of the Microwave Radiometers of ERS, TOPEX, GFO, Jason, and Envisat', *Marine Geodesy*, 27(1-2), pp. 279-297.

Scharroo, R. and Smith, W. H. F. (2010) 'A global positioning system-based climatology for the total electron content in the ionosphere', *Journal of Geophysical Research: Space Physics*, 115(A10).

Scharroo, R. (2012). RADS version 3.1 - User Manual and Format Specification. *In:* NOAA, D. (ed.).

Schmid, R., Steigenberger, P., Gendt, G., Ge, M. and Rothacher, M. (2007) 'Generation of a consistent absolute phase-center correction model for GPS receiver and satellite antennas', *Journal of Geodesy*, 81(12), pp. 781-798.

Shako, R., Förste, C., Abrikosov, O., Bruinsma, S., Marty, J.-C., Lemoine, J.-M., Flechtner, F., Neumayer, H. and Dahle, C. (2014) 'EIGEN-6C: A High-Resolution Global Gravity Combination Model Including GOCE Data', in Münch, U., Stroink, L., Mosbrugger, V. and Wefer, G. (eds.) *Observation of the System Earth from Space - CHAMP, GRACE, GOCE and Future Missions*. Heidelberg, New York , Dordrecht, London: Springer

Sibthorpe, A., Brown, S., Desai, S. D. and Haines, B. J. (2011) 'Calibration and Validation of the Jason-2/OSTM Advanced Microwave Radiometer Using Terrestrial GPS Stations', *Marine Geodesy*, 34(3-4), pp. 420-430.

SL_cci (2016) 'Climate Change Initiative - Sea Level Newsletter', (10).

Snajdrova, K., Boehm, J., Willis, P., Haas, R. and Schuh, H. (2005) 'Multi-technique comparison of tropospheric zenith delays derived during the CONT02 campaign', *Journal of Geodesy*, 79(10-11), pp. 613-623.

Soussi, B., Urien, S., Soulat, F., Muir, A., Roca, M. and Cotton, D. (2011) *ENVISAT ALTIMETRY Level 2 User Manual*. ESA.

Sprintall, J., Gordon, A. L., Koch-Larrouy, A., Lee, T., Potemra, J. T., Pujiana, K. and Wijffels, S. E. (2014) 'The Indonesian seas and their role in the coupled ocean–climate system', *Nature Geoscience*, 7(7), pp. 487-492.

Stanley, H. R. (1979) 'The Geos 3 Project', *Jounal of Geophysical Research*, 84-B8, pp. 3779-3782.

Steunou, N., Picot, N., Sengenes, P., Noubel, J. and Frery, M. L. (2015) 'AltiKa Radiometer: Instrument Description and In–Flight Performance', *Marine Geodesy*, 38(sup1), pp. 43-61.

Strassburg, M. W., Hamlington, B. D., Leben, R. R., Manurung, P., Lumban Gaol, J., Nababan, B., Vignudelli, S. and Kim, K. Y. (2015) 'Sea level trends in Southeast Asian seas', *Climate of the Past*, 11(5), pp. 743-750.

Stum, J., Sicard, P., Carrere, L. and Lambin, J. (2011) 'Using Objective Analysis of Scanning Radiometer Measurements to Compute the Water Vapor Path Delay for Altimetry', *IEEE Transactions on Geoscience and Remote Sensing*, 49(9), pp. 3211-3224.

Tai, C.-K. and Fu, L.-L. (1986) 'On crossover adjustment in satellite altimetry and its oceanographic implications', *Journal of Geophysical Research*, 91(C2), pp. 2549.

Thayer, G. D. (1974) 'An improved equation for the radio refractive index of air', *Radio Science*, 9(10), pp. 803-807.

Townsend, W. F. (1980) 'An initial assessment of the perfomance achieved by the SEASAT altimeter', *IEEE Journal of Oceanic Engineering*, Vol. OE-5 No. 2, pp. 80-92.

Tozuka, T., Qu, T., Masumoto, Y. and Yamagata, T. (2009) 'Impacts of the South China Sea Throughflow on seasonal and interannual variations of the Indonesian Throughflow', *Dynamics of Atmospheres and Oceans*, 47(1-3), pp. 73-85.

Tran, N., Vandemark, D., Chapron, B., Labroue, S., Feng, H., Beckley, B. and Vincent, P. (2006) 'New models for satellite altimeter sea state bias correction developed using global wave model data', *Journal of Geophysical Research*, 111(C9).

Tran, N., Philipps, S., Poisson, J.-C., Urien, S., Bronner, E. and Picot, N. (2012) 'Impact of GDR_D standards on SSB corrections'. *OSTST*, Venice, Italy.

Unal, Y. S. and Ghill, M. (1995) 'Interannual and interdecadal oscillation patterns in sea level', *Climate Dynamics*, 11, pp. 255-278.

van Sebille, E., Sprintall, J., Schwarzkopf, F. U., Gupta, A. S., Santoso, A., England, M. H., Biastoch, A. and Boning, C. W. (2014) 'Pacific-to-Indian Ocean connectivity: Tasman leakage, Indonesian Throughflow, and the role of ENSO', *J. Geophys. Res. Oceans*, 119, pp. 1365–1382.

Vandemark, D., Tran, N., Beckley, B. D., Chapron, B. and Gaspar, P. (2002) 'Direct estimation of sea state impacts on radar altimeter sea level measurements', *Geophysical Research Letters*, 29(24), pp. 1-4

Vermeer, M. and Rahmstorf, S. (2009) 'Global sea level linked to global temperature', *Proc Natl Acad Sci U S A*, 106(51), pp. 21527-32.

Vignudelli, S., Berry, P. and Roblou, L. (2008) 'Satellite altimetry near coasts-current practices and a look at the future', *Submitted to the book*, 15 Years of Progress in Radar Altimetry.

Vignudelli, S., Cipollini, P., Gommenginger, C., Gleason, S., Snaith, H. M., Coelho, H., Fernandes, M. J., Lázaro, C., Nunes, A. L., Gómez-Enri, J., Martin-Puig, C., Woodworth, P., Dinardo, S. and Benveniste, J. (2011) 'Satellite Altimetry: Sailing Closer to the Coast', pp. 217-238.

Wahr, J. (1995) 'Earth Tides', in Ahrens, T.J. (ed.) *Global earth physics: a handbook of physical constants*. Washington, DC: American Geophysical Union.

Wahr, J., Nerem, R. S. and Bettadpur, S. V. (2015) 'The pole tide and its effect on GRACE time-variable gravity measurements: Implications for estimates of surface mass variations', *Journal of Geophysical Research: Solid Earth*, 120(6), pp. 4597-4615.

Wakker, K. F., Naeije, C., Wisse, E., Scharroo, R., Visser, P. N. A. M. and Ambrosius, B. A. C. (1993) 'Geosat and ERS-1 Radar Altimetry Over the North Atlantic', *Journal of Adv. Space Res.*, Vol.13, No.11, pp. 305-314.

Wei, J., Li, M. T., Malanotte-Rizzoli, P., Gordon, A. L. and Wang, D. X. (2016) 'Opposite Variability of Indonesian Throughflow and South China Sea Throughflow in the Sulawesi Sea', *Journal of Physical Oceanography*, 46(10), pp. 3165-3180.

Willis, J. K., Chambers, D. P. and Nerem, R. S. (2008) 'Assessing the globally averaged sea level budget on seasonal to interannual timescales', *Journal of Geophysical Research*, 113(C6).

Wingham, D. J., Francis, C. R., Baker, S., Bouzinac, C., Brockley, D., Cullen, R., de Chateau-Thierry, P., Laxon, S. W., Mallow, U., Mavrocordatos, C., Phalippou, L., Ratier, G., Rey, L., Rostan, F., Viau, P. and Wallis, D. W. (2006) 'CryoSat: A mission to determine the fluctuations in Earth's land and marine ice fields', *Advances in Space Research*, 37(4), pp. 841-871.

Wolter, K. and Timlin, M. S. (1993) 'Monitoring ENSO in COADS with a Seasonally Adjusted Principal Component Index'. *Proc. of the 17th Climate Diagnostics Workshop*, Oklahoma, U.S. of America. Norman, OK: NOAA/NMC/CAC, NSSL, Oklahoma Clim. Survey, CIMMS and the School of Meteor., Univ. of Oklahoma.

Wolter, K. and Timlin, M. S. (2011) 'El Niño/Southern Oscillation behaviour since 1871 as diagnosed in an extended multivariate ENSO index (MEI.ext)', *International Journal of Climatology*, 31(7), pp. 1074-1087.

Wöppelmann, G. and Marcos, M. (2016) 'Vertical land motion as a key to understanding sea level change and variability', *Reviews of Geophysics*, 54(1), pp. 64-92.

Wunsch, C. and Stammer, D. (1997) 'Atmospheric loading and the oceanic "inverted barometer" effect', *Reviews of Geophysics*, 35(1), pp. 79-107.

Yildiz, H., Andersen, O. B., Simav, M., Aktug, B. and Ozdemir, S. (2013) 'Estimates of vertical land motion along the southwestern coasts of Turkey from coastal altimetry and tide gauge data', *Advances in Space Research*, 51(8), pp. 1572-1580.

Zawadzki, L., Ablain, M., Carrere, L., Ray, R. D., Zelensky, N. P., Lyard, F., Guillot, A. and Picot, N. (2016) 'Reduction of the 59-day error signal in the Mean Sea Level derived from TOPEX/Poseidon, Jason-1 and Jason-2 data with the latest FES and GOT ocean tide models', *Ocean Science Discussions*, pp. 1-20.

Zerbini, S., Negusinia, M., Romagnolib, C., Domenichinia, F., Richterc, B. and Simonc, D. (2002) 'Multi-parameter continuous observations to detect ground deformation and to study environmental variability impacts', *Global and Planetary Change*, 34, pp. 37-58.

Zlotnicki, V. and Desai, S. D. (2004) 'Assessment of the Jason Microwave Radiometer's Measurement of Wet Tropospheric Path Delay Using Comparisons to SSM/I and TMI', *Marine Geodesy*, 27(1-2), pp. 241-253.

Zumberge, J. F., Heflin, M. B., Jefferson, D. C., Watkins, M. M. and Webb, F. H. (1997) 'Precise point positioning for the efficient and robust analysis of GPS data from large networks', *Journal of Geophysical Research: Solid Earth*, 102(B3), pp. 5005-5017.

ANNEX

Assessment of Altimetric Range and Geophysical Corrections and Mean Sea Surface Models—Impacts on Sea Level Variability around the Indonesian Seas

Article: Remote Sens. ***2017****, 9, 102; doi:10.3390/rs9020102*

This page is intentionally left blank

remote sensing

MDPI

Article

Assessment of Altimetric Range and Geophysical Corrections and Mean Sea Surface Models—Impacts on Sea Level Variability around the Indonesian Seas

Eko Yuli Handoko [1,2,*], Maria Joana Fernandes [1,3] and Clara Lázaro [1,3]

1 Faculdade de Ciências, Universidade do Porto, 4169-007 Porto, Portugal; mjfernan@fc.up.pt (M.J.F.); clazaro@fc.up.pt (C.L.)
2 Department of Geomatics Engineering, Institut Teknologi Sepuluh Nopember, 60111 Surabaya, Indonesia
3 Centro Interdisciplinar de Investigação Marinha e Ambiental (CIIMAR/CIMAR), Universidade do Porto, 4450-208 Porto, Portugal
* Correspondence: ekoyh@geodesy.its.ac.id

Academic Editors: Raphael M. Kudela, Xiaofeng Li and Prasad S. Thenkabail
Received: 14 October 2016; Accepted: 18 January 2017; Published: 24 January 2017

Abstract: The focus of this study is the assessment of the main range and geophysical corrections needed to derive accurate sea level time series from satellite altimetry in the Indonesia seas, the ultimate aim being the determination of sea level trend for this region. Due to its island nature, this is an area of large complexity for altimetric studies, a true laboratory for coastal altimetry. For this reason, the selection of the best corrections for sea level anomaly estimation from satellite altimetry is of particular relevance in the Indonesian seas. The same happens with the mean sea surface adopted in the sea level anomaly computation due to the large gradients of the mean sea surface in this part of the ocean. This study has been performed using altimetric data from the three reference missions, TOPEX/Poseidon, Jason-1 and Jason-2, extracted from the Radar Altimeter Database System. Analyses of sea level anomaly variance differences, function of distance from the coast and at altimeter crossovers were used to assess the quality of the various corrections and mean sea surface models. The selected set of corrections and mean sea surface have been used to estimate the sea level anomaly time series. The rate of sea level rise for the Indonesian seas was found to be 4.2 ± 0.2 mm/year over the 23-year period (1993–2015).

Keywords: satellite altimetry; geophysical corrections; sea level variability; Indonesian Seas

1. Introduction

As a consequence of climate change, sea level rise can be a serious problem for inhabitants of coastal regions. Sea level rise may cause inundation of low-lying areas, flooding, and salt seawater intrusion into surface water and aquifers [1]. Furthermore, these effects have a significant impact on national socio-economics, infrastructure and environment due to land-loss around coastal areas, where more than 10% of the world's population lives [2].

Since the end of the 19th century, tide gauges have been installed to record sea level variability along coastlines and islands, although in a limited amount and distribution in some regions of the world. Tide gauge measurements in the 20th century (1900 to 2009) indicated that the mean rate of sea level rise was 1.6–1.8 mm·year^{-1} [3,4]. Tide gauge measurements have some limitations due to their density of distribution, local impacts and are particularly affected by vertical land movements such as land subsidence [5,6].

The era of satellite altimetry brought revolution in sea level measurement. In 1992, NASA (National Aeronautics and Space Administration, Washington, DC, USA) and CNES (Centre National

d'Études Spatiales, Paris, France) launched the TOPEX/Poseidon joint mission and later in 2001 the Jason-1 satellite. These were followed by the Jason-2/OSTM (NASA/EUMETSAT (European Organisation for the Exploitation of Meteorological Satellites) in 2008. Being able to measure the entire global sea level up to $\pm 66^{\circ}$ latitudes in 10 days, satellite altimetry provides precise and continuous datasets for sea level studies with global coverage and moderate spatiotemporal resolution.

A satellite altimeter measures the vertical range between the satellite and the sea surface. It emits a short pulse of microwave radiation from the on-board radar antenna towards the sea surface, part of the signal being reflected back to the satellite. By measuring the two-way travel time of the signal, the range can be determined. Thus, the sea surface height (SSH) is obtained by the difference between the satellite height above the known reference ellipsoid and the range of the satellite to the sea surface. In spite of the simple principle of the range measurement from satellite altimetry, the technical challenges to get accurate measurements are substantial. Not only precise satellite orbit determination, but also the precise knowledge of the corrections that affect the range measurement is required. Each of the corrections that must be applied to the measured range for accurate determination of sea surface heights must be known with centimetric accuracy. These include instrument corrections, atmospheric refraction corrections (dry and wet troposphere and ionosphere), sea-state bias and geophysical corrections (geoid, tides and atmospheric pressure loading) [7].

Most satellite radar altimeter missions such as TOPEX/Poseidon, Jason-1, Jason-2, ERS-1 and 2 and Envisat use the pulse-limited mode altimeter or low-resolution mode (LRM). The signal is transmitted from the antenna towards the sea surface point at nadir and its echo is received backwards. The area of the reflecting surface which is illuminated by the altimeter, known as footprint, has a size depending on the satellite altitude, surface slope and roughness, pulse duration and width of the analysis window [7]. The footprint size of an LRM altimeter is usually several kilometres. Unlike conventional radar altimeters, the SAR altimeter mode performs with a higher spatial resolution than LRM. In this mode, the radar footprint is divided into strips of cells (Doppler cells) and the pulse-repetition frequency is increased to allow coherent processing of the echoes along-track. This improves the resolution up to 300 m in the along-track direction [8,9], being an added value to coastal altimetry. For example, CryoSat-2, an altimeter mission with special emphasis on land and marine ice monitoring, carries a Synthetic Interferometric Radar ALtimeter (SIRAL) and is the first SAR altimeter, with an along-track resolution of approximately 250 m [10–12].

Currently, global sea level rise (GSLR) observed by satellite altimetry has been estimated to be about 3.2–3.3 mm/year [13,14]. However, sea level is not rising uniformly across the globe. In some regions sea level is rising rapidly due to non-uniform ocean warming and variation of salinity [15]. Some regions, such as the Western Pacific and Eastern Indian Ocean, have large inter-annual and decadal sea-level variability due to El Niño Southern Oscillation (ENSO) phenomena [16,17]. Sea level variability of the Indonesia seas, enclosed by the Western Pacific Ocean, the Eastern Indian Ocean and the South China Sea (SCS) (Figure 1), has been influenced by ENSO and is higher than the global average. Sea level rise in the Indonesian seas has been measured as 1.7–8 mm/year from 1993 to 2011 based on satellite altimetry [18–20].

As one of the largest archipelagic countries, Indonesia is characterized by its unique geographical and geophysical setting. Indonesia consists of 17,600 islands, 81,000 km coastline and 5.8 million km^2 of sea area. More than 60% of the Indonesian population lives in coastal zones [21]. Due to the unique characteristics of Indonesia, understanding sea level changes in this area is crucial. Considering the potential impacts of sea-level rise in this region, the continuous monitoring of sea level variability becomes urgent.

In order to monitor sea level variability around the Indonesian seas with high precision using satellite altimetry, accurate range and geophysical corrections are required. Sea level anomaly (SLA) estimated with respect to a mean sea surface (MSS) is a common variable used in sea level studies. The determination of SLA from altimeter measurements requires the correction for all instrument, range and geophysical corrections. *SLA* is determined as [7,22]

$$SLA = H - R_{Obs} - \Delta RGeo_{Corrs} - MSS \quad (1)$$

where H is satellite height above a reference ellipsoid, R_{obs} is the range between the sea surface and the spacecraft antenna, which is determined from the travel time of the radar pulse using a ultra-stable oscillator (USO) and the speed of the radar pulse, $\Delta RGeo_{Corrs}$ includes all range and geophysical corrections and MSS is the sea surface height above the same ellipsoid given by a known mean sea surface model. R_{Obs} is the observed range already corrected for all required instrument corrections. $\Delta RGeo_{Corrs}$ refers to the set of range and geophysical corrections: dry and wet tropospheric corrections, ionospheric correction, sea state bias, dynamic atmospheric correction, tides (solid earth, ocean, load and pole) and reference frame offset, as shown in Equation (2) [23].

$$\Delta RGeo_{Corrs} = \Delta R_{dry} + \Delta R_{wet} + \Delta R_{iono} + \Delta R_{SSB} + \Delta R_{DAC} + \Delta R_{tides} + R_{RFO} \quad (2)$$

ΔR_{dry}, ΔR_{wet}, ΔR_{iono} and ΔR_{SSB} are range corrections due to the interaction between the radar signal with the atmosphere and with the sea surface, respectively. ΔR_{DAC} and ΔR_{tides} are corrections related with geophysical phenomena that must be accounted for in order to separate them from the signal of interest. R_{RFO} is the reference frame offset, only required when multi mission data are used.

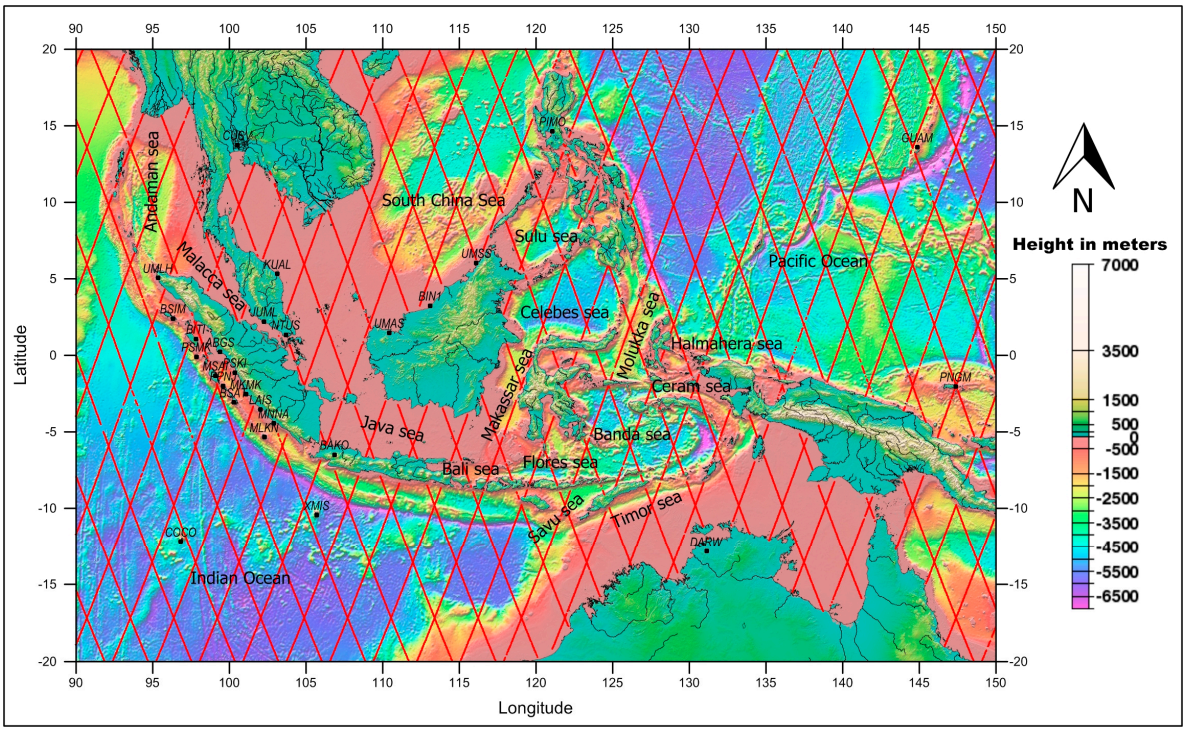

Figure 1. Geographical setting and location of the local GNSS network around the Indonesian seas that was used in this study. Red points indicate Jason-1 tracks for cycle 018 (Credit: Scripps Institution of Oceanography; http://TOPEX.ucsd.edu/marine_topo/).

All corrections must be considered to estimate sea level anomaly. However, particular problems arise when satellite altimetry approaches the coastal zone. The waveform measurements are influenced by the noisier return signals, which are contaminated by land. The less reliable range and geophysical corrections in coastal regions are also important factors contributing to measurement degradation [24]. Several improvements are needed to overcome the specific problems in the coastal areas. Retracking is used to recover altimeter data near the coast. Specific retracking algorithms are expected to give better accuracy than the standard open ocean retrackers. For example, the Adaptive Leading Edge

Subwaveform (ALES) retracker, by [25], is an algorithm to retrack both open and coastal data with the same accuracy. It is a method that can potentially be applied for most missions. The wet tropospheric correction (WTC) derived from the on-board microwave radiometer (MWR) is still a significant uncertainty in coastal regions due to land contamination in the MWR footprint, a circle of 10–50 km diameter depending on the frequency. The use of a coastal-improved path delay algorithm can reduce the WTC error near the coastline up to 1.5 cm, when applied on the Advanced Microwave Radiometer (AMR) of Jason-2 [26]. Another method to improve the WTC in the coastal regions is the Global Navigation Satellite Systems (GNSS) derived Path Delay (GPD) algorithm, which is based on the combination of wet path delays derived from GNSS, valid MWR measurements and tropospheric delays from atmospheric models [27,28]. In addition, local models are also needed to improve global ocean tide models, which in general possess large errors near the coast.

The objectives of this paper are: (i) to assess the accuracy of range and geophysical corrections and mean sea surface models in the Indonesian seas; (ii) to determine sea level variation in this region by selecting the best choice of corrections and models for each mission.

A description of the data and the method of assessment used in this study are described in the next section. The results for the assessment of the various corrections and MSS models using SLA variance analysis are presented in Section 3. Section 3 also describes the sea level variation in the Indonesia region by using the selected set of corrections and MSS models. Section 4 presents the discussion of the results and, finally, the last section summarizes the conclusions of this study.

2. Materials and Methods

The present study focuses on the analysis of sea level variability in the Indonesian seas for the latitude range 20°S–20°N and longitude range 90°E–150°E. The area covers all the Indonesia seas surrounded by the west Pacific Ocean, the eastern Indian Ocean and the South China Sea (see Figure 1).

In order to investigate the performance of the various range and geophysical corrections and mean sea surface models, several datasets have been prepared. Data from the so-called reference altimetric missions (TOPEX/Poseidon, Jason-1 and Jason-2) have been extracted from the Radar Altimeter Database System (RADS), which is developed by Delft Institute for Earth-Oriented Space Research (DEOS) and NOAA Laboratory for Satellite Altimetry [29]. The data cover a period of more than 23 years (1993–2015).

In this study the analysis of SLA variance, derived from different datasets, was used to study the coastal effects of the various corrections applied to altimeter data and assess their quality. The rationale behind this is the assumption that the more accurate is a range or geophysical correction, the smaller is the corresponding SLA variance estimated using that correction.

The analysis of SLA variance is a common technique to assess the quality of the various terms in Equation (1), which affect the final accuracy of the derived SLA. Using "variance" to measure the dispersion of data is common in statistical analysis. Since variance is a quadratic measure, its values are larger than those for example of the standard deviation, making it easier to detect small differences between the analysed data sets. However, variance is very sensitive to noisy or extreme data values and this can only be overcome by using appropriate criteria for removing those values. This approach has been adopted in this study by applying to the SLA values the standard rejection criteria for example for the acceptable maximum and minimum values for the SLA and for the various range and geophysical corrections used in the SLA computation [28].

The comparison and evaluation of the various range and geophysical corrections and mean sea surface models are performed using SLA variance analysis: along-track analysis (spatial pattern and function of distance from the coast) and crossover analysis. SLA datasets are first derived, for each cycle, using the various corrections or MSS under comparison. Then, in the first case, the difference between the variance of each SLA dataset, computed using all along-track points, is estimated for each cycle. The variance of co-located along-track SLA measurements for a given period and using each correction and MSS, is computed in regular latitude $\times$ longitude grids ($4^\circ \times 4^\circ$) intervals (or bins) or

in bins of distance from coast and then the differences considered. In the second case, crossovers are first estimated using each SLA dataset, the SLA variance at crossovers is then computed in regular latitude $\times$ longitude grids ($4^\circ \times 4^\circ$) and subtracted for selected pairs of SLA datasets. It is commonly accepted in the altimeter community that using SSH crossover differences with a maximum time lag of 10 days reduces the impact of ocean variability, mainly capturing differences due to measurement errors [20,28]; therefore, only crossover points with time difference less than 10 days have been considered. The along-track and crossover variance analyses are two complementary diagnostics, helpful in the assessment of the various analysed variables.

In this study, the following geophysical corrections and mean sea surface models (see Table 1) are evaluated to analyse their impact on sea level estimation:

- **Dry troposphere**: The dry tropospheric correction (DTC) can be determined from several sources of surface pressure data, such as in situ surface pressure measurements, a Numerical Weather Model (NWM) and a climatology such as the Global Pressure and Temperature Model (GPT) [30]. In this paper, NWM is used to model the DTC due to the limited number and distribution of in situ surface pressure measurements. The most common sources of NWM are the European Centre for Medium-Range Weather Forecasts (ECMWF) and the National Centers for Environmental Prediction (NCEP). For all missions (TOPEX/Poseidon (TP), Jason-1 (J1) and Jason-2 (J2)) the corrections are those derived from the following atmospheric models: (i) ECMWF Re-Analysis (ERA) Interim [31]; (ii) NCEP [32].
- **Wet troposphere**: the on-board near-nadir-looking microwave radiometer is the best source of information to compute the wet tropospheric correction for altimeter data. The main problem of the MWR-derived WTC in coastal areas is associated with the invalid MWR data measurements due to the large footprint of the instrument that is contaminated by land. Meteorological models are alternative sources to determine the WTC. From these, the ERA-Interim model provides better quality than ECMWF operational model, particularly before 2004 [28,33]. Another WTC source in the coastal zone is the GNSS-derived Path Delay (GPD) corrections provided by the University of Porto. The GPD is an algorithm primarily implemented to estimate an improved WTC in the coastal regions, which combines zenith wet path delay (ZWD) derived from GNSS coastal and island stations, valid onboard microwave radiometer measurements and total column water vapour observations from scanning imaging MWR (SI-MWR) on board remote sensing satellites [27,28,34]. In this paper, the following corrections were used: (i) from the onboard microwave radiometer (MWR); (ii) from the ERA-Interim model; (iii) from the GNSS-derived Path Delay Plus (GPD+) algorithm, the latest GPD version [34].
- **Ionosphere:** the altimeter satellites TOPEX/Poseidon, Jason-1 and Jason-2 operate in two different frequencies (Ku-band: ~13.6 GHz and C-band: ~5.3 GHz) to determine the ionospheric correction. Three ionospheric models are available in RADS: the JPL (Jet Propulsion Laboratory) GIM (Global Ionosphere Map), NIC09 (NOAA Ionosphere Climatology 2009) and IRI (International Reference Ionosphere). The JPL GIM provides the vertical total electron content (TEC) based on the dual-frequency GNSS data. The GIM is available in two-hourly global grids with a spatial resolution of 2.5° in latitude and 5° in longitude [35]. The NIC09 is a climatology based on the JPL GIM for the period 1998–2008 and variation of solar activity; see details in [36]. The IRI model is a climatology mainly based on ionosonde data measurement since the 1930s. The IRI model has a good accuracy for the northern-mid latitudes, but is less accurate for low and high latitudes, due to poor spatial distribution of ionosode stations [37,38]. According to [36,38], JPL GIM and NIC09 are better than IRI model. Therefore, the ionospheric corrections used in this study for all missions are the smoothed dual frequency and JPL-GIM ionospheric corrections. However, for TOPEX/Poseidon, since GIM is only available since cycle 220, NIC2009 was used for all cycles prior to 220 (1–219).
- **Sea State Bias (SSB)**: In this study, two major types of SSB models usually used in altimetric studies were compared: parametric models, based on three or four parameters and non-parametric

models. The SSB correction is commonly estimated as a function of two input parameters: significant wave height and wind speed. In the SBB Tran model [39,40], ocean wave period data are used within a three-input estimator. For TOPEX, the parameter model BM-4 based on [41] and the non-parametric CLS model [42] were applied. The non-parametric CLS and Tran2012 SSB models were applied for Jason-1 and Jason-2.

- **Ocean and Load tides**: Two main models for ocean and load tides are available in RADS: Finite Element Solution (FES) and Global Ocean Tide (GOT) [43] models. The last version of the GOT ocean and load tide models is GOT 4.10, while one of the latest available FES ocean tide model is FES2012 [44]. The GOT 4.10 load tide should be used to complement FES2012 model since tide loading effects have not yet been computed for FES2012. Therefore, in order to assess the ocean and load tide models, the GOT 4.10 (GOT 4.10 ocean and load tides) and FES2012 (FES2012 ocean tide and GOT4.10 load tide) models were used.
- **Mean Sea Surface (MSS)**: A MSS model is needed to compute the SLA. This study used two MSS models: the CNESCLS2011 [45] and one of the latest releases from DTU (DTU13MSS) [46].
- **Other corrections:** In addition to the above mentioned corrections, the following were applied: Dynamic Atmospheric Correction (DAC) [47], solid earth and pole tides and reference frame offset [22].

In this study, all corrections were used as they are made available in RADS, except for GPD+, provided by the University of Porto.

Table 1. Various range and geophysical corrections and mean sea surface models assessed in this study, aiming at determining sea level variability around the Indonesian Seas.

Parameter	TOPEX/Poseidon	Jason-1	Jason-2
Cycles	001–364	001–259	001–280
Dry Troposphere	ERA-Interim & NCEP	ERA-Interim & NCEP	ERA-Interim & NCEP
Wet Troposphere	On-board MWR, ERA-Interim & GPD+	On-board MWR, ERA-Interim & GPD+	On-board MWR, ERA-Interim & GPD+
Ionosphere	Smoothed Dual Frequency & NIC09 (cycles: 1–219), GIM (cycles: 220–364)	Smoothed Dual Frequency & GIM	Smoothed Dual Frequency & GIM
Sea State Bias	Parametric BM4 & Non-parametric: CLS	Non-parametric: CLS & Tran2012	Non-parametric: CLS & Tran2012
Dynamic atmospheric correction (DAC)	MOG2D	MOG2D	MOG2D
Ocean Tide and Loading Tide	FES2012 & GOT4.10	FES2012 & GOT4.10	FES2012 & GOT4.10
Mean Sea Surface	CNESCLS 2011 & DTU2013	CNESCLS 2011 & DTU2013	CNESCLS 2011 & DTU2013

In the computations, weighted SLA (weights are function of the co-sine of latitude) were used. Sea level variability around the Indonesian Seas was analysed by combining the time series from TOPEX/Poseidon, Jason-1 and Jason-2. The inter-satellite SLA altimetric series should be calibrated using data for the periods of the tandem phases between consecutive missions. The tandem cycles for TOPEX/Poseidon and Jason-1 are cycles 343–364 and 001–020 respectively, while for Jason-1 and Jason-2 the corresponding tandem cycles are 240–259 and 001–020 respectively. The relative difference between TP and J1 (J1, TP) was determined by averaging the differences between all corresponding tandem mission cycles. Similarly, the relative difference (J2, J1) was determined by the average of the differences from all tandem cycles between Jason-2 and Jason-1.

$$SLA_{Corrected}(\mathrm{J1}) = SLA(\mathrm{J1}) - bias(\mathrm{J1},\ \mathrm{TP}) \quad (3)$$

$$SLA_{Corrected}(\mathrm{J2}) = SLA(\mathrm{J2}) - bias(\mathrm{J2},\mathrm{J1}) - bias(\mathrm{J1},\ \mathrm{TP}) \quad (4)$$

All missions were linked together by applying the computed relative differences in order to determine the 23-year sea level anomaly time series. In addition, the annual and inter-annual signals were obtained using Seasonal Trend decomposition based on LOESS (STL) [48] and the sea level slope was computed by original least squares (OLS).

3. Results

This section presents the results of the impacts of selected corrections and MSS models on SLA estimation, for TOPEX/Poseidon, Jason-1 and Jason-2 altimetry data around the Indonesian seas. The SLA estimated from various corrections (dry troposphere, wet troposphere, ionosphere, sea state bias, tides (ocean tide and load tide)) and mean sea surface models, were compared.

3.1. Dry Tropospheric Correction

The path of the radar altimetry signal through the atmosphere is delayed by the presence of neutral gasses in the troposphere. This effect is called dry tropospheric correction (DTC). The absolute value of the dry path delay at sea level is around 2.3 m. Although the DTC is the largest range correction in satellite altimetry, it can be modelled from surface pressure measurements at sea level (sea level pressure, SLP). Due to the limited number and distribution of in situ measurements, SLP can be acquired from a NWM, such as the ECMWF or NCEP model. Data are distributed on regular grids at six hourly intervals. ECMWF provides two models: the operational model at $0.125^\circ \times 0.125^\circ$ and ERA-Interim at $0.75^\circ \times 0.75^\circ$, while for NCEP, data are provided in RADS at $2.5^\circ \times 2.5^\circ$.

Recent studies indicate that the dry tropospheric correction is not significantly affected by land [22], but it is influenced by the way the height dependence of the corrections is handled [23]. Several authors reported that the accuracy of DTC in coastal areas is about 0.7 cm for T/P [49], Jason-1 [50] and Jason-2 [51]. Concerning the assessment of the DTC models, SLA variance differences, along-track (Figure 2), function of distance from coast (Figure 3) and at crossovers (Figure 4) between ERA-Interim and NCEP were computed and analysed. Along-track and crossovers SLA variance differences were computed on regular latitude x longitude $4^\circ \times 4^\circ$ grids. In these computations only crossover points with time difference less than 10 days have been considered.

Figure 2 shows the along-track SLA variance differences between two models, ERA-NCEP. It is clear that NCEP DTC is better for TOPEX/Poseidon (shown by yellow to red), but not for Jason-1 and Jason-2 (shown by light to dark blue).

The results in Figure 3 confirm those shown in Figure 2. It shows that NCEP DTC reduces the SLA variance with respect to ERA-Interim model for TOPEX/Poseidon and ERA-Interim DTC reduces the SLA variance with regard to NCEP for Jason-1 and Jason-2. Figure 3 indicates that DTC is unaffected by coastal regions. Figure 4 indicates that the SLA differences at crossovers between ERA-Interim and NCEP are small, mostly negative in open-ocean. This means that DTC from ERA-Interim is better than NCEP in general.

In all cases the variance differences are very small, less than 1 cm^2. Thus, for consistency, the DTC from ERA Interim should be adopted.

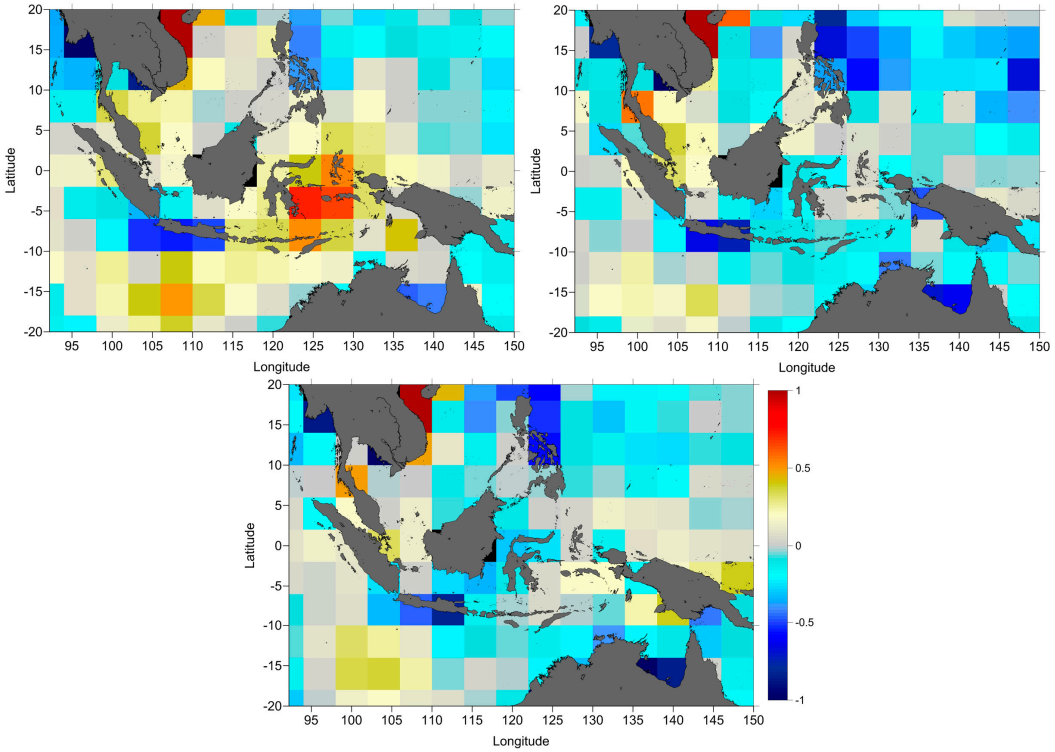

Figure 2. Along-track SLA variance differences (cm^2), ERA − NCEP, for TOPEX/Poseidon cycles 1 to 364 (**top-left**); Jason-1 cycles 1 to 259 (**top-right**) and Jason-2 cycles 1 to 280 (**bottom-middle**).

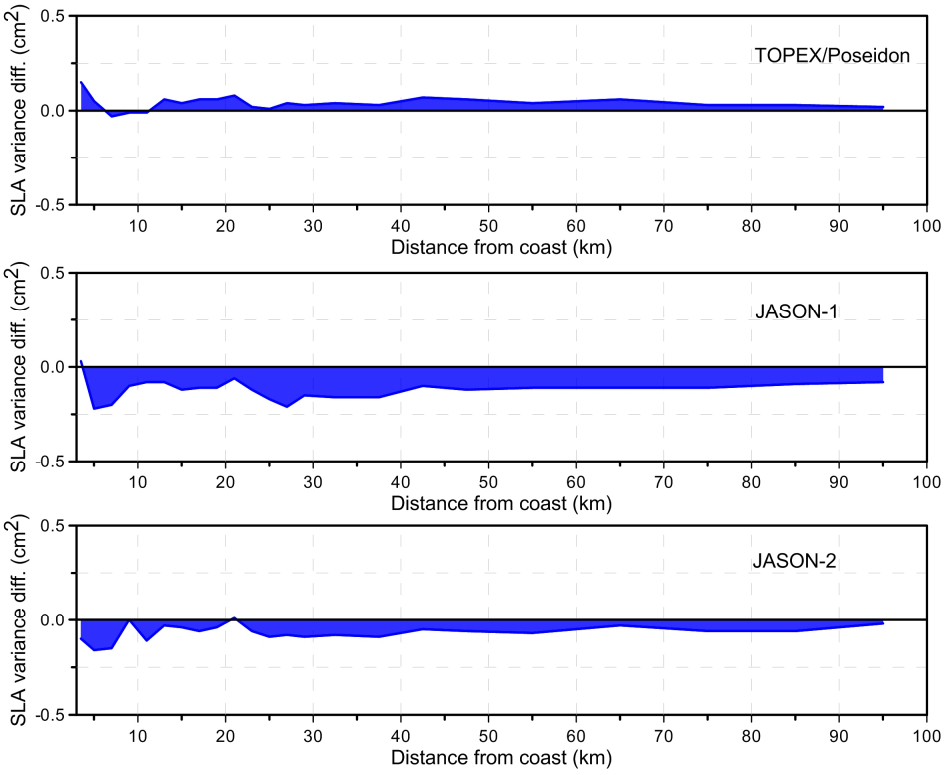

Figure 3. SLA variance differences (cm^2) of DTC (ERA − NCEP), function of the distance from coast: for TOPEX/Poseidon cycles 1 to 364 (**top**), Jason-1 cycles 1 to 259 (**middle**) and Jason-2 cycles 1 to 280 (**bottom**).

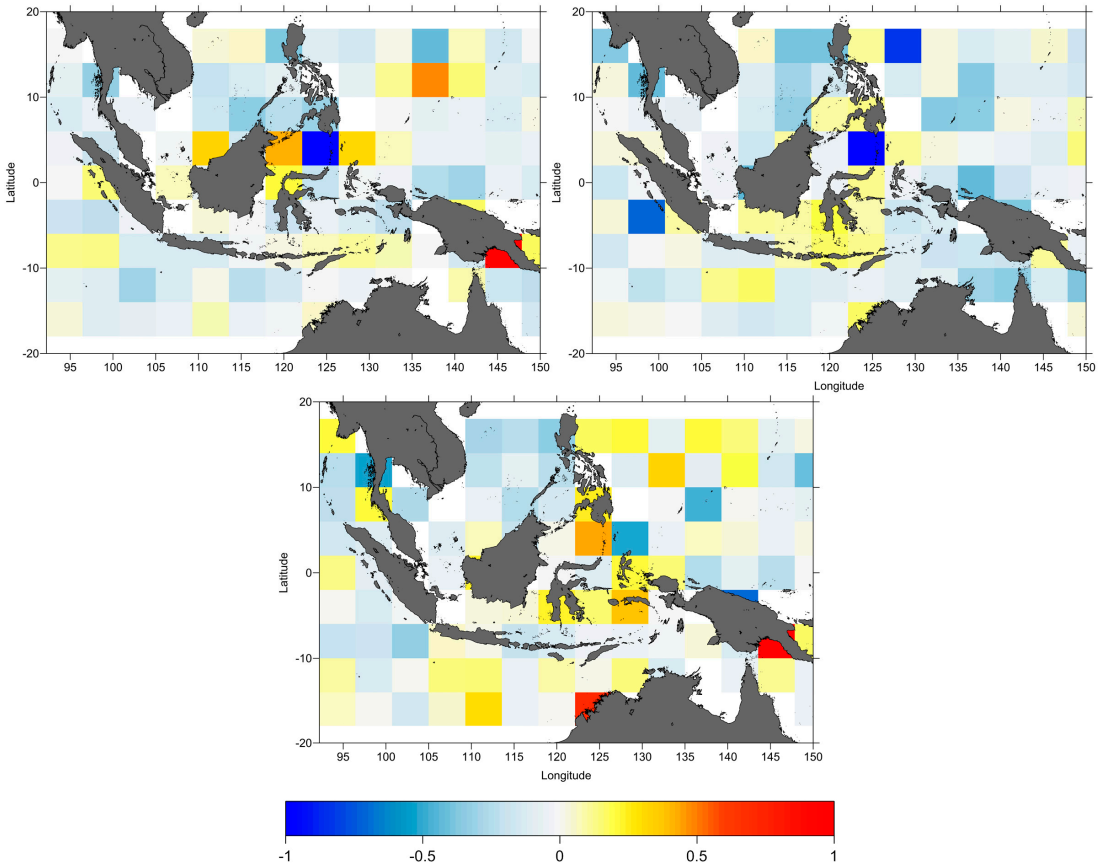

Figure 4. SLA variance differences at crossovers (cm^2), ERA − NCEP, for TOPEX/Poseidon cycles 1 to 364 (**top-left**); Jason-1 cycles 1 to 259 (**top-right**) and Jason-2 cycles 1 to 280 (**bottom-middle**).

3.2. Wet Tropospheric Correction

For the long-term estimation of sea level, it is important to ensure the consistency and stability of altimetry measurements. One factor that causes uncertainty in satellite altimetry is the path delay due to water vapour in the atmosphere; this is called wet tropospheric correction (WTC). Although the absolute value of the WTC is about 50 cm, it has high variability, both in space and time, and thus is not easy to model.

The wet tropospheric correction is computed from onboard microwave radiometers by measuring the brightness temperature (TBs) at two or three frequencies in the range of 18 and 37 GHz, in spectral bands sensitive to water vapour and cloud liquid water. TOPEX/Poseidon carried the three-channel TOPEX Microwave Radiometer (TMR), which operated at 18, 21 and 37 GHz, while for Jason-1 and Jason-2 the Jason-1 Microwave Radiometer (JMR) and the Advanced Microwave Radiometer (AMR) operate at 18.7, 23.8 and 34 GHz, respectively.

The algorithm for the TMR/JMR/AMR performs the retrieval in three steps. First, a term analogous to a surface "radiometer wind" and a term due to cloud liquid water are estimated using a linear combination of the TBs from the 3 channels. Then, a first approximation of the wet path delay is estimated. Finally, the wet path delay is obtained by adding to the cloud liquid water term a term obtained from a log-linear combination of the TBs from the 3 channels, with coefficients depending on the "radiometer wind" and wet path delay class interval obtained in the first two steps [52].

The radiometer instrument drift can cause an error that will affect the long-term sea level estimation. Concerning the reduction of this potential error, a number of authors have investigated the microwave radiometer instrument drifts [53–59].

In the open ocean, WTC can be retrieved within a few cm accuracy using onboard microwave radiometers. However, this does not apply to the coastal regions. The differences between ocean emissivity (around 0.5) and land emissivity (around 0.9) cause the radiometer footprint, as it approaches the coast, to contain portions of surfaces with different emissivity. Therefore, the WTC ocean retrieval algorithm originates invalid measurements in the regions close to the coast or land. The invalid data for TMR and JMR start from about 50 km from the coast; while for AMR on Jason-2 begin around 25 km from land [26,60]. However, the JMR and AMR data present on RADS are already enhanced near the coast [26], thus these effects are expected to be much smaller for these satellites when compared to TOPEX/Poseidon.

As an alternative to the WTC from onboard microwave radiometers, a number of atmospheric models, such as ECMWF and NCEP, which provide data on regular grids, can be used to derive tropospheric path delays. Using ECMWF parameters such as sea level pressure (SLP), surface temperature (2-metre temperature, 2T) and total column water vapour (TCWV), the WTC can be calculated. The model grids of WTC are then used to estimate the WTC at each satellite ground track point by bilinear interpolation in space, followed by a linear interpolation in time. The comparison between the WTC derived from the ECMWF operational and ERA-Interim, performed by [28,61] showed that the use of the ECMWF operational model prior to 2004 is not advisable for altimetry studies. For this reason, the ECMWF operational model is not used in this study, only the ERA-Interim, being the best available model for the whole altimeter era.

To reduce the WTC errors, particularly in coastal regions where the onboard microwave radiometer measurements become invalid due to land contamination in the radiometer footprint, a method to determine the troposphere wet path delays, by space-time objective analysis from the combination of data from various sources, was proposed by the University of Porto (UPorto), Portugal (see details in [27,28]. Global GPD solutions have been derived by UPorto for the main altimetry missions (ERS-1, ERS-2, Envisat, TOPEX/Poseidon (TP), Jason-1 (J1), Jason-2 (J2), CryoSat-2 (CS2) and SARAL/AltiKa (SA)) using more than 800 GNSS stations in coastal and island regions [28]. In particular, a local network of nearly 30 GNSS stations, located mostly along Sumatera Island, has been used to improve the GNSS coverage in the Indonesian region (Figure 1).

To ensure the long-term stability of the WTC, the large set of radiometers used in the estimations of the GPD+, the most recent version of these corrections, have been calibrated with respect to the Special Sensor Microwave Imager (SSM/I) and the SSM/I Sounder (SSM/IS). In addition to the inter-calibration with respect to SSM/I and SSM/IS, the new features of the GPD+ corrections with respect to previous versions include: (i) incorporation of additional datasets from a set of 19 SI-MWR; (ii) new grid of spatial correlation scales; (iii) improved criteria for detecting valid/invalid MWR values; (iv) adoption of ECMWF Operational model for computing the first guess of the most recent missions such as CryoSat-2 and Jason-2; (v) adoption of ERA Interim to compute the first guess for older missions such as TOPEX/Poseidon and Jason-1 [34].

The comparison between the SLA computed using the various WTC, from onboard microwave radiometer (MWR), atmospheric model (ERA-Interim) and GNSS-derived Path Delay Plus (GPD+), was performed. The results are shown as SLA variance differences, spatial pattern of along-track SLA variance differences (Figure 5), function of distance from the coast (Figure 6) and SLA variance differences at crossovers (Figure 7) for all three missions. As before, in these computations only crossover points with time difference less than 10 days have been considered.

Figures 5–7 illustrate the results, showing that overall, the GPD+ significantly reduces the SLA variance both with respect to ERA and to the on-board MWR, particularly for TOPEX/Poseidon and near the coast.

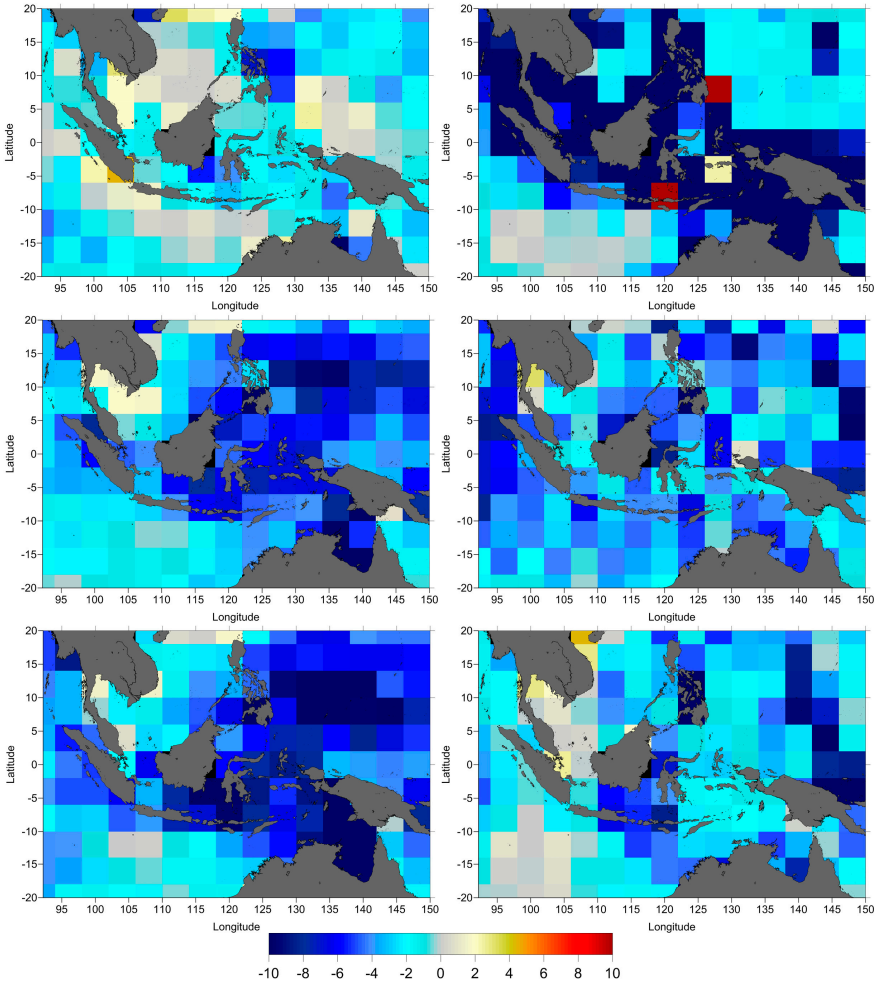

Figure 5. Along-track SLA variance differences (cm^2), GPD+ − ERA (**left**) and GPD+ − MWR (**right**), for TOPEX/Poseidon (**top**) cycles 1 to 364; Jason-1 (**middle**) cycles 1 to 259 and Jason-2 (**bottom**) cycles 1 to 280.

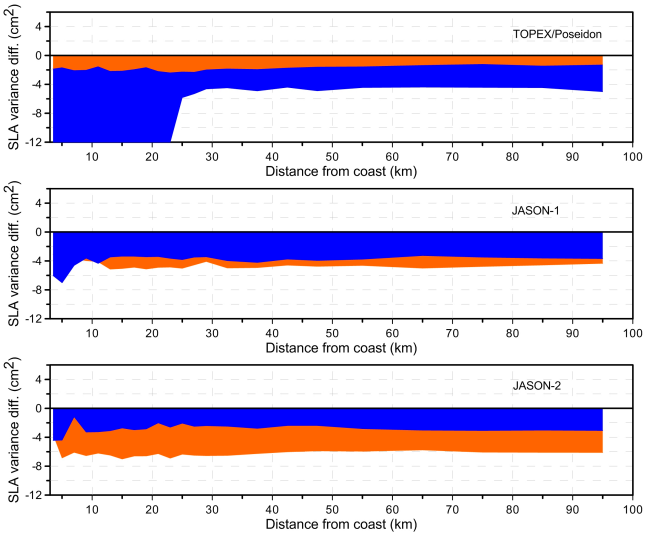

Figure 6. SLA variance differences of WTC, function of distance from coast, GPD+ − ERA (orange) and GPD+ − MWR (blue), for TOPEX/Poseidon cycles 1 to 364, Jason-1 cycles 1 to 259 and Jason-2 cycles 1 to 280.

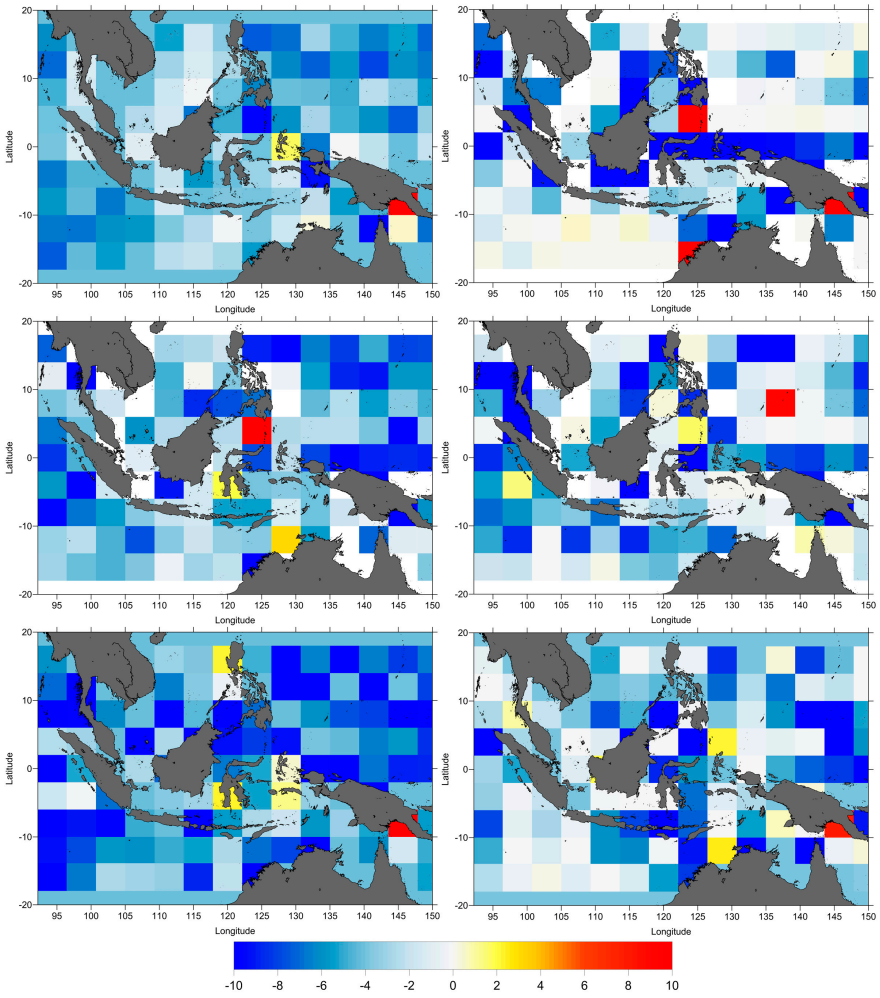

Figure 7. SLA variance differences at crossovers (cm^2), GPD+ − ERA (**left**) and GPD+ − MWR (**right**); for TOPEX/Poseidon (**top**) cycles 1 to 364; Jason-1 (**middle**) cycles 1 to 259 and Jason-2 (**bottom**) cycles 1 to 280.

3.3. Ionospheric Correction

The ionosphere layer contains free electrons and ions that can influence the propagation of electromagnetic waves both in the speed and in the propagation direction of the signal. The velocity of the signal is slowed by the free electrons in the atmosphere. The ionization process is driven by the sun activity, varies in time of the day, the season of the year and geographical position. The ionosphere delay can be determined in terms of total electron content (TEC), which is the integral of the electron density along the signal path. TEC is measured in Total Electron Content Unit (TECU), with 1 TECU equivalent to 10^{16} electrons/m^2. As a dispersive medium, the ionosphere refraction is frequency-dependent. The ionosphere delay can be determined as function of the frequency [22]:

$$\Delta R_{iono} = k \frac{TEC}{f^2} \tag{5}$$

where k is a constant of 0.40250 m·GHz^2/TECU, TEC is the total electron content, f is the frequency in GHz and ΔR_{iono} is given in meters.

Satellite altimetry missions such as TOPEX, Jason-1 and Jason-2 carry dual frequency instruments to provide the ionosphere information. The primary frequency, Ku-band, is operating at 13.6 GHz and the secondary frequency, C-band, is at 5.3 GHz. Using two frequencies it is possible to directly detect

TEC along the satellite track. Due to the fact that the second frequency is less precise than the Ku-band, the differencing dual frequency creates an additional noise in the derived ionospheric correction which needs to be smoothed around 200 km along the track in order to reduce this error [22].

The global ionosphere maps (GIM) of vertical TEC is an observational model based on more than hundred GPS stations from the International GNSS Service (IGS) network. This model, developed by the Jet Propulsion Laboratory (JPL) and the University of Berne, is available in 2-hourly TEC maps and 2.5° in latitude and 5° in longitude spatial resolution [35]. In addition, NIC09 (NOAA Ionosphere Climatology 2009) is a climatology model based on GIM for the period from 1998 to 2008, which can be applied to estimate the ionospheric correction prior to 1998 [36]. In this study, all ionospheric corrections were used as they are made available in RADS.

In order to assess the accuracy of the ionospheric corrections, two sources were compared; the smoothed dual frequency and JPL-GIM for all missions. Since JPL-GIM has only been available since 1998, for TOPEX prior to 1998 (cycles 1 to 219) the smoothed dual-frequency correction was compared with the NIC09 model.

The impact of the ionospheric model in the estimation of the SLA is quantified by plotting the spatial pattern of the along-track SLA variance differences (Figure 8), SLA variance differences function of the distance from coast (Figure 9) and the SLA variance differences at crossovers (Figure 10).

As shown in Figures 8–10, in general, the altimeter SLA performances are significantly improved with the smoothed dual frequency (shown as negative variance differences) apart from some degradation sometimes observed near the coast. Overall, the smoothed dual frequency shows a significant improvement when compared with NIC09 and JPL GIM for TOPEX/Poseidon. However, for Jason-1 and Jason-2 the improvements are not uniform, particularly for Jason-1 (Figure 8). For Jason-2, the improvement of smoothed dual frequency begins at 12 km from coast (Figure 9).

Figure 10 displays the spatial distribution of the crossover SLA variance differences. The negative values (blue) indicate that the SLA performances are improved by the smoothed dual frequency correction but that this improvement is not uniform.

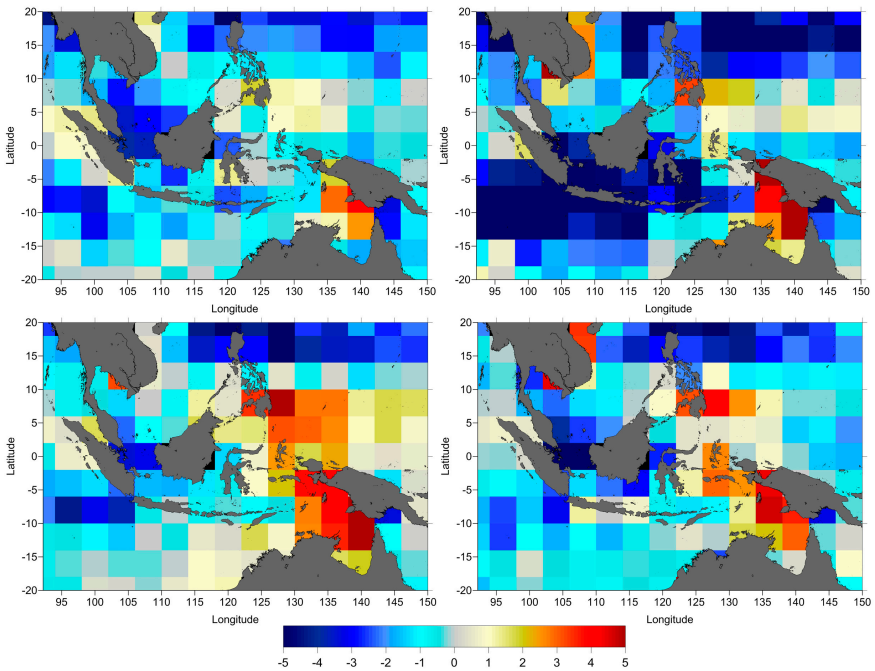

Figure 8. Along-track SLA variance differences (cm^2), between the smoothed dual-frequency and NIC2009 for TOPEX/Poseidon cycles 1–219 (**top left**) and between the smoothed dual-frequency and JPL GIM for TOPEX/Poseidon cycles 220 to 364 (**top right**); Jason-1 cycles 1 to 259 (**bottom left**) and Jason-2 cycles 1 to 280 (**bottom right**).

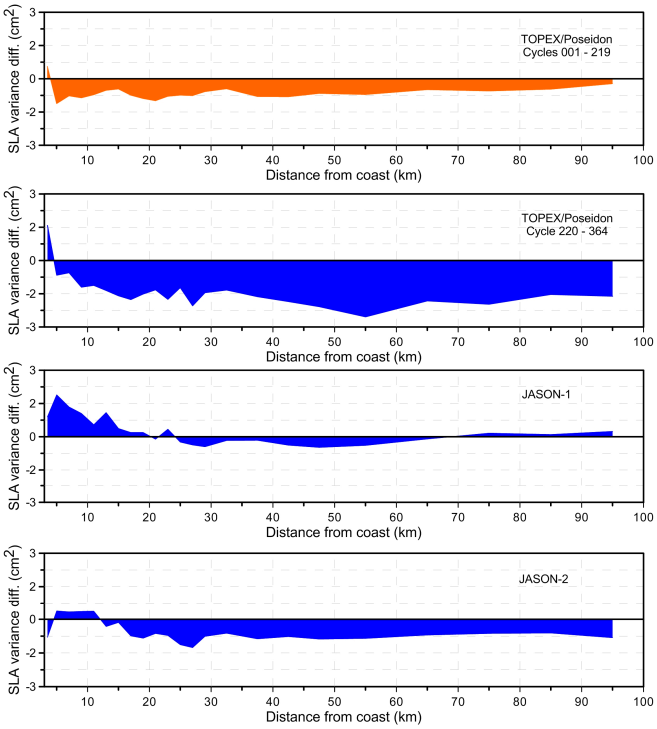

Figure 9. SLA variance differences (cm^2) function of the distance from the coast; **top** to **bottom**: between the smoothed dual-frequency and NIC2009 (orange) for TOPEX/Poseidon cycles 1–219 and between the smoothed dual-frequency and JPL GIM (blue) for TOPEX/Poseidon cycles 220 to 364, Jason-1 cycles 1 to 259 and Jason-2 cycles 1 to 280.

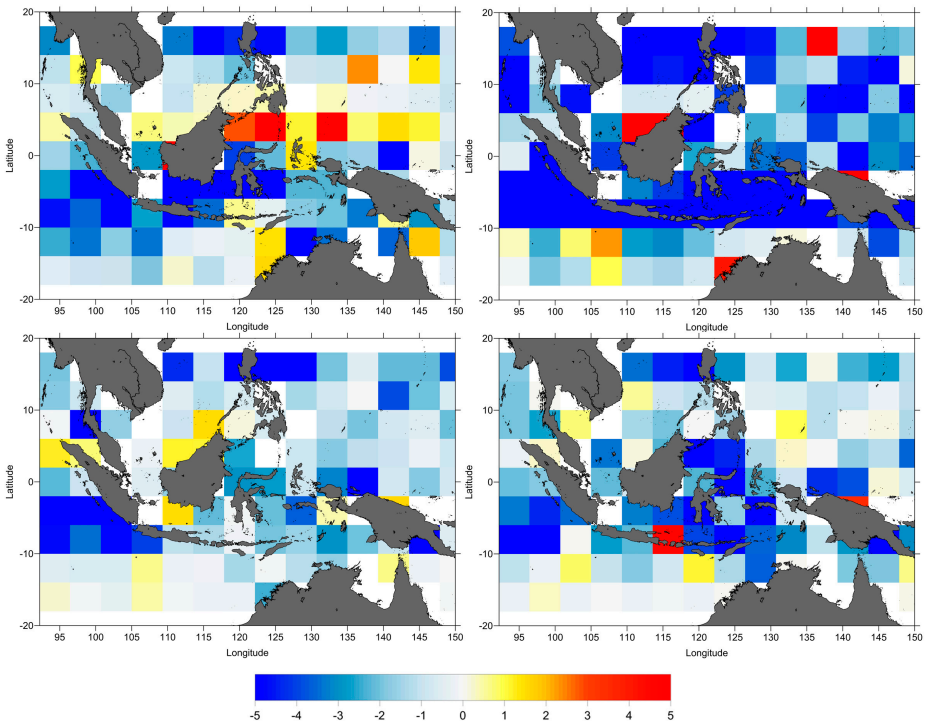

Figure 10. SLA variance differences at crossovers (cm^2), between the smoothed dual-frequency and NIC2009 for TOPEX/Poseidon cycles 1–219 (**top left**) and between the smoothed dual-frequency and JPL GIM for TOPEX/Poseidon cycles 220 to 364 (**top right**); Jason-1 cycles 1 to 259 (**bottom left**) and Jason-2 cycles 1 to 280 (**bottom right**).

3.4. Sea State Bias

Sea state bias (SSB) is an altimeter ranging error caused by the influence of sea-state effects in the radar altimeter measurements, since the surface scattering elements do not contribute equally to the radar return. SSB correction consists of the electromagnetic bias (EMB), tracker bias and skewness. The electromagnetic bias is due to the fact that ocean wave troughs are better radar reflectors than wave crests, thus overestimating the measured satellite-to-surface range. The tracker bias is caused by onboard tracker instrument errors and errors associated with the re-tracking algorithm, while skewness is linked to the effect of a non-Gaussian surface height distribution, inducing an error due to the difference between the determined median sea surface and the true mean sea surface [62,63]. The sea state bias is associated to the ionosphere, due to the frequency-dependent nature of these corrections. An error in the SSB model will cause an error in the ionosphere correction of about 0.175 in scale for TOPEX and Jason-1, function of Ku-band and C-band frequencies [64].

The sea state bias is usually estimated using two-input estimators: the significant wave height (SWH) and wind speed (U_{10}). Parametric models are usually given by three or four parameters, the function of SWH and U_{10}. The coefficients are derived by, e.g., the least square fit of the crossover height differences [41]. The BM4 parametric model is given by the following equation (see also Table 2):

$$SSB = SWH\left(a_1 + a_2 SWH + a_3 U + a_4 U^2\right) \quad (6)$$

where SWH is the significant wave height (in meters), U is the altimeter-derived wind speed (in meters per second), and $a_1, \ldots, a_4$ are coefficients of BM4.

Table 2. Coefficients of BM4 model for satellite altimetry [41].

Mission	a_0	a_1	a_2	a_3	a_4
TOPEX A	0.012450	−0.030578	0.002776	−0.002962	0.000127
TOPEX B	0.028889	−0.032113	0.002992	−0.002780	0.000101
Poseidon	0.015731	−0.062778	0.001894	−0.001194	0.000057

The CLS non-parametric sea state bias model was derived by a statistical methodology based on kernel smoothing [62]. Millions of crossover points can be used to estimate sea state bias on a regular grid of wave height and wind speed. This method can resolve the problem of parameter-derived SSB due to the complexity of the relation between sea state bias, wave height and wind speed [65]. The Tran (non-parametric) model, proposed by [39,40], uses three-input estimators, SWH, U_{10} and the mean gravity wave period (T_m) from a numerical ocean wave model, NOAA's WAVEWATCH III (NWW3). The Tran model gives a good result by reducing SSH variance at global and regional scales.

In order to evaluate the parametric BM4 SSB and the non-parametric CLS SSB models, the comparison of these models was performed for TOPEX. Due to instrument degradation there were two different TOPEX altimeters, TOPEX_A being replaced by TOPEX_B by the end of cycle 235. TOPEX BM4 SSB was determined using data for TOPEX_A for cycles 1 to 235 (leading to TOPEX_A BM4 coefficients) and data for TOPEX_B for cycle 236 to 364 (leading to TOPEX_B BM4 coefficients). For Jason-1 and Jason-2, the non-parametric Tran2012 and CLS SSB models are compared. The results are shown in Figure 11 (along-track SLA variance differences), Figure 12 (SLA variance differences as function of distance to coast) and Figure 13 (SLA variance differences at crossovers). Results show that, while for TOPEX_A the CLS model is a significant improvement with respect to BM4, for TOPEX_B it has a worse performance. For both Jason-1 and Jason-2, Tran2012 leads to a variance reduction with respect to CLS SSB model. By adding one more estimator, mean gravity wave period (T_m) from a numerical ocean wave model (NWW3), the Tran model (3 Parameters) gives an improvement by reducing sea surface height variance, particularly for Jason-2.

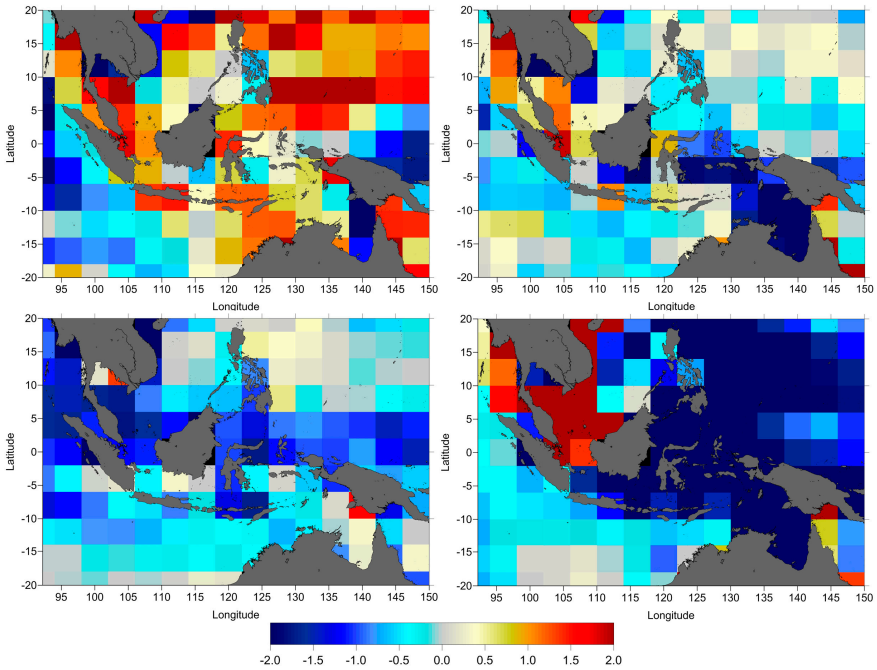

Figure 11. Along-track SLA variance differences (cm^2), **Top** panels: between Sea State Bias Non-Parametric CLS and Sea State Bias Parametric BM4 for TOPEX ((**left**) TOPEX-A cycles 1 to 235; (**right**) TOPEX-B cycles 236 to 264); **Bottom** panels: corresponding differences between Sea State Bias Non-Parametric Tran2012 and CLS SSB models for Jason-1 cycles 1 to 259 (**left**) and Jason-2 cycles 1 to 280 (**right**).

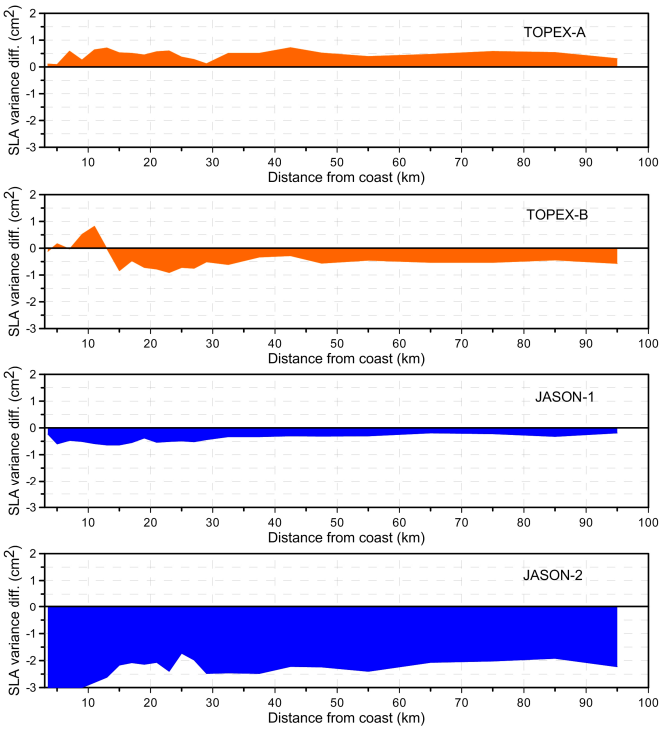

Figure 12. SLA variance differences (cm^2) function of distance from the coast between Sea State Bias Non-Parametric CLS and Sea State Bias Parametric BM4 for TOPEX (orange): TOPEX-A cycles 1 to 235 and TOPEX-B cycles 236 to 264; and Sea State Bias Tran and Non-Parametric CLS (blue): Jason-1 cycles 1 to 259 and Jason-2 cycles 1 to 280.

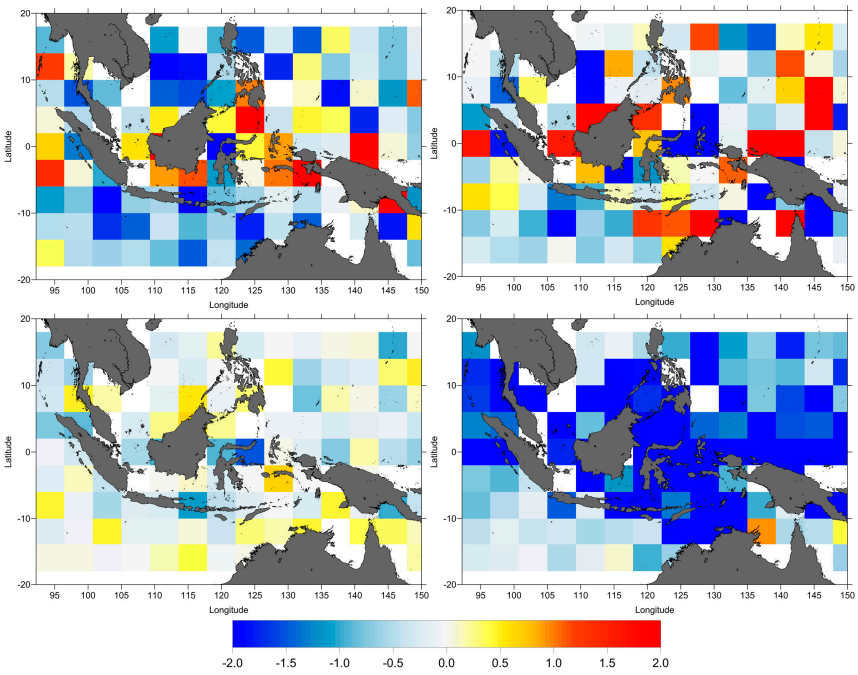

Figure 13. **Top** panels: SLA variance differences at crossovers (cm^2), between Sea State Bias Non-Parametric CLS and Sea State Bias Parametric BM4 for TOPEX ((**left**) TOPEX-A cycles 1 to 235; (**right**) TOPEX-B cycles 236 to 264); **Bottom** panels: corresponding differences between Sea State Bias Non-Parametric Tran2012 and CLS SSB models for Jason-1 cycles 1 to 259 (**left**) and Jason-2 cycles 1 to 280 (**right**).

3.5. Tides Correction

The ocean tide dominates the ocean tide signal, representing more than 80% of the total signal. There are several tidal signals which have smaller amplitudes than the ocean tide: load tide, solid earth tide and pole tide. Using appropriate mathematical formulation, solid earth and pole tide can be derived with centimetric accuracy. In the current study, only the ocean tide and load tide are analysed.

Various models for the ocean and load tides are available in RADS. In the absence of a local ocean tide model for the study region the relatively recent models FES2012 and GOT4.10 were used in this research. FES model, developed by Le Provost [65], was determined by using finite element based on bathymetry and tide gauge data. The FES2012 is provided in RADS as a new tide model which replaced the FES2004. FES2012 is an assimilation model which used the altimetry data and tide gauges in addition to the hydrodynamic model. Using more than 1.5 million nodes and high-resolution global bathymetry, this model proved to be more accurate than FES2004 and GOT4.8 particularly in shallow water and coastal regions [44]. The model is distributed on 1/16° grids and consists of 32 tidal constituents. Unfortunately, tide-loading effects have not yet been computed for FES2012; therefore, GOT load tide model should be used to complete the FES2012 ocean and load tide model [44], and GOT 4.10 is used in this study. The other tide model selected for comparison with FES2012 is GOT4.10 which is the newest model from the set of Global Ocean Tide (GOT) models provided in RADS. GOT models are empirical models derived from satellite altimetry data [43]. In contrast with FES2012 tide model which has 1/16° spatial resolution, GOT 4.10 is provided in rectangular grids 0.5° × 0.5°. The size of grids becomes a problem in coastal regions when the grids do not cover the coastal area. Another version of GOT is GOT-e 4.10c model which has been extrapolated to the shoreline by smoothly extrapolating the GOT4.10 grids. Because no new information has been added, comparisons made for the Indonesia region (not shown) indicate that the GOT-e 4.10c is not more accurate than the original GOT4.10.

To assess the accuracy of the two models, analysis of SLA variance differences along-track, function of the distance from coast and at crossovers was performed. The comparisons between FES2012 and GOT4.10 are presented in Figure 14, illustrating the along-track SLA variance differences, in Figure 15 showing the SLA variance differences function of distance from coast, and in Figure 16 showing SLA variance differences at crossovers. These indicate that, overall and for all three missions, FES2012 leads to a very large reduction in SLA variance compared with GOT4.10 in the coastal zone, for distances less than 60 km, while in the open-ocean GOT4.10 seems to be better than FES2012.

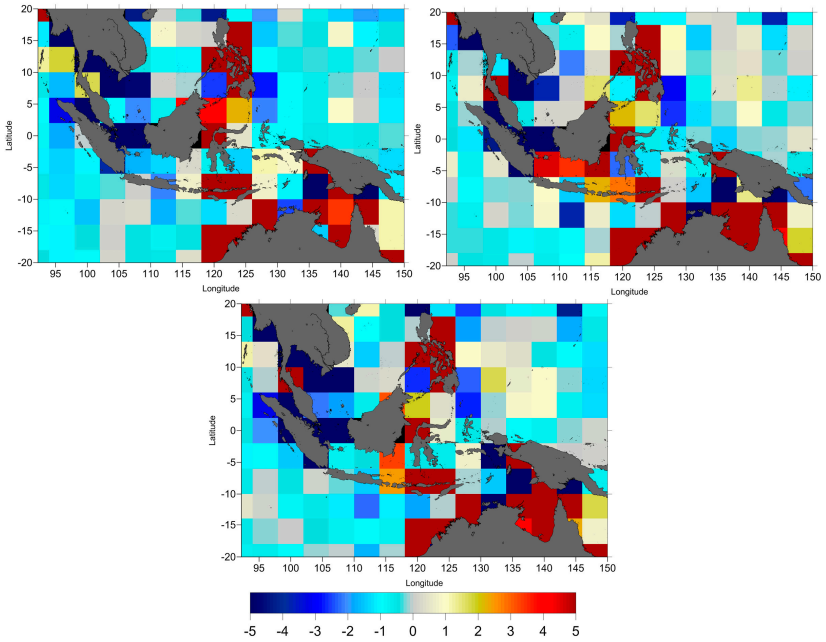

Figure 14. Along-track SLA variance differences (cm^2), between GOT4.10 and FES2012 tide model for TOPEX/Poseidon cycles 1–364, Jason-1 cycles 1 to 259 and Jason-2 cycles 1 to 280.

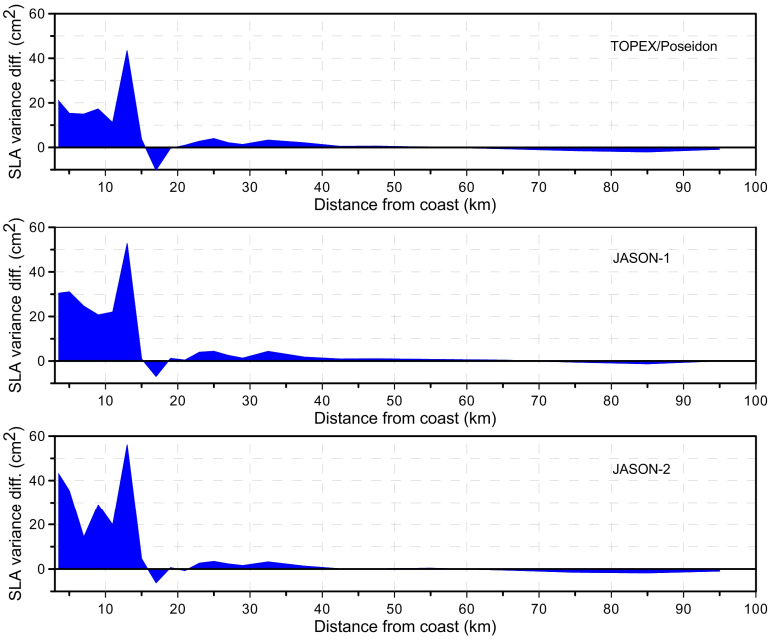

Figure 15. SLA variance differences (cm^2) function of distance from the coast between GOT4.10 and FES2012 tide models for TOPEX cycles 1 to 364, Jason-1 cycles 1 to 259 and Jason-2 cycles 1 to 280.

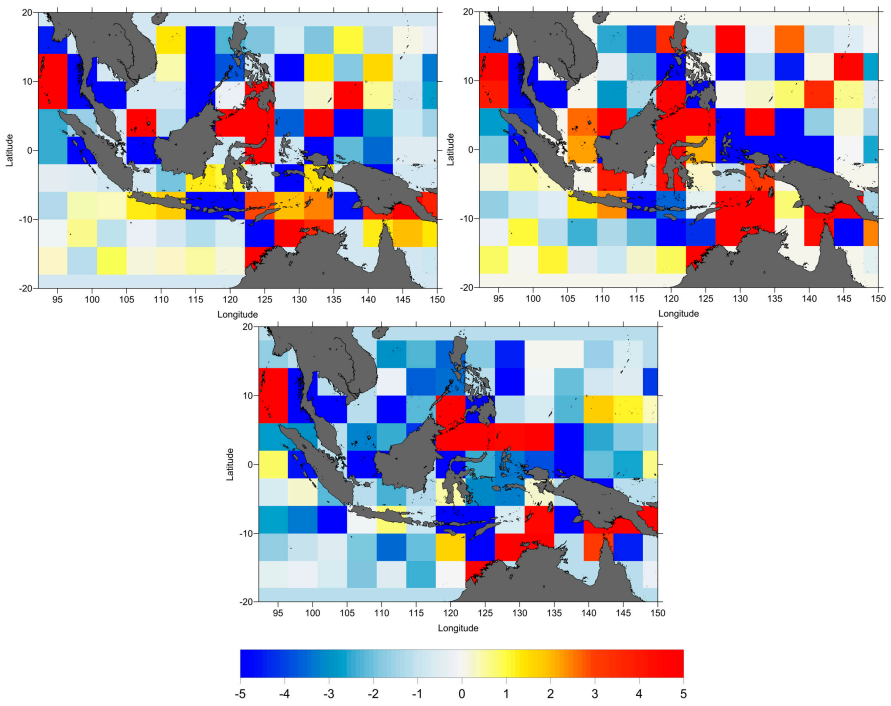

Figure 16. SLA variance differences at crossovers (cm^2), between GOT4.10 and FES2012 tide model for TOPEX/Poseidon cycles 1–364, Jason-1 cycles 1 to 259, and Jason-2 cycles 1 to 280.

3.6. Mean Sea Surface

The mean sea surface is the most important reference surface in studies of sea level variation and it is used to estimate SLA aiming at removing the temporal mean of dynamic sea surface topography [66]. The MSS is the sum of the geoid and the ocean mean dynamic topography (MDT), as follows:

$$h_{MSS} = h_{geoid} + h_{MDT} \tag{7}$$

The most recent improvement in the estimation of geoid models consists in using data from dedicated gravimetric satellites, such as the Gravity Recovery and Climate Experiment (GRACE) and the Gravity Field and Steady-State Ocean Circulation (GOCE). The geoid undulation (geoid height above a reference ellipsoid) reaches about ±100 m. In Indonesia, the geoid undulation ranges from −60 m in western Indonesia to +85 m in eastern Indonesia (Figure 17). Unlike the geoid, the MDT has a variation of only a few meters. Therefore, the MSS range variations are very similar to those of the geoid, thus between −60 m and +85 m in the Indonesia region. It is possible to observe that the MSS has large gradients in this region and that the range of the MSS heights above the reference ellipsoid over the study region is close to the maximum range for the whole world. For this reason, the MSS plays a very important role in sea level estimation in this region.

Various MSS models are available in RADS: CNESCLS2011, DTU10, DTU13, DTU15 and EGM2008. In this study, the CNESCLS2011 and DTU13 MSS were chosen. We did not choose the newest DTU15 MSS because, at the time of the writing of this paper, in RADS it was only available for CryoSat-2, Jason-2, Jason-3 and SARAL/AltiKa satellites [29]. The CNESCLS2011 MSS is a mean sea surface model from CLS/CNES, derived from observations covering 16 years of multiple satellite altimeters (TOPEX/Poseidon, ERS-1 Geodetic Mission, ERS-2, Jason-1, TOPEX/Poseidon interleaved mission, GFO and Envisat) [45]. The DTU13 MSS was derived using 9 different satellites for a 20-year period [46]. These MSS models have been compared aiming at assessing model suitability for use in the Indonesian seas.

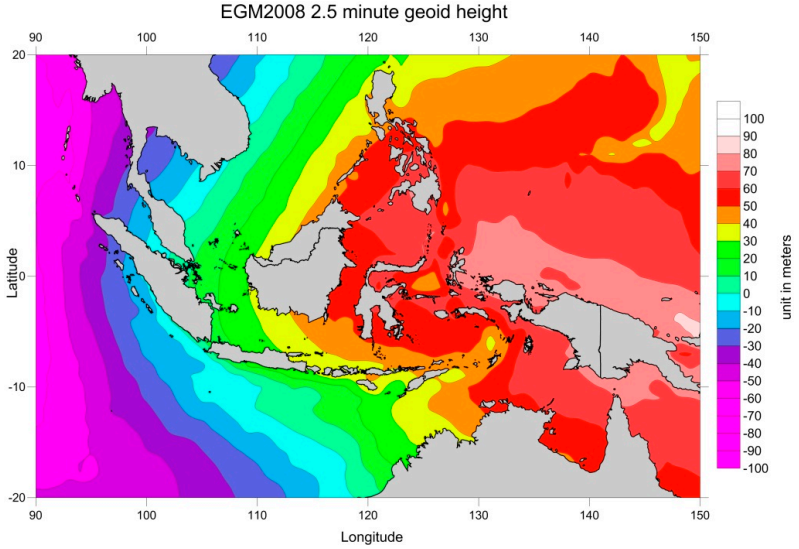

Figure 17. EGM2008 geoid height around the Indonesia seas (Credit: NGA Office of Geomatics; http://earth-info.nga.mil/GandG/wgs84/gravitymod/egm2008/egm08_gis.html).

The results for the comparison between the two analysed MSS models (DTU13 and CNESCLS2011) are shown in Figures 18–20. In the coastal zone, the CNESCLS2011 MSS reduces the SLA variance significantly for distances up to 40 km from the coast when compared with DTU13 (Figure 19). In the open ocean, the SLA variance differences at crossovers between DTU13 MSS and CNESCLS2011 are small (average less than 2 cm^2) (Figure 20) but mainly positive (indicated by yellow to red colours). Due to the nature of the MSS errors, which are time invariant, the along-track SLA variance differences are larger than the corresponding differences at crossovers but also reinforce that CNESCLS2011 is generally better than DTU13 in the coastal regions. The large differences on the coastal areas are mainly due to differences in the methods adopted by each model to extrapolate the MSS values from the sea to land regions.

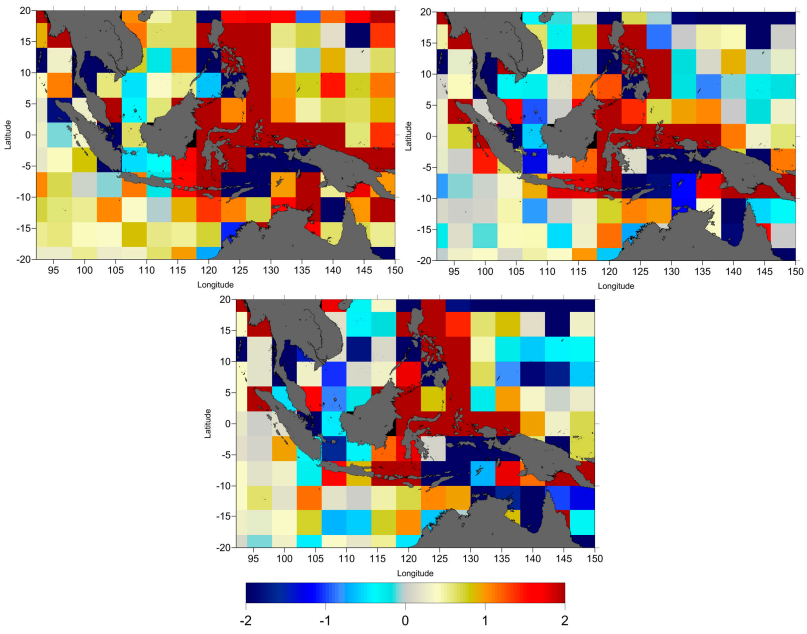

Figure 18. Along-track SLA variance differences (cm^2), between DTU13 and CNESCLS2011 MSS models for TOPEX/Poseidon cycles 1 to 364, Jason-1 cycles 1 to 259 and Jason-2 cycles 1 to 280.

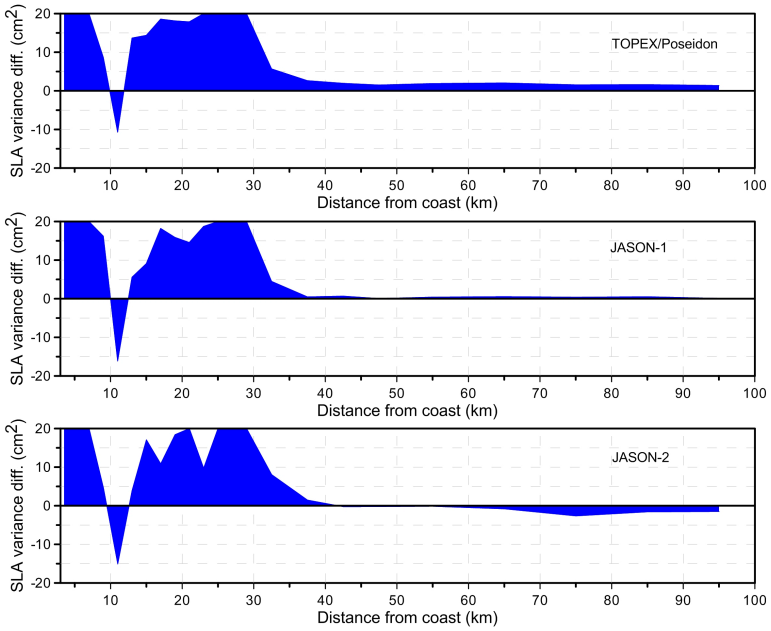

Figure 19. SLA variance differences (cm^2) function of distance from the coast between DTU13 and CNESCLS2011 MSS models for TOPEX/Poseidon cycles 1 to 364, Jason-1 cycles 1 to 259 and Jason-2 cycles 1 to 280.

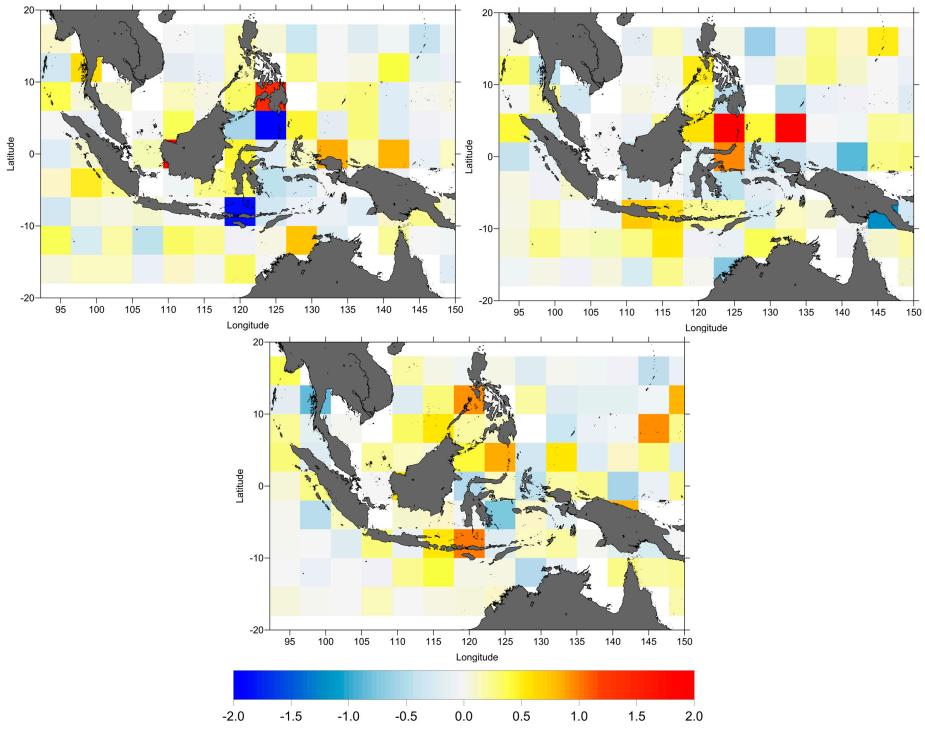

Figure 20. SLA variance differences at crossovers (cm^2), between DTU13 and CNESCLS2011 MSS models for TOPEX/Poseidon cycles 1 to 364, Jason-1 cycles 1 to 259 and Jason-2 cycles 1 to 280.

3.7. Sea Level Variability around the Indonesian Seas

The various range and geophysical corrections and mean sea surface models have been compared and analysed in the previous sections. Table 3 shows the selected range and geophysical corrections and mean sea surface model for use in SLA estimation in the study region.

Table 3. Selected range and geophysical corrections and mean sea surface model.

	TOPEX/Poseidon	Jason-1	Jason-2
Dry Troposphere	ERA-Interim	ERA-Interim	ERA-Interim
Wet Troposphere	GPD+	GPD+	GPD+
Ionosphere	Smoothed Dual Frequency	Smoothed Dual Frequency	Smoothed Dual Frequency
Sea State Bias	TOPEX_A: BM4 TOPEX_B: NP-CLS Poseidon: BM4	Tran2012 Model	Tran2012 Model
Ocean and Load Tide	FES2012 for <60 km GOT 4.10 for >60 km	FES2012 for <60 km GOT 4.10 for >60 km	FES2012 for <60 km GOT 4.10 for >60 km
Mean Sea Surface	CNES CLS 2011	CNES CLS 2011	CNES CLS 2011

In order to build a continuous SLA time series of TOPEX/Poseidon, Jason-1 and Jason-2 altimetric data, the relative difference between consecutive missions must be applied. The relative differences have been computed by analysing the SLA differences between corresponding cycles of the respective tandem missions as shown in Figure 21. By computing the average difference for the 20 cycles of Jason-1 and TOPEX/Poseidon, a relative difference of 4.6 $\pm$ 9.7 mm was found. Similarly, the average of 20 cycle-per-cycle differences of sea level anomaly for Jason-1 and Jason-2 was computed and a relative difference of 30.1 $\pm$ 2.7 mm obtained. Despite the fact that the relative difference between Jason-2 and Jason-1 is slightly bigger than the corresponding relative difference between TP and Jason-1, the standard deviation of Jason-2/Jason-1 differences is small and the pattern of the differences between Jason-1 and Jason-2 seems more homogenous. This may be due to the identical instrument of the Jason-1 and Jason-2 altimeters [67], but also mainly due to the fact that different corrections were applied to each mission. Using TOPEX/Poseidon as a reference, relative differences of 4.6 mm and 34.7 mm were applied to Jason-1 and Jason-2 data, respectively.

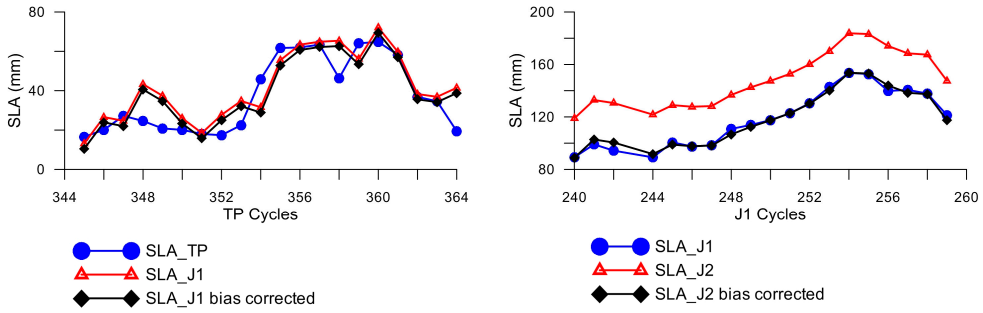

Figure 21. Mean SLA values (mm) for the cycles of the TOPEX/Poseidon–Jason-1 tandem mission (**left**) and for the Jason-1–Jason-2 tandem mission (**right**). Jason-1 values corrected for the (TP, J1) bias and J2 values corrected for the (J1, J2) bias are also shown.

Figure 22 presents the inter-calibrated, relative difference-corrected sea level anomaly time series around the Indonesian seas from all three missions between 1993 and 2015. A 60-day filtering has been applied after removing the seasonal signal (sinusoidal cycle at the annual and semi-annual frequencies) (green line). The raw data are shown in grey dots, the annual variation as a red line and the inter-annual signal is shown as a blue line. The linear trend is computed using least squares. The mean rate of sea level rise is 4.2 $\pm$ 0.2 mm/year over 1993–2015.

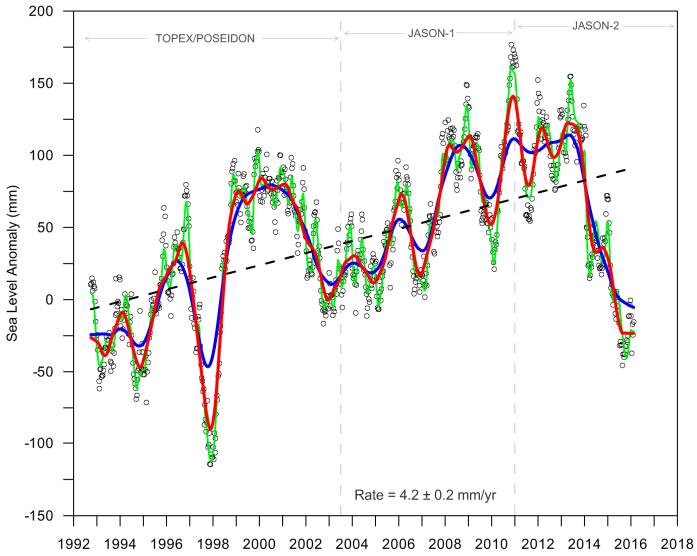

Figure 22. Sea level anomaly (mm) time series around the Indonesian seas from three different satellite altimeters (grey dots), with 60-day smoothing, semi-annual and annual seasonal signals removed (green line), annual variation (red line), and inter-annual variation (blue line) and SLA linear trend (dashed line). The two vertical lines refer to the separation of the periods of the various missions.

It has been shown by [68], that some range and geophysical corrections have a direct impact in mean sea level trend estimation. Considering the corrections analysed in this study, the one with the potential largest impacts is the WTC, due to radiometer instrument drifts and instabilities [54]. Since the GPD+ WTC adopted in this study are a set of corrections that have been calibrated against SSM/I and SSM/IS [34], to investigate the potential impact of this calibration, the mean sea level curve has also been derived with a previous version of these corrections, the so-called GPD, for which no calibration has been performed. The result is shown in Figure 23, illustrating that the difference is very small: 4.3 mm/year for the curve obtained with the non-calibrated GPD versus 4.2 mm/year for the calibrated GPD+ corrections.

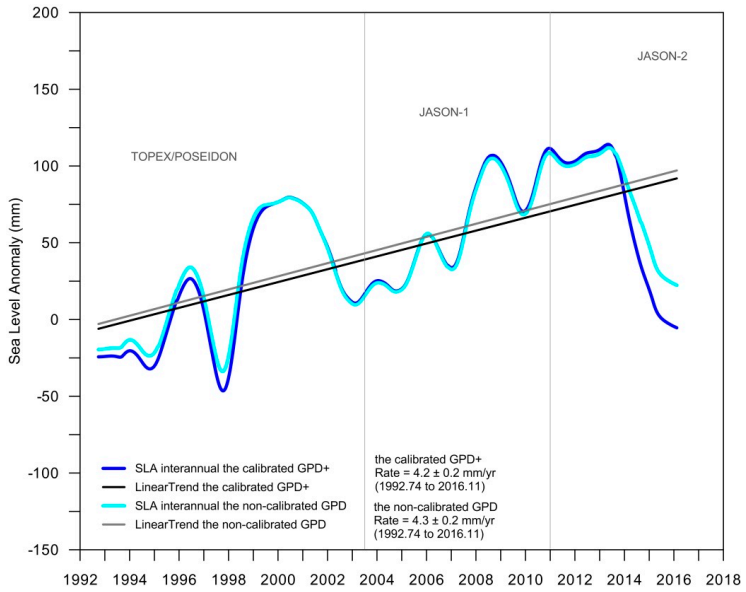

Figure 23. Inter-annual mean sea level variation in the Indonesian seas using the calibrated GPD+ (blue) and corresponding linear trend (black). Inter-annual mean sea level variation in the Indonesian seas using the non-calibrated GPD (cyan) and corresponding linear trend (grey).

Figure 24 shows that the rates of sea level change during the 23-year period (1993–2015) in most areas around the Indonesian seas are higher than the rate of global mean sea level (GMSL). The higher rate is located around the western Pacific (~7 mm/year). The lowest rate is in the Indian Ocean (~2 mm/year).

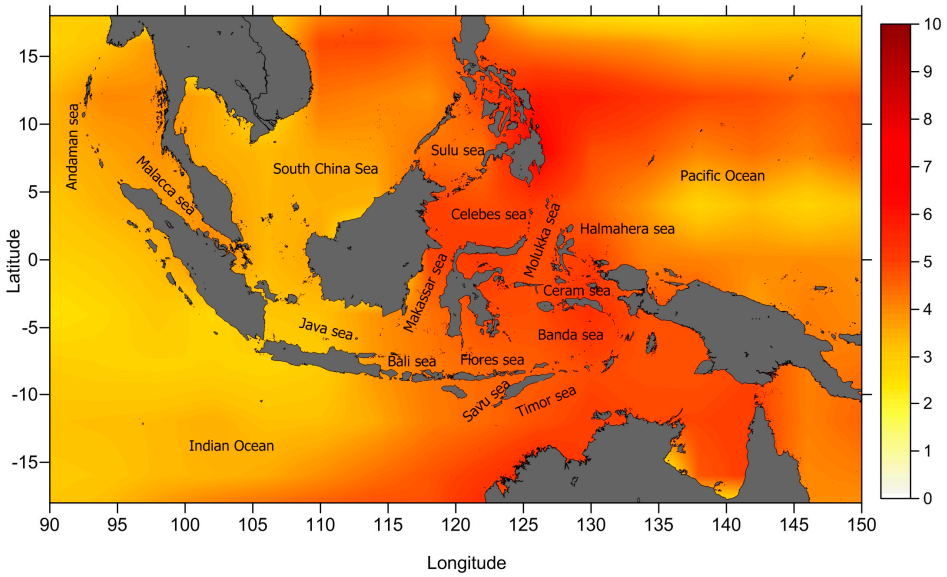

Figure 24. The map of sea level trend (unit in mm/year) around the Indonesian seas, estimated from three different satellite altimeters (T/P, Jason-1 and Jason-2) over 23 years. The map has been computed from the SLA time series of mean cycle values, of 4° × 4° grid, and MSL slope has been determined using least squares.

4. Discussion

Results performed in this study (Figures 2–4) show that when considering two different DTC, the SLA variance differences are very small, less than 0.2 cm^2 near the coast and less than 0.4 cm^2 in the open ocean, indicating that the DTC impact on SLA estimation is negligible. These results are in agreement with [22] who illustrate that the DTC is unaffected by the presence of land and is not degraded close to the coast. For consistency, DTC from ERA Interim was adopted for all satellites.

Figure 6 shows that for TOPEX/Poseidon, the wet tropospheric correction from GPD+ reveals a significant improvement with respect to the MWR correction present in RADS, particularly near the coast for distances less than 25 km and still has a small improvement with respect to ERA-Interim (less than 2 cm^2). For Jason-1 and Jason-2, the GPD+ WTC significantly reduces the SLA variance with respect to the ERA model (about 6 cm^2). Regarding the comparison with the onboard MWR-derived WTC, for Jason-1, the GPD+ correction shows a significant improvement (average differences 4 cm^2). For Jason-2, the GPD+ correction shows a smaller, still significant improvement (less than 3 cm^2), in spite of the fact that this correction is already improved in coastal regions [26].

Figure 5 (along-track SLA variance differences) and Figure 7 (SLA variance differences at crossovers) indicate that GPD+ is an improved correction with respect with ERA-Interim for all three missions, not only near the coast but also in open-ocean. This is expected since GPD+ is based on actual observations, not only from the on-board MWR but also from GNSS and SI-MWR. Results also show that the improvement with respect to ERA is more pronounced for the most recent missions. However, the most significant result is the improvement of the GPD correction with respect to the on-board MWR in the coastal regions, particularly for TP. This is due to the presence of land contaminated and erroneous measurements due to instrument malfunction present in TOPEX/Poseidon data, which rarely occur for Jason-1 and Jason-2 [28]. Figure 23 shows that, for the Indonesian region, while at the

time scale of each individual mission GPD+ WTC has noticeable impacts on sea level trend, for the 23-year period the impact is negligible (4.2 mm/year versus 4.3 mm/year).

Regarding the ionospheric correction, Figure 9 shows that, for TOPEX, the smoothed dual frequency leads to a large improvement for all cycles, particularly for cycles 220 to 364 with a variance reduction up to 2.5 cm^2. Although the ionosphere is insensitive to the coastline, for Jason-1 and Jason-2 the smoothed dual frequency reduces the SLA variance with respect to the JPL-GIM, except for the distances less than 25 km close to the coast. This degradation of the dual-frequency correction in the coastal regions may be due to sea state bias and short-wavelength in the wind field [22]. This may also be due to remaining land contamination still present in the smoothed dual frequency correction. The figures with the along-track SLA variance differences (Figure 8) and at crossovers (Figure 10) show that for TOPEX (cycles 1 to 219), Jason-1 and Jason-2, the smoothed dual frequency does not improve the results homogeneously for the whole Indonesian region, particularly in the Banda Sea, Ceram Sea and Western Pacific and in the Indian Ocean which coincide with unstable regions of the ionosphere [22].

Regarding the SSB correction, Figure 12 shows that, for TOPEX_A, the BM4 parametric model reduces the SLA variance when compared to non-parametric CLS SSB by an average value about 0.5 cm^2; in contrast, TOPEX_B non-parametric CLS sea state bias significantly reduces the SLA variance with respect to BM4 parametric model by about 1 cm^2 with a larger reduction near the coast. For Jason-1 and Jason-2, Tran2012 model shows a significant reduction of the SLA variance when compared to non-parametric CLS SSB, indicated by negative values. The average of SLA variance differences between Tran2012 and CLS SSB (Tran2012 minus CLS SSB) in coastal areas, for Jason-1 is less than 1 cm^2 and for Jason-2 is about 2.5 cm^2. Figures 11 and 13 also indicate that the differences between the non-parametric CLS and parametric BM4 SSB have a coastal signature. For TOPEX/Poseidon, SSB CLS slightly increases the SLA variance near the coast (indicated by colours in the yellow to red range). For Jason-1, the SLA variance differences at crossover show that Tran2012 model is a small improvement with respect to CLS SSB. A significant reduction in SLA variance at crossovers is shown for Jason-2 when SSB Tran2012 model replaces the SSB CLS model (indicated by light to dark blue colours). In addition, for Poseidon (PN), BM4 SSB reduces the SLA variance with respect to BM3 SSB by about 3 cm^2 (the result is not shown).

Figure 15 shows that FES2012 tide model significantly reduces SLA variance compared with GOT4.10 in the coastal zone, for distances up to about 60 km from coast, for all three missions. These results are similar to those by [44], for the comparison of SLA variance between FES2012 and GOT 4.8, who reported significant differences between the models near the coast (less than 60 km from coast). However, FES2012 shows lower performances in some areas due to the lack of assimilated data (no data were available for assimilation in the southern Ocean). Although FES2012 model shows good improvement in the coastal regions, the same does not happen in the open ocean, as shown in Figures 14 and 16. When compared with FES2012, GOT4.10 tide model generally reduces the SLA variance at crossovers in the open ocean and increases it near the coast. The largest differences between the two models occur around deep seas, such as Celebes Sea, Ceram Sea, and Banda Sea. This is partly due to the fact that the grids of the GOT models, which are provided at $0.5^\circ \times 0.5^\circ$, do not extend to the shoreline everywhere, making it problematic to utilize GOT for tidal corrections in the coastal zones, while in FES2012 model more than 1.5 million nodes were used up to the coast. According to the results from the comparison of tide models in this research (Figures 18–20), the global tide models can have very large differences in the coastal zones, suggesting that local tide models are required to account for local ocean variability. Unfortunately, no local tide model is available for the Indonesian region.

Concerning the MSS, results for the study region show that CNESCLS11 leads to a large reduction in along-track SLA variance with respect to DTU13, particularly near the coast for distances up to 60 km. As expected, the results are the same for all satellites, since a given MSS model is a time invariant field.

According to [45], the comparison between CNESCLS2011 MSS with a previous DTU model (DTU10) showed that the DTU10 MSS is less well adjusted for ocean variability studies. The high differences between CNESCLS2011 MSS and DTU10 MSS occur mainly near the coast and at high latitudes. A change in the mean sea surface model adopted in the computation of the SLA affects the SLA variance in a different way than a change in a range or geophysical correction. While e.g., two different WTC affect both the temporal and spatial variability of the sea level, a change in the MSS only affects the spatial variability, the temporal variance at each point remaining constant. In spite of that, Figures 18–20 show that the change in the mean sea surface has a strong impact in this region, particularly in the coastal regions. Figure 20 illustrates that the largest differences between DTU13 and CNESCLS2011 MSS occur on the triple junction area, the junction of the Sunda-Australia-Philippine-Pacific plates. The triple junction area between the island of Sulawesi and the Moluccas in the eastern Indonesia is highly seismically active and presents a very complex tectonic scenario (shown as Figure 25) [69]. The activities of plates will affect the gravity and geoid changes. Since the MSS is correlated with the geoid (Equation (5)), changes in the geoid will have impact in the determination of the MSS.

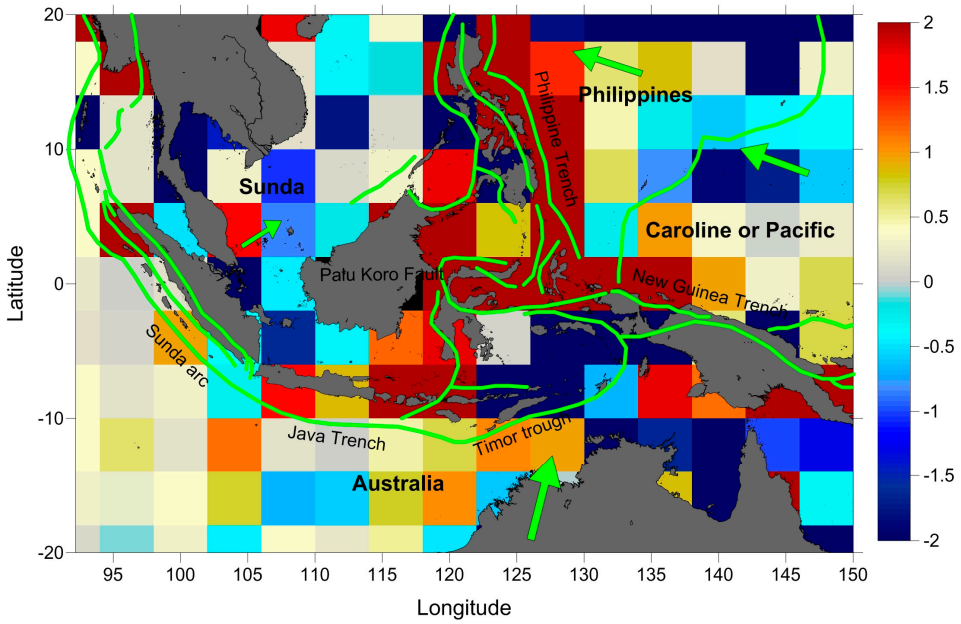

Figure 25. Overlaying along-track SLA variance differences (cm^2), between DTU13 and CNESCLS2011 MSS models for Jason-2 and Structure map of the Sunda-Australia-Philippine-Pacific plates junction area. The green lines are the plate boundaries and the arrows depict the far-field velocity of the plates with respect to Eurasia [69].

The global impact of the El Niño-Southern Oscillation (ENSO) event affects the inter-annual variation of GMSL, particularly over the tropical and sub-tropical Pacific Ocean [16]. ENSO phenomenon is an important component of global climate change, characterised by the appearance of warmer surface water along the equatorial Eastern Pacific Ocean at 2–7 years intervals that can change the precipitation rate, temperature and water vapour during that period. Its effect on the Indonesian seas is significant. The Indonesia seas are considered an oceanic pathway for the Pacific and Indian Oceans where the waters from the Pacific Ocean flow to the Indian Ocean through the Indonesian seas, the so-called Indonesian Throughflow (ITF) [70]. Since the Western Pacific and the Eastern Indian Ocean have a large variability due to inter-annual sea level variability associated with ENSO, the sea level around the Indonesia seas are significantly related with the ENSO event. During El Niño periods, the sea surface height and temperature in the Indonesian seas decrease. In contrast, during La Niña events the trade winds, sea surface height and sea surface temperature increase [16,71–73].

Figure 22 shows that, for the 23-year period the MSL trend for the Indonesian seas is 4.2 mm/year. It is also clearly seen in the same figure that the time series of SLA shows high inter-annual variability. Due to this high variability, the sea level trend determined by fitting a straight line to this curve is strongly dependent on the analysed period. For this reason, the comparison of the trend found in the present work with other studies performed in this region is difficult. For example, the authors in [18] reported that the trend in sea level measured using satellite altimetry during the period 1993–2011 was about 4 mm/year at near selected tide gauge stations. In [19], sea level rise in the Indonesian seas were separated into several sea areas according to the Limit of Ocean and Seas published by the International Hydrographic Organization (IHO) in 1953. For these areas they report sea level trends from 4 to 8 mm/year, based on altimetric measurements during 1993 to 2009. However, in [20], the trends of several seas in the Indonesian region, derived using Cryosat data and retracked Envisat data using ALES, are 2.9 mm/year, 2.9 mm/year, 1.7 mm/year and 3.3 mm/year for Java sea, Flores sea, Banda sea and Ceram sea, respectively, during the period 2002 to 2015.

In order to investigate the correlation between SLA and the ENSO event in the Indonesian seas region, we used the Multivariate ENSO Index (MEI) from NOAA during the study period. MEI is an index which is determined from the varying principle component of six atmospheric-ocean of the Comprehensive Ocean-Atmosphere Data Set (COADS) parameters measured over the tropical pacific and can reflect multiple characteristics of the ENSO phenomena [74]. Figure 26 shows the detrended SLA around the Indonesian seas overlaid with the Multivariate ENSO Index (MEI). The El Niño periods are indicated in red while La Niña periods are shown in blue. The striking feature of this figure is a perfect match of the periods when SLA is positive with those when MEI is negative and of the periods when SLA is negative with those when MEI is positive.

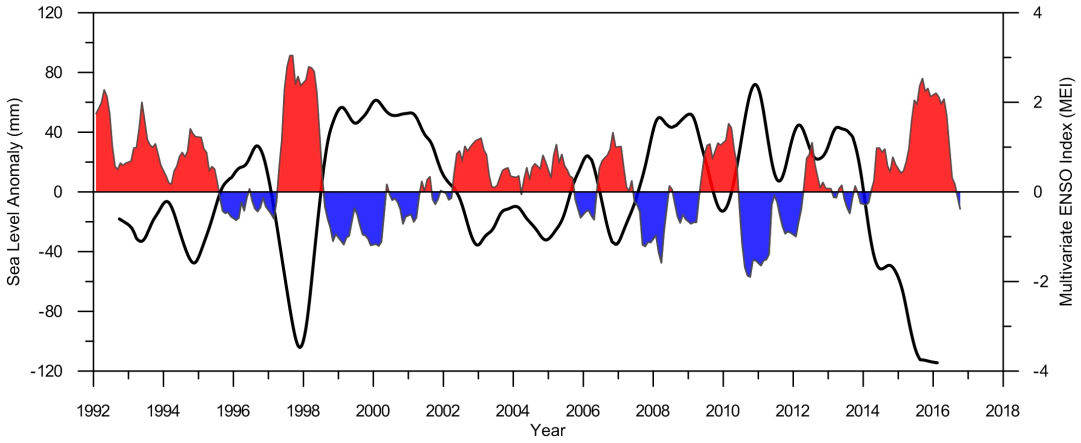

Figure 26. The detrended SLA around the Indonesian Seas (black line) and Multivariate ENSO Index (MEI): El Niño (red) and La Niña (blue).

The ENSO event appeared around the Indonesian seas in several periods, but the strongest El Niño was during 1997–1998 and the strongest La Niña was in 2011. Another noticeable feature of the inter-annual variability seen in Figure 22 is the strong decrease in sea level since 2013, associated with the most recent El Niño.

In addition, the Indonesian seas have correlated behaviour with the surrounding seas, mainly from the South China Sea (SCS) [75]. The fresh and low-saline water from SCS flows into the Indonesian seas through the Java Sea to the Indian Ocean. The SCS water also flows through the Luzon strait to the Makasar strait and thus can influence the variability of ITF [76].

5. Conclusions

In this study, the assessment of various range and geophysical corrections and mean sea surface models has been performed for the Indonesia seas using TOPEX/Poseidon, Jason-1 and Jason-2 data

for a period of 23 years. Table 3 shows the selected set for the various range and geophysical corrections and mean sea surface models, which were used to estimate the SLA time series for this region.

In summary, the best choice and adopted models for the range corrections are, for all missions: the ERA-Interim model for the dry tropospheric correction, the wet tropospheric correction from the GNSS-derived Path Delay algorithm and the smoothed dual-frequency ionospheric correction; the parametric sea state bias (SSB) BM4 model for TOPEX-A and Poseidon, the non-parametric-CLS model for TOPEX-B; the Tran2012 model for Jason-1 and Jason-2. Regarding the geophysical effects, the ocean tide FES2012 shows the best performance in the coastal area up to 60 km while GOT4.10 evidences the best overall performance in the open ocean. The CNESCLS_2011 mean sea surface model was adopted for all missions due to the SLA variance reduction this model causes, particularly in the coastal band up to about 40 km from the coast, when compared with DTU13 MSS.

Using the selected set of corrections and models, the sea level trend in the Indonesia seas has been estimated as 4.2 ± 0.2 mm/year over the 23 years of the altimetric period (1993–2015). If glacial isostatic adjustment (GIA) (0.3 mm/year) is applied, sea level rise is 4.5 mm/year. The rate of sea level rise in this region, derived from altimeter missions over 23 years is higher than the global mean sea level rate about 3.2–3.3 mm/year [13,14]. The positive values of sea level trend in this study are about 2–7 mm/year in agreement with other results in the same areas using altimetry [18–20]. The variability of sea level around the Indonesia seas is high mainly due to the effect of ENSO event (El Niño/La Niña). Due to the strong inter-annual signal, we show that the sea level trend in this region is very sensitive to the time span used in the analysis and to the set of adopted corrections. We show that the detrended SLA time series for the Indonesia region has a strong negative correlation (–0.79) with the Multivariate ENSO Index (MEI).

In this study, the sea level rate has been deduced only from satellite altimetry data. Complementary and relevant information on sea level variation can be derived from tide gauge data. However, due to the instability of the region, tide gauge measurements are often not reliable. Moreover, when analysing tide gauge data, the vertical movement caused by tectonic and volcanic activities and anthropogenic subsidence directly affects the tide gauge measurements. For example, Jakarta, the capital of Indonesia, has subsidence rates about 3–10 mm/year for the period 1974 to 2010 [77] and sea level rise derived by tide gauge time series measurement and satellite altimetry for periods 1993 to 2009 are about 23 mm/year and 3.8 mm/year, respectively [18]. For the future work, due to the high seismic activity around Indonesia, the analysis of altimetry, tide gauge measurement and information of vertical motion can be expected to better characterise the actual sea level change in the Indonesian region, particularly at coastal areas.

Acknowledgments: This work was supported by a grant from the Directorate General of Higher Education (DIKTI), Ministry of Research, Technology and Higher Education of the Republic of Indonesia. The authors would like to acknowledge the Radar Altimeter Database System (RADS) for providing the altimetric data and IGS, Earth Observatory of Singapore (EOS), Geospatial Information Agency (BIG) of Indonesia, Système d'Observation du Niveau des Eaux Littorales (SONEL) for providing the GPS data. We appreciate the valuable comments from 4 anonymous reviewers.

Author Contributions: Eko Handoko and Joana Fernandes conceived the experiments. Eko Handoko designed and performed the experiments; Eko Handoko wrote the manuscript. All authors analysed the data, reviewed the study and edited the manuscript.

Conflicts of Interest: The authors declare no conflict of interest.

References

1. Nicholls, R.J. Impact of and responses to sea-level rise. In *Understanding Sea-Level Rise and Variability*; Church, J.A., Woodworth, P.L., Aarup, T., Wilson, W.S., Eds.; John Wiley & Sons: Chichester, UK, 2010; pp. 17–44.
2. McGranahan, G.; Balk, D.; Anderson, B. The rising tide: Assessing the risks of climate change and human settlements in low elevation coastal zones. *Environ. Urban.* **2007**, *19*, 17–37. [CrossRef]

3. Church, J.A.; White, N.J. Sea-level rise from the late 19th to the early 21st century. *Surv. Geophys.* **2011**, *32*, 585–602. [CrossRef]
4. Intergovernmental Panel on Climate Change (IPCC). *Climate Change 2014: Synthesis Report. Contribution of Working Groups I, II and III to the Fifth Assessment Report of the Intergovernmental Panel on Climate Change*; IPCC: Geneva, Switzerland, 2014.
5. Wöppelmann, G.; Marcos, M. Vertical land motion as a key to understanding sea level change and variability. *Rev. Geophys.* **2016**, *54*, 64–92. [CrossRef]
6. Yildiz, H.; Andersen, O.B.; Simav, M.; Aktug, B.; Ozdemir, S. Estimates of vertical land motion along the southwestern coasts of Turkey from coastal altimetry and tide gauge data. *Adv. Space Res.* **2013**, *51*, 1572–1580. [CrossRef]
7. Chelton, D.B.; Ries, J.C.; Haines, B.J.; Fu, L.L.; Callahan, P.S. Satellite altimetry. In *Satellite Altimetry and Earth Sciences: A Handbook of Techniques and Applications*; Fu, L.L., Cazenave, A., Eds.; Academic Press: San Diego, CA, USA, 2001; pp. 1–132.
8. Wingham, D.J.; Francis, C.R.; Baker, S.; Bouzinac, C.; Brockley, D.; Cullen, R.; de Chateau-Thierry, P.; Laxon, S.W.; Mallow, U.; Mavrocordatos, C.; et al. Cryosat: A mission to determine the fluctuations in earth's land and marine ice fields. *Adv. Space Res.* **2006**, *37*, 841–871. [CrossRef]
9. Ricker, R.; Hendricks, S.; Helm, V.; Gerdes, R. Classification of CryoSat-2 radar echoes. In *Towards an Interdisciplinary Approach in Earth System Science*; Lohmann, G., Meggers, H., Unnithan, V., Wolf-Gladrow, D., Notholt, J., Bracher, A., Eds.; Springer: Berlin/Heidelberg, Germany, 2015; pp. 149–158.
10. Ray, C.; Martin-Puig, C.; Clarizia, M.P.; Ruffini, G.; Dinardo, S.; Gommenginger, C.; Benveniste, J. SAR altimeter backscattered waveform model. *IEEE Trans. Geosci. Remote Sens.* **2015**, *53*, 911–919. [CrossRef]
11. Rey, L.; Chateau-Thierry, P.D.; Phalippou, L.; Mavrocordatos, C.; Francis, R. SIRAL, a high spatial resolution radar altimeter for the Cryosat mission. In Proceedings of the IEEE 2001 International Geoscience and Remote Sensing Symposium, Sydney, Ausralia, 9–13 July 2001; Volume 3087, pp. 3080–3082.
12. European Space Agency (ESA); University College of London (UCL). *Cryosat Product Handbook*; ESRIN-ESA and Mullard Space Science Laboratory, University College London: London, UK, 2012.
13. Cazenave, A.; Dieng, H.-B.; Meyssignac, B.; von Schuckmann, K.; Decharme, B.; Berthier, E. The rate of sea-level rise. *Nat. Clim. Chang.* **2014**, *4*, 358–361. [CrossRef]
14. Church, J.A.; Clark, P.U.; Cazenave, A.; Gregory, J.M.; Jevrejeva, S.; Levermann, A.; Merrifield, M.A.; Milne, G.A.; Nerem, R.S.; Nunn, P.D.; et al. Sea level change. In *Climate Change 2013: The Physical Science Basis*; Contribution of Working Group I to the Fifth Assessment Report of the Intergovernmental Panel on Climate Change; Stocker, T.F., Qin, D., Plattner, G.-K., Tignor, M., Allen, S.K., Boschung, J., Nauels, A., Xia, Y., Bex, V., Midgley, P.M., Eds.; Cambridge University Press: Cambridge, UK; New York, NY, USA, 2013; pp. 1137–1216.
15. Nicholls, R.J.; Cazenave, A. Sea-level rise and its impact on coastal zones. *Science* **2010**, *328*, 1517–1520. [CrossRef] [PubMed]
16. Church, J.A.; White, N.J.; Hunter, J.R. Sea-level rise at tropical Pacific and Indian Ocean Islands. *Glob. Planet. Chang.* **2006**, *53*, 155–168. [CrossRef]
17. Cazenave, A.; Henry, O.; Munier, S.; Delcroix, T.; Gordon, A.L.; Meyssignac, B.; Llovel, W.; Palanisamy, H.; Becker, M. Estimating ENSO influence on the global mean sea level, 1993–2010. *Mar. Geod.* **2012**, *35*, 82–97. [CrossRef]
18. Fenoglio-Marc, L.; Schöne, T.; Illigner, J.; Becker, M.; Manurung, P.; Khafid. Sea level change and vertical motion from satellite altimetry, tide gauges and GPS in the Indonesian region. *Mar. Geod.* **2012**, *35*, 137–150. [CrossRef]
19. Strassburg, M.W.; Hamlington, B.D.; Leben, R.R.; Manurung, P.; Lumban Gaol, J.; Nababan, B.; Vignudelli, S.; Kim, K.Y. Sea level trends in southeast Asian seas. *Clim. Past* **2015**, *11*, 743–750. [CrossRef]
20. Passaro, M.; Dinardo, S.; Quartly, G.D.; Snaith, H.M.; Benveniste, J.; Cipollini, P.; Lucas, B. Cross-calibrating ales envisat and cryosat-2 delay–doppler: A coastal altimetry study in the Indonesian seas. *Adv. Space Res.* **2016**, *58*, 289–303. [CrossRef]
21. Dahuri, R.; Rais, J.; Ginting, S.P.; Sitepu, M.J. *Pengelolaan Sumber Daya Pesisir Dan Lautan Secara Terpadu*, 1st ed.; Balai Pustaka: Jakarta, Indonesia, 2008.

22. Andersen, O.B.; Scharroo, R. Range and geophysical corrections in coastal regions: And implications for mean sea surface determination. In *Coastal Altimetry*; Vignudelli, S., Kostianoy, A.G., Cipollini, P., Benveniste, J., Eds.; Springer: Berlin/Heidelberg, Germany, 2011; pp. 103–145.
23. Fernandes, M.; Lázaro, C.; Nunes, A.; Scharroo, R. Atmospheric corrections for altimetry studies over inland water. *Remote Sens.* **2014**, *6*, 4952–4997. [CrossRef]
24. Gommenginger, C.; Thibaut, P.; Fenoglio-Marc, L.; Quartly, G.; Deng, X.; Gómez-Enri, J.; Challenor, P.; Gao, Y. Retracking altimeter waveforms near the coasts. In *Coastal Altimetry*; Vignudelli, S., Kostianoy, A.G., Cipollini, P., Benveniste, J., Eds.; Springer: Berlin/Heidelberg, Germany, 2011; pp. 61–101.
25. Passaro, M.; Cipollini, P.; Vignudelli, S.; Quartly, G.D.; Snaith, H.M. ALES: A multi-mission adaptive subwaveform retracker for coastal and open ocean altimetry. *Remote Sens. Environ.* **2014**, *145*, 173–189. [CrossRef]
26. Brown, S. A novel near-land radiometer wet path-delay retrieval algorithm: Application to the Jason-2/OSTM advanced microwave radiometer. *IEEE Trans. Geosci. Remote Sens.* **2010**, *48*, 1986–1992. [CrossRef]
27. Fernandes, M.J.; Lázaro, C.; Nunes, A.L.; Pires, N.; Bastos, L.; Mendes, V.B. GNSS-derived path delay: An approach to compute the wet tropospheric correction for coastal altimetry. *IEEE Geosci. Remote Sens. Lett.* **2010**, *7*, 596–600. [CrossRef]
28. Fernandes, M.J.; Lázaro, C.; Ablain, M.; Pires, N. Improved wet path delays for all ESA and reference altimetric missions. *Remote Sens. Environ.* **2015**, *169*, 50–74. [CrossRef]
29. Scharroo, R. *RADS Version 3.1: User Manual and Format Specification*; Delft University of Technology: Delft, The Netherlands, 2012.
30. Boehm, J.; Werl, B.; Schuh, H. Troposphere mapping functions for GPS and very long baseline interferometry from European Centre for Medium-range Weather Forecasts operational analysis data. *J. Geophys. Res. Solid Earth* **2006**, *111*. [CrossRef]
31. Dee, D.P.; Uppala, S.M.; Simmons, A.J.; Berrisford, P.; Poli, P.; Kobayashi, S.; andrae, U.; Balmaseda, M.A.; Balsamo, G.; Bauer, P.; et al. The ERA-interim reanalysis: Configuration and performance of the data assimilation system. *Q. J. R. Meteorol. Soc.* **2011**, *137*, 553–597. [CrossRef]
32. Caplan, P.; Derber, J.; Gemmill, W.; Hong, S.Y.; Pan, H.L.; Parrish, D. Changes to the 1995 NCEP operational medium-range forecast model analysis–forecast system. *Weather Forecast.* **1997**, *12*, 581–594. [CrossRef]
33. Legeais, J.F.; Ablain, M.; Thao, S. Evaluation of wet troposphere path delays from atmospheric reanalyses and radiometers and their impact on the altimeter sea level. *Ocean Sci.* **2014**, *10*, 893–905. [CrossRef]
34. Fernandes, M.; Lázaro, C. GPD+ wet tropospheric corrections for CryoSat-2 and GFO altimetry missions. *Remote Sens.* **2016**, *8*, 851. [CrossRef]
35. Komjathy, A.; Sparks, L.; Wilson, B.D.; Mannucci, A.J. Automated daily processing of more than 1000 ground-based GPS receivers for studying intense ionospheric storms. *Radio Sci.* **2005**, *40*. [CrossRef]
36. Scharroo, R.; Smith, W.H.F. A Global Positioning System-based climatology for the total electron content in the ionosphere. *J. Geophys. Res. Space Phys.* **2010**, *115*. [CrossRef]
37. Bilitza, D. *International Reference Ionosphere 1990*; National Space Science Data Center: Lanham, MD, USA, 1990.
38. Bilitza, D.; Reinisch, B.W. International reference ionosphere 2007: Improvements and new parameters. *Adv. Space Res.* **2008**, *42*, 599–609. [CrossRef]
39. Tran, N.; Vandemark, D.; Chapron, B.; Labroue, S.; Feng, H.; Beckley, B.; Vincent, P. New models for satellite altimeter sea state bias correction developed using global wave model data. *J. Geophys. Res.* **2006**, *111*. [CrossRef]
40. Tran, N.; Philipps, S.; Poisson, J.-C.; Urien, S.; Bronner, E.; Picot, N. *Impact of GDR_d Standards on SSB Corrections*; OSTST: Venice, Italy, 2012.
41. Scharroo, R.; Lillibridge, J. Non-Parametric Sea-State Bias Models and Their Relevance to Sea Level Change Studies. In Proceedings of the 2004 Envisat & ERS Symposium (ESA SP-572), Salzburg, Austria, 6–10 September 2004.
42. Gaspar, P.; Labroue, S.; Ogor, F.; Lafitte, G.; Marchal, L.; Rafanel, M. Improving nonparametric estimates of the sea state bias in radar altimeter measurements of sea level. *J. Atmos. Ocean. Technol.* **2002**, *19*, 1690–1707. [CrossRef]
43. Ray, R.D. *A Global Ocean Tide Model from TOPEX/POSEIDON Altimetry: Got99.2*; NASA Technical Memorandum: NASA/TM-1999-209478; Goddard Space Flight Center: Greenbelt, MD, USA, 1999; p. 58.

44. Carrère, L.; Lyard, F.; Cancet, M.; Guillot, A.; Roblou, L. Fes 2012: A New Global Tidal Model Taking Advantage of Nearly 20 Years of Altimetry. In Proceedings of the 20 years of Progress in Radar Altimetry, Venice, Italy, 24–29 September 2012.
45. Schaeffer, P.; Faugére, Y.; Legeais, J.F.; Ollivier, A.; Guinle, T.; Picot, N. The CNES_CLS11 global mean sea surface computed from 16 years of satellite altimeter data. *Mar. Geod.* **2012**, *35*, 3–19. [CrossRef]
46. Andersen, O.; Knudsen, P.; Stenseng, L. The DTU13 MSS (mean sea surface) and MDT (mean dynamic topography) from 20 years of satellite altimetry. In *International Association of Geodesy Symposia*; Springer: Berlin/Heidelberg, Germany, 2015.
47. Carrère, L.; Lyard, F. Modeling the barotropic response of the global ocean to atmospheric wind and pressure forcing—Comparisons with observations. *Geophys. Res. Lett.* **2003**, *30*. [CrossRef]
48. Cleveland, R.B.; Cleveland, W.S.; McRae, J.E.; Terpenning, I. STL: A seasonal-trend decomposition procedure base on loess. *J. Off. Stat.* **1990**, *6*, 3–73.
49. Fu, L.-L.; Christensen, E.J.; Yamarone, C.A.; Lefebvre, M.; Ménard, Y.; Dorrer, M.; Escudier, P. TOPEX/Poseidon mission overview. *J. Geophys. Res.* **1994**, *99*, 24369. [CrossRef]
50. Menard, Y.; Fu, L.L.; Escudier, P.; Parisot, F.; Perbos, J.; Vincent, P.; Desai, S.; Haines, B.J.; Kunstmann, G. The Jason-1 mission. *Mar. Geod.* **2003**, *26*, 131–146. [CrossRef]
51. Lambin, J.; Morrow, R.; Fu, L.-L.; Willis, J.K.; Bonekamp, H.; Lillibridge, J.; Perbos, J.; Zaouche, G.; Vaze, P.; Bannoura, W.; et al. The OSTM/Jason-2 mission. *Mar. Geod.* **2010**, *33*, 4–25. [CrossRef]
52. Keihm, S.; Ruf, C.S. Role of water vapor radiometers for in-flight calibration of the TOPEX microwave radiometer. *Mar. Geod.* **1995**, *18*, 139–156. [CrossRef]
53. Haines, B.J.; Bar-Sever, Y.E. Monitoring the TOPEX microwave radiometer with GPS: Stability of columnar water vapor measurements. *Geophys. Res. Lett.* **1998**, *25*, 3563–3566. [CrossRef]
54. Scharroo, R.; Lillibridge, J.L.; Smith, W.H.F.; Schrama, E.J.O. Cross-calibration and long-term monitoring of the microwave radiometers of ERS, TOPEX, GFO, Jason and Envisat. *Mar. Geod.* **2004**, *27*, 279–297. [CrossRef]
55. Desai, S.D.; Haines, B.J. Monitoring measurements from the Jason-1 microwave radiometer and independent validation with GPS. *Mar. Geod.* **2004**, *27*, 221–240. [CrossRef]
56. Edwards, S.; Moore, P.; King, M. Assessment of the jason-1 and TOPEX/Poseidon microwave radiometer performance using GPS from offshore sites in the North Sea. *Mar. Geod.* **2004**, *27*, 717–727. [CrossRef]
57. Macmillan, D.S.; Beckley, B.D.; Fang, P. Monitoring the TOPEX and Jason-1 microwave radiometers with GPS and VLBI wet zenith path delays. *Mar. Geod.* **2004**, *27*, 703–716. [CrossRef]
58. Sibthorpe, A.; Brown, S.; Desai, S.D.; Haines, B.J. Calibration and validation of the Jason-2/OSTM advanced microwave radiometer using terrestrial GPS stations. *Mar. Geod.* **2011**, *34*, 420–430. [CrossRef]
59. Zlotnicki, V.; Desai, S.D. Assessment of the Jason microwave radiometer's measurement of wet tropospheric path delay using comparisons to SSM/I and TMI. *Mar. Geod.* **2004**, *27*, 241–253. [CrossRef]
60. Desportes, C.; Obligis, E.; Eymard, L. On the wet tropospheric correction for altimetry in coastal regions. *IEEE Trans. Geosci. Remote Sens.* **2007**, *45*, 2139–2149. [CrossRef]
61. Fernandes, M.; Nunes, A.; Lázaro, C. Analysis and inter-calibration of wet path delay datasets to compute the wet tropospheric correction for CryoSat-2 over ocean. *Remote Sens.* **2013**, *5*, 4977–5005. [CrossRef]
62. Gommenginger, C.P.; Srokosz, M.A. Sea State Bias—20 Years on. In Proceedings of the 15 Years of Progress in Radar Altimetry, Venice, Italy, 13–18 March 2006.
63. Pires, N.; Fernandes, M.; Gommenginger, C.; Scharroo, R. A conceptually simple modeling approach for Jason-1 sea state bias correction based on 3 parameters exclusively derived from altimetric information. *Remote Sens.* **2016**, *8*, 576. [CrossRef]
64. Chambers, D.P.; Hayes, S.A.; Ries, J.C.; Urban, T.J. New TOPEX sea state bias models and their effect on global mean sea level. *J. Geophys. Res.* **2003**, *108*. [CrossRef]
65. Le Provost, C.; Genco, M.L.; Lyard, F.; Vincent, P.; Canceil, P. Spectroscopy of the world ocean tides from a finite element hydrodynamic model. *J. Geophys. Res.* **1994**, *99*, 24777. [CrossRef]
66. Andersen, O.B.; Knudsen, P. DNSC08 mean sea surface and mean dynamic topography models. *J. Geophys. Res.* **2009**, *114*. [CrossRef]
67. Nerem, R.S.; Chambers, D.P.; Choe, C.; Mitchum, G.T. Estimating mean sea level change from the Topex and Jason Altimeter missions. *Mar. Geod.* **2010**, *33*, 435–446. [CrossRef]
68. Fernandes, M.J.; Barbosa, S.M.; Lázaro, C. Impact of altimeter data processing on sea level studies. *Sensors* **2006**, *6*, 131–133. [CrossRef]

69. Socquet, A.; Simons, W.; Vigny, C.; McCaffrey, R.; Subarya, C.; Sarsito, D.; Ambrosius, B.; Spakman, W. Microblock rotations and fault coupling in SE Asia triple junction (Sulawesi, Indonesia) from GPS and earthquake slip vector data. *J. Geophys. Res.* **2006**, *111*. [CrossRef]
70. Gordon, A.L. Oceanography of the Indonesian seas and their throughflow. *Oceanography* **2005**, *18*, 14–27. [CrossRef]
71. Merrifield, M.A.; Thompson, P.R.; Lander, M. Multidecadal sea level anomalies and trends in the western tropical pacific. *Geophys. Res. Lett.* **2012**, *39*. [CrossRef]
72. England, M.H.; Huang, F. On the interannual variability of the Indonesian throughflow and its linkage with ENSO. *J. Clim.* **2005**, *18*, 1435–1444. [CrossRef]
73. Potemra, J.T.; Schneider, N. Interannual variations of the Indonesian throughflow. *J. Geophys. Res.* **2007**, *112*. [CrossRef]
74. Wolter, K.; Timlin, M.S. El Niño/Southern Oscillation behaviour since 1871 as diagnosed in an extended multivariate ENSO index (MEI.ext). *Int. J. Climatol.* **2011**, *31*, 1074–1087. [CrossRef]
75. Gordon, A.L.; Huber, B.A.; Metzger, E.J.; Susanto, R.D.; Hurlburt, H.E.; Adi, T.R. South China Sea throughflow impact on the Indonesian throughflow. *Geophys. Res. Lett.* **2012**, *39*, L11602. [CrossRef]
76. Liu, Q.; Huang, R.; Wang, D.; Xie, Q.; Huang, Q. Interplay between the Indonesian throughflow and the south china sea throughflow. *Chin. Sci. Bull.* **2006**, *51*, 50–58. [CrossRef]
77. Abidin, H.Z.; Andreas, H.; Gumilar, I.; Brinkman, J.J. Study on the risk and impacts of land subsidence in Jakarta. *Proc. Int. Assoc. Hydrol. Sci.* **2015**, *372*, 115–120. [CrossRef]